

UNDERSTANDING THE CIRCUMGALACTIC MEDIUM THROUGH  
HYDRODYNAMIC SIMULATIONS AND *HUBBLE'S* COSMIC ORIGINS  
SPECTROGRAPH

by  
Amanda Brady Ford

---

A Dissertation Submitted to the Faculty of the  
DEPARTMENT OF ASTRONOMY  
In Partial Fulfillment of the Requirements  
For the Degree of  
DOCTOR OF PHILOSOPHY  
In the Graduate College  
THE UNIVERSITY OF ARIZONA

2014

THE UNIVERSITY OF ARIZONA  
GRADUATE COLLEGE

As members of the Dissertation Committee, we certify that we have read the dissertation prepared by Amanda Brady Ford entitled “Understanding the Circumgalactic Medium Through Hydrodynamic Simulations and *Hubble’s* Cosmic Origins Spectrograph” and recommend that it be accepted as fulfilling the dissertation requirement for the Degree of Doctor of Philosophy.

\_\_\_\_\_  
Romeel Davé Date: 8 May 2014

\_\_\_\_\_  
George Rieke Date: 8 May 2014

\_\_\_\_\_  
Phil Pinto Date: 8 May 2014

\_\_\_\_\_  
Chris Walker Date: 8 May 2014

\_\_\_\_\_  
Desika Narayan Date: 8 May 2014

Final approval and acceptance of this dissertation is contingent upon the candidate’s submission of the final copies of the dissertation to the Graduate College.

I hereby certify that I have read this dissertation prepared under my direction and recommend that it be accepted as fulfilling the dissertation requirement.

\_\_\_\_\_  
Dissertation Director: Romeel Davé Date: 8 May 2014

## STATEMENT BY AUTHOR

This dissertation has been submitted in partial fulfillment of requirements for an advanced degree at The University of Arizona and is deposited in the University Library to be made available to borrowers under rules of the Library.

Brief quotations from this dissertation are allowable without special permission, provided that accurate acknowledgment of source is made. Requests for permission for extended quotation from or reproduction of this manuscript in whole or in part may be granted by the head of the major department or the Dean of the Graduate College when in his or her judgment the proposed use of the material is in the interests of scholarship. In all other instances, however, permission must be obtained from the author.

SIGNED: Amanda Brady Ford

## ACKNOWLEDGMENTS

I would like to thank my advisor, Romeel Davé, for all the guidance, for being willing to Skype at all hours of night and day, and for sending me to conferences all around the world. I would also like to thank my chief collaborator, Ben Oppenheimer, who has become a friend. Many thanks are also due to my other collaborators for contributing their expertise and time so I could more fully integrate the various facets of this field: Neal Katz, Juna Kollmeier (who let me use her supercomputer!), David Weinberg, Jason Tumlinson, Jessica Werk, Molly Peeples, Jason X. Prochaska, Robert Thompson, Charlotte Christensen, and the whole COS-Halos team.

I'd like to also thank my committee. George, thank you for your guidance and support from the first month of graduate school onward. Desika, thank you for your career advice and encouragement, as well as your enthusiasm for this work. Phil, thanks to you I have actually written, from scratch, a working SPH code! Chris, thank you for your kindness and excellent teaching.

I would like to thank other Steward faculty, including Daniel Einsenstein, Yancy Shirley, Rodger Thompson, and Nick Wolfe, for help early on. Also, many thanks to Dr. Randall Correll and Brigadier General (retired) Pete Worden, Ph.D., for their encouragement and support as I decided to go back to graduate school.

Finally, to the other graduate students who have helped me over the years, in particular Suresh Sivanandam, Amelia Stutz, Moire Prescott, Kristian Finlator, Andy Marble, Megan Reiter, Kyle Penner, Xiao Xu, Greg Walth, and Jared Gabor: thank you.



## DEDICATION

This thesis is dedicated to my family. To my mom, who made multiple trips to Tucson to help care for my family while I went on travel; to my siblings, who took the time to try to understand my work; to my in-laws, who offered lots of practical assistance; and to my extended family who were excited for me and my progress.

Most especially, this is dedicated to my husband Dan, who helped in virtually every possible way, and to our three-year-old son Ivan, who (blissfully, gleefully, joyfully) most definitely did not help *at all*.

## TABLE OF CONTENTS

LIST OF FIGURES . . . . .	9
LIST OF TABLES . . . . .	17
ABSTRACT . . . . .	18
1 INTRODUCTION . . . . .	19
1.1 Defining the CGM . . . . .	20
1.2 Motivation . . . . .	21
1.2.1 Observational Opportunity . . . . .	22
1.2.2 Theoretical Understanding . . . . .	25
1.3 The Multi-Phase, Metal-Rich CGM . . . . .	26
1.4 Nature of Outflows . . . . .	28
1.5 Inflows and Outflows: Understanding the CGM's Baryon Cycle . .	30
1.6 Connection to COS Observations . . . . .	33
1.7 Introduction Summary . . . . .	34
2 HYDROGEN AND METAL LINE ABSORPTION AROUND LOW-REDSHIFT GALAXIES IN COSMOLOGICAL HYDRODYNAMIC SIMULATIONS . . . . .	35
2.1 Introduction . . . . .	1
2.2 Simulations & Analysis . . . . .	3
2.2.1 The Code and Input Physics . . . . .	3
2.2.2 Simulation Runs . . . . .	5
2.2.3 Generating Spectra with SPECEXBIN . . . . .	9
2.2.4 Ion Selection . . . . .	11
2.2.5 Generating and Analysing Simulated Spectra . . . . .	13
2.3 Physical Conditions of Absorbers . . . . .	17
2.3.1 The CGM in Absorption . . . . .	17
2.3.2 Phase Space Plots . . . . .	18
2.3.3 Physical Conditions vs. Ionisation Potential . . . . .	26
2.3.4 Physical Conditions vs. Halo Mass . . . . .	32
2.4 Absorption around galaxies in redshift space . . . . .	34
2.5 Absorption around galaxies versus impact parameter . . . . .	40
2.6 Column Density Distributions . . . . .	46
2.7 Variations with outflow model . . . . .	53
2.8 Conclusions . . . . .	62
2.9 Acknowledgements . . . . .	66
3 TRACING INFLOWS AND OUTFLOWS WITH ABSORPTION LINES IN CIRCUMGALACTIC GAS . . . . .	67
3.1 Introduction . . . . .	1

3.2	Simulations & Analysis . . . . .	6
3.2.1	The Code and Input Physics . . . . .	6
3.2.2	Generating spectra with SPECEXBIN . . . . .	9
3.3	Inflows and Outflows . . . . .	11
3.3.1	Identifying Inflowing and Outflowing Gas . . . . .	11
3.3.2	Mass Budgets . . . . .	19
3.3.3	Relation to Dynamics . . . . .	26
3.4	Observables . . . . .	30
3.4.1	Column Density vs. Impact Parameter . . . . .	32
3.4.2	Fractional Column Density Distributions . . . . .	36
3.4.3	Covering Fractions . . . . .	38
3.5	Physical Conditions . . . . .	41
3.5.1	Mass and metal profiles . . . . .	41
3.5.2	Velocity and kinematics . . . . .	44
3.5.3	Phase Space Plots . . . . .	44
3.6	Numerical Considerations . . . . .	52
3.7	Conclusions . . . . .	55
3.8	Acknowledgements . . . . .	59
4	BARYON CYCLING IN THE LOW-REDSHIFT CIRCUMGALACTIC MEDIUM: A COMPARISON OF OBSERVATIONS TO SIMULATIONS . . . . .	61
4.1	Introduction . . . . .	1
4.2	COS-Halos Data Set . . . . .	3
4.3	Simulation Methods . . . . .	4
4.3.1	The Code and Input Physics . . . . .	4
4.3.2	Generating Spectra With Specexbin . . . . .	6
4.4	Comparison of Direct Observables . . . . .	8
4.4.1	Overall CGM Absorption . . . . .	8
4.4.2	Equivalent Widths vs. Impact Parameter . . . . .	10
4.4.3	Covering Fractions . . . . .	15
4.4.4	Ion Ratios . . . . .	20
4.4.5	Kinematics . . . . .	24
4.5	Amount and Physical Conditions of CGM Gas . . . . .	27
4.5.1	Halo Mass-Stellar Mass Relationship . . . . .	27
4.5.2	Baryonic Fractions within Halos . . . . .	30
4.5.3	Mass Budgets of Inflowing and Outflowing Gas . . . . .	32
4.6	Comparison of Data to Inflows and Outflows in Simulations . . . . .	35
4.7	Conclusions . . . . .	40
4.8	Acknowledgements . . . . .	43

5	CONCLUSIONS . . . . .	44
5.1	Summary . . . . .	44
5.2	Next Steps . . . . .	45
5.2.1	Evolution of CGM with Redshift . . . . .	46
5.2.2	Effects of Mergers and Starbursts on the CGM-Galaxy Relationship . . . . .	47
5.2.3	Further Comparisons of Wind Models to Observations . . . . .	48

## LIST OF FIGURES

1.1	Images of M82 and surrounding halo in the optical, infrared, and X-ray. Credit for left two panels: NASA/JPL Caltech/C. Engelbracht (Steward Observatory) and the SINGS team. Credit for right panel: NASA, ESA, CXC, and JPL-Caltech. . . . .	21
1.2	Schematic of the quasar absorption line spectroscopy technique, as applied to studying the CGM. Image courtesy of Todd Tripp. . . . .	22
1.3	Traditional interpretation of inflows and outflows (black and grey); my contribution (in red). Values for $\Delta t$ and $\Delta x$ for recycled accretion from Oppenheimer & Davé (2008). . . . .	32
2.1	Simulated spectra for three galaxies at $z=0.25$ , convolved with the COS line spread function and noise added with a $S/N=30$ . Each column corresponds to a representative galaxy with the labelled halo mass. We plot lines of sight at distances of 10 kpc (red), 100 kpc (green), and 1 Mpc (blue) away from the galaxy. The top two panels show the Hi optical depth-weighted density and temperature, and the lower panels show simulated spectra for Hi and other ions. All units are physical, for a Hubble parameter $h = 0.7$ . . . . .	14
2.2	Columns one and two show the median log overdensity and median log temperature; subsequent columns show median log column densities for each ion as labelled, all at $z=0.25$ . First three rows are for vzw; the first row is for mass bin $10^{11} M_{\odot}$ , second for $10^{12} M_{\odot}$ , and the third for $10^{13} M_{\odot}$ . The fourth and fifth rows are for $10^{12} M_{\odot}$ halos in the constant wind and no wind models, respectively, and are discussed further in §7. Note the colour scales for HI and Ne VIII are different than for the other ions. All panels are 658 kpc across. . . . .	16

- 2.3 Phase space plots showing the location, in density and temperature space, of H I (left) and Mg II (right) for  $M_h = 10^{12} M_\odot$  at  $z=0.25$ . Each coloured point represents an absorption system found along targeted lines of sight at 10 kpc (top row), 100 kpc (second), 1 Mpc (third), and along random lines of sight (bottom). The grey shading shows the mass-weighted absorption for all gas below  $n_H = 0.13 \text{ cm}^{-3}$  outside of all galaxies in the simulation volume, at each location in phase space. The red and grey histograms show the distributions in identified absorbers and the entire volume, respectively, collapsed along each axis. These are identical for each ion. The histograms are linearly scaled, and the integral under the red and grey histograms are set to be equal. Note that the absorber colour scale is different for H I. . . . . 19
- 2.4 Analogous to Figure 2.3, phase space plots showing the location, in density and temperature space, of Si IV (left) and C IV (right) absorbers, for  $M_h = 10^{12} M_\odot$ , at the impact parameters indicated. . . . . 20
- 2.5 Analogous to Figure 2.3, phase space plots showing the location, in density and temperature space, of O VI (left) and Ne VIII (right) absorbers, for  $M_h = 10^{12} M_\odot$ , at the impact parameters indicated. . . . . 21
- 2.6 *Top panel:* Median column density-weighted overdensity as a function of ionisation energy for the six ions we consider. Four points for each ion are plotted, corresponding to three different  $b$  values (all for mass bin  $10^{12}$ ) and random LOS. 100 kpc (green squares) and random (black circles) are plotted at the energy in eV at which the labeled ion is ionised to the next higher level; 10 kpc (red triangles) and 1 Mpc (blue diamonds) are shifted for visibility. Points are plotted at the well-defined median; vertical range (not error) bars (shown only on the 100 kpc case for clarity) span the 16% to 84% enclosing values. The dotted horizontal line represents the virial overdensity at  $z = 0.25$ . *Bottom panel:* Similar to the top panel, but for column density-weighted temperatures. . . . . 28
- 2.7 Median column density-weighted overdensity and temperature vs. halo mass for H I (left panels), O VI (middle panels), and Ne VIII (right panels). For all panels, the different colours correspond to the three different impact parameters: 10 kpc (red triangle), 100 kpc (green square), and 1 Mpc (blue diamond) (offset for clarity). The range bars span the 16% to 84% enclosing values, and the dotted horizontal line represents the virial overdensity. . . . . 35

- 2.8 Median column density ( $N$ ) vs. velocity separation ( $\Delta v$ ) from the central galaxy  $\Delta v$  for  $M_h = 10^{11,12,13} M_\odot$  (dotted, solid, and dashed lines, respectively). We show results at three impact parameters: 10 kpc (red), 100 kpc (green), and 1 Mpc (blue). Vertical dotted lines mark  $300 \text{ km s}^{-1}$ . . . . . 36
- 2.9 The total column density (not number density) per unit redshift versus impact parameter around galaxies in halos of  $10^{11} M_\odot$  (dotted),  $10^{12} M_\odot$  (solid) and  $10^{13} M_\odot$  (dashed). For halos,  $dN/dz$  is the summed column density for the given ion along all lines of sight at the given impact parameter over the velocity range  $\pm 300 \text{ km s}^{-1}$ , divided by  $\Delta z = (\text{Number of halos in sample}) \times (600 \text{ km s}^{-1}) / (1 + z)$ . The black symbols indicate  $dN/dz$  for random lines of sight. Note that the vertical range for each ion varies, although it always spans 4 dex. The vertical dotted line corresponds to 300 kpc. Error bars show the cosmic variance across sixteen simulation sections of equal volume. . . . . 41
- 2.10 Total column density per unit redshift ( $dN/dz$ ) for targeted LOS around  $10^{12} M_\odot$  halos, for all gas particles (black solid line, identical to Figure 3.7), and for gas within the specified radius of a galaxy (coloured lines). Black line is labeled "all", indicating that we consider absorption from all SPH particles (i.e. the full simulation) intersecting the targeted LOS. Coloured lines indicate  $dN/dz$  where we only include absorption from SPH particles that are within a sphere of the indicated physical radius from *any* galaxy in our simulation (not just the targeted one). Dotted purple shows  $dN/dz$  for gas within 30 kpc (physical) of a galaxy, Dashed green line is for 100 kpc, and dash-dot red is for 300 kpc. . . . . 44
- 2.11 Top panel: Column density distributions (CDDs) for galaxies with  $M_{halo} = 10^{12} M_\odot$ .  $f(N) \equiv d^2 n / dN dz$ . We multiply  $f(N)$  by  $N^2$  to show from where most of the absorption per unit log column density arises. The black line is the column density distribution for random LOS, red, green, and blue are for targeted LOS at 10 kpc, 100 kpc, and 1 Mpc, respectively. Circles (which increase in size with increasing  $b$ ) mark the peak of the distribution, i.e., where 50% of the column density is below that value and 50% above it. Bottom: Same as the top panel for galaxies in halos of  $10^{11} M_\odot$  (dotted line) and  $10^{13} M_\odot$  (dashed line). Triangles and squares mark the peak of the distribution for  $10^{11} M_\odot$  and  $10^{13} M_\odot$  respectively, also increasing in size with increasing  $b$ , while circles mark peak for random distribution, as in top panel. Vertical lines show the completeness limit of the CDDs for  $S/N=30$  per  $6 \text{ km s}^{-1}$  pixel. . . . 47

- 2.12 Median overdensity, temperature, and metallicity vs. impact parameter for three different wind models: momentum-driven “vzw”, constant wind “cw”, and no wind “nw”. Sight lines are all around galaxies with halo masses of  $10^{12} M_{\odot}$ . The top two rows are similar to the first two columns of Figure 2.2, but collapsing the image down to one dimension. . . . . 54
- 2.13 Thin lines: Metal mass fraction of all gas particles within spheres of radius  $r$  around all galaxies  $M_* \geq 10^{9.1} M_{\odot}$  in our simulation at  $z=0.25$ , relative to the total metal mass of gas particles in the whole simulation volume, for momentum-driven winds (solid line), no winds (dashed line), and constant winds (dotted line). The vertical dotted line delineates 300 kpc. Thick lines: Total mass fraction for all species, not just metals. . . . . 57
- 2.14 The total column density per unit redshift for the vzw, vzw-cie, cw, and nw models, all for galaxies in  $10^{12} M_{\odot}$  halos. The diamonds indicate the  $dN_{ion}/dz$  value for random lines of sight for each wind model. The symbols are shifted slightly to the left of 1 Mpc, and separated for easier viewing. In some cases the symbols are lower than the scale of the plot so do not appear. . . . . 59
- 2.15 The median column density (N) vs. velocity separation from the central galaxy ( $\Delta v$ ) for galaxies in  $10^{12} M_{\odot}$  halos for the vzw, cw, and nw models. We show results at three impact parameters: 10 kpc (red), 100 kpc (green), and 1 Mpc (blue). The vertical dotted marks  $300 \text{ km s}^{-1}$ . . . . . 60
- 3.1 Left panels: SPH particles around a galaxy at  $z = 0.25$  with halo mass  $M_{halo} = 10^{13} M_{\odot}$  and a panel width of 525 physical kpc. Right panels: SPH particles around a galaxy with halo mass  $M_{halo} = 10^{11} M_{\odot}$ , panel width is 225 kpc. Top panels show recycled accretion (dark blue), and pristine accretion (light blue). Middle panels show young outflows (green) and ancient outflows (orange). Lower panels show ambient gas (red). All panels also include stars (white). . . . . 14
- 3.2 The time (relative to  $z = 0.25$ ) since last wind ejection vs. density at  $z = 0$  of all gas not in the ISM at  $z = 0.25$ . The vertical line denotes ISM densities at  $z = 0$ . Gas to the right of the line is defined as accreting, because it will join the ISM of a galaxy by  $z = 0$ . Gas to the left is defined as not accreting, unless it forms a star or gets launched into a wind (not shown on this plot). The horizontal line at 9.0 shows the separation of young from ancient outflows. . . . . 17



- 3.3 The non-ISM gas mass budget (left) and gas-phase metal budget (right) at  $z = 0.25$ . Upper plots show the full simulation, and lower plots show only gas within the virial radius of a halo at  $z = 0.25$ , for high (middle) and low (bottom) mass halos. Ambient is gas that has never been in a wind, before or after  $z = 0.25$ , that is not accreting. Ancient outflow is for non-accreting gas particles ejected in a wind more than 1 Gyr before  $z = 0.25$ . Young outflow is for non-accreting gas particles ejected in a wind  $\leq 1$  Gyr before  $z = 0.25$ . Recycled accretion is gas that has been ejected in a wind by  $z = 0.25$ , and will join or pass through the ISM of a galaxy or become a star by  $z = 0$ . Pristine accretion is gas that has not been ejected in a wind by  $z = 0.25$  and will join or pass through the ISM of a galaxy or become a star by  $z = 0$ . . . . . 20
- 3.4 Upper panel: the fraction of baryons that are hot ( $> 10^5$  K; red), cool ( $< 10^5$  K; light blue), the ISM (i.e. star-forming; dark blue), and in stars (orange) vs. halo mass at  $z = 0.25$ . We plot the total baryon fraction in halos (solid black). The black horizontal dot-dot-dot-dash line represents the global ratio  $\Omega_b/\Omega_m$ . We also plot the fraction of baryons in just the hot phase (middle panel) and the cold phase (bottom panel) vs. halo mass divided into categories as labelled. . . . . 24
- 3.5  $v/v_{\text{vir}}$  vs. wind age for all non-ISM gas particles in the simulation at  $z = 0.25$ . . . . . 27
- 3.6  $V \cdot r/\text{abs}(r)$  (divided by the virial velocity) vs. radial distance from the host galaxy (divided by the virial radius), for non-ISM gas at  $z = 0.25$  divided into each of the categories as labelled. To guide the eye, we have added solid horizontal lines at  $v = 0$ , and dotted horizontal lines at  $v = \pm v_{\text{vir}}$ . . . . . 31
- 3.7 The average column density per LOS for targeted lines of sight around  $10^{11} M_\odot$  (left panels) and  $10^{13} M_\odot$  (right panels) halos for different species (as labelled). The black solid line includes all the gas. Coloured lines indicate results from including only absorption from: pristine accretion (light blue dashed), recycled accretion (dark blue dotted), young outflows (green dot-dashed), ancient outflows (orange dot-dot-dashed), and ambient (red long-dashed). Vertical lines indicate the approximate virial radius at the midpoint of each mass bin. Note the yrange is not the same for each ion, though it always spans 4 dex. . . . . 33

- 3.8 Fractional column density distributions, i.e. the fraction of absorption in bins of size  $\log N = 0.5$  owing to the various categories for different species (as labelled) at impact parameters of 25 kpc (top panels) and 100 kpc (bottom panels), for  $10^{11} M_{\odot}$  halos (left panels) and  $10^{13} M_{\odot}$  halos (right panels). Where lines do not extend, there is no column density in that bin from any gas. . . . . 37
- 3.9 Covering fractions for  $10^{11} M_{\odot}$  (left panels) and  $10^{13} M_{\odot}$  (right panels) halos, showing the fraction of sight lines with equivalent widths  $> 0.05 \text{ \AA}$  for the species as labelled. The black line includes all the gas and the broken coloured lines are split into the categories as labelled. Note the different y-axis range for Ne VIII, and note that individual categories are computed separately and do not sum to the black line. . . . . 40
- 3.10 Left panels: fraction of the total mass of non-ISM gas particles in various categories as a function of  $R/R_{\text{vir}}$  at  $z = 0.25$ , as labelled. Right panels: fraction of the total *metal* mass. Top panels are for  $10^{13} M_{\odot}$  halos and the lower panels are for  $10^{11} M_{\odot}$  halos. Only central galaxies are considered. . . . . 42
- 3.11 Histograms of velocity, relative to the galaxy systemic velocity, of absorbers split into recycled accretion (blue), young outflows (green), and ancient outflows (orange), for Mg II & O VI, at 25 kpc & 100 kpc as labelled for  $10^{13} M_{\odot}$  (top panels) and  $10^{11} M_{\odot}$  (bottom panels) halos. Vertical lines demarcate the escape velocity at the midpoint of each mass bin for  $R=25$  kpc or 100 kpc as labelled. (Escape velocity for  $10^{13} M_{\odot}$  halos at 25 kpc,  $590 \text{ km s}^{-1}$ , is outside the range of the plot). Note the different y-axis range for each panel. . . 45
- 3.12 Distribution of gas in temperature-density phase space, for our five categories and for all non-ISM gas, as labelled. We overplot the location of strong ( $N > 10^{14}$ ) absorbers of Mg II and O VI in  $10^{13} M_{\odot}$  halos at 25 kpc, for all non-ISM gas, as well as broken out by category for recycled accretion, young outflows, and ancient outflows. In the pristine accretion and ambient panels, where there is no strong Mg II or O VI absorption in  $10^{13} M_{\odot}$  halos at 25 kpc, we overplot the location of H I absorbers of various strengths as labeled. The colourbar is the same in each panel, showing the log number of particles. . . . . 46

3.13	Phase space distributions as in Figure 3.12. We overplot the location of strong ( $N > 10^{14}$ ) absorbers of C IV and O VI in $10^{13} M_{\odot}$ halos at 100 kpc, for all non-ISM gas, as well as broken out by category for recycled accretion, young outflows, and ancient outflows. In the pristine accretion and ambient panels, where there is no strong C IV or O VI absorption in $10^{13} M_{\odot}$ halos at 100 kpc, we overplot the location of H I absorbers of various strengths as labeled. The colourbar is the same in each panel, showing the log number of particles. . . . .	47
4.1	Summed equivalent width divided by total pathlength (dEW/dz) over all LOS at a given impact parameter, as a function of impact parameter. Black points are from the COS-Halos dataset, with error bars averaged from well-constrained detections only, no limits or non-detections. Blue solid lines are for the ezw model, red dotted lines from the cw models. Both models have range bars showing 16%-84% of the model values. The errors on the model points have been horizontally offset slightly for easier viewing. . . . .	9
4.2	Equivalent width vs. impact parameter for observed points (black — circles for exact values, up and down facing triangles for lower and upper limits respectively); as well as ezw (blue crosses) and cw (red diamonds) models. Ions are ordered according to increasing ionization energy (right to left, top to bottom). See Table 4.1 for detection thresholds. Model points do not smoothly decrease, owing to degeneracy between stellar mass and impact parameter. .	12
4.3	Stellar mass vs. impact parameter for the observed COS-Halos data set. Star forming galaxies are separated from passive galaxies at $sSFR = 10^{11} M_{\odot}/yr$ , as given by Tumlinson et al. (2011). . . . .	13
4.4	Covering fraction of COS-Halos data (black solid lines are values, black dotted lines are errors), compared to model points from the ezw (blue squares) and cw (red diamonds) simulations. Open symbols are plotted at impact parameters with corresponding low stellar masses ( $< 10^{11} M_{\odot}$ ), filled symbols are for high stellar masses.	17
4.5	sSFR rate vs. stellar mass for the galaxies in the ezw (blue) and cw (red) models that match the COS-Halos LOS. Some galaxies have $sSFR=0$ , those are plotted as downward facing triangles at the bottom of the plot. . . . .	19

4.6	Comparison between the log of the ratio of equivalent width (in milliÅ) in the COS-Halos data set (black symbols: circles for constrained values, downward triangles for upper limits, upward triangles for lower limits, and diamonds for less constrained values, such as a lower limit divided by a lower limit), as well as ezw model (blue crosses) and cw model (red diamonds). Left panels show various metals vs. H I, probing metallicity. Right panels show metal ratios, probing physical conditions. . . . .	23
4.7	Distribution of column density along the line of sight. Ezw model data has been binned both in impact parameter and in velocity space (cw, not shown here, is similar). Blue blocks show that 30% or more of the column density between -600 and +600 is concentrated in that velocity bin. Green shows 20-30%, yellow between 10-20%, and orange less than 10%. Overplotted as black diamonds are the COS-Halos observed points. . . . .	26
4.8	Stellar mass-halo mass relationship for central galaxies in the ezw (black) and cw (blue) at $z=0.25$ . The points show values for individual galaxies, the lines show medians. The stellar mass range of the COS-Halos data set is bounded by dashed red lines. . . . .	29
4.9	Baryonic content of selected galaxies for ezw (solid) and cw (dotted) wind models as a function of enclosed radius. The black lines show total baryon fraction in selected halos for ezw and cw models. Dark blue, red, light blue, and orange lines show fractions of ISM (star-forming) gas, hot gas ( $> 10^5$ K), cool gas ( $< 10^5$ K), and stars, respectively. . . . .	31
4.10	Mass budgets of all non-ISM gas within (defined as $r < R_{vir}$ ) our selected ezw halos (left) and cw halos (right). Top level shows all non-ISM gas particles, lower row is metals only. . . . .	36
4.11	Equivalent width versus impact parameter for the COS-Halos data set (black circles, both panels), as well as for ezw (upper) and cw (lower) models (colored triangles), for various ions ordered from low to high ionization energy. The model points represent the median value of all LOS at that impact parameter. Light blue triangles show pristine accretion, dark blue crosses recycled accretion, green asterisks young outflow, orange diamonds ancient outflow, and red crosses ambient. To avoid clutter, we only plot the category with the greatest contribution to the overall equivalent width at each impact parameter. . . . .	38

LIST OF TABLES

2.1 Comparison of r48n384vzw models. . . . . 7

2.2 For each ion, we give the percentage of absorption from particles within 300 kpc of any galaxy in our simulations, at each impact parameter listed. Values in this table are derived from the difference between the red dash-dotted and black solid lines in Figure 2.10 at impact parameters of 10, 100, and 300 kpc. . . . . 45

3.1 Fate of the accreting material . . . . . 18

4.1 Ion Properties . . . . . 7

## ABSTRACT

My dissertation focuses on a relatively new field of study: the region immediately around galaxies known as the circumgalactic medium (CGM). The CGM holds vast quantities of mass and metals, yet its connection to galaxies is not well understood. My work uses cosmological hydrodynamic simulations and comparisons to data from *Hubble's* Cosmic Origins Spectrograph (COS) to understand the CGM's connection to galaxy evolution, gas accretion, outflows, star formation, and baryon cycling. This includes studies of the CGM's extent and physical conditions; the cause and nature of outflows; gas dynamics, including the first comprehensive study of tracers of inflowing and outflowing gas at low redshift ( $z = 0.25$ ); and direct comparison of theoretical results to observational data.

Chapter 1 introduces my research and show its connection to galaxy evolution. Chapter 2 investigates hydrogen and metal line absorption around low-redshift galaxies in cosmological hydrodynamic simulations. This chapter studies different models for stellar outflows, physical conditions, and dependencies on halo mass. Chapter 3 examines the flow of gas into, out of, and around galaxies using a novel particle tracking technique. This chapter examines the baryon cycle in detail for our preferred model of stellar outflows. Chapter 4 compares our model results, including two separate prescriptions for outflows, with data from COS. We contrast these wind models, showing how they cycle baryons differently, and show degeneracies in observational diagnostics. In Chapter 5, I summarize and discuss plans for future research in this field, and how it can be more fully leveraged to understand galaxy evolution.

## CHAPTER 1

## INTRODUCTION

Current studies of galaxy formation and evolution have yet to fully leverage our knowledge of the region immediately around galaxies known as the circumgalactic medium (CGM). The region contains vast quantities of baryons (at least half of the “missing” baryons from galaxy dark matter halos, see Werk et al., 2014), as well as extremely energetic outflows. This CGM gas interacts with the galaxy (and vice versa) in ways that are vital yet poorly constrained.

The CGM holds information. The amount, physical state, and kinematics of CGM gas are powerful clues into what drives a galaxy’s formation and evolution. The CGM holds information not only about a galaxy’s *present* (why it has the stars and gas it does) but also its *past* (because the material currently in the CGM was once in stars in the galaxy) and its *future* (because some of the material in the CGM may again join the galaxy). Studying the CGM can be thought of as “galactic archaeology”, with different phases of the CGM tracing different phases of the galaxy’s evolution, including the evolution of its stars.

As a field, we know the CGM is important. We can directly observe its high velocity outflows, we can quantify its baryonic mass content (possibly comparable to the mass of a galaxy’s stars and ISM gas, as shown by Peeples et al., 2013), and (based on presence of metals), we can infer ways in which a galaxy and its CGM interact. Many questions remain, however. We do not know how exactly the CGM and galaxy are related, nor exactly how CGM processes affect star formation (or quenching) in galaxies. We do not know the exact mass content of the CGM, and we have yet to fully explore any cosmological implications this may have. We do not have a self-consistent way of describing outflows, nor do we

have a complete description of the physical conditions, phases, or dynamics of the CGM. Much remains to be done.

This thesis presents detailed studies of the CGM at low redshift. This work uses cosmological hydrodynamic simulations and comparisons to data from *Hubble's* Cosmic Origins Spectrograph (COS) to understand the CGM's connection to a variety of key questions in galaxy evolution, including gas accretion, inflows and outflows, star formation, and baryon cycling. This includes studies of the CGM's extent and physical conditions; the cause and nature of outflows; characterization of gas dynamics, including the first comprehensive study of tracers of inflowing and outflowing gas at low redshift; and direct comparison of theoretical results to observational data.

## 1.1 Defining the CGM

Up until 5-10 years ago, extragalactic astronomers mostly thought in terms of galaxies, groups, filaments, and the intergalactic medium (IGM). Recent work in both observations and theory (see below) have brought galactic halos, and the area around galaxies generally, into more prominent consideration. Figure 1.1 shows a nice example of why this area is worthy of study.

In the optical (left panel), the more or less canonical picture of a galaxy is apparent: a nice tight disk (viewed edge-on) with lots of visible starlight. In the infrared (middle panel), there is now material seen outside the star-forming region of a galaxy — this is emission from polycyclic aromatic hydrocarbons (PAHs). The X-ray image (right) also shows material outside the galaxy that is energetic enough to produce X-rays. This area around the galaxy, not part of the interstellar medium (ISM) but not part of the broader IGM, is now known as the CGM. We generally think of the CGM as starting where the ISM ends and continuing



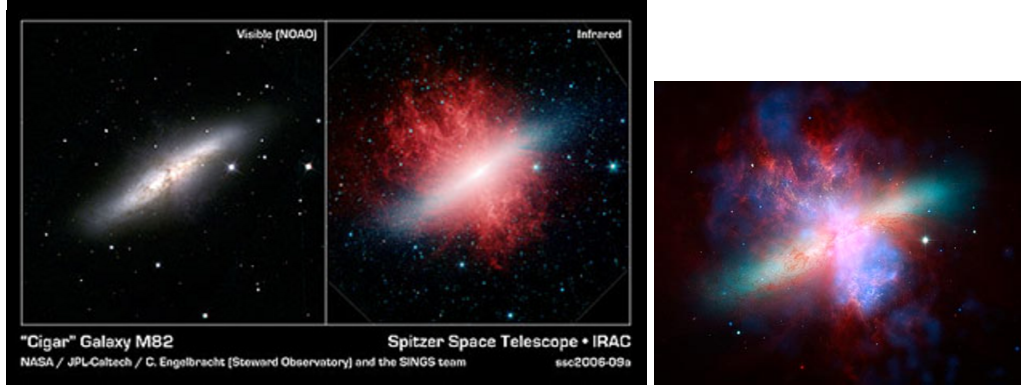


Figure 1.1: Images of M82 and surrounding halo in the optical, infrared, and X-ray. Credit for left two panels: NASA/JPL Caltech/C. Engelbracht (Steward Observatory) and the SINGS team. Credit for right panel: NASA, ESA, CXC, and JPL-Caltech.

out to  $\sim 300$  kiloparsecs (Ford et al., 2013b; Rudie et al., 2013; Prochaska et al., 2011) — roughly the virial radius for a Milky Way-size galaxy at low redshift — or within the virial radius of the galaxy’s dark matter halo (Stocke et al., 2013). In some cases the CGM can extend much further, out to  $\sim 1$  Mpc (Ford et al., 2013a). These images, while just for M82, illustrate much broader trends: there is more to a galaxy than just its active star-forming region; whatever is happening is powerful enough to produce very high energy photons; and the region around a galaxy is possibly multi-phase, since the fragile PAH molecules should not be able to survive in the presence of hot X-ray gas, yet they somehow do. To fully understand galaxy evolution, we need to understand the CGM region.

## 1.2 Motivation

This thesis began in spring 2010, when the opportunity arose for me to work as a theorist on a new collaboration called COS-Halos. This collaboration, led by Dr. Jason Tumlinson at STScI, consists of observers and theorists across several

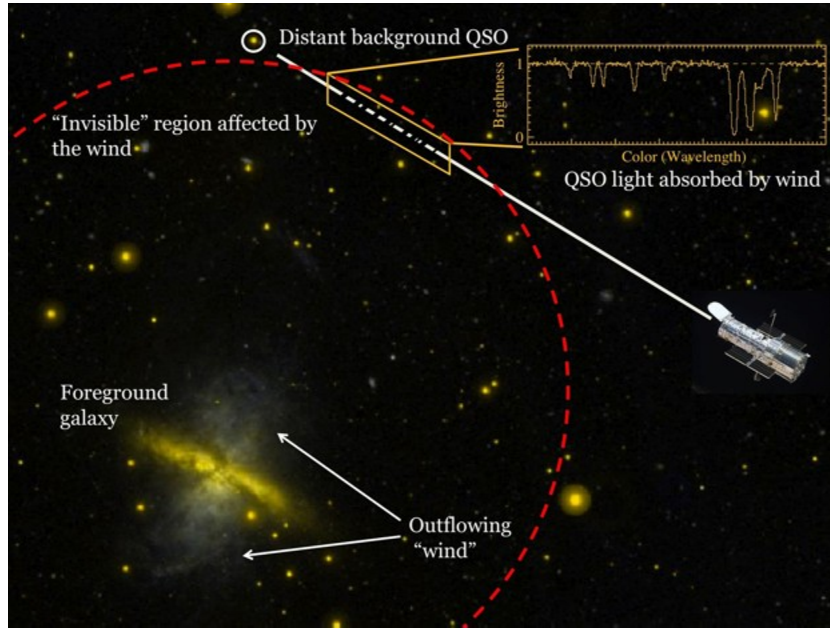


Figure 1.2: Schematic of the quasar absorption line spectroscopy technique, as applied to studying the CGM. Image courtesy of Todd Tripp.

institutions interested in the halos around galaxies. There had recently been great advances in both instrumentation and theoretical understanding, so the opportunity was ripe to make rapid progress in this field.

### 1.2.1 Observational Opportunity

Because galactic halos are generally too hot and too diffuse to emit, one uses absorption line spectroscopy to detect the presence of halo gas. Figure 1.2 shows a schematic: a distant background quasar (or QSO) illuminates the otherwise invisible halo around a galaxy. That material causes telltale absorption features in the QSO spectra, allowing observers to detect the presence of gas. The absorption lines can give information about mass, metallicity, kinematics, and physical conditions.

Quasar absorption line spectroscopy requires a very sensitive spectrograph to

be successful. COS is uniquely well-suited to this task. It is more sensitive than its predecessors, allowing selection of galaxies first, rather than quasars first. This means galaxies can be selected based on mass, redshift, and star formation rate; one can then search for a quasar behind them. With earlier generations of (less sensitive) spectrographs, one simply picked a quasar and hoped for something interesting along the line of sight (LOS). Being able to select LOS based on galaxy properties was a huge step forward. In addition to time on COS itself, the COS-Halos team was also awarded time on ground-based telescopes for follow-up, allowing for a complete survey.

CGM observations by the COS-Halos team (Tumlinson et al., 2013; Werk et al., 2012, 2013) are part of a much broader effort to understand the CGM. The COS-GTO team based at the University of Colorado Boulder has also made huge advances with COS. Work by Stocke et al. (2013) has used COS, as well as another spectrograph, the Space Telescope Imaging Spectrograph (STIS), to probe the CGM out to several hundred kiloparsecs, and Danforth et al. (2010, 2011) have used COS to characterize Lyman- $\alpha$  absorbers, and warm-hot baryons in the CGM (respectively). Recently, Danforth et al. (2014) published COS observations of over 4,000 lines of sight in the low-redshift CGM.

In addition to the COS data, there is a great wealth of observational data on the content and characteristics of the CGM from a variety of groups. Work by Tripp & Song (2012) and Steidel et al. (2010) has been able to probe the CGM out to several hundred kiloparsecs, and absorption in Mg II has been used to probe the CGM closer to galaxies on scales of tens of kiloparsecs (Churchill et al., 2000; Bordoloi et al., 2011; Chen, 2012; Kacprzak et al., 2012; Rubin et al., 2012). In fact, there is now so much data on Mg II absorbers in halos that it has been assembled into a publicly available catalog (Nielsen et al., 2013). In addition to Mg II, there

are also a variety of observations of O VI, making it the most commonly observed high ionization potential metal absorber at low redshift (e.g., Tumlinson et al., 2011; Danforth & Shull, 2008; Thom & Chen, 2008; Bregman, 2007; Stocke et al., 2006; Chen & Mulchaey, 2009; Prochaska et al., 2011; Sembach et al., 2003; Tripp et al., 2000, 2008). Many other ions, such as Ne VIII (Tripp et al., 2011; Mulchaey & Chen, 2009), Si IV (Werk et al., 2012) and C IV (Steidel et al., 2010) have been observed in the CGM as well. From these types of observations, one can infer total mass and metal budgets, as shown in Peebles et al. (2013).

How did all of this material, particularly metals, end up outside of galaxies? Presumably, this material was carried into the CGM in some sort of an outflow. Over the last 10-15 years there has been a buildup of observations directly showing gas flowing out of galaxies at a variety of redshifts. At high redshift ( $z = 2-3$ ), there have been direct observations of outflows (Pettini et al., 2001; Veilleux et al., 2005), indicating that every UV-selected star-forming galaxy hosts a galactic wind (Steidel, 2001). At intermediate redshifts ( $z = 1-1.5$ ), there are also direct detections of outflows (Rubin et al., 2012), which appear to be ubiquitous for star-forming galaxies (Weiner, 2009). These winds can be extremely fast,  $500 \text{ km s}^{-1}$  Weiner (2009) or faster. There are also observations of outflows at low redshift ( $z < 1$ ) (Martin, 2005; Rupke et al., 2005; Tremonti et al., 2007). There have even been observations of outflows in molecular gas in M82, indicating the presence of winds (Walker, 1991). All of this suggests that galaxies are losing some portion of their mass, at least some of which ends up in the CGM itself, as evidenced by detection of metals in the CGM (e.g. Songaila, 2001; Becker et al., 2011; Simcoe et al., 2011; Tripp et al., 2000, 2008; Thom & Chen, 2008; D’Odorico et al., 2010; Tumlinson et al., 2011; Cooksey et al., 2013; Tilton et al., 2012; Werk et al., 2013; Prochaska et al., 2013). More indirectly, we know galaxies have to be losing some

of their metals, otherwise the observed mass-metallicity relationship (Tremonti et al., 2004; Erb et al., 2006) would be off, and there would be an excess of metals in galaxies.

These observations are invaluable, but not yet complete. We are in the very early stages of this field, only just beginning to understand the CGM's role. In addition to more observations, simulations are needed to help connect various observations and explain the CGM: its phases, structure, inflows, outflows, evolution, and relation to its host galaxy.

### 1.2.2 Theoretical Understanding

Simulations provide the opportunity to complement observational efforts, as there are many tests one can do in a simulation that are difficult or impossible to do observationally. At present, simulations are better than ever before, due to the improved ability to describe outflows and movement of gas. This is largely thanks to pioneering work by Schaye et al. (2010); Davé et al. (2013); Oppenheimer & Davé (2009, 2006); Dekel et al. (2009); Kereš et al. (2005); Kereš & Hernquist (2009) and Stinson et al. (2012), among many others. In a simulation, we can track baryons through time, probe different phases, separate inflows and outflows, and test different physical models. This thesis builds directly upon earlier work by Davé et al. (2010) and Oppenheimer & Davé (2009) that developed and explored different prescriptions for outflows, a key physical process in the CGM. The simulations used in this thesis are smoothed particle hydrodynamics (SPH), using our modified (Oppenheimer & Davé, 2008) version of the N-body+entropy-conserving smooth particle (EC-SPH) code GADGET-2 (Springel, 2005). We model a cosmological volume, create thousands of galaxies, and evolve to  $z = 0$ . Further details on the simulations can be found in the individual thesis chapters.

### 1.3 The Multi-Phase, Metal-Rich CGM

In November 2011, the COS-Halos collaboration published a major paper in *Science* (Tumlinson et al., 2011) based on observations of just one ion, O VI. In observing the CGM around star-forming galaxies, we calculated that the amount of oxygen in the CGM was huge: at least as much, likely far more than, the mass of oxygen in the ISM of those galaxies! This result was significant, as it showed metals have been ejected *en masse* from the ISM (Tripp et al., 2011). It was also startling: the idea that there is more oxygen *outside* a galaxy than *inside* it was definitely not the conventional wisdom at the time. The response to the Tumlinson et al. paper has been huge: the result made NASA's home page, the top ten on Google Science, and headlines in faraway places, including Russia and Pakistan. We as astronomers have been focusing on stars and galaxies, but this result means that the CGM requires much greater attention.

My thesis work has helped interpret and extend this result (see chapter 2). First, I have shown that O VI can extend significantly beyond the 150 kpc region observed by Tumlinson et al. (2011), out to  $> 1$  Mpc (Ford et al., 2013a). Extending out to 1 Mpc would mean an even greater oxygen mass in the CGM, relative to the ISM. Second, I have shown that different ions trace different phases of the CGM, with O VI tracing only a very limited region of density-temperature phase space. Using targeted LOS in simulations, I have tracked a whole suite of ions with a range of ionization potentials, not just one or two as in other work, and found strong trends with ionization potential. I have found that metal lines with low ionization potential, like Mg II, generally trace the cold, dense regions close to galaxies, while high ionization potential lines like O VI, are much more spread out. This means that O VI (and every ion, for that matter) traces only a limited region of the CGM (see chapter 2 for more details). Cold, dense material will

generally not be seen in O VI. Clearly, the Tumlinson et al. (2011) result showing quantities of oxygen in the CGM comparable to the ISM is only the beginning. There are phases of the CGM at other densities and temperatures, not seen in OVI, indicating that there is even more CGM mass than that result suggests.

In defining the multiphase nature of the CGM, we emphasize that we have used different *ionization states* of various elements to probe different phases, not neutral *elements*. The material traced by Mg II does not represent all the magnesium, nor does O VI trace all the oxygen. In general, the ratio of different elements (for example, magnesium to oxygen or silicon to carbon) remains constant as a function of impact parameter in our simulations, but the ratio of different ionization states (O V to O VI, Mg I to Mg II, and hence Mg II to O VI) does vary with impact parameter, because the ionization conditions that give rise to different ionization states depend on impact parameter.

Because of the multi-phase nature of the CGM, and the fact that each ionization state traces only a limited region, it is difficult to tell exactly how much metal mass is contained in the CGM. However, we can estimate using observational constraints. Metals that are produced in stars have several possible fates. They may remain in stars, turn into ISM gas or ISM dust, be ejected into the CGM, be ejected into the IGM, or remain locked up in stellar remnants, such as white dwarves, neutron stars, or black holes. While the majority of metals produced end up in stellar remnants (Fukugita et al., 1998; Fukugita & Peebles, 2004), the quantity of these metals are hard to track, so we instead compare the amount of metals in the galaxy (stars+ISM gas + ISM dust, excluding stellar remnants) versus in the CGM or IGM. Recent work by Peebles et al. (2013) found that galaxies in the mass range  $M_{\text{stellar}} = 10^{9-11.5} M_{\odot}$  (the stellar mass range of the COS-Halos data set), retain in stars, ISM, and dust only 20-25% of the metals they have pro-

duced by  $z = 0$ . Peeples et al. (2013) also finds that for star-forming galaxies, an additional 25-30% of metals produced by  $z = 0$  (excluding those locked up in remnants) can be found in the CGM (defined in that work as approximately 150 kpc away from galaxies).

In the simulations used in this thesis, we find that the metal content of the CGM depends on halo mass (see Figure 3.4) and wind model (see Figure 4.9). For our preferred wind model, for galaxies in the stellar mass range of COS-Halos ( $M_{\text{stellar}} = 10^{9-11.5} M_{\odot}$ ), assuming CGM gas is  $0.1 Z_{\odot}$  and ISM stars and gas are  $1 Z_{\odot}$ , we find that the gas phase metal content of the CGM is 19% of the metal content in stars+ISM gas of the galaxy (see Figure 4.9). This accounting neglects dust and stellar remnants.

#### 1.4 Nature of Outflows

Understanding the CGM requires understanding outflows, a dominant physical process in the CGM (if not *the* dominant physical process). We know that mass and metals leave the galaxy and get into the CGM largely via some sort of outflow (also called winds or feedback). We can observe both these winds and their effects, but the mechanism that drives them is unclear. Supernovae, stellar winds, active galactic nuclei (AGN), or some combination may drive the winds, and they may do so by merely pushing the gas (momentum) and/or heating it (thermal expansion). Whatever the mechanism, the loss of metals from the galaxy can have drastic consequences. The star formation rate drops substantially, by half an order of magnitude or more (depending on the properties of the wind), since much of the raw material to make new stars has been driven out of the galaxy. The ability of the galaxy to accrete new material to make up for this loss can also be compromised: a sufficiently powerful outflow can heat inflowing gas, preventing



it from cooling and condensing onto the galaxy.

In this thesis, I investigated a variety of different wind models, prescriptions for how these winds may operate in nature. We are essentially trying to model what happens when supernova explode, blasting huge quantities of mass and metals out of the ISM, into the CGM and even beyond. In the absence of outflows, our models predict that roughly 80% of gas-phase metals are within 10 kpc of a galaxy, but with variable winds that number drops to 35%, with another 45% in the CGM and 20% in the IGM (see Figure 2.13). The details of this process of driving material out of galaxies are extremely complicated, and we are not yet able to model outflows self-consistently, although efforts are underway to make them more consistent. These include efforts by Jared Gabor and others in our group, as well as Claude-André Faucher-Giguère, Dušan Kereš, and Phil Hopkins, among others. Instead, we use somewhat simple, yet physically motivated models to build insight and span the range of parameter space of how winds may be operating. In this thesis I have used a no wind model (see chapter 2), a constant wind model (meaning all galaxies eject the same portion of their mass, at the same velocity, see chapters 2 and 4), and two varieties of variable wind models (meaning the strength of the wind depends on the mass of the galaxy, see chapters 2-4). These variable models include scalings for wind properties that are derived from conservation of momentum (Murray et al., 2005) and conservation of energy (Murray et al., 2010; Hopkins et al., 2012).

I investigated the effects of these wind models extensively. I published one of the first comprehensive predictions for metal absorption lines in targeted LOS around galaxies and showed that different models predict fundamentally different metal distributions that lead to differences in the strength and quantity of metal absorption lines (chapter 2). I also looked into differences in random

lines of sight, and made predictions for physical conditions in both targeted and random LOS. Based on this and other work, we have ruled out models that are contradicted by observations. Through these comparisons, we are learning something fundamental about how these winds are actually operating in nature. We know how strong (meaning how fast and how much mass is carried) the winds have to be. If a wind is too weak, it will not produce the observed CGM metal content. If a wind is too strong, it will take metals too far from the galaxy, out of the CGM, where they are less likely to accrete onto the galactic disk.

### 1.5 Inflows and Outflows: Understanding the CGM’s Baryon Cycle

While outflows are incredibly important to understanding the CGM, they are just part of the picture. Inflows, which fuel the galaxy, comprise 5% of the total non-ISM gas mass and 36% of the non-ISM gas-phase metal mass (in our favored wind model). “Ambient” material that is neither inflowing nor outflowing contributes a whopping 85% of the non-ISM gas mass at  $z = 0.25$  (see Figure 3.3). My thesis work (see chapters 3-4) has helped categorize, quantify, and improve our understanding of inflows, outflows, ambient material, and the broader cycle of gas in and out of galaxies. This “baryon cycle”, where continual inflows of gas from the intergalactic medium (IGM) (e.g., Kereš et al., 2005; Brooks et al., 2009; Dekel et al., 2009; Bouché et al., 2010; Davé et al., 2012; van de Voort et al., 2012), balanced by galactic-scale outflows (e.g., Oppenheimer et al., 2010; Davé et al., 2011a), set the growth rate of gas and stars within galaxies, has become the modern view of galaxy formation. And yet, the details of this cycle (how much material cycles, over what timescale, how much mixing is involved, etc.) are poorly constrained.

In my thesis (see chapters 3 and 4), I have implemented a novel particle track-

ing technique to directly follow particles as they flow (or do not flow) in and out of galaxies. Using this particle tracking technique, I have categorized and quantified inflows and outflows. My latest work shows that even the categories of inflow and outflow are too broad and vague. At CGM conferences, researchers often state that inflows should be metal-poor, because they are coming in from the pristine, metal-poor IGM. But I have found that, particularly at low redshift, there is a substantial contribution (42% of the non-ISM, gas-phase metal mass within  $L_*$  halos, see Figure 3.3) from recycled inflows, where gas goes into the galaxy, forms a star, gets kicked out in a wind, and then comes back down again as part of a halo fountain (aka recycling). Another contribution of my work is more rigorously treating outflows. Outflows are normally thought of as material currently flowing out, or at least coming out fairly recently, but my work shows that material from long-ago outflows has a large contribution (25% of the mass, 47% of the metal mass within  $L_*$  halos, see Figure 3.3). By adding recycled inflows and ancient outflows to the discussion about inflows and outflows (see Figure 1.3), we have been able to move the field forward. Other CGM experts now speak in terms of "recycled accretion" and "ancient outflows", categories defined in this thesis.

Combined, these additional categories – recycled inflows and ancient outflows – compromise the majority (89% for high-mass halos, 87% for low-mass halos) of gas-phase metals within halos at low- $z$ . Their presence alters the way we view the CGM and its potential for helping us understand galaxy evolution. This also means that we can detect their presence using metal absorption lines. A main goal of my thesis was to find observational diagnostics to distinguish between inflowing and outflowing material, and using the particle tracking technique, we have been able to do that. Additionally, we have found that most of

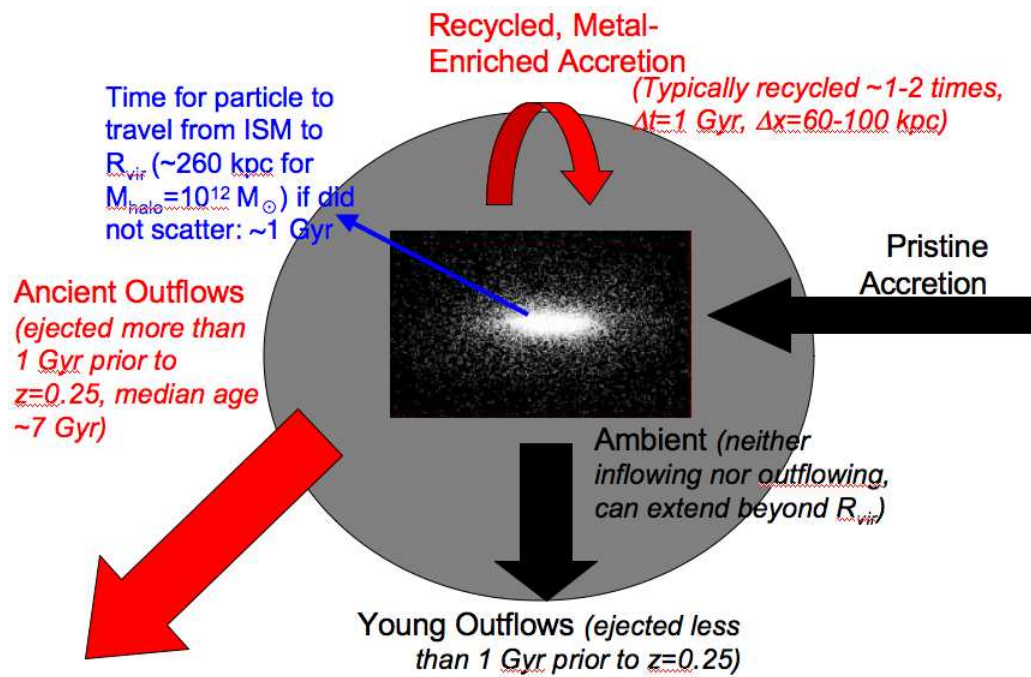


Figure 1.3: Traditional interpretation of inflows and outflows (black and grey); my contribution (in red). Values for  $\Delta t$  and  $\Delta x$  for recycled accretion from Oppenheimer & Davé (2008).

the non-ISM, gas-phase metals (65% by mass) in the low- $z$  CGM trace material from previous epochs ( $\geq 1$  Gyr prior to  $z=0.25$ ) of star formation and outflows, some of which have turned around and become inflows. This means the current CGM is largely a relic from a much earlier era.

## 1.6 Connection to COS Observations

The fourth chapter of this thesis compares theoretical results directly to observations by the COS-Halos team. This data set includes 39 quasars within  $R < 160$  kpc of 44 galaxies with  $0.1 L^* < L < 3 L^*$  at  $z \approx 0.2$ . We investigate a variety of ions that span a range of ionization potentials, including H I, Mg II, Si II, C II, Si III, Si IV, C III, and O VI. For each COS-Halos LOS, we select galaxies in our simulation with similar stellar mass to the observed galaxy, and then draw LOS at the impact parameter that corresponds with that sight line. This represents the first comparison of our wind models against targeted LOS at low redshift. In doing this comparison, we hoped to strengthen our case that our favored wind model, a variable wind model, would be a significantly better match to the COS-Halos data than a constant wind model. Interestingly, this is not what we found. Because different wind models have different halo mass-stellar mass relationships, and because we matched simulation LOS on stellar, not halo mass, the two wind models end up both matching the data, with little difference between them. The differences in wind model are offset nearly perfectly by differences in halo mass. In this chapter we also investigate how the baryon cycle would operate under a constant wind model, not just the variable wind model studied in chapter 3. We find that a constant, stronger wind excludes more material from the baryon cycle (87% of the gas mass in low-mass halos is in either ambient or pristine accretion in the variable wind model versus 96% in the constant wind model, see Figure

4.10). This is because the winds blow the gas too far away to allow it to recycle.

## 1.7 Introduction Summary

In this thesis, I have studied the strength and extent of HI and metal line absorption for both targeted and random LOS; dependencies of absorption on halo mass; physical conditions of gas; baryonic content of halos; kinematics, dynamics, and the baryon cycle; observational diagnostics of inflows and outflows; and direct comparisons to data — all in the CGM, all as a function of wind model. I am excited to present this work.

## CHAPTER 2

HYDROGEN AND METAL LINE ABSORPTION AROUND LOW-REDSHIFT  
GALAXIES IN COSMOLOGICAL HYDRODYNAMIC SIMULATIONS

This chapter was published in Monthly Notices of the Royal Astronomical Society in 2013, Volume 432, page 89. Co-authors on this chapter include **Benjamin D. Oppenheimer** (Leiden Observatory, Leiden University, PO Box 9513, 2300 RA Leiden, Netherlands), **Romeel Davé** (Astronomy Department, University of Arizona, Tucson, AZ 85721, USA), **Neal Katz** (Astronomy Department, University of Massachusetts, Amherst, MA 01003, USA), **Juna A. Kollmeier** (Observatories of the Carnegie Institution of Washington, Pasadena, CA 91101, USA), and **David H. Weinberg** (Astronomy Department and CCAPP, Ohio State University, Columbus, OH 43210, USA).

## Abstract

We study the physical conditions of the circum-galactic medium (CGM) around  $z = 0.25$  galaxies as traced by H I and metal line absorption, using cosmological hydrodynamic simulations that include galactic outflows. Using lines of sight targeted at impact parameters from 10 kpc to 1 Mpc around galaxies with halo masses from  $10^{11} - 10^{13} M_{\odot}$ , we study the physical conditions and their variation with impact parameter  $b$  and line-of-sight velocity  $\Delta v$  in the CGM as traced by H I, Mg II, Si IV, C IV, O VI, and Ne VIII absorbers. All ions show a strong excess of absorption near galaxies compared to random lines of sight. The excess continues beyond 1 Mpc, reflecting the correlation of metal absorption with large-scale structure. Absorption is particularly enhanced within about  $\Delta v < 300 \text{ km s}^{-1}$  and roughly 300 kpc of galaxies (with distances somewhat larger for the highest ion), approximately delineating the CGM; this range contains the majority of global metal absorption. Low ions like Mg II and Si IV predominantly arise in denser gas closer to galaxies and drop more rapidly with  $b$ , while high ions O VI and Ne VIII trace more diffusely distributed gas with a comparatively flat radial profile; C IV is intermediate. All ions predominantly trace  $T \sim 10^{4-4.5} \text{ K}$  photo-ionised gas at all  $b$ , but when hot CGM gas is present (mostly in larger halos), we see strong collisionally-ionised O VI and Ne VIII at  $b \leq 100 \text{ kpc}$ . Larger halo masses generally produce more absorption, though overall the trends are not as strong as that with impact parameter. These findings arise using our favoured outflow scalings as expected for momentum-driven winds; with no winds, the CGM gas remains mostly unenriched, while our outflow model with a constant velocity and mass loading factor produce hotter, more widely dispersed metals.



## 2.1 Introduction

The intergalactic medium (IGM) contains most of the cosmic baryons at all epochs (e.g., Davé et al., 2001). It also contains a substantial fraction of cosmic metals (e.g., Ferrara et al., 2005; Davé & Oppenheimer, 2007; Wiersma et al., 2009b), products of star formation within galaxies that have been dispersed out of galaxies presumably via large-scale galactic outflows (e.g., Aguirre et al., 2001a; Oppenheimer & Davé, 2006). The distribution and physical state of these metals thus provide a powerful tracer of galactic outflow processes, which are a key uncertainty in current galaxy formation models.

Oppenheimer et al. (2012) argued from cosmological simulations with outflows that the IGM is enriched in an “outside-in” manner, with low-density regions enriched at earlier epochs, and that subsequently produced metals tend to remain closer to galaxies over the last 10 Gyr of cosmic time. In simulations by Oppenheimer & Davé (2008) that broadly reproduce IGM enrichment observations, outflowing metals reach a median distance of roughly 100 physical kpc before turning around, which is well outside the virial radius of small early galaxies but results in “halo fountains” within larger, present-day systems. Hence by low redshifts, a large fraction of the ejected metals are expected to reside close to galaxies, within what is now frequently called the circum-galactic medium (CGM). Indeed, observations indicate that C IV, Mg II and O VI absorbers can often be associated with galaxies within tens or hundreds of kpc (e.g., Steidel & Sargent, 1992; Stocke et al., 2006; Wakker & Savage, 2009; Prochaska et al., 2011; Chen et al., 2001; Chen & Mulchaey, 2009). The CGM thus provides a fossil record of early IGM enrichment combined with the gravitational growth of structure, in addition to metals deposited by more recent outflows.

Recent observations using *Hubble’s* Cosmic Origins Spectrograph (COS) pro-

vide a greatly enhanced view of CGM metals at low redshifts. Tumlinson et al. (2011) showed that the CGM around star-forming galaxies contains an amount of oxygen comparable to or possibly exceeding that in the interstellar medium (ISM) of those galaxies, thereby directly demonstrating that metals have been expelled *en masse* from the ISM (Tripp et al., 2011). The sensitivity of COS not only permits the selection of more numerous, fainter background sources that can probe the CGM of low-redshift galaxies, but also enables the detection of weaker and less common ions such as Ne VIII and Si IV. These data will provide new and stringent constraints on theoretical models of outflows that connect galaxies and their surrounding gas.

Cosmological hydrodynamic simulations offer a uniquely well-suited platform to study the co-evolution of galaxies and their surrounding gas. Such simulations dynamically incorporate galactic outflows driven by star formation, thereby self-consistently enriching the IGM and CGM with the by-products of stellar death, as well as accounting for the movement and physical state of such metals driven by hierarchical structure formation. With simulations of representative cosmological volumes, one can test outflow models by comparing the predicted statistics directly to absorption line observations of H I and metals, around galaxies and in the diffuse IGM. Tracking the complex inflow and outflow processes that govern both galaxies and the IGM is necessary to fully understand how IGM and CGM enrichment occur, and to properly interpret present and upcoming data with COS and other facilities.

In this paper we continue our exploration of H I and metal absorption in the low-redshift IGM using cosmological hydrodynamic simulations, building on the work presented by Davé et al. (2010) and Oppenheimer et al. (2012). In those papers we studied absorption properties along random lines of sight through cos-

mological volumes, which only occasionally intercepted the CGM of galaxies. In this work, we select targeted lines of sight at various impact parameters around galaxies in our simulations to directly probe the absorption properties and physical conditions of gas within the CGM. The goal of this paper is to understand the relationship between galaxy properties and HI and metal absorbers that probe the gas around those galaxies.

We explore a range of metal ionisation potential states from low (Mg II) to high (Ne VIII), as well as H I, and find that the behaviour of many CGM absorption line properties shows distinct trends with the ionisation level of the tracer species. CGM absorption lines also show trends with halo mass. These predictions set the stage for a more detailed understanding of CGM observations and provide a more complete picture for how metals trace the motion of gas in and out of galaxies.

Our paper is organised as follows: In §2.2 we explain our methods, in §2.3 we show the density and temperature of absorbers, in §2.4 we explore absorption around galaxies in redshift space, in §2.5 we study absorption as a function of impact parameter, in §2.6 we examine the column density distributions as a function of impact parameter and halo mass, in §2.7 we examine trends with outflow model, and in §2.8 we present our conclusions.

## 2.2 Simulations & Analysis

### 2.2.1 The Code and Input Physics

We use our modified version (Oppenheimer & Davé, 2008) of the N-body+smooth particle hydrodynamic (SPH) code GADGET-2 (Springel, 2005), which is more fully described in §2.1 of Davé et al. (2010). The only code update since Oppenheimer & Davé (2008) is the option to include metal-line cooling rates from

Wiersma et al. (2009a), as we discuss below.

Briefly, GADGET-2 computes gravitational forces on a set of particles using a tree-particle-mesh algorithm and uses an entropy-conserving formulation of SPH (Springel & Hernquist, 2002) to simulate pressure forces and hydrodynamic shocks. We include radiative cooling assuming ionisation equilibrium for primordial species following Katz et al. (1996) and metals based on the tables of Wiersma et al. (2009a) that assume ionisation equilibrium in the presence of the Haardt & Madau (2001) background. In our older simulations, and our ancillary wind model simulations in this paper, we employ metal-line cooling rates based on the collisional ionisation equilibrium (CIE) models of Sutherland & Dopita (1993). The latter rates incorrectly over estimate metal-line cooling as photo-ionisation equilibrium (PIE) suppresses cooling of metal-enriched gas as demonstrated by Smith (2011) and Tepper-García et al. (2011). We show comparisons of these two cooling models in §2.7.

Star formation follows a Schmidt (1959) Law calibrated to the Kennicutt (1998) relation, following Springel & Hernquist (2003). The interstellar medium (ISM) is modelled using the analytic sub grid recipe of McKee & Ostriker (1977), where supernova energy is returned to ISM particles using the two-phase SPH formulation of Springel & Hernquist (2003). Star particles are spawned from ISM particles probabilistically according to the instantaneously calculated star formation rate (SFR); an ISM particle can spawn up to two star particles.

Star formation-driven kinetic feedback is implemented in these simulations by giving a velocity kick ( $v_w$ ) to ISM particles chosen probabilistically at a rate proportional to their star formation rate. The ratio of the mass outflow rate to the star formation rate is termed the mass loading factor ( $\eta$ ). We use the relations for

$v_w$  and  $\eta$  of momentum-driven winds formulated by Murray et al. (2005):

$$v_w = 3\sigma\sqrt{f_L - 1} \quad (2.1)$$

$$\eta = \sigma_o/\sigma, \quad (2.2)$$

where  $f_L$  is the luminosity in units of the Eddington luminosity required to expel gas from a galaxy potential,  $\sigma_o = 150 \text{ km s}^{-1}$ , and  $\sigma$  is the galaxy's internal velocity dispersion (Oppenheimer & Davé, 2008). We refer to this wind model as “vzw” and refer the reader to Oppenheimer & Davé (2008) for a more complete description. We also evolve a model without winds (“nw”) and a constant wind (“cw”) model with  $v_w = 680 \text{ km s}^{-1}$  and  $\eta = 2$  for all galaxies, as described in Davé et al. (2010).

### 2.2.2 Simulation Runs

Our main model in this paper is a  $48h^{-1}\text{Mpc}, 2 \times 384^3$  simulation with vzw winds. This simulation is identical to the r48n384vzw simulation used by Oppenheimer et al. (2010, 2012) and Davé et al. (2010, 2011a,b) except that it uses Wiersma et al. (2009a) metal-line cooling rates.

We choose the vzw wind model as our fiducial model owing to its successes fitting important properties of galaxies and the IGM at a variety of redshifts. At high redshift, simulations with vzw winds provide adequate fits to the  $z = 2$  mass-metallicity relationship (Finlator et al., 2008; Davé et al., 2011a), the  $z \geq 6$  galaxy luminosity function (Davé & Oppenheimer, 2007; Finlator et al., 2011), and observations of IGM metal enrichment at redshifts  $\geq 1.5$  (Oppenheimer & Davé, 2006; Oppenheimer et al., 2009). Simulations evolved to  $z = 0$  reproduce the observed galactic stellar mass function (Bell et al., 2003; Baldry, Glazebrook, & Driver, 2008) below  $5 \times 10^{10} M_\odot$  (Oppenheimer et al., 2010), various statistical properties of present-day galaxies (Davé et al., 2011a,b), and HI and metal-line

statistics from quasar absorption line (QAL) spectra (Oppenheimer & Davé, 2009; Oppenheimer et al., 2012). Oppenheimer et al. (2012) explored a small,  $16h^{-1}\text{Mpc}$ ,  $2 \times 128^3$  simulation incorporating vzw winds and Wiersma et al. (2009a) metal-line cooling, finding it to be their preferred model owing to its theoretically motivated feedback prescription capable of reproducing the above-listed observations, combined with a more correct treatment of metal-line cooling. Oppenheimer et al. (2012) also compared the vzw model, as well as a constant wind and no wind model, to observations of random lines of sight, as shown in Figures 6-8, 10, 14-15, 18 and 21. We note that these simulations do not include any additional mechanisms such as black hole feedback to quench star formation in massive galaxies to reproduce the observed galaxy red sequence (e.g., Gabor et al., 2011).

Because the old r48n384vzw evolved with CIE cooling was featured prominently in a number of our previous publications (Oppenheimer et al., 2010; Davé et al., 2010, 2011a,b; Oppenheimer et al., 2012), we list the differences in some relevant quantities relative to using PIE cooling rates in Table 2.1 at  $z = 0.25$ . It shows that the differences that result from replacing CIE with PIE metal-line cooling rates are minor to moderate. The fraction of baryons in diffuse (i.e. non-star forming) gas with  $T \geq 10^5$  K increases by 3.6%, while the associated metals increase by 18%. Less cooling allows more baryons and especially metals to remain in the warm-hot intergalactic medium (WHIM), defined as where  $T > 10^5$  K and  $\delta < \delta_{th}$ , where  $\delta_{th}$  is the division between bound and unbound gas (Oppenheimer et al., 2012; Davé et al., 2010). The total integrated star formation (i.e. baryon fraction in stars) is reduced by 10%, and the instantaneous star formation rate is reduced by 11%, both because enriched winds are less capable of cooling and hence recycling onto galaxies (Oppenheimer et al., 2010). Considering  $\text{Ly}\alpha$  ab-

Table 2.1: Comparison of r48n384vzw models.

Z-Cooling	CIE <sup>a</sup>	PIE <sup>b</sup>
$f_{\text{bar}}(T \geq 10^5 \text{K})^c$	0.394	0.408
$f_{\text{metals}}(T \geq 10^5 \text{K})^d$	0.056	0.066
$\Omega_*/\Omega_b^e$	0.084	0.076
$\rho_{\text{SFR}}^f$	0.074	0.066
$\text{dN}/\text{dz}(N_{\text{HI}} \geq 10^{14} \text{cm}^{-2})^g$	8.88	7.94
$\Omega_{\text{OVI}}^h$	57.6	38.8
$\Omega_{\text{CIV}}^h$	33.9	23.7
$\Omega_{\text{SiIV}}^h$	10.2	7.9

<sup>a</sup>Collisional ionisation equilibrium metal cooling rates from Sutherland & Dopita (1993).

<sup>b</sup>Photo-ionisation equilibrium metal cooling rates using Wiersma et al. (2009a).

<sup>c</sup>Fraction of diffuse, non-ISM baryons with  $T \geq 10^5 \text{ K}$  at  $z = 0.25$ .

<sup>d</sup>Fraction of diffuse, non-ISM metals with  $T \geq 10^5 \text{ K}$  at  $z = 0.25$ .

<sup>e</sup>Fraction of baryons in stars at  $z = 0.25$ .

<sup>f</sup>Instantaneous SFR at  $z = 0.25$  in  $M_{\odot} \text{ yr}^{-1} \text{ Mpc}^{-3}$

<sup>g</sup>Frequency of H I components with  $N_{\text{HI}} \geq 10^{14} \text{cm}^{-2}$  at  $z = 0.25$ .

<sup>h</sup> $\Omega$  summed from all gas outside galaxies at  $z = 0.25$ , in units of  $10^{-8}$ .

sorption tracing the IGM, the frequency of single Voigt-profile-fitted components with  $N_{\text{HI}} \geq 10^{14} \text{cm}^{-2}$  drops by 10.6%. Common metal ion species observed by COS all decline by 23-33%, which was also found by Oppenheimer et al. (2012) and shown to provide as good if not better agreement with the available observations. Hydrogen and metal-line absorption primarily arise from  $T < 10^5$  K gas, which is reduced with PIE cooling, and more so for metals. The relative differences between these two vzw simulations using CIE or PIE metal cooling is less than it would be for a stronger wind model such as that used in Wiersma et al. (2009a), because with vzw winds diffuse metals are placed at higher overdensities where they cool rapidly in either cooling scheme (Oppenheimer et al., 2012).

In §7, we compare these vzw wind models to two other wind models, a constant wind and a no wind model, both with  $48h^{-1} \text{Mpc}$  size and  $2 \times 384^3$  resolution. The constant wind model presented here has Wiersma et al. (2009a) metal-line cooling, included because Oppenheimer et al. (2012) found that PIE cooling was more important for metals pushed to lower densities by these stronger winds. We use the same no wind simulation as in Oppenheimer et al. (2010). Since metals rarely reach densities where PIE metal cooling is important, there is no need to rerun a no wind simulations with PIE metal cooling.

Finally, the cosmology used in our r-series simulations is:  $\Omega_{\text{m}} = 0.28$ ,  $\Omega_{\Lambda} = 0.72$ ,  $h = 0.7$ , spectral index  $n = 0.96$ ,  $\sigma_8 = 0.82$ , and  $\Omega_{\text{b}} = 0.046$ . This agrees with the WMAP-7 constraints (Jarosik et al., 2011). The gas particle mass is  $3.56 \times 10^7 M_{\odot}$ , and the dark matter particle mass is  $1.81 \times 10^8 M_{\odot}$  giving an effective galaxy mass resolution of about  $2.3 \times 10^9 M_{\odot}$  and a dark matter halo mass resolution of about  $1.21 \times 10^{10} M_{\odot}$ . In this paper we will focus on galaxies and halos generally well above these resolution limits. Unless otherwise specified, we quote distances



in physical (not comoving) units, and we usually refer to them in Mpc rather than  $h^{-1}$  Mpc.

### 2.2.3 Generating Spectra with SPECEXBIN

We use our spectral generation code SPECEXBIN to calculate physical properties of the gas. SPECEXBIN is described in more detail in §2.5 of Oppenheimer & Davé (2006) and more recently in §2.3 of Davé et al. (2010). Briefly, SPECEXBIN averages physical properties including the gas density, the temperature, the metallicity and the velocity of SPH particles in physical coordinates along a sight line. It then uses look-up tables calculated with CLOUDY (Ferland et al., 1998, version 08.00) to find the ionisation fraction for the relevant ionic species.

These look-up tables, functions of density, temperature, and redshift, have been calculated assuming collisional plus photo-ionisation equilibrium with a uniform Haardt & Madau (2001) background. SPECEXBIN then converts to velocity coordinates using Hubble’s Law, accounting for the peculiar velocities of the SPH particles, and adds thermal broadening using the temperature and atomic weights of the various ion species. To match the mean observed absorption we multiply the Haardt & Madau (2001) spectrum by factors of 1.5 for the vzw model, and 1.11 for the no wind and constant wind models, as found in Davé et al. (2010).

Since our last published work with SPECEXBIN, we have updated the code to include an approximate physically motivated self-shielding from the ionisation background. This is significant here owing to the fact that we are interested in absorption close to galaxies that may arise in fairly dense (and possibly self-shielded) gas. The self-shielding correction is purely local and is done on a particle-by-particle basis. We compute the fraction of each particle’s mass that is internally self-shielded from the ionising background by integrating the HI col-

umn density inwards from the particle's edge, assuming that it has a density profile given by the SPH smoothing kernel, until the column density crosses a threshold; within that radius we assume that all the hydrogen is neutral. We choose a threshold of  $10^{18} \text{cm}^{-2}$ , which provides the best fit to the neutral fractions obtained in the full radiative transfer models of Faucher-Giguère et al. (2009). In practise, because of a reasonably tight correlation between column density and physical density (e.g., Davé et al., 2010), this results in a fairly sharp density threshold of  $0.01 \text{cm}^{-3}$  above which the gas is fully neutral. If the gas density is greater than  $0.13 \text{cm}^{-3}$  our star formation algorithm assumes that it is star-forming. In this case we assume that the gas is completely neutral, which is reasonable since the cold fraction in the two-phase medium always dominates by mass over the hot fraction. This choice of self-shielding correction also moves all the magnesium into Mg II, which is what one expects for magnesium in neutral hydrogen based upon the ionisation potentials of magnesium. For random sight lines, we rarely probe these densities, but for targeted lines of sight particularly within 10 kpc of a galaxy, the effects of self-shielding can be significant. We also put in a transition from neutral to molecular HI for ISM gas using the Blitz & Rosolowsky (2006) pressure criterion.

Our spectral extraction implicitly assumes that all metals are in the gas phase, but the observed correlation of quasar colours with projected separation from foreground galaxies suggests substantial amounts of intergalactic dust (Ménard et al. , 2010). Zu et al. (2011) show that our vzw simulations can reproduce the Ménard et al. (2010) observations if roughly 25% of extragalactic metals (by mass) are depleted onto dust with an SMC-like grain size distribution. Precise accounting is difficult because of uncertainties in the observations, in the composition and size distribution of the dust grains, and in the destruction and pro-

duction rates as a function of time and galactocentric distance. Dust depletion is an inevitable source of uncertainty in metal-line absorption predictions from cosmological simulations; it could plausibly lower our predicted absorption for refractory elements such as carbon and silicon by 25-50%.

#### 2.2.4 Ion Selection

We investigate six different species: H I 1216, Mg II 2796, Si IV 1394, C IV 1548, O VI 1032, and Ne VIII 770. These represent some of the most common metal ions that COS probes, along with H I. All the metal lines have doublets, making their identification in observed spectra more straightforward. While H I in the Ly $\alpha$  forest is associated with diffuse baryons tracing large-scale structures in the Universe (e.g., Davé et al., 1999), stronger H I absorbers are associated with higher-density structures in the CGM (e.g., Fumagalli et al., 2011; van de Voort, 2011) and are sensitive to the outflow model used in the simulation (e.g., Davé et al., 2010) as well as the cooling implementation (see Table 2.1).

Mg II is one of the most common observed lines in QAL spectra, and it appears to be associated with the CGM environments of galaxies, especially star-forming ones (e.g., Kacprzak et al., 2007), and may indicate recent outflows (e.g., Bordoloi et al., 2011; Bouche et al., 2012; Matejek & Simcoe, 2012) and/or inflowing gas (Kacprzak et al., 2010). Mg II is often associated with H I absorbers of  $N_{\text{HI}} = 10^{16.5} - 10^{21.0} \text{ cm}^{-2}$  (e.g., Hellsten et al., 1998), indicating that Mg II frequently arises from self-shielded gas. Since our cosmological simulations do not have the resolution to fully resolve this self-shielding, we make the assumption that all magnesium in a self-shielded region is Mg II, because the ionisation potential of Mg II is above the H I ionisation energy while Mg I is below it. We cannot resolve the true substructure of Mg II, but we hope to understand the typical densities and environments from which this absorption arises. This prescription pro-

duces equivalent widths that roughly match recent observations by Rubin et al. (2012), suggesting that our Mg II modelling is not dramatically wrong.

Si IV and C IV are relatively strong lines that fall within the far-UV window often probed by COS. These are mid-ionisation potential lines that typically arise in optically thin gas, but still probe fairly overdense regions at low redshifts (Oppenheimer et al., 2012).

O VI is the most commonly observed high ionisation potential metal absorber at low redshifts (e.g., Tumlinson et al., 2011; Danforth & Shull, 2008; Thom & Chen, 2008; Bregman, 2007; Stocke et al., 2006; Chen & Mulchaey, 2009; Prochaska et al., 2011; Sembach et al., 2003; Tripp et al., 2000, 2008). Oppenheimer & Davé (2009) examined the nature of diffuse O VI absorbers in these simulations using random lines of sight through their simulation volume and found that it traces mostly photo-ionised gas in the diffuse IGM, warm-hot gas, and gas within halos. Here we focus on O VI absorption within halo gas, which we will compare to the previous results from Oppenheimer et al. (2012) on diffuse IGM O VI.

The highest ionisation potential line that we consider is Ne VIII, and it is valuable because it can trace  $10^{5-6}$  K gas (Savage et al., 2005) better than any other UV resonance line. Nonetheless, as argued in Oppenheimer et al. (2012), very weak Ne VIII can arise in gas photo-ionised by the metagalactic background. Recent observations of Ne VIII by Tripp et al. (2011) and Mulchaey & Chen (2009) have been interpreted to suggest that Ne VIII absorption arises from a transitional phase on the surfaces of cold clouds moving through hotter material. Unfortunately, our simulations are not able to resolve such surfaces, so we may be missing this component of Ne VIII absorption in our models. Nonetheless, we do find a significant number of such absorbers, in rough agreement with data (Oppenheimer et al., 2012).

### 2.2.5 Generating and Analysing Simulated Spectra

We examine both targeted and random lines of sight (LOS). For our targeted LOS we randomly select central galaxies for each of three different halo mass bins:  $10^{10.75-11.25} M_{\odot}$  (labelled  $10^{11} M_{\odot}$ ) ;  $10^{11.75-12.25} M_{\odot}$  (labelled  $10^{12} M_{\odot}$ ) and  $10^{12.75-13.25} M_{\odot}$  (labelled  $10^{13} M_{\odot}$ ). For  $10^{11} M_{\odot}$  and  $10^{12} M_{\odot}$ , we select 250 galaxies, while for  $10^{13} M_{\odot}$  there are only 86 central galaxies in the simulation so we use all of them in our sample. Because we do not properly model the detailed internal structure of the ISM in our galaxies, we do not present results through the centres of the galaxies, but rather start at  $b = 10$  kpc. We choose impact parameters  $b$  ranging from 10 kpc (centre) out to 1 Mpc, with the spacing increasing with  $b$ . For each impact parameter  $b$ , we produce four LOS per galaxy, meaning  $x+b$ ,  $x-b$ ,  $y+b$ ,  $y-b$ , for a total of 1,000 LOS per  $b$  per mass bin (344 for  $10^{13} M_{\odot}$ ).

We also generate random LOS, to compare with our targeted LOS. For our random LOS, we choose a  $100 \times 100$  grid spanning the simulation in  $x-y$  space, for a total of 10,000 LOS. These are similar to the spectra generated for Oppenheimer et al. (2012).

After generating optical depths with SPECExBIN, we construct artificial spectra by convolving our data with COS's line spread function (LSF) and adding Gaussian random noise with  $S/N=30$  per  $6 \text{ km s}^{-1}$  pixel. The LSF is roughly Gaussian with a  $\approx 17 \text{ km/s}$  FWHM, but it has some non-Gaussianity in the wings. Also, there is a small wavelength dependence to the LSF; for simplicity, we choose the G130M LSF at  $1450 \text{ \AA}$  as representative of all wavelengths to avoid complications in our interpretations owing to variations in the LSF.

Figure 2.1 shows examples of our simulated spectra. For each column, a single central galaxy is chosen from that mass bin, and we plot spectra at impact parameters of 10 kpc (red), 100 kpc (green), and 1 Mpc (blue) away from that

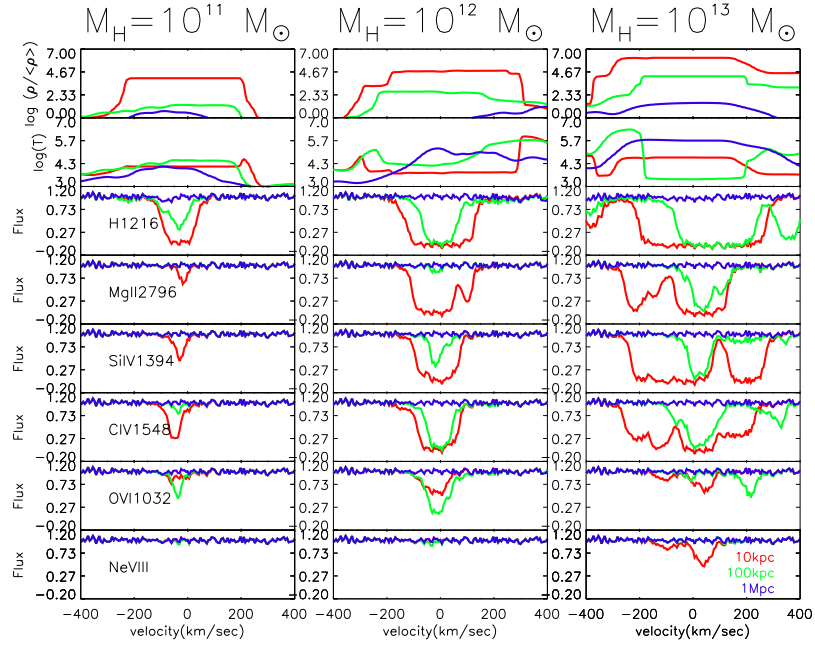


Figure 2.1: Simulated spectra for three galaxies at  $z=0.25$ , convolved with the COS line spread function and noise added with a  $S/N=30$ . Each column corresponds to a representative galaxy with the labelled halo mass. We plot lines of sight at distances of 10 kpc (red), 100 kpc (green), and 1 Mpc (blue) away from the galaxy. The top two panels show the H I optical depth-weighted density and temperature, and the lower panels show simulated spectra for H I and other ions. All units are physical, for a Hubble parameter  $h = 0.7$ .

galaxy. These particular galaxies were chosen for this figure since they have many absorption features, which illustrates the methodology well, although that is not necessarily typical.

The top two panels show the gas temperature and density weighted by H I optical depth, and the lower panels show simulated spectra for H I and other ions as labelled. As expected, the gas density is higher at smaller impact parameters, which yields stronger absorption in most ions. Also, more massive halos generally have more absorption. While this figure only shows three selected galaxies, one can already see some of the trends that will be explored and quantified later in this paper, although other trends are statistical in nature and not well depicted in this figure.

We fit Voigt profiles to the absorption features using AUTOVP (Davé et al., 1997), which yields column densities, line widths, (rest) equivalent widths, and redshifts for each absorber. We set the detection significance criterion to  $4\sigma$ , which should be quite conservative given that the noise is Gaussian random by construction. Since the details of deblending absorption features into multiple components can be quite sensitive to the noise level and algorithmic details, we generally focus on absorption *systems*, in which we combine all lines that have separations  $< 100$  km/s. This mitigates the sensitivity to these issues, and allows for a more robust comparison to the observations, at the cost of discarding some of the information available about the internal kinematics of the absorption features. Some of our figures below plot median line properties, and since weak lines outnumber strong lines, median properties necessarily depend on the lower cutoff. Our results should be taken to refer to the population of lines detectable with typical  $S/N=30$  COS spectra, with closely separated components combined into systems.

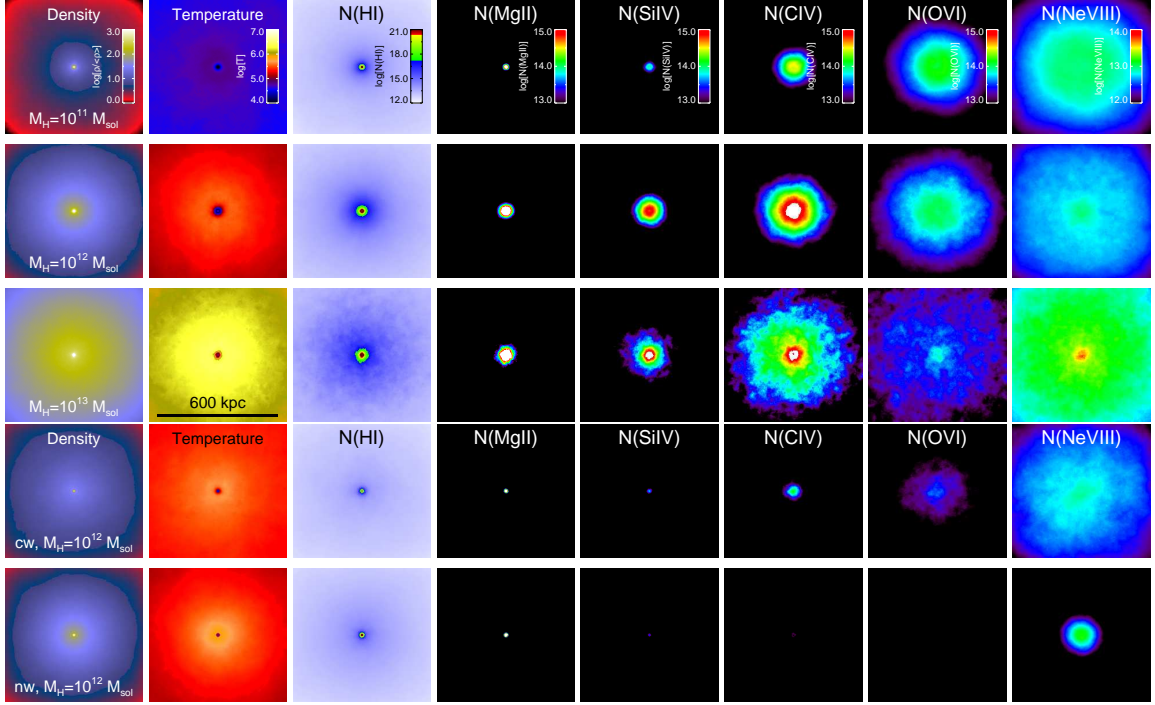


Figure 2.2: Columns one and two show the median log overdensity and median log temperature; subsequent columns show median log column densities for each ion as labelled, all at  $z=0.25$ . First three rows are for vzw; the first row is for mass bin  $10^{11} M_{\odot}$ , second for  $10^{12} M_{\odot}$ , and the third for  $10^{13} M_{\odot}$ . The fourth and fifth rows are for  $10^{12} M_{\odot}$  halos in the constant wind and no wind models, respectively, and are discussed further in §7. Note the colour scales for HI and Ne VIII are different than for the other ions. All panels are 658 kpc across.



## 2.3 Physical Conditions of Absorbers

### 2.3.1 The CGM in Absorption

We seek to understand the density and temperature of the CGM and how those conditions give rise to the presence of various observable ions. We begin by presenting a pictorial overview of the simulated CGM, as seen in physical conditions and line absorption, to build our intuition as to how these physical conditions relate to observables.

Figure 2.2 shows a stacked median image of the galaxies around which we generate our targeted lines of sight. We generate the images by taking the pixel-by-pixel median of each given quantity for the 250 galaxies in the mass bin of  $10^{11} M_{\odot}$  (top row) and  $10^{12} M_{\odot}$  (middle row), and the 86 galaxies in the  $10^{13} M_{\odot}$  mass bin (bottom row). Because this is a pixelized median, the satellites are effectively removed. The depth of the image is 658 kpc centred at the redshift of the galaxy ( $\approx 1.2\%$  of the full simulation depth). The first two columns show the median overdensity and median temperature of all the gas. The remaining plots show, in each column, the absorption in the various ions that we consider in this paper, again for each of our three halo mass bins. Note the colour scale for HI, subdividing HI into damped Lyman $\alpha$  systems (red), Lyman-limits systems (green) and the Ly $\alpha$  forest (blue), consistent with Pontzen et al. (2008) and van de Voort et al. (2012), is different from the metal lines. We also include, in the lower two panels, results for two different wind models, a constant wind “cw” model and a no wind “nw” model for the  $10^{12} M_{\odot}$  halo mass bin (see §7).

As expected, the gas density is strongly concentrated towards the (stacked) central galaxy. Galaxies in more massive halos have a larger extent. The temperatures increase with mass bin, with the  $10^{13} M_{\odot}$  mass bin showing halo gas that is predominantly near the virial temperature, but other halos showing more sub-

virial temperatures. This reflects the now well-understood division at  $10^{12} M_{\odot}$  between cold and hot-gas-dominated halos (e.g., Kereš et al., 2005; Dekel & Birnboim, 2006; Gabor et al., 2011). Some cool gas must be present in  $10^{13} M_{\odot}$  mass halos, however, since we find significant HI absorption (see §3.4). We reiterate that our simulations do not include a prescription to quench star formation in hot halos, which is required to produce red and dead galaxies (Gabor et al., 2011), so more realistic models might have less cool gas in  $10^{13} M_{\odot}$  halos. However, recent observations (Thom et al. 2012, in preparation), suggest that even early type galaxies have prevalent HI absorption, so perhaps whatever mechanism quenches star formation does not greatly impact the cooler halo gas.

The morphology of the absorption (neglecting individual satellite contributions) is strongly dependent on the ion being probed. Mg II is highly centrally concentrated, and shows very little qualitative morphological difference between the different halo masses (on this plot scale). At the opposite extreme, Ne VIII shows very diffuse, extended absorption in the lower mass halos, and is more centrally concentrated in the highest halo mass bin. The other ions lie in between these two extremes, progressing smoothly through Si IV, C IV, and O VI. We foreshadow our upcoming results by ordering these ions by increasing ionization potential, which we will demonstrate provides an intuitive guide towards understanding how absorption traces physical conditions.

### 2.3.2 Phase Space Plots

To begin to quantify the physical conditions giving rise to HI and metal absorption around galaxies, it is useful to examine the location of absorption systems in density-temperature phase space. This provides a valuable overview of the physical conditions of the gas traced by the various absorption species and sets the stage for discussing how various observable properties trace these underly-

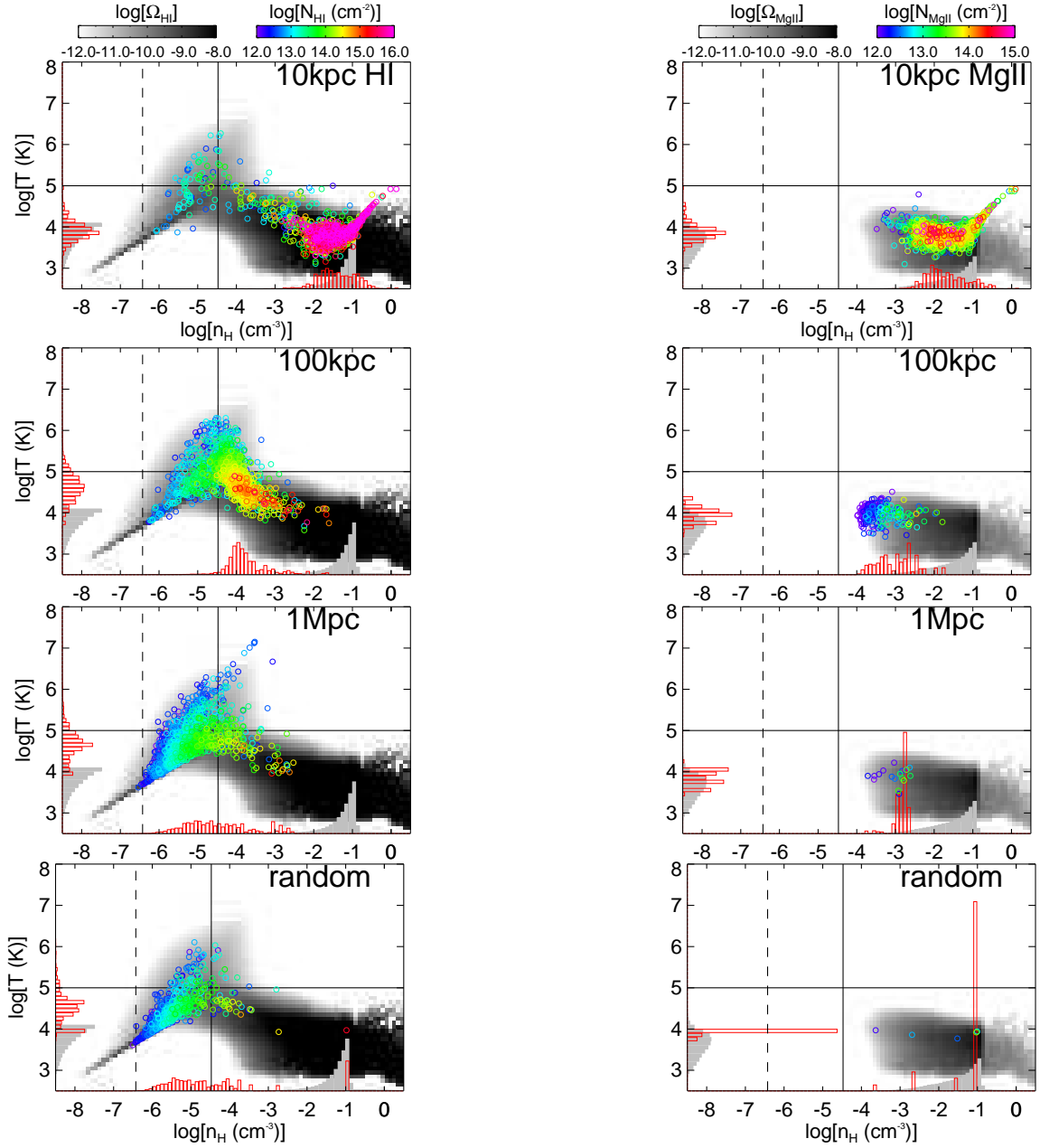


Figure 2.3: Phase space plots showing the location, in density and temperature space, of HI (left) and Mg II (right) for  $M_h = 10^{12} M_\odot$  at  $z=0.25$ . Each coloured point represents an absorption system found along targeted lines of sight at 10 kpc (top row), 100 kpc (second), 1 Mpc (third), and along random lines of sight (bottom). The grey shading shows the mass-weighted absorption for all gas below  $n_H = 0.13 \text{ cm}^{-3}$  outside of all galaxies in the simulation volume, at each location in phase space. The red and grey histograms show the distributions in identified absorbers and the entire volume, respectively, collapsed along each axis. These are identical for each ion. The histograms are linearly scaled, and the integral under the red and grey histograms are set to be equal. Note that the absorber colour scale is different for HI.

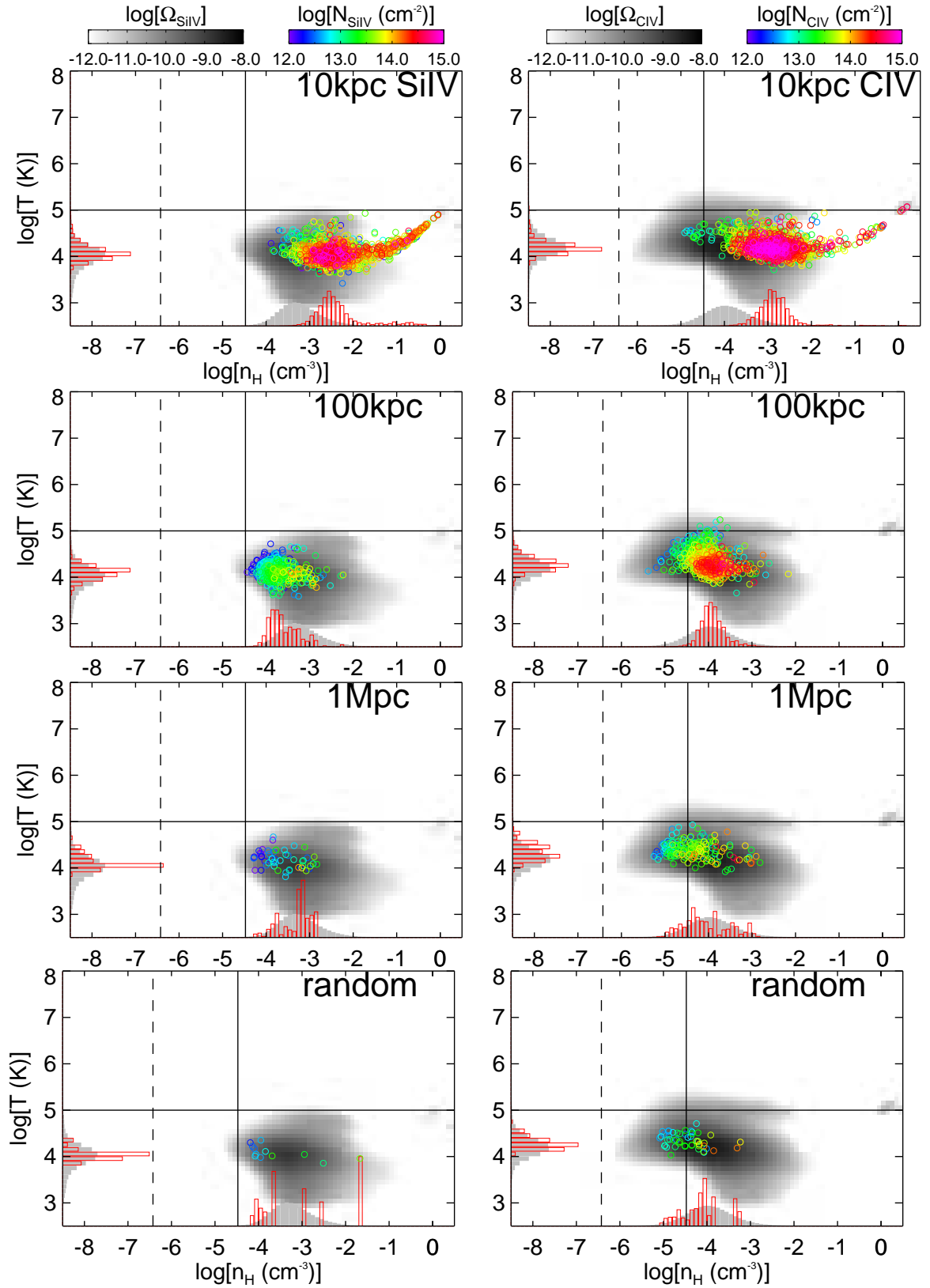


Figure 2.4: Analogous to Figure 2.3, phase space plots showing the location, in density and temperature space, of Si IV (left) and C IV (right) absorbers, for  $M_h = 10^{12} M_\odot$ , at the impact parameters indicated.

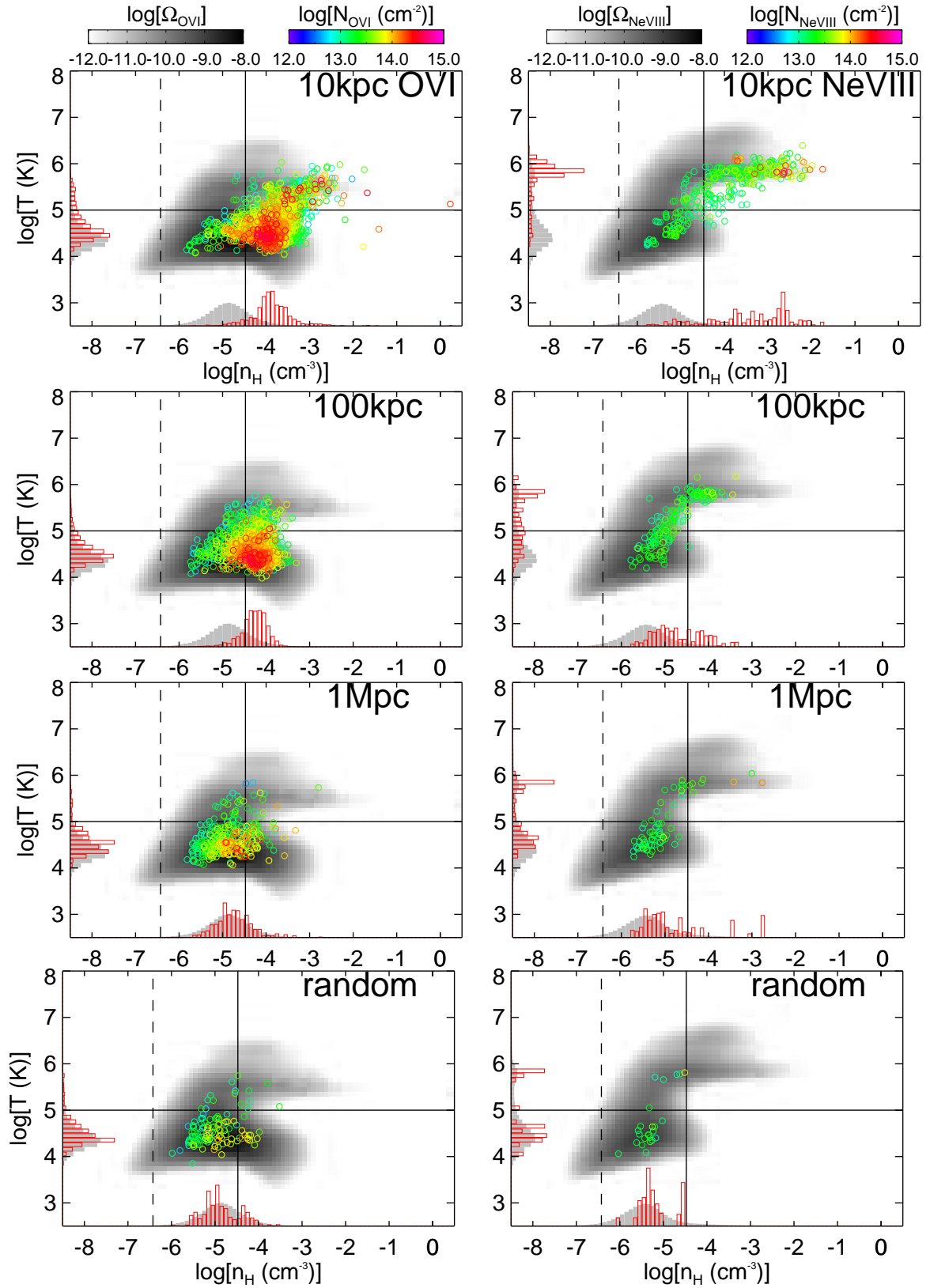


Figure 2.5: Analogous to Figure 2.3, phase space plots showing the location, in density and temperature space, of OVI (left) and Ne VIII (right) absorbers, for  $M_h = 10^{12} M_\odot$ , at the impact parameters indicated.

ing physical conditions. We thus begin by examining where our systems appear in phase space as a function of impact parameter.

In Figures 2.3–2.5 we show the overdensity-temperature space locations of absorption systems (circles, colour-coded by column density) at different impact radii as labelled, overlaid on the global (i.e. cosmic) mass distribution of that ion ( $\Omega_{\text{ion}}$ ) computed for all non star-forming gas ( $n_{\text{H}} < 0.13 \text{ cm}^{-3}$ ) in the simulation volume (grey shading). We plot this for galaxies in our  $10^{12} M_{\odot}$  halo mass bin. The vertical dashed line shows the cosmic mean density at  $z = 0.25$  ( $n_{\text{H}} = 10^{-6.43} \text{ cm}^{-3}$ ), and the solid horizontal and vertical lines subdivide this cosmic phase space into the four regions defined by Davé et al. (2010). The temperature cut at  $T = 10^5 \text{ K}$  divides “hot” phases from “cool” phases, and the density cut distinguishes halo gas ( $n_{\text{H}} > 10^{-4.47} \text{ cm}^{-3}$ , i.e. the virial radius density at  $z = 0.25$ ) from diffuse, intergalactic gas. The four quadrants, going clockwise starting at the upper right, therefore, correspond to: hot halo, condensed, diffuse, and WHIM gas.

In targeted sight lines, components found within  $\pm 300 \text{ km s}^{-1}$  of the targeted galaxy are considered to be associated with the galaxy (as described further in §2.4). Those components are then grouped into systems. Our definition of a system is all the components that lie within  $100 \text{ km s}^{-1}$  of any other component within that system. We do this because fitting detailed line profiles can be non-unique and quite sensitive to the assumed S/N, as described further in §2.5. The temperatures and densities of the systems are calculated as the column density-weighted means of the individual components. In most cases, a single component dominates a system.

The histograms along the temperature and overdensity axes indicate the relative fractions of the cosmic mass density (grey histograms) and the absorption systems found in our lines of sight (red) as a function of temperature and over-

density. Comparing the red and grey histograms indicates how well the absorption seen in each ion at a given impact parameter traces the underlying density and temperature distribution of all such ions within the volume. Note that the histograms are linearly (not logarithmically) scaled, and that the integral under the red and grey histograms are set to be equal. The grey histograms are the same for all plots of a given ion, and sum only gas outside galactic ISM. In contrast, the red histograms vary depending on the absorption found for the targeted sight lines at various  $b$ . To avoid outliers dominating the computation, the red histograms have been generated with a cap in column density of  $10^{16} \text{ cm}^{-2}$  for H I and  $10^{15} \text{ cm}^{-2}$  for the metal lines. All the lines above these values have been set to this value when summing the column density-weighted histogram, to avoid having the histograms skewed by single large, saturated absorbers, since such absorbers generally have highly uncertain column densities from Voigt profile fitting. This affects 1.3% of all H I absorbers and no more than 0.7% of all metal-line systems.

The vertical column of panels show the distribution at three different targeted impact parameters, 10 kpc, 100 kpc, and 1 Mpc, along with random LOS (bottom) for each ionic species. The different columns correspond to different ions, beginning with H I and then ordered by increasing ionisation potential (discussed below in Figure 2.6), namely Mg II, Si IV, C IV, O VI, and Ne VIII. Each galaxy has four LOS per impact parameter, and there are 250 galaxies per mass bin. Therefore, each panel of the top three rows represent 1000 lines of sight. We use a velocity window of  $\pm 300 \text{ km s}^{-1}$  for the targeted LOS throughout, which we explain in §4 as the rough window containing the majority of absorption associated with the galaxy. Hence, the total path length in each panel is  $6 \times 10^5 \text{ km s}^{-1}$  or  $\delta z = 2.52$ . In the bottom row, we subsample the absorbers from the random lines

of sight chosen to cover an equivalent redshift pathlength.

The first clear trend from these figures is that the number of systems goes down with increasing impact parameter. The rate at which the number drops shows some differences among the various ions; we will explore this further in §6. The straightforward explanation for this is that both the metallicity and the gas density drop as one moves away from the galaxy, which translates into less metal absorption. Nonetheless, it is clear that even at 1 Mpc, there are more systems than in the random LOS (see §6).

Examining the plots more closely, one sees that for some ions there is a distinct shift in the overdensities probed by that ion as one moves out in impact parameter. This is most clear for the higher ionisation potential lines of O VI and Ne VIII, where the peak of the red histograms moves to lower overdensities at higher impact parameter, but it is also true for all other ions except Mg II. We remind the reader that the grey histograms are the same in every panel for each species because they correspond to the cosmic mass density of that ion, and thus we can interpret the red histograms as tracing a subset of the cosmic mass density.

To illustrate some of the information contained within these plots and histograms, consider C IV. At impact parameters of 10 kpc, C IV traces an average  $n_{\text{H}} \sim 10^{-3} \text{ cm}^{-3}$  (red histogram), but the cosmic mass-averaged C IV density is  $n_{\text{H}} \sim 10^{-4} \text{ cm}^{-3}$  (grey histogram). In fact, there is very little cosmic C IV at  $n_{\text{H}} > 10^{-3} \text{ cm}^{-3}$ . However, 10 kpc from a galaxy inside a  $10^{12} M_{\odot}$  halo corresponds to a rare location in the Universe where there are high levels of metal enrichment and high densities, and hence C IV traces these metals. At impact parameters of 100 kpc, the red histogram for C IV peaks at  $10^{-4} \text{ cm}^{-3}$ , similar to the cosmic averaged peak in the grey histogram. However, the distribution of densities is narrower, indicating that absorbers at this impact parameter do



not account for the full range of densities giving rise to all the C IV absorption. At impact parameters of 1 Mpc, C IV traces overdensities similar to the cosmic average. Finally, the random LOS C IV should theoretically trace the cosmic distribution of C IV and the red and grey histograms should overlap. However, as discussed in Oppenheimer et al. (2012), the absorber histogram is biased towards lower densities. The random LOS sample covering  $\delta z = 2.5$  does not adequately sample densities with  $n_{\text{H}} > 10^{-4} \text{ cm}^{-3}$  because this pathlength is not long enough to probe these rare high density regions. This illustrates a central tenet of this paper, namely that close-in targeted LOS probe regions of density that are not well-sampled via randomly chosen quasar absorption sight lines.

We can similarly examine other metal ions. Random LOS showing absorption from Mg II usually probe gas within roughly 10 kpc of galaxies. As a result, random LOS with Mg II absorption have the same overdensity as the 10 kpc gas. Meanwhile, Mg II absorption from further away generally probes lower density gas. For mid-ions, the random LOS have significant absorption farther away, and hence 10 kpc LOS pick out especially dense gas, but there is little distinction between 100 kpc, 1 Mpc, and random. For high ions, these arise in more diffuse gas so that the random LOS can probe quite low overdensities, and hence the LOS at 10 and 100 kpc pick out particularly denser gas.

Finally, for comparison, we examine neutral hydrogen. H I most closely resembles the general behaviours of Mg II, in that the cosmic density of H I is heavily weighted toward  $n_{\text{H}} > 10^{-2} \text{ cm}^{-3}$  and most cosmic H I arises at small impact parameters going through ISM gas. There are, of course, a few key differences between the well-understood behaviour of H I and a metal-line species like Mg II. Most cosmic H I is in damped Ly $\alpha$  systems (DLAs), gas that is either within or near the galactic ISM (Wolfe et al., 2005), as indicated by the steadily

rising grey histograms for H I. The Ly $\alpha$  forest tracing diffuse gas, i.e. column densities  $N_{\text{H I}} \sim 10^{13} - 10^{15} \text{ cm}^{-2}$ , corresponds to an insignificant fraction of the total cosmic H I, unlike the high ionisation potential metal lines where most of the cosmic absorption arises from IGM and CGM densities. Also, H I can trace a relatively large range of phase space because: (i) hydrogen is present at all densities, (ii) Ly $\alpha$  has a high oscillator strength, and (iii) its presence does not rely on metal enrichment. A comparison of the red absorber histograms to the grey cosmic density histograms makes little sense for H I since all absorbers  $> 10^{16} \text{ cm}^{-2}$  have been reduced in our analysis to  $10^{16} \text{ cm}^{-2}$ , which hides most of the Ly $\alpha$  absorption from damped Ly $\alpha$  and Lyman-limit systems. However, the red histograms show a significant downward shift in overdensity going from impact parameter of 10 kpc out to 1 Mpc, reflecting the very different densities probed at these three impact parameters.

### 2.3.3 Physical Conditions vs. Ionisation Potential

Overall, the phase space plots illustrate a key general trend: the higher the ionisation potential of the metal species, the lower the overdensity that it traces on average, *and hence the further away from galaxies it arises*. We will argue that this is the case in our simulation because these metal species that we explore are primarily photo-ionised, except for high ionisation potential lines in massive halos.

To quantify these trends, Figure 2.6 plots the column density-weighted median overdensity (upper panel) – i.e., the overdensity above which 50% of the absorption occurs – of absorption systems of various ions, as a function of their ionisation potential for going from that ion into the next higher ionisation state. To compute the column-density weighted median value, we take, for each ion, all the systems for all the lines of sight and bin them according to their corresponding overdensity (or temperature), as in the red histograms from figures 2.3,

2.4 and 2.5. We then sum the column densities of all the systems in a given bin. We plot the overdensity (or temperature) corresponding to where half of the total column density (for all the bins) is above/below that value.

We also plot the column density-weighted median temperature (lower panel), i.e. the temperature above which 50% of the absorption occurs. Points are plotted for the well-defined median for a sample of 250 galaxies. To illustrate the range, we show vertical range bars (not error bars) that span the 16% to 84% enclosing values for the 100 kpc bin, as an example. This is the range of the overdensity (or temperature) above which 16% of the absorption occurs to the overdensity (or temperature) above which 84% of the absorption occurs. The different colour points represent the three different impact parameters, with black points showing the global values from the random LOS for comparison. These plots are for galaxies in halos with  $M_{\text{halo}} \approx 10^{12} M_{\odot}$ . We plot here the full range of column densities shown in Figures 2.3-2.5, but these findings do not depend significantly on the column density range probed.

Figure 2.6 (top panel) shows that the median density of metal absorption decreases steadily with ionisation potential, but that the rate of the decrease depends on impact parameter. Far from galaxies, the decrease is roughly two orders of magnitude from Mg II to Ne VIII. This reflects the predominantly photoionised nature of our absorption lines arising in diffuse gas far from galaxies, as elements require lower densities to achieve higher ionisation levels. The mean overdensity at 1 Mpc is essentially indistinguishable from that of the random LOS. At 10 kpc there is nearly as large a decrease in the median overdensity as a function of ionisation parameter as at 1 Mpc, but in each case the median overdensity is around two orders of magnitude larger at 10 kpc than at 1 Mpc. Impact parameters of 100 kpc are an interesting counterpoint, showing less than an or-

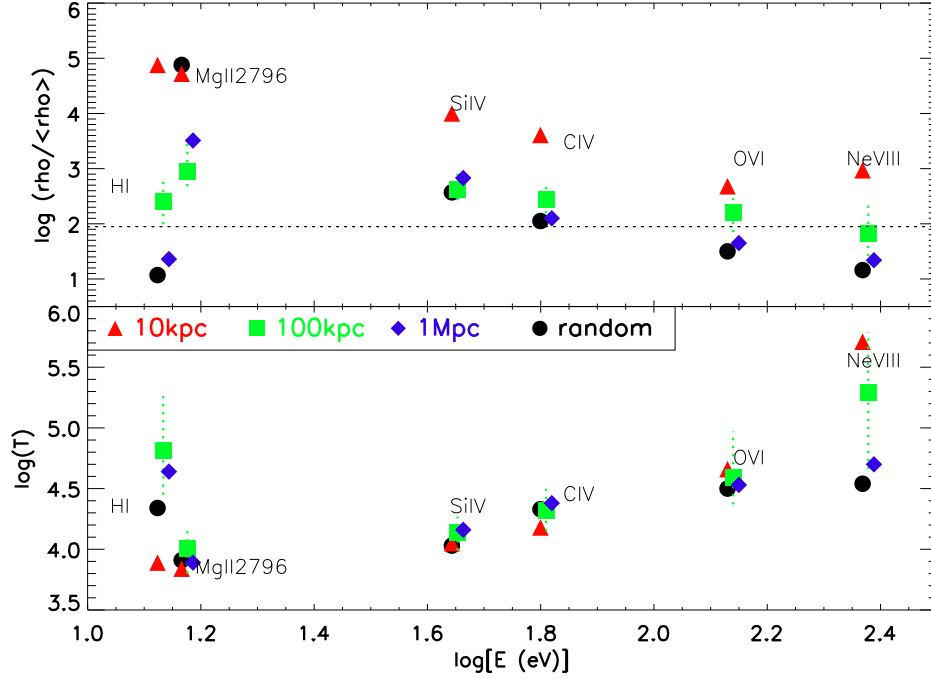


Figure 2.6: *Top panel:* Median column density-weighted overdensity as a function of ionisation energy for the six ions we consider. Four points for each ion are plotted, corresponding to three different  $b$  values (all for mass bin  $10^{12}$ ) and random LOS. 100 kpc (green squares) and random (black circles) are plotted at the energy in eV at which the labeled ion is ionised to the next higher level; 10 kpc (red triangles) and 1 Mpc (blue diamonds) are shifted for visibility. Points are plotted at the well-defined median; vertical range (not error) bars (shown only on the 100 kpc case for clarity) span the 16% to 84% enclosing values. The dotted horizontal line represents the virial overdensity at  $z = 0.25$ . *Bottom panel:* Similar to the top panel, but for column density-weighted temperatures.

der of magnitude difference in the mean overdensity from Mg II to Ne VIII. As we will discuss, this arises because in  $10^{12} M_{\odot}$  halos the high ionisation potential lines start to have an additional contribution from collisionally ionised gas that occurs in the denser regions closer to galaxies.

The horizontal dotted line approximately delineates the overdensity boundary of virialised halos using Equation 1 from Davé et al. (2010). At 10 kpc, unsurprisingly, all the absorption in all the ions arises in gas that is within halos. At larger impact parameters and for the random LOS, the median overdensity depends strongly on the ionisation state, with ions having ionisation potentials lower than C IV generally arising in halo gas for  $10^{12} M_{\odot}$  halos, while higher ionisation potential absorption often arises in gas with overdensities lower than that corresponding to galaxy halos. Unfortunately, this absorption is usually weak and photo-ionised (Oppenheimer et al., 2012), and hence generally still does not trace the so-called missing baryons in the WHIM.

Turning to the temperatures, Figure 2.6 shows that the median temperature of metal absorption rises steadily with ionisation potential. It also shows that, with the exception of Ne VIII, there is essentially no dependence of metal absorption gas temperature on the impact parameter. This reflects the fact that the majority of metal ions all arise in  $\sim 10^{4-4.5}$  K gas, i.e. photo-ionised gas temperatures, regardless of the impact parameter. Note that the virial temperature in this halo mass range is about a million degrees, the upper boundary of the plot.

For Ne VIII at large impact parameters, the median temperature is around 30,000 K, still considerably lower than its collisional ionisation peak temperature of  $10^6$  K, and owes to photo-ionised gas. This begins to change as one approaches galaxies. At 100 kpc, about half of the absorption comes from gas above 200,000 K, and at 10 kpc most of the Ne VIII is hot, with half the absorption com-

ing from gas above 500,000 K that is collisionally ionised. Since (as is evident from the phase space plots) these Ne VIII absorbers are also stronger, we obtain a result matching that of Oppenheimer et al. (2012) that strong Ne VIII absorbers are more often collisionally ionised. By using our targeted LOS, we show here that this mostly arises from Ne VIII within 100 kpc of galaxies, at least in these  $10^{12} M_{\odot}$  halos. As hypothesised in Oppenheimer et al. (2012), these strong lines are probably the only ones that have been studied carefully with COS to date (e.g., Tripp et al., 2011), but larger and deeper samples should uncover a population of photo-ionised Ne VIII arising in more diffuse gas.

This hot gas close to galaxies is also evident in the H I, where at 100 kpc half the H I absorption traces gas that is above 50,000 K, and much of this gas is above the halo virial density. Even at 1 Mpc there is some hot H I, as the median temperature is still fairly high at 40,000 K, even though the median overdensity is quite low. As one can see from Figure 2.3, there are a number of absorbers than can arise from both hot halo gas and truly diffuse WHIM gas. Hence, in principle, broad H I absorbers could trace truly diffuse WHIM gas (i.e. the missing baryons), but one has to be careful not to count hot halo gas, which may be detectable by other means.

Our simulations predict that even high ions are mostly photo-ionised at all radii. This is at odds with recent work by Stinson et al. (2012), whose simulations find that O VI is predominantly collisionally ionised in their individual galaxy simulations. Their model has the advantage of having higher resolution than ours, but our models have the advantage that our feedback prescription has been carefully constrained to match a broad range of observations, including IGM enrichment. The main difference is likely that their feedback model relies on super-heating gas within the ISM that drives hot gaseous outflows, whereas

our model follows scalings expected for momentum-driven winds in which the gas is pushed out via radiation pressure, and therefore is not super-heated. Our outflows do heat once they interact with surrounding gas, but since they are typically quite enriched, the metal-enhanced cooling rates are rapid. Simply put, their feedback model adds hot gas to the halo by construction, while ours adds cooler gas by construction; it is not immediately evident which is closer to correct, and likely depends on the details of how winds are actually launched which is currently not well understood. Stinson et al. (2012) did not show the O VI temperature as a function of radius, area-weighted as would be appropriate for an absorption line survey, so it is difficult to compare our results directly. But these differences highlight that modeling the CGM is not a fully solved problem. Examining such detailed statistics as line ratios and alignment statistics between O VI and H I (and low metal ions, e.g. Si III) provides a way to characterize the temperature of the O VI gas and discriminate between such scenarios. We note that at least in the random lines of sight examined in Oppenheimer & Davé (2009), the observed alignment statistics between O VI and H I were better reproduced in a momentum-driven wind scalings model as opposed to our constant wind model that yielded more collisionally-ionised O VI. We are conducting such comparisons now against COS-Halos data.

In summary, different metal ions probe different physical conditions around galaxies, with lower ionisation potential lines probing denser gas. Mg II absorbers probe very high density gas in and around the ISM of galaxies, while high ionisation potential lines probe diffuse gas in the outskirts of halos and beyond the virial radius. The absorbing gas temperatures generally reflect the photo-ionised nature of metal absorption even down to small impact parameters in our models, with the notable exception of Ne VIII lines that can arise in hot gas near

galaxies. In the next section we will show that O VI in larger halos where a hot CGM is present is also mostly collisionally ionised. These results demonstrate that spanning a range of ions with low to high ionisation potentials can in principle probe a wide range of physical conditions in the CGM, but that when a range of ions are seen in a single system, it is probably unwise to assume that they all arise from the same gas (for the purposes, e.g., of CLOUDY modeling). Throughout the rest of this paper, we will discuss our results in terms of low (Mg II), mid (Si IV and C IV), and high ionisation (O VI and Ne VIII) lines, since this provides an underlying physical context for understanding the behaviour of these various metal absorbers.

#### 2.3.4 Physical Conditions vs. Halo Mass

The previous section focused entirely on  $10^{12} M_{\odot}$  halos, as representative of a typical  $L^*$  galaxy halo. However, the increasing collisional ionisation contribution to the higher ionisation potential species might suggest that there could be some halo mass dependence since, as is evident in Figure 2.2 and has been shown by e.g. Kereš et al. (2005), large halos have substantially more hot gas.

To investigate any trends with halo mass in Figure 2.7, we plot in the top panels the column density-weighted median overdensity and temperature as in Figure 2.6, here as a function of halo mass, focusing on H I (left panel), O VI (middle panel), and Ne VIII (right panel). As in Figure 2.6, we plot the full range of column densities shown in Figures 2.3-2.5, but these findings do not depend much on column density range probed. We show three different impact parameters, slightly offset horizontally for ease of visibility, and here we show the 16 – 84% range for all cases. The points for galaxies in halos of  $10^{12} M_{\odot}$  are identical to those shown in Figure 2.6. We do not show the random LOS here; the values are similar to the 1 Mpc case. We also do not show the other ions, because in those



cases there are no discernible trends with halo mass.

At 10 kpc, for H I, the absorption arises from low temperature gas for all mass bins. While Figure 2.2 shows halos of mass  $10^{13}M_{\odot}$  have high median temperatures, Figure 2.7 shows the H I absorption mostly comes from low temperature gas present in these halos. For absorption around galaxies in halos of  $10^{11}M_{\odot}$ , most of the O VI and Ne VIII absorption owes to gas with overdensities lower than that found in galaxy halos, since the densities are below the dotted virial overdensity line. The exception is O VI at 10 kpc, where about half the absorption comes from the outskirts of halos. Both high ionisation potential lines have a median temperature within the photo-ionised regime at all impact parameters (although for Ne VIII there is a tail to higher temperatures for impact parameters of 1 Mpc). Hence O VI and Ne VIII absorption around galaxies with halo masses of  $10^{11}M_{\odot}$  actually traces photo-ionised, diffuse IGM gas. This occurs because there is so little hot gas in these small halos (Kereš et al., 2005) that there is little opportunity for these ions to trace collisionally ionised gas.

For galaxies in  $10^{12}M_{\odot}$  halos, the temperatures are still mostly representative of photo-ionised gas for O VI, but Ne VIII begins to trace somewhat hotter gas, already indicating a contribution from collisionally ionised gas at smaller impact parameters. At impact parameters of 10 kpc, this gas is within galaxy halos for both ions, and even at 100 kpc almost all the O VI absorption and about half the Ne VIII absorption owes to gas with an overdensity consistent with being within galaxy halos. At impact parameters of 1 Mpc, the gas giving rise to this high ionisation potential absorption still mostly arises from gas outside of galaxy halos.

Finally, for galaxies in  $10^{13}M_{\odot}$  halos, we see a strong dependence of physical conditions on impact parameter, with the density and temperature both being substantially higher at smaller impact parameters. At impact parameters of 10

kpc and 100 kpc for both ions, all the absorption owes to gas within galaxy halos that is at temperatures indicative of collisional ionisation. This reflects the substantial presence of hot, virial-temperature gas within these halos. At impact parameters of 1 Mpc, however, the absorption still mostly arises from photo-ionised, diffuse IGM gas.

In summary, the high ionisation potential lines tend to trace collisionally ionised hot gas when it is present. But this gas is generally only present abundantly well inside of halos, at impact parameters of less than 100 kpc, and only in massive halos where a hot gaseous atmosphere can form. In those cases, these (and other high ion) lines may trace hot gas in halos that are not easily probed by X-ray emission (or absorption lines), offering a unique opportunity to study these baryons.

#### 2.4 Absorption around galaxies in redshift space

The distance of an absorber from a galaxy can be observationally characterised by two parameters: the line-of-sight velocity difference  $\Delta v$  and the impact parameter  $b$ . In this section we discuss the former, i.e. how absorption properties vary with the velocity distance from the central galaxy. We seek to answer questions like the following: Does the absorption drop off with  $\Delta v$  at different rates for different ions? Can we identify a characteristic LOS velocity distance over which the galaxy provides a clear excess of absorption? How do these tendencies reflect the physical conditions of the absorbing gas?

Figure 2.8 shows the column density ( $N$ ) versus velocity separation ( $\Delta v$ ) from the central galaxy for each of our six ions, with the species ordered by increasing ionisation potential going down the columns. The lines show the median column densities for all lines of sight at the three different impact parameters: 10 kpc (red), 100 kpc (green), 1 Mpc (blue), for the three different halo masses:  $10^{11} M_{\odot}$

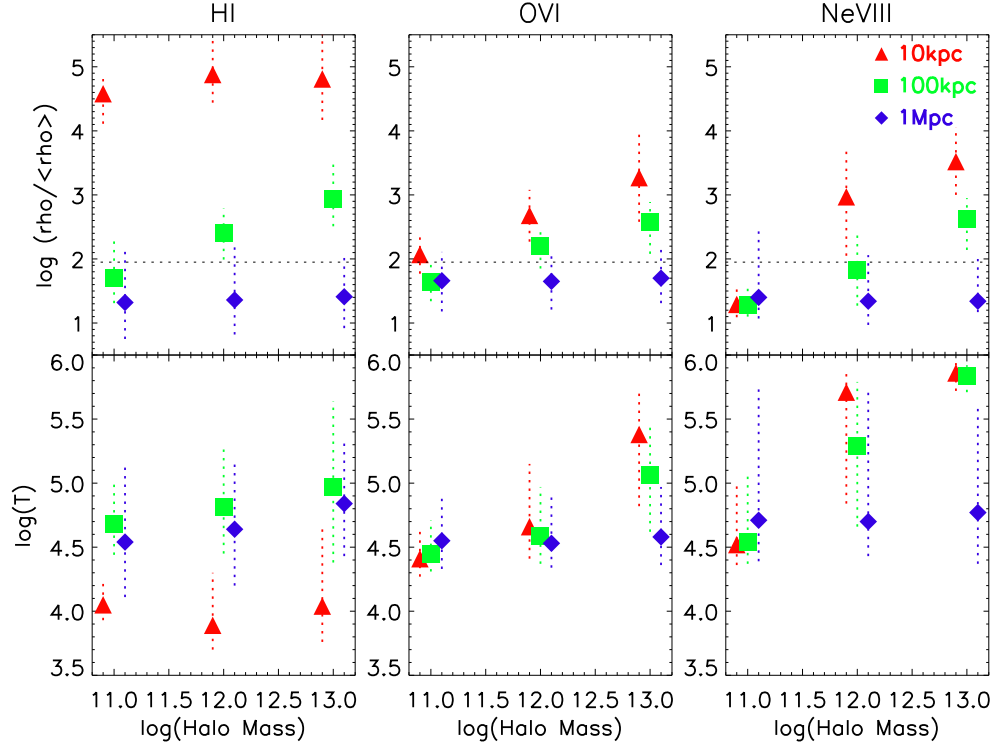


Figure 2.7: Median column density-weighted overdensity and temperature vs. halo mass for HI (left panels), OVI (middle panels), and Ne VIII (right panels). For all panels, the different colours correspond to the three different impact parameters: 10 kpc (red triangle), 100 kpc (green square), and 1 Mpc (blue diamond) (offset for clarity). The range bars span the 16% to 84% enclosing values, and the dotted horizontal line represents the virial overdensity.

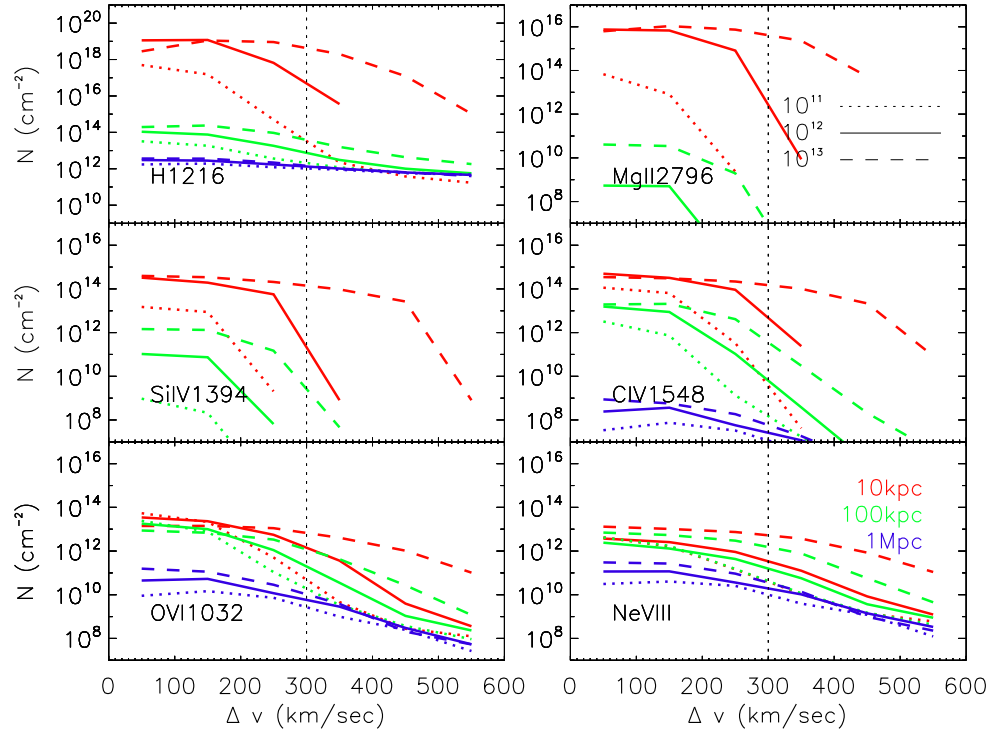


Figure 2.8: Median column density ( $N$ ) vs. velocity separation ( $\Delta v$ ) from the central galaxy  $\Delta v$  for  $M_h = 10^{11,12,13} M_\odot$  (dotted, solid, and dashed lines, respectively). We show results at three impact parameters: 10 kpc (red), 100 kpc (green), and 1 Mpc (blue). Vertical dotted lines mark  $300 \text{ km s}^{-1}$ .

(dotted),  $10^{12} M_{\odot}$  (solid), and  $10^{13} M_{\odot}$  (dashed). We use  $100 \text{ km s}^{-1}$  bins and plot at the bin's midpoint. For example,  $\Delta v = 150 \text{ km s}^{-1}$  plots the total column density between  $\pm(100 - 200) \text{ km s}^{-1}$ . Note that the y axis has a rather large range; most of this range is not accessible observationally, but we include it to accentuate the trends.

The median column density decreases with increasing  $\Delta v$  for all the ions, following the trend highlighted before that the absorption tends to be higher near galaxies. Except at high halo masses, there are drops in these curves before  $\pm 300 \text{ km s}^{-1}$ . Conservatively, we may say that the vast majority of absorption generally occurs within  $\pm 300 \text{ km s}^{-1}$  of the central galaxy's velocity, although in many cases the majority occurs within a smaller velocity interval. We choose to define the velocity window associated with the galaxy as  $300 \text{ km s}^{-1}$  to account for as much absorption in the higher mass halos as possible while not going far beyond the drops in the lower mass halos. We note that  $\pm 300 \text{ km s}^{-1}$  is roughly consistent with recent observational work by Prochaska et al. (2011). Quantitatively, we can consider the total amount of absorption within  $\pm 300 \text{ km s}^{-1}$  relative to total absorption within  $\pm 600 \text{ km s}^{-1}$ . Looking at all three impact parameters, O VI has at least 96% of its column density within this velocity limit for  $M_{\text{halo}} = 10^{11} M_{\odot}$ , 97% for  $M_{\text{halo}} = 10^{12} M_{\odot}$ , and 88% for  $M_{\text{halo}} = 10^{13} M_{\odot}$ . The absorption of lower ionisation potential metal species falls off even faster with increasing velocity difference. This indicates that in general one has to look only within the central  $600 \text{ km s}^{-1}$  window around a galaxy to find most of the absorption associated with it.

Absorption around galaxies in our most massive halo bin,  $10^{13} M_{\odot}$ , shows a shallower decrease with increasing  $\Delta v$ , reflecting these halos' larger virial velocities and hence larger peculiar motions of gas and satellites. While the  $\pm 300 \text{ km s}^{-1}$

cut misses some absorption in the large halos at small  $b$ , LOS passing so close to such massive galaxies are rare. Henceforth, we only consider absorption within  $\pm 300 \text{ km s}^{-1}$  of galaxies for our targeted LOS in the subsequent figures.

Now we examine the differences between the various metal ions. The low ionisation potential ions decrease in absorption more rapidly with increasing impact parameter than high ionisation potential ions. The column densities of Si IV and C IV at fixed  $\Delta v$  drop rapidly from 10 kpc to 100 kpc, and at 1 Mpc they are not even visible in this plot. In contrast, the high ionisation potential ions, O VI and Ne VIII, show essentially no decrease in absorption at fixed  $\Delta v$  when the impact parameter increases from 10 kpc to 100 kpc, and the drop from 100 kpc to 1 Mpc is more modest than for low ionisation absorbers. The decrease in column density is also more dramatic with increasing  $\Delta v$  for the low ionisation potential ions. This occurs because high ionisation potential lines arise in more extended gas distributions at lower overdensities, which trace the general large-scale structure in which galaxies live, while the low ionisation potential ions are more confined to the high-density gas found closer to galaxies (as seen in Figure 2.2).

In this plot, H I behaves much like a high ionisation potential line – note the similarity in the shapes of the curves between H I and O VI, although there is a large difference in the magnitude of the column densities. This reflects the fact that H I can arise in a wide range of physical conditions, and even at small impact parameters there is a substantial contribution to the column density from gas along the LOS out to large  $\Delta v$ 's (Kollmeier et al., 2003; Kollmeier et al., 2006). At 1 Mpc, H I absorption does not depend much on the central halo mass. H I is observed almost everywhere that metal ions are seen, and in almost every case has a column density greater than any metal ion.

Finally, we examine the trends with halo mass. Nominally, the larger peculiar

velocities within larger halos should result in greater  $\Delta v$ 's; each factor of 10 in halo mass should correspond to a factor of  $10^{1/3} \approx 2.2$  in  $\Delta v$ . In practise, one would expect  $\Delta v$  differences that are somewhat lower than this because one integrates the column density through the entire halo. Low ionisation potential ions like Mg II are close to this expectation, with the differences between the curves being roughly a factor of 1.7 in  $\Delta v$ . This indicates that Mg II basically arises only when the LOS intercepts a galaxy, and at large  $\Delta v$  the satellite galaxies giving rise to the absorption are tracing the underlying halo potential. The mid ionisation potential ions Si IV and C IV are similar to Mg II, indicating that the denser gas giving rise to these ions also traces the underlying potential. Moving towards higher ionisation potential lines, we see somewhat smaller differences as a function of halo mass, as absorption in these ions starts to pick up gas that is outside the virial radius and hence not dominated by the halo potential. It is important to note once again that all the massive galaxies in the vzw simulation have star formation rates well above comparable-mass galaxies in the real Universe, owing to a lack of a quenching mechanism in our simulations (e.g. Gabor & Davé, 2012). Therefore, the absorption trends at higher mass may not be reflective of the real Universe, where the observed O VI declines in strength in more massive halos (Tumlinson et al., 2011). Nonetheless, to first order for all ions, close to galaxies it is the dynamics of the host halo that establishes the  $\Delta v$  distribution of the absorption.

In summary, all ions have the vast majority of their absorption arising within a redshift-space distance of (conservatively)  $\Delta v \pm 300 \text{ km s}^{-1}$  around galaxies for all but the most massive halos. Low ionisation species show a sharp drop with  $\Delta v$ , while high ionisation species show a more gradual drop. More massive halos show a broader absorption distribution in  $\Delta v$  reflecting their larger potential

wells. For low ionisation lines, absorption drops very rapidly with impact parameter, while for high ionisation lines, the drop with impact parameter is much slower. These trends broadly reflect the overall morphology of absorption relative to galaxies, in the sense that lower ionisation lines are more confined to dense gas closer to galaxies.

## 2.5 Absorption around galaxies versus impact parameter

We now turn to examining the extent of absorption around galaxies in physical space, as quantified by the impact parameter  $b$ . From the previous section, we know that much of the absorption occurs within approximately  $\pm 300$  km/s of a galaxy (the mild exception being for low ionisation potential lines in massive halos). Hence, we will examine how absorption within this  $\Delta v$  range varies with impact parameter, as a function of both ionisation level and halo mass.

In Figure 3.7 we plot the summed column density per unit redshift along all lines of sight with a given impact parameter, with the impact parameters ranging from 10 – 1000 kpc. We show results from our vzw simulation for galaxies in halos with masses of  $10^{11} M_{\odot}$  (dotted lines),  $10^{12} M_{\odot}$  (solid), and  $10^{13} M_{\odot}$  (dashed). We show error bars owing to cosmic variance (since statistical errors are small). To calculate those, we divide our simulation volume into sixteen sections of equal volume and compute the  $dN/dz$  values for lines of sight within each section, and compute the dispersion over the sixteen sections. We ignore the (rare) sections that have no absorption when calculating the dispersion.

Here, we have chosen to plot a summed column density, instead of a median one. This is because we are interested in predicting the total absorption along the line of sight as one moves out in impact parameter. The median value can be highly dependent on the resolution and noise level of the spectra, since better



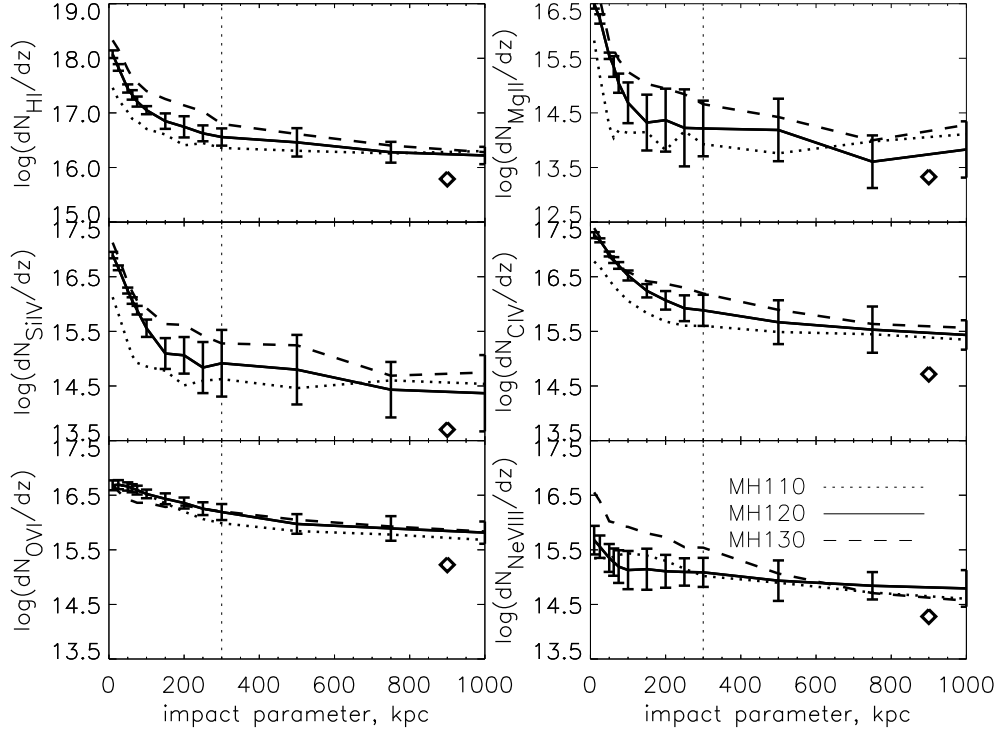


Figure 2.9: The total column density (not number density) per unit redshift versus impact parameter around galaxies in halos of  $10^{11} M_{\odot}$  (dotted),  $10^{12} M_{\odot}$  (solid) and  $10^{13} M_{\odot}$  (dashed). For halos,  $dN/dz$  is the summed column density for the given ion along all lines of sight at the given impact parameter over the velocity range  $\pm 300 \text{ km s}^{-1}$ , divided by  $\Delta z = (\text{Number of halos in sample}) \times (600 \text{ km s}^{-1}) / (1 + z)$ . The black symbols indicate  $dN/dz$  for random lines of sight. Note that the vertical range for each ion varies, although it always spans 4 dex. The vertical dotted line corresponds to 300 kpc. Error bars show the cosmic variance across sixteen simulation sections of equal volume.

quality spectra will result in many more weak lines. In contrast, the summed absorption is a more robust quantity. However, it does have the disadvantage that it can be biased by a single, very large absorber. To mitigate this, we apply here the same column density caps as described in §3.2. Lines above  $10^{16} \text{ cm}^{-2}$  for H I and  $10^{15} \text{ cm}^{-2}$  for metal lines are reset to  $10^{16} \text{ cm}^{-2}$  and  $10^{15} \text{ cm}^{-2}$ , respectively. While this particular statistic has yet to be determined observationally as a function of impact parameter, this could certainly be done, and would provide a robust quantitative estimate of the total amount of absorption as one moves away from galaxies.

The trends seen here in physical space are qualitatively similar to those seen in redshift space in the previous section. All the ions show enhanced absorption near galaxies; even at 1 Mpc the  $dN_{ion}/dz$  for targeted LOS is noticeably higher than that for random LOS, shown as the diamond at 1 Mpc in each plot. For low and mid ionisation potential ions, the decline is very steep with increasing radius, and beyond a few hundred kpc,  $dN_{ion}/dz$  is almost independent of impact parameter. For Mg II, the  $dN/dz$  value has dropped by two orders of magnitude by 100 kpc. For mid ions, the sharp drops in  $dN/dz$  happen at slightly further impact parameters, roughly 200-300 kpc. For high ionisation potential ions, the decline is not as steep with impact parameter, but there is still a clear enhancement within roughly 300 kpc; about a factor of two for O VI and about a factor of four for Ne VIII.

There are also trends with halo mass, although they are not strong as in Figure 2.8. The general trend is that there is somewhat more absorption at higher halo masses, at most impact parameters. To first order, this reflects the increased gas density both in and around larger halos. There are some interesting exceptions; for instance, O VI shows less absorption within 200 kpc for galaxies

in massive halos. This may reflect temperatures deep within group-sized halos that exceed the collisional ionisation temperature of O VI (Davé, Oppenheimer, & Sivanandam, 2008) combined with densities that exceed the photo-ionisational densities of O VI (Oppenheimer & Davé, 2009). When one reaches 1 Mpc impact parameters, the  $dN_{ion}/dz$  values for H I and the high ionisation potential ions for the various halo masses all have essentially converged.

We have argued above somewhat indirectly that most metal absorption arises from gas within roughly 300 kpc of galaxies (depending on the ion), but in simulations we can test this hypothesis directly. To do so, we tag gas particles in our simulations that lie within a chosen radius  $r$  from any resolved SKID-identified galaxy ( $M_* \geq 10^{9.1} M_\odot$ ), and then regenerate our LOS with contributions only from those tagged particles. We exclude galaxies below this mass limit as they are not well resolved in our simulations (Finlator et al., 2006). Figure 2.10 shows the resulting summed  $dN_{ion}/dz$  values as a function of impact parameter, analogous to Figure 3.7, with the different lines showing the contribution from particles within  $r < 30$  kpc (blue dotted),  $r < 100$  kpc (green dashed), and  $r < 300$  kpc (red dot-dashed) from galaxies. We show here results for the  $10^{12} M_\odot$  halo mass bin, but the results are not significantly different for other halo masses. For comparison, the solid black line includes absorption from all gas, reproduced from Figure 3.7.

Explaining further, in this Figure we use the same galaxies as in Figure 3.7, with the same LOS at the same impact parameters. But we no longer consider absorption from every SPH particle that intersects the targeted LOS. We now consider absorption from the SPH particles along the line of sight *only* if they are within a given physical radius from *any* galaxy in our simulation volume, *not just the targeted one*. The reader will note that, for example, the red 300 kpc

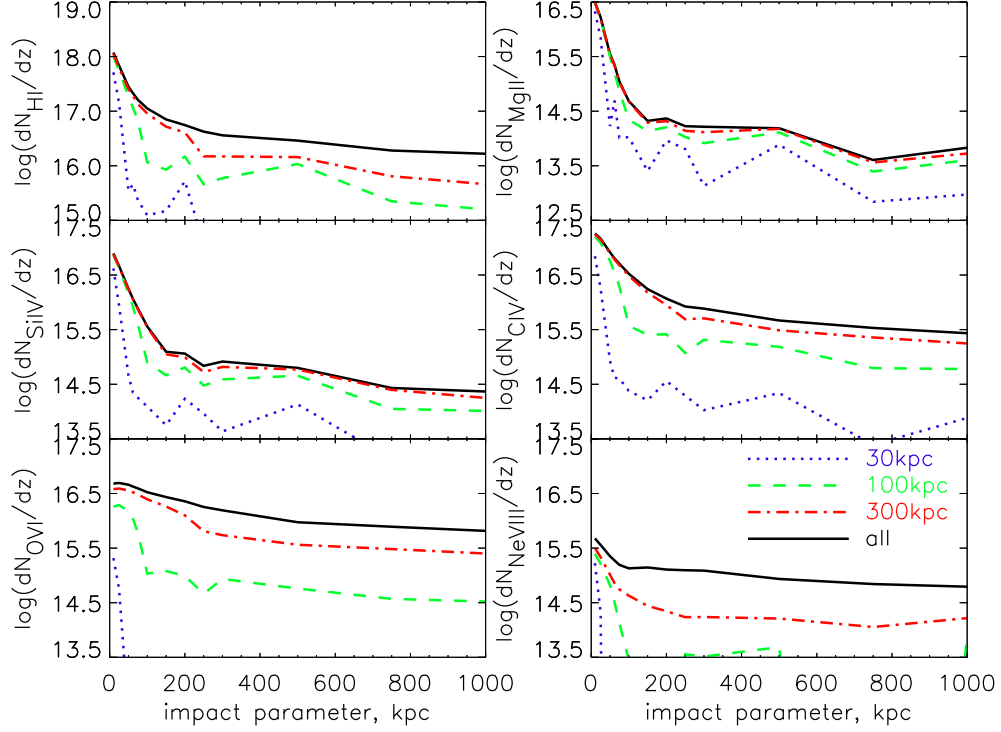


Figure 2.10: Total column density per unit redshift ( $dN/dz$ ) for targeted LOS around  $10^{12}M_{\odot}$  halos, for all gas particles (black solid line, identical to Figure 3.7), and for gas within the specified radius of a galaxy (coloured lines). Black line is labeled "all", indicating that we consider absorption from all SPH particles (i.e. the full simulation) intersecting the targeted LOS. Coloured lines indicate  $dN/dz$  where we only include absorption from SPH particles that are within a sphere of the indicated physical radius from *any* galaxy in our simulation (not just the targeted one). Dotted purple shows  $dN/dz$  for gas within 30 kpc (physical) of a galaxy, Dashed green line is for 100 kpc, and dash-dot red is for 300 kpc.

Table 2.2: For each ion, we give the percentage of absorption from particles within 300 kpc of any galaxy in our simulations, at each impact parameter listed. Values in this table are derived from the difference between the red dash-dotted and black solid lines in Figure 2.10 at impact parameters of 10, 100, and 300 kpc.

	10 kpc	100 kpc	300 kpc
H I	94%	81%	41%
Mg II	97%	97%	80%
Si IV	96%	97%	80%
C IV	96%	92%	66%
O VI	79%	74%	35%
Ne VIII	67%	32%	14%

line extends past 300 kpc. This is due to clustering. A targeted line of sight can find absorbers at, for example, 750 kpc because those absorbers are from particles within 300 kpc of another galaxy, as opposed to the targeted one.

For the low and mid metal ions, particles within 300 kpc are responsible for the great majority of the absorption at all impact parameters, as given in Table 2.2. For low ionisation species, particles within even smaller radii are responsible for the majority of absorption. For Mg II, most of the absorption owes to particles within only 100 kpc, and typically around half of the Mg II absorption owes to gas within only 30 kpc of galaxies. For mid ions Si IV and C IV, essentially all the absorption comes from within 300 kpc of galaxies, with the majority of it from within 100 kpc, and only a small fraction within 30 kpc. For O VI and Ne VIII, how much absorption comes from particles within 300 kpc depends upon impact parameter, as shown in Table 2.2. For these high ions, very little of the absorption comes from particles within 100 kpc, and in fact a substantial fraction can

come from particles further than 300 kpc from galaxies. The contributions to the 100 kpc curves at  $b > 100$  kpc, for example, must come from gas associated with other galaxies, either satellite systems or galaxies projected along the LOS with  $|\Delta v| < 300 \text{ km s}^{-1}$ .

In summary, the extent of metal ions around galaxies – that is, the range containing the vast majority of metal absorption – is roughly  $300 \text{ km s}^{-1}$  in velocity space (although in some cases much less than that), and roughly 300 kpc in physical separation (except for O VI and Ne VIII at large impact parameter). Low ionisation potential metal ions are more confined around galaxies in both velocity and physical space. This is consistent with the visual impression of the column density images in Figure 2.2. We reiterate that metal ions are more likely to be found within 300 kpc or  $300 \text{ km s}^{-1}$  of *some* galaxy, not necessarily the target galaxy. In particular, the excess of low ions at large radii in Figures 3.7 and 2.10 arises from satellites and neighboring galaxies.

## 2.6 Column Density Distributions

The column density distribution (CDD), i.e. the number of absorption systems per unit column density per unit redshift, represents the most basic counting statistic for characterising absorption line systems. Examining the CDDs as a function of impact parameter tells us how absorption drops off with distance as a function of column density, and thereby gives us a more detailed view of how absorption varies around galaxies compared to the aggregate statistics presented in the previous sections.

Figure 3.8 shows CDDs plotted as  $N^2 \times f(N)$  where  $f(N) \equiv d^2n/dNdz$  for all our ions, where  $N$  is the column density,  $n$  is the number of lines, and  $dz$  is the redshift-space path length, corresponding to  $\pm 300 \text{ km s}^{-1}$ . We plot this at

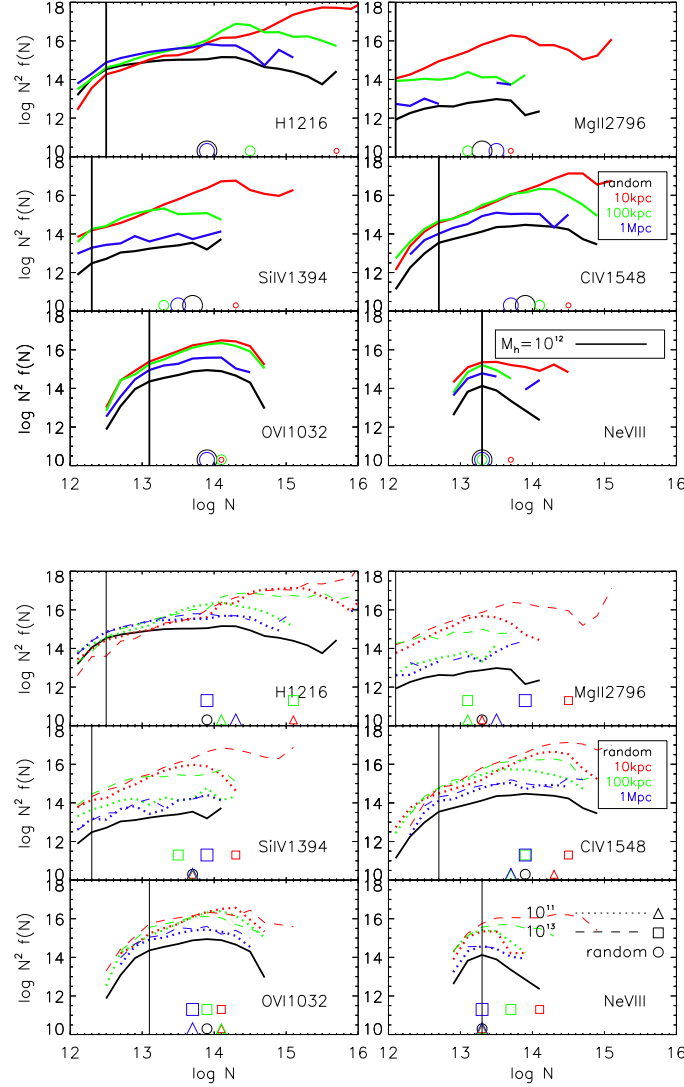


Figure 2.11: Top panel: Column density distributions (CDDs) for galaxies with  $M_{\text{halo}} = 10^{12} M_{\odot}$ .  $f(N) \equiv d^2n/dNdz$ . We multiply  $f(N)$  by  $N^2$  to show from where most of the absorption per unit log column density arises. The black line is the column density distribution for random LOS, red, green, and blue are for targeted LOS at 10 kpc, 100 kpc, and 1 Mpc, respectively. Circles (which increase in size with increasing  $b$ ) mark the peak of the distribution, i.e., where 50% of the column density is below that value and 50% above it. Bottom: Same as the top panel for galaxies in halos of  $10^{11} M_{\odot}$  (dotted line) and  $10^{13} M_{\odot}$  (dashed line). Triangles and squares mark the peak of the distribution for  $10^{11} M_{\odot}$  and  $10^{13} M_{\odot}$  respectively, also increasing in size with increasing  $b$ , while circles mark peak for random distribution, as in top panel. Vertical lines show the completeness limit of the CDDs for  $S/N=30$  per  $6 \text{ km s}^{-1}$  pixel.

three impact parameters of 10 kpc (red), 100 kpc (green), and 1 Mpc (blue), and for comparison we also plot the CDD for random LOS (black; similar to those in Oppenheimer et al., 2012). As before, we combine ions with separations  $\Delta v < 100 \text{ km s}^{-1}$  into systems before measuring the CDD, and apply column density caps (see §3.2). In the top panel, we add colored circles indicating the center of the distribution, i.e., where 50% of the total column density is below that value and 50% above it. In the bottom panel we indicate these central values with triangles and squares for  $10^{11} M_{\odot}$  and  $10^{13} M_{\odot}$ , respectively. The top panels show the results for galaxies in halos of  $\approx 10^{12} M_{\odot}$ . The bottom panels show analogous CDDs for galaxies in halos of  $\approx 10^{11} M_{\odot}$  (dotted lines) and  $\approx 10^{13} M_{\odot}$  (dashed) to assess the dependence on halo mass.

We multiply  $f(N)$  by  $N^2$  to obtain a quantity that reflects the (relative) amount of absorption per unit redshift at each column density in that ion: the value of  $N^2 \times f(N)$  at  $N = 10^{14} \text{ cm}^{-2}$ , for example, represents the total column density per unit redshift contributed by lines in a  $\Delta \ln N = 1$  interval centered at  $N = 10^{14} \text{ cm}^{-2}$ . Multiplying by  $N^2$  also enhances the visibility of trends by mitigating the typically steep power-law dependence of  $f(N)$ . In previous work (Oppenheimer et al., 2012; Davé et al., 2010), we had plotted  $N \times f(N)$  just for visibility's sake. Here we add an additional power of  $N$ , because this means that the crest of the  $N^2 \times f(N)$  curve represents the column density contributing the most absorption per logarithmic interval in that ion. These crests are typically shallow — indicating absorption that is spread over a fairly wide range of column densities — but they correspond well to the centers of the cumulative distributions marked by the circles.

We plot a vertical line that represents the 50% completeness limit for the CDD of absorbers identified in our artificial spectra with  $S/N=30$ . We determine



this limit by comparing these CDDs to those derived from artificial spectra with  $S/N=100$  (not shown) and by identifying the column density where the  $S/N=30$  CDD begins to deviate by more than 50% from the CDD derived with  $S/N=100$ . We determine this limit using random LOS since this sample contains the largest total number of lines owing to its large path length. Since we employ the same  $S/N$  in all spectra, this completeness limit should also be applicable for the targeted LOS.

The first thing that one gleans from these figures is that for the metals, even at impact parameters of 1 Mpc there is clearly more absorption near galaxies than in the random LOS. This is true for every ion and for the full range of halo masses that we explore in this paper. For low ions that arise predominantly near galaxies, this reflects the large-scale auto correlation function of galaxies, which extends to many megaparsecs. For high ionisation potential ions, the absorption arises in less dense (diffuse and WHIM) gas that still correlates with galaxies living in large-scale structures.

We also see that the cosmic absorption in every metal ion peaks in the range of  $N \approx 10^{13} - 10^{14.5} \text{ cm}^{-2}$ . These peaks are generally above the completeness limit for all the ions except Ne VIII, where the lines are intrinsically weak. For the lower ionisation potential ions (Mg II, Si IV, C IV), this peak moves to larger columns as one goes to smaller impact parameters, while for the high ionisation potential ions the peak remains mostly independent of the impact parameter. In addition, for high ionisation potential ions (and for Mg II) one must probe to fairly low column densities to capture the bulk of the cosmic absorption, e.g.,  $N_{\text{OVI}} \sim 10^{14} \text{ cm}^{-2}$  and  $N_{\text{NeVIII}} \lesssim 10^{13.5} \text{ cm}^{-2}$ . Hence, while many O VI and Ne VIII absorption systems are now being detected in COS data (Tumlinson et al., 2011; Tripp et al., 2011), our models predict that higher  $S/N$  observations that probe

to  $N \sim 10^{13.5} \text{ cm}^{-2}$  are needed to capture the bulk of cosmic absorption in these ions.

Now let us examine H I, as this ion is relatively well understood in terms of its connection with galaxies and large-scale structure (e.g., Davé et al., 1999; Davé et al., 2010). H I shows a clear trend of having an increasing number of high column density absorption systems as one approaches a galaxy, i.e. as one goes to small impact parameters. In contrast, as one goes to smaller impact parameters the number of lower column density absorption systems does not change as significantly. In fact, below  $N \sim 10^{14} \text{ cm}^{-2}$  the trend actually reverses with the number of systems increasing as one goes to larger impact parameters. This can be easily understood. The strong absorbers mostly arise in the dense gas around galaxies, while the weak absorbers arise more in the surrounding large-scale structure, even when the impact parameter is small. This is consistent with the strong correlation between H I column density and overdensity predicted in the models (e.g., Davé et al., 2001; Schaye, 2001; Davé et al., 2010; Hui et al., 1997).

For the metal lines, the variation in the shape of the CDD with impact parameter shows interesting trends as a function of ionisation level. As one moves from impact parameters of 100 kpc to 10 kpc, for lower column density absorbers there is little change in the incidence of absorption. However, as one moves to higher column densities, the number of absorbers increases and the peak moves to higher column densities. The column density where the increase to small impact parameter becomes noticeable increases with ionisation level. For instance, for Mg II the 10 kpc and 100 kpc curves differ at  $N_{\text{MgII}} \gtrsim 10^{12} \text{ cm}^{-2}$ , while for C IV they differ at  $N_{\text{CIV}} \gtrsim 10^{14} \text{ cm}^{-2}$ . For O VI and Ne VIII, there are only minimal differences in the CDDs at impact parameters of 10 kpc and 100 kpc. At impact parameters of 1 Mpc the number of absorbers is smaller at all columns for all the

metal ions, with the peak also generally occurring at lower column densities. The random LOS continue this trend. In short, the lower the ionisation potential, the more sensitive the ion's CDD is to the proximity of a galaxy.

It is conventional to fit the CDD with a power law in column density for a given ion:  $f(N) \propto N^{-\beta}$ . For random lines of sight, the observed power-law slopes for H I, O VI, and C IV are generally between  $1.5 \lesssim \beta \lesssim 2.2$  (Danforth et al., 2006; Cooksey et al., 2010). Davé et al. (2010), using similar simulations, found a slope for the H I CDD of  $\beta = 1.70$ , which is (unsurprisingly) similar to what we find here. The slope for O VI depends on the range of column densities over which the fit is done, since a pure power law is not a good descriptor. Using the full range above our completeness limit, we obtain  $\beta \approx 2.3$ , which is comparable to Danforth et al. (2006) who found  $\beta = 2.2 \pm 0.1$ . C IV likewise is not a perfect power law, but we find a slope of  $\beta \approx 1.9$ , which is steeper than observations by Cooksey et al. (2010) that yield  $\beta = 1.5^{+0.17}_{-0.19}$ , but probably within uncertainties given that incompleteness in the data which has poorer quality than our simulated spectra will generically lead to shallower slopes. Given the variations in spectral quality between all these data sets, we consider our simulations to be broadly in agreement with current measures of CDD slopes for these ions. Observations have yet to constrain the slope as a function of impact parameter, but our models predict that the slope does not vary dramatically, and mainly only the amplitude increases substantially to small impact parameter. This prediction will be testable with upcoming observations that have sufficient statistics to examine  $f(N)$  as a function of impact parameter.

Looking at the bottom panels of Figure 3.8, absorption around galaxies in halos of larger and smaller masses continues these same general trends. At impact parameters of 10 kpc, as one goes from halo with masses of  $10^{11} M_{\odot}$  to  $10^{13} M_{\odot}$  one

sees similar trends as when one went from impact parameters of 100 kpc to 10 kpc in halos of fixed mass; there is agreement of the CDDs at small column densities and more absorption at high column densities, and the transition occurs at a column density that increases as the ionisation potential of the ion increases. Hence in this regard, going to higher halo masses is equivalent to going to smaller impact parameters in a halo of fixed mass. The CDDs are relatively insensitive to the mass of the galaxy halo for impact parameters of 1 Mpc.

Ne VIII exhibits an interesting trend at high halo masses, arising from its strong collisional ionisation contribution when a hot gaseous atmosphere is present. We see in Figure 2.5 that Ne VIII has a low-density, photo-ionised component probing the diffuse IGM, which gives it the more extended characteristics of a high ionisation potential ion like O VI that is itself mostly photo-ionised. However, Ne VIII also traces  $10^{5.5-6.0}$  K hot halo gas, which is both denser and at lower impact parameters, where cooler ions like Si IV and C IV are also found. Therefore for large halos and impact parameters inside of 100 kpc, there is a substantial population of (collisionally ionised) Ne VIII absorbers. Note that this Ne VIII could be coincident with lower ionisation potential ions, as has been observed by Tripp et al. (2011), but arises in a different gas component.

In summary, the CDD of H I and metal ions shows trends with impact parameter that reflect correlations of absorption with both nearby galaxies and large-scale structure. All ions show increased absorption closer to galaxies. Low ionisation potential ions are more influenced by the presence of nearby galaxies. These CDDs represent a prediction of hierarchical models that enrich the IGM using outflows from star-forming galaxies and can in principle be tested and constrained by observations (e.g., Tumlinson et al., 2011). The full COS-Halos data set is being analyzed now (Werk et al., 2012), and in future work we will under-

take a detailed comparison to CDD and other observed statistics, including an artificial spectra sample that more closely mimics the COS-Halos spectra.

## 2.7 Variations with outflow model

One expects the enrichment of the surrounding CGM gas to depend sensitively on the properties of the enriching outflows. So far we have only considered our favoured outflow model with momentum-driven wind scalings. Here we consider how the absorption properties around galaxies depend on our assumed outflow model, using two other wind prescriptions: a simulation with no winds (nw) and a constant wind (cw) model where we assume a constant mass loading factor of  $\eta = 2$  and a constant wind speed from all galaxies of  $v_w = 680 \text{ km s}^{-1}$ . The latter is similar to that used in the Overwhelmingly Large Simulations (OWLS) reference model of Schaye et al. (2010). The cw version used in this paper is identical to that described in Davé et al. (2010), except that it was re-run using Wiersma et al. (2009a) metal-line cooling rates, for consistency with the vzw model used here.

To begin, Figure 2.2 shows a pictorial representation of how the physical conditions and absorption vary with wind model. In Figure 2.12, for easier comparison, we collapse the density and temperature information given in Figure 2.2 down into one dimension by taking the azimuthal average of those images. In Figure 2.12, we show a larger region than in Figure 2.2 to illustrate larger-scale trends, and include metallicity to more fully understand the cooling processes.

In the top panel of Figure 2.12, vzw curiously shows more similarities to the no wind model (nw) than to the constant wind model (cw). This illustrates that the high wind speeds from all galaxies in the cw model cause significantly more spatial dispersal of mass (along with metals, as we show below) on  $\sim \text{Mpc}$  scales

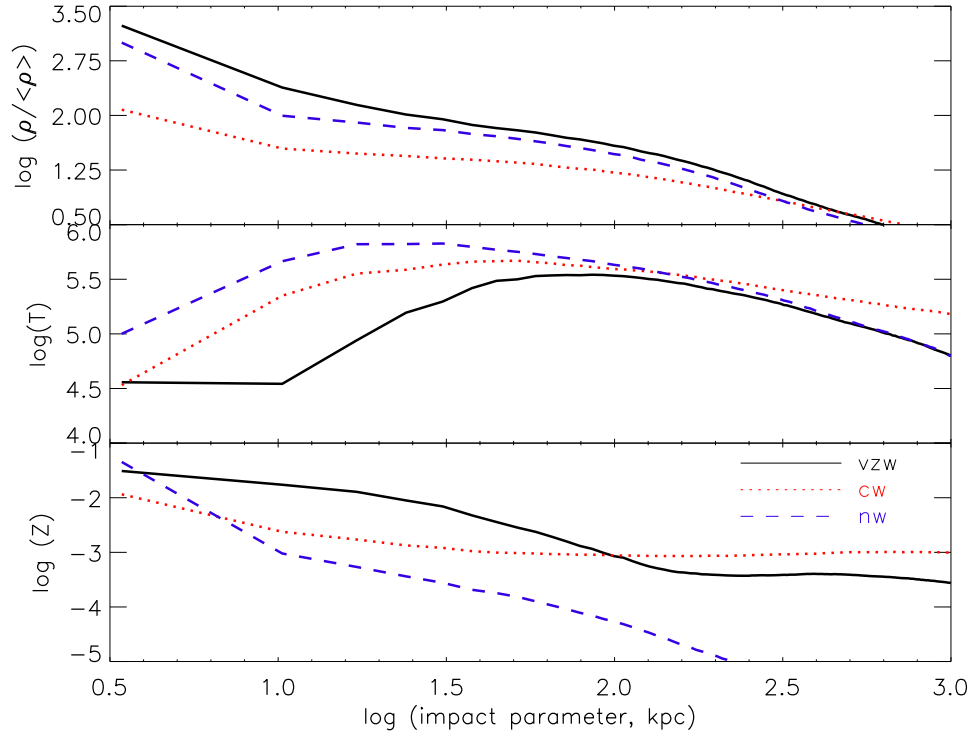


Figure 2.12: Median overdensity, temperature, and metallicity vs. impact parameter for three different wind models: momentum-driven “vzw”, constant wind “cw”, and no wind “nw”. Solid lines are all around galaxies with halo masses of  $10^{12} M_{\odot}$ . The top two rows are similar to the first two columns of Figure 2.2, but collapsing the image down to one dimension.

around galaxies. The vzw model has lower velocity winds that do not have such a dramatic impact on large scales, but do have a strong impact on smaller (CGM) scales. The vzw model pushes more mass via winds into the CGM relative to the no wind model, but this mass is close enough that it recycles back onto the galaxy in much less than a Hubble time (Oppenheimer et al., 2010). We note that the galaxy population is broadly more similar in the two wind models, as they both suppress global star formation substantially relative to the no-wind case (for a fuller discussion of these properties, see Oppenheimer et al., 2010; Davé et al., 2011a,b), but Figure 2.12 shows that they are quite different in where they deposit the ejected material.

The middle and lower panels of Figure 2.12 illustrate how winds affect the CGM. Here vzw and cw actually trend in the opposite direction relative to the no-wind case! In the vzw case, the area around the galaxy is slightly colder than with no winds. This is because the lower wind speeds deposit more metals around galaxies (lower panel), and this results in an increased amount of metal cooling (Oppenheimer et al., 2012) that more than offsets the shock heating from the winds. In contrast, the cw model expels gas at high velocities, around the escape velocity for  $10^{12} M_{\odot}$  halos, even from small galaxies. This means the enrichment is more widespread – past 100 kpc, cw shows greater metallicity than the vzw or nw model. Moreover, the wind energy is deposited into less dense gas where it does not have a chance to radiate away its energy.

The HI maps shown in Figure 2.2 illustrate that winds do not make a large difference to HI absorption, at least on the large scales depicted here, similar to results at high redshift (e.g., Kollmeier et al., 2003; Kollmeier et al., 2006). However, there is an increase in HI on small scales, roughly 100 kpc. The metal absorption, in contrast, shows more dramatic differences between the wind models.

In the no-wind case, all the metals are essentially confined to be in and around galaxies, showing that even the distribution of metals within the CGM requires winds. These differences should be manifest in the statistics of absorbers around galaxies, providing an opportunity to constrain wind models.

To further quantify the extent of the metal distribution, Figure 2.13 shows the fraction of all cosmic metal mass that lies within a given radius from galaxies with  $M_* \geq 10^{9.1} M_\odot$  in the simulation volume. We also plot the fraction of all cosmic mass for all species, in addition to just metals. The procedure for this was discussed in §2.5. Here the impact of winds on distributing cosmic metals is shown clearly: the no wind model keeps essentially all metals confined very close to galaxies, while the constant wind model disperses them over large scales, with the momentum-driven wind model intermediate between the two. This figure also shows that the constant wind model also pushes the total mass further out, while the momentum-driven wind and no wind models are more similar. For our favoured momentum-driven wind scaling model, 83% of the metal mass is in gas within 300 kpc from galaxies. For the cw model, only 40% is within this radius. Hence the basic extent of metals around galaxies can already provide a discriminant between wind models.

We now aim to quantify these differences in metal distribution using absorption line statistics. Figure 2.14 is similar to Figure 3.7, except that it compares the three wind models, using the same column density caps as explained in §3.2. Here, we also include a comparison to our old vzw simulation that used collisionally ionised equilibrium (CIE) metal line cooling, labeled as vzw-cie, as opposed to our current vzw model that uses the Wiersma et al. (2009a) (PIE) cooling. For the most part, the differences between the vzw-cie model and our current vzw model are small compared to the differences between wind models, and hence



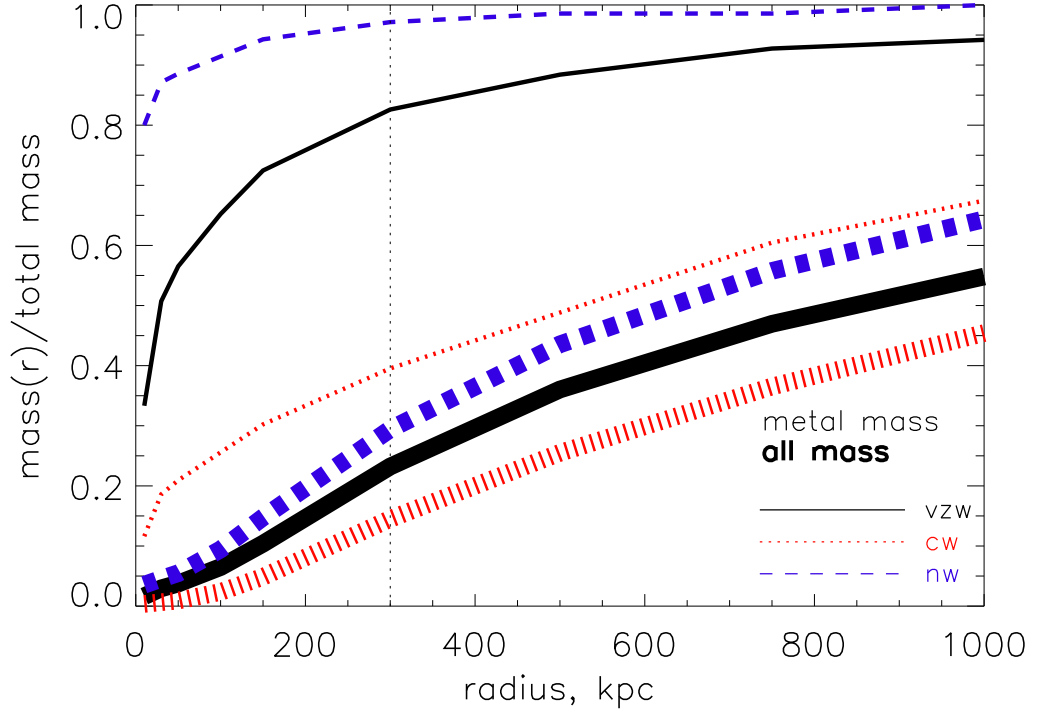


Figure 2.13: Thin lines: Metal mass fraction of all gas particles within spheres of radius  $r$  around all galaxies  $M_* \geq 10^{9.1} M_\odot$  in our simulation at  $z=0.25$ , relative to the total metal mass of gas particles in the whole simulation volume, for momentum-driven winds (solid line), no winds (dashed line), and constant winds (dotted line). The vertical dotted line delineates 300 kpc. Thick lines: Total mass fraction for all species, not just metals.

this aspect of our modeling does not introduce a large uncertainty into the results. The differences between *vzw* and *vzw-cie* are small because the winds have moderate velocities, preventing large amounts of gas to reach lower overdensities. Instead, they remain in moderate-density gas where cooling times are short regardless of photo-ionisation suppression. Note that when we generate spectra, we compute ionic abundances including photoionisation in both cases; it is only during the evolution of the simulation that *vzw-cie* is different.

In this figure, as in Figure 3.7, we also show  $dN_{ion}/dz$  for random LOS for each wind model as the diamonds near the right edge. For all models and ions,  $dN_{ion}/dz$  values at 1 Mpc are still higher than  $dN_{ion}/dz$  for random LOS. Note that for all the metal ions, there is so little absorption in the no wind model that the random LOS  $dN_{ion}/dz$  (purple diamonds) falls off the bottom of this plot. Similarly, the *cw* model shows so little Si IV and Mg II absorption in random LOS that the red diamonds fall off the bottom of the plot.

For all the metal ions, the no wind model gives significantly less absorption than any of the wind models, even down to the smallest impact parameters probed here. However, there is not a large difference between models with winds and the model without winds for H I. Without outflows, metals basically exist outside the ISM only owing to tidal or ram pressure stripping processes that remove material from the ISM of the central or satellite galaxies. It is evident from this plot (as with the images in Figure 2.12) that such stripping processes provide only a small contribution to the CGM metal absorption in these halos, though it can be more substantial in large halos (e.g., Davé, Oppenheimer, & Sivanandam, 2008; Zu et al., 2011). Hence, we predict metals seen at any impact parameter beyond that of the ISM of typical galaxies arise almost exclusively owing to outflows.

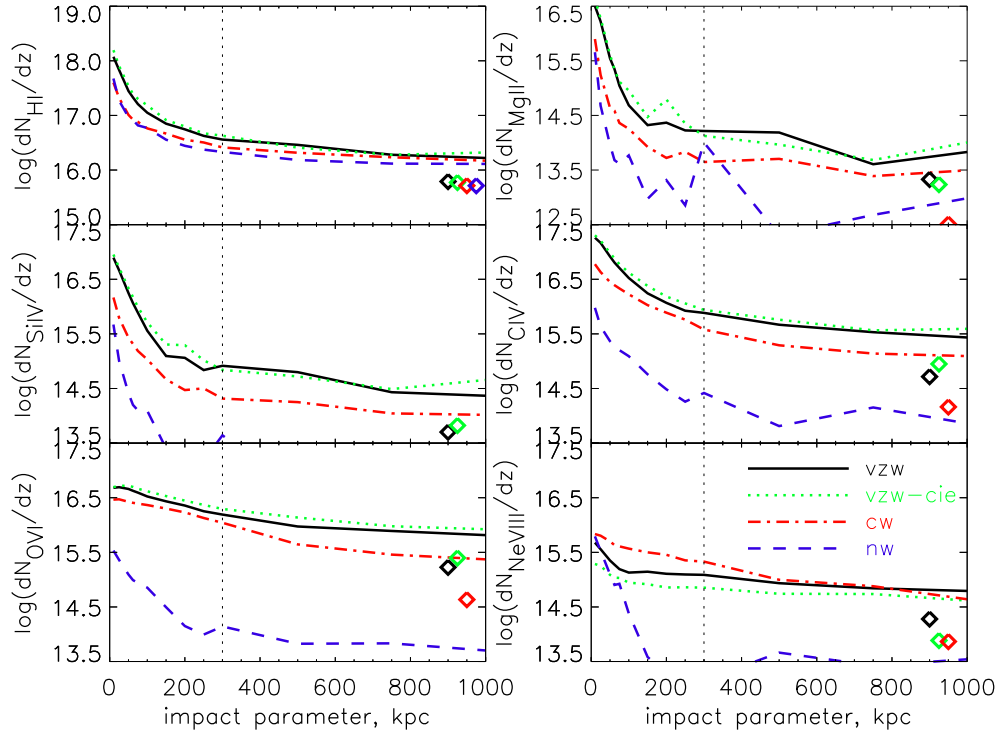


Figure 2.14: The total column density per unit redshift for the vzw, vzw-cie, cw, and nw models, all for galaxies in  $10^{12}M_{\odot}$  halos. The diamonds indicate the  $dN_{ion}/dz$  value for random lines of sight for each wind model. The symbols are shifted slightly to the left of 1 Mpc, and separated for easier viewing. In some cases the symbols are lower than the scale of the plot so do not appear.

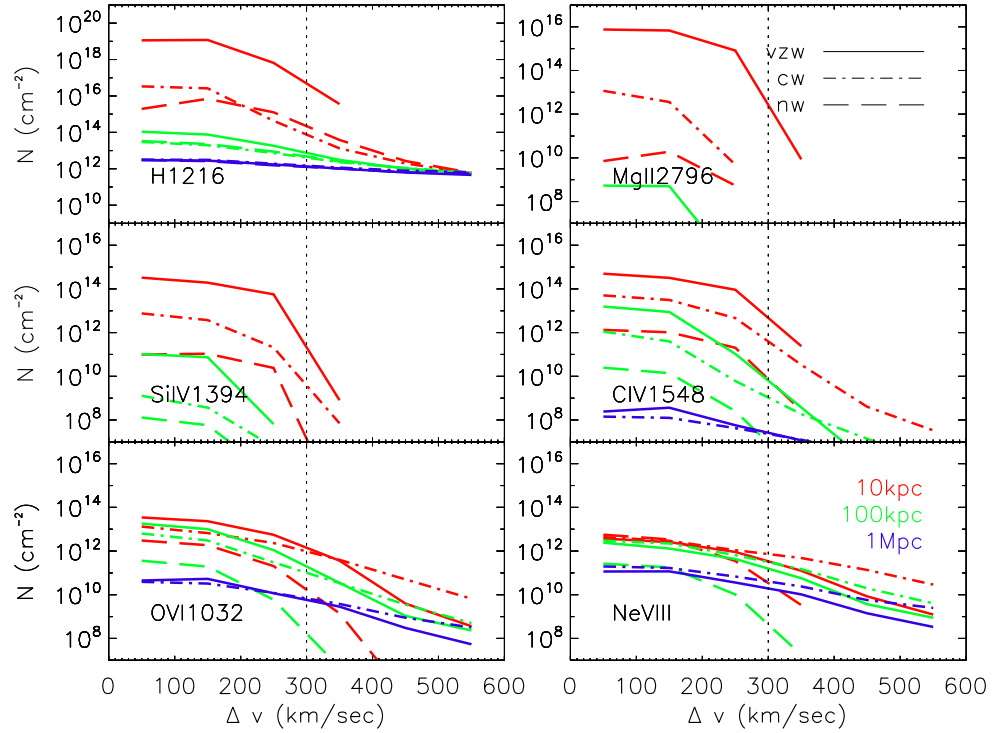


Figure 2.15: The median column density ( $N$ ) vs. velocity separation from the central galaxy ( $\Delta v$ ) for galaxies in  $10^{12} M_{\odot}$  halos for the vzw, cw, and nw models. We show results at three impact parameters: 10 kpc (red), 100 kpc (green), and 1 Mpc (blue). The vertical dotted marks  $300 \text{ km s}^{-1}$ .

The differences between the constant wind and momentum-driven wind cases are more subtle. The global trends with ionisation state are as before: lower ionisation potential species are more highly peaked at small impact parameters in both wind models. The main significant difference is an overall offset. In general, the cw model has lower absorption for low ionisation potential species, and higher absorption for high ionisation potential species relative to the vzw (or vzw-cie) model. The lower absorption arises in part because the cw model produces less metals overall owing to its reduced cosmic star formation (Oppenheimer et al., 2012). Going to higher ionisation species, absorption in the cw model becomes only slightly less than absorption in the vzw model. For Ne VIII, cw shows more absorption than vzw. This reflects the impression from Figure 2.12 that the cw model expels metals to greater distances and heats this diffuse gas more (Oppenheimer et al., 2012). Hence, the global absorption strength as a function of ionisation state provides another potential discriminant between outflow models.

In Figure 2.15, we plot the median column density versus velocity, analogous to Figure 2.8 except now we vary the wind model as opposed to the halo mass. Not surprisingly, for H I all the wind models give similar results; however vzw does show an increase over nw and cw at 100 kpc, because these winds push more cool gas to CGM distances. For the metal lines, once again the no-wind case shows virtually no absorption except perhaps very (dynamically) close to galaxies ( $\pm 100 \text{ km s}^{-1}$ ). Hence, tidal effects and other stripping processes are ineffective in distributing metals in velocity space, just as in physical space.

In this figure, we see similar trends with wind model as we did in Figure 2.14. For low ionisation potential metal species, the vzw model produces higher column densities, while the opposite is true for high ionisation potential species.

Previous work (Oppenheimer et al., 2012) has shown that the cw and vzw models enrich the dense gas in quite different ways. The cw model, with its high velocities emanating even from small galaxies, deposits fewer metals into the high density regions very close to galaxies and more metals into the diffuse IGM. Accordingly, metal ions that show more absorption in the cw model than in the vzw model have more absorption from more diffuse IGM gas.

In summary, the rate of the decrease in absorption of metal lines as one moves away from the central galaxy provides a potentially strong discriminant between outflow models that enrich the diffuse IGM to fairly similar levels. Winds are required to enrich the CGM of normal galaxies to any significant level. Our currently favoured momentum-driven wind scaling model predicts more low ionisation potential absorption close to galaxies than the constant wind model and less high ionisation potential absorption farther from galaxies. Quantitative comparisons with present and upcoming COS data should yield more stringent constraints on outflow propagation.

## 2.8 Conclusions

We have examined the absorption line properties of H I and five key metal ions in the vicinity of galaxies at  $z = 0.25$  in cosmological hydrodynamic simulations that include galactic outflows, as a function of velocity separation, impact parameter between the galaxy and the line of sight, and halo mass. Our chosen metal ions span a range of ionisation potentials, from low (Mg II) to mid (Si IV & C IV) to high (O VI & Ne VIII). This is the first absorption line study of metal absorption around galaxies in cosmological hydrodynamic simulations with a self-consistently generated outflow model that matches a wide range of galaxy and IGM observables. Our work is motivated by the upcoming wealth of data

from *Hubble's* Cosmic Origins Spectrograph, and hence our artificial spectra are generated with resolutions and noise characteristics comparable to the best data that will be obtained with COS.

Our primary conclusions are:

1. Absorption in all ions is enhanced closer to galaxies. This is true in terms of both impact parameter and velocity separation. A velocity separation of  $\pm 300 \text{ km s}^{-1}$  around galaxies encompasses most of the cosmic metal line absorption (although in some cases it can be less), and absorption is also significantly stronger within 300 kpc around a galaxy, particularly for lower ionisation potential lines. These ranges are somewhat larger around bigger galaxies. In our favoured momentum-driven wind simulation,  $\approx 80\%$  of all cosmic metals lie within 300 kpc of a galaxy.
2. The dependence of metal absorption strength on distance from a galaxy in either physical or redshift space depends monotonically on the ionisation potential of the absorbing ion. Ions with a low ionisation potential (Mg II, Si IV) arise in higher density gas that tends to drop off more quickly with impact parameter and velocity separation than ions with higher ionisation potentials (C IV, O VI, Ne VIII). High ionisation potential absorbers are more associated with gas at halo-like overdensities, and the overall large-scale structure that contains galaxies, while low ionisation potential lines arise more in the dense gas close to individual galaxies. Regardless of ionisation level, even out to 1 Mpc, targeted LOS show an excess of absorption over random LOS, reflective of large-scale matter clustering.
3. The majority of cosmic absorption in the ions considered here occurs in photo-ionised gas at  $T < 10^5 \text{ K}$ . The exception to this is for the high ion-

isation lines O VI and Ne VIII at impact parameters  $\lesssim 100$  kpc arising in massive halos containing substantial hot gas; these lines are predominantly collisionally ionised.

4. The dependence of the column density distributions on impact parameter also shows trends with ionisation potential. Species with lower ionisation potentials are more affected by the proximity of a galaxy. Excepting Ne VIII, our spectra (comparable to COS data quality) directly trace the majority of cosmic absorption; i.e. there is not a large population of smaller absorbers that is inaccessible to COS that would dominate the total cosmic absorption.
5. Without winds, even gas within  $\approx 100$  kpc of galaxies remains mostly un-enriched; hence outflows are required to enrich the CGM as well as the IGM. The differences in metal absorption between our favoured momentum-driven wind scaling model and a constant wind model are evident both for lower ionisation potential species close to galaxies and for high ionisation potential species farther from galaxies. The models are clearly distinguishable from each other using the combined CGM statistics of O VI and H I.

These results provide a starting point for understanding how absorption lines trace the metal enrichment around galaxies. We have highlighted some basic trends, and shown that quantifying this distribution as a function of impact parameter and velocity separation can provide interesting constraints on key physical processes such as galactic outflows, as well as the density and temperature state of the metal-enriched IGM.

While we have considered only five metal ions in this paper, the basically monotonic trends with ionisation potential suggest that the behaviour of any other ion can be predicted just based on its ionisation potential. Our simulations



predict that higher ionisation potential ions should fall off more slowly at larger impact parameters and velocity separations, because they are tracing lower density, mostly photo-ionised gas. This suggests a physical structure of CGM gas in which O VI is more extended than C IV, which is more extended than Si IV, and so on. Ne VIII and O VI, if probed at sufficiently low column densities, trace the most remote and diffuse metals of any UV resonance line, but their strongest lines arise in hot collisionally ionised gas near large galaxies.

This work is the first step in a series of works to confront successful models for galaxy-IGM coevolution with absorption line observations around galaxies in the low- $z$  universe. We examine redshift  $z = 0.25$ , but the basic trends are applicable to all redshifts probed by COS ( $z \lesssim 1$ ), as recent work by Davé et al. (2010) and Oppenheimer et al. (2012) show little evolution in the IGM from  $z = 1 \rightarrow 0$ . We caution, though, that detailed comparisons to observations are premature for the simulated spectra presented here, since quantitative trends can be sensitive to the details of spectral resolution, noise level, etc. Furthermore, our massive galaxies ( $M_{\text{halo}} = 10^{13} M_{\odot}$ ) are all star-forming in these simulations, in clear conflict with observations of mostly passive galaxies in this halo mass range, and hence the predictions for such halos may be influenced by physical effects not included in our current models. Nonetheless, we believe that the basic intuition of understanding metal absorption surrounding galaxies in terms of the ionisation potential of the tracer ion is robust, and provides a clear intuition for interpreting current and future observations. As observations progress, particularly with COS, simulations like these will provide a critical testbed for galaxy formation models, and will help elucidate the physical processes that drive the enrichment of the intergalactic and circumgalactic medium.

## 2.9 Acknowledgements

We thank Jason Tumlinson, Todd Tripp, Molly Peeples, Joop Schaye, Ben Weiner, Greg Walth, and Greg Stinson for useful discussions. Partial support for this work came from NASA ATP grant NNX10AJ95G, HST grants HST-GO-11598 and HST-GO-12248, NASA ADP grant NNX08AJ44G, and NSF grants AST-0847667, AST-0907998, and AST-133514. The simulations used here were run on the University of Arizona's SGI cluster, ICE, and on computing facilities owned by the Carnegie Observatories. Computing resources used for this work were made possible by a grant from the the Ahmanson foundation, and through grant DMS-0619881 from the National Science Foundation.

## CHAPTER 3

TRACING INFLOWS AND OUTFLOWS WITH ABSORPTION LINES IN  
CIRCUMGALACTIC GAS

This chapter was submitted to Monthly Notices of the Royal Astronomical Society in 2013. We have received a referee report on this paper and have addressed the issues in that report. We expect acceptance of this paper soon. It has also been posted to [arxiv.org/abs/1309.5951](https://arxiv.org/abs/1309.5951).

Co-authors on this chapter include **Romeel Davé** (University of the Western Cape, Bellville, Cape Town 7535, South Africa; South African Astronomical Observatories, Observatory, Cape Town 7925, South Africa; African Institute for Mathematical Sciences, Muizenberg, Cape Town 7945, South Africa; Astronomy Department, University of Arizona, Tucson, AZ 85721, USA), **Benjamin D. Oppenheimer** (Leiden Observatory, Leiden University, PO Box 9513, 2300 RA Leiden, Netherlands; CASA, Department of Astrophysical and Planetary Sciences, University of Colorado, Boulder, CO 80309, USA), **Neal Katz** (Astronomy Department, University of Massachusetts, Amherst, MA 01003, USA), **Juna A. Kollmeier** (Observatories of the Carnegie Institution of Washington, Pasadena, CA 91101, USA), **Robert Thompson** (Astronomy Department, University of Arizona, Tucson, AZ 85721, USA) and **David H. Weinberg** (Astronomy Department and CCAPP, Ohio State University, Columbus, OH 43210, USA).

## Abstract

We examine how H I and metal absorption lines within low-redshift galaxy halos trace the dynamical state of circumgalactic gas, using cosmological hydrodynamic simulations that include a well-vetted heuristic model for galactic outflows. We categorize inflowing, outflowing, and ambient gas based on its history and fate as tracked in our simulation. Following our earlier work showing that the ionisation level of absorbers was a primary factor in determining the physical conditions of absorbing gas, we show here that it is also a governing factor for its dynamical state. Low-ionisation metal absorbers (e.g. Mg II) tend to arise in gas that will fall onto galaxies within several Gyr, while high-ionisation metal absorbers (e.g. O VI) generally trace material that was deposited by outflows many Gyr ago. Inflowing gas is dominated by enriched material that was previously ejected in an outflow, hence accretion at low redshifts is typically substantially enriched. Recycling wind material is preferentially found closer to galaxies, and is more dominant in lower-mass halos since high-mass halos have more hot gas that is able to support itself against infall. Low-mass halos also tend to re-eject more of their accreted material, owing to our outflow prescription that employs higher mass loading factors for lower-mass galaxies. Typical H I absorbers trace unenriched ambient material that is not participating in the baryon cycle, but stronger H I absorbers arise in cool, enriched inflowing gas. Instantaneous radial velocity measures of absorbers are generally poor at distinguishing between inflowing and outflowing gas, except in the case of very recent outflows. These

results suggest that probing halo gas using a range of absorbers can provide detailed information about the amount and physical conditions of material that is participating in the baryon cycle.

### 3.1 Introduction

The modern view of galaxy formation relies on continual inflows of gas from the intergalactic medium (e.g. Kereš et al., 2005; Brooks et al., 2009; Dekel et al., 2009; Bouché et al., 2010; Davé et al., 2012; van de Voort et al., 2012), counteracted by strong galactic-scale outflows (e.g. Oppenheimer et al., 2010; Davé et al., 2011a), which in concert establish the growth rate of gas and stars within galaxies at all cosmic epochs. This “baryon cycle” view of galaxy formation has alleviated many of the classic problems in galaxy formation such as overcooling (e.g. White & Frenk, 1991; Balogh et al., 2001; Springel & Hernquist, 2003) and the formation of overly compact disk galaxies (e.g. Governato et al., 2007; Brook et al., 2012). The amount of ejected material in these types of models is typically comparable to or exceeds the star formation rate (e.g. Oppenheimer & Davé, 2008), and thus the inflow rate is expected to be several to many times the star formation rate.

Despite the large amounts of mass purportedly moving in and out of galaxies, direct comparison between observations and theoretical predictions remain difficult. Outflows are seen emanating from low (e.g. Martin, 2005; Rupke et al., 2005; Tremonti et al., 2007), intermediate (e.g. Weiner, 2009; Rubin et al., 2012) and high (e.g. Pettini et al., 2001; Steidel, 2001; Veilleux et al., 2005) redshift star-forming galaxies, but the amount of mass involved is difficult to estimate directly (e.g. Genzel et al., 2010; Martin et al., 2013) owing to complex ionisation conditions and the tenuous, multi-phase nature of the outflowing material. Inflows, meanwhile, are even more difficult to detect, and there are only tantalising hints from redshifted IGM absorption lines (Rubin et al., 2012), though it has been argued that Lyman-alpha blobs (Goerdt et al., 2010), Lyman limit absorption systems (e.g. Fumagalli et al., 2011; Lehner et al., 2012), low metallicity gas (Lehner et al., 2013) and high column density HI systems (van de Voort et al., 2012) may

be indirect markers of such accretion, and Faucher-Giguère & Kereš (2011) argue that cold accretion streams would have very low covering fractions. Nonetheless, simple arguments from observed galaxy properties such as the gas-phase metallicity (e.g. Erb et al., 2006) and the evolution of the gas content (Tacconi et al., 2010) strongly suggest that inflows and outflows must be occurring. Clearly, a better understanding of the physical processes involved is crucial for establishing a complete view of how galaxies evolve across cosmic time. This paper examines the dynamics and origin of accreting and outflowing gas in a cosmological hydrodynamic simulation, at redshift  $z=0.25$ , and discusses absorption-line diagnostics that can trace these components.

A separate aspect of cosmic baryons influenced by galactic outflows is the metal content of the intergalactic medium (IGM). Intergalactic metals are seen in quasar absorption line spectra from almost the earliest epochs where such data can be obtained (e.g. Songaila, 2001; Becker et al., 2011; Simcoe et al., 2011), as well as at lower redshift (e.g. Tripp et al., 2000, 2008; Thom & Chen, 2008; D’Odorico et al., 2010; Tumlinson et al., 2011; Cooksey et al., 2013; Tilton et al., 2012; Werk et al., 2013), indicative of enrichment by strong galactic outflows (Aguirre et al., 2001b; Oppenheimer & Davé, 2006). IGM enrichment observations can thus place tight constraints on the properties of outflows (Oppenheimer & Davé, 2006; Wiersma et al., 2010; Oppenheimer et al., 2012). However, the enrichment observed far from galaxies may only track the ancient relics of outflows, rather than the actively ongoing baryon cycle. Also, such metal lines may not trace inflows effectively if the accreting material is metal-poor.

Recently, much attention has been focused on the circumgalactic medium (CGM), a loosely-defined term that can alternately mean the gas within some fixed distance of a galaxy (e.g. Rudie et al., 2012; Ford et al., 2013a), within the

typical metal-enriched region around a galaxy (e.g. Prochaska et al., 2013), or within the virial radius of the galaxy’s dark matter halo (Stocke et al., 2013). The CGM is where the baryon cycle is expected to be in action, where material is both flowing into galaxies to fuel star formation, and being expelled from galaxies on its journey into the IGM. Hence a potentially powerful tool to explore the baryon cycle is to examine inflowing and outflowing gas in the CGM, either in emission or, as we discuss here, in absorption against background sources whose lines of sight pass through a galaxy’s CGM.

The recent installation of the Cosmic Origins Spectrograph aboard *Hubble* has enabled the CGM to be probed in absorption in unprecedented detail. As an example, the COS-Halos project (Tumlinson et al., 2011, 2013) examines the CGM around more than 70 galaxies spanning a range in mass and colour, providing a comprehensive look at the CGM within  $\sim 150$  kpc of galaxies ranging in size from  $L^*$  to Magellanic-sized dwarfs (Werk et al., 2013). Other studies have targeted randomly situated bright quasars but have obtained extensive galaxy redshift information along their lines of sight, and are thus able to probe the CGM out to several hundred kpc (e.g. Tripp & Song, 2012; Stocke et al., 2013). The Mg II doublet, which redshifts into the optical at  $z \gtrsim 0.2$ , has long been used as a probe of CGM gas (Churchill et al., 2000; Bordoloi et al., 2011; Chen, 2012; Kacprzak et al., 2012) out to many tens of kpc. These studies have already highlighted some interesting results, including the fact that the presence of O VI is highly correlated with specific star formation rate (Tumlinson et al., 2011), but the presence of low-ionisation lines such as strong H I (Thom et al., 2012), Mg II (Chen, 2012), and Si III (Werk et al., 2013) is not.

One would like to assemble the multitude of observed absorption features, from H I, to low-ionisation IGM metal lines, to high-ionisation lines that presum-



ably trace more diffuse or hotter gas, into a coherent picture for how the baryon cycle operates. To properly place these data within a cosmological context, interpretive models must be cosmological in nature, and they must explicitly include galactic outflows and properly account for inflows. However, modelling the detailed physics of the interaction between inflowing, outflowing, and ambient gas remains a great challenge. Inflows are thought to be filamentary but some simulations predict highly collimated and cold filaments (e.g. Dekel et al., 2009), others suggest more diffuse, warmer filaments (e.g. Torrey et al., 2013), while still others suggest that filaments may break up via thermal instabilities depending on the environment (Kereš & Hernquist, 2009). Outflows also have large modelling uncertainties, as the way in which outflows are powered is still not fundamentally understood, and different approaches can lead to different results regarding the nature of the CGM gas and its absorption signatures (Stinson et al., 2012; Hummels et al., 2013; Ford et al., 2013a). Finally, it is possible that conductive interfaces on cold clouds moving through the CGM may be responsible for high-ionisation metal lines such as O VI and Ne VIII in particular (e.g. Tripp et al., 2011), and such interfaces would be well beyond the ability for any current cosmological simulation to resolve. Hence, these are early days in understanding how to interpret CGM absorption data, and much work remains. Nonetheless, some basic characteristics of the CGM and its relation to the baryon cycle are likely to be robust in such models.

In this series of papers, we explore the physical conditions and observable properties of the CGM using smoothed particle hydrodynamics (SPH)-based cosmological simulations. In Ford et al. (2013a), we examined the general physical properties of the CGM, as well as absorption statistics as a function of impact parameter, for H I, Mg II, Si IV, C IV, O VI, and Ne VIII. In our simulations, the

physical conditions traced by any given ion are often a monotonic function of its ionisation potential, such that low ionisation potential ions (which we will call low ions) generally trace high-density gas very close to galaxies at photo-ionisation temperatures (around  $10^4\text{K}$ ), higher ionisation potential ions (which we will call high ions) trace increasingly more diffuse, lower-density gas, and the highest ions can trace hot gas when present (typically in halos with masses  $\gtrsim 10^{12}M_\odot$ ). We presented predictions for the integrated column density and column density distributions for these absorbers, as a function of impact parameter, and showed that low ion absorbers increase in strength dramatically when lines of sight pass close to galaxies, while higher ions show a more modest increase closer to galaxies. These trends can be tested quantitatively against current and forthcoming observations; we are conducting comparisons now and will present those results in future work.

In this paper, we continue our focus on the physical state of the CGM by examining the dynamical state of the CGM gas and its impact on observable absorption line properties. In particular, we ask the question: Can we distinguish inflowing, outflowing, and ambient gas based on CGM absorption signatures? Here we focus on examining this at low redshifts ( $z \sim 0 - 0.25$ ), in anticipation of exploring the constraints on models enabled by COS-Halos and similar CGM projects; we leave an examination of this question at high redshifts for future work.

To explore the dynamical state of CGM baryons, we implement an analysis scheme that tracks gas as it moves in and out of galaxies. Such tracking, we note, is uniquely enabled by our particle-based simulation methodology. By tracking exactly where the gas originates and where it will eventually reside, we can definitively identify which gas is inflowing, outflowing, and ambient over a certain timescale. Moreover, this enables us to track material that once flowed out

of a galaxy but that will eventually return to a galaxy, a process we call *wind recycling* (Oppenheimer et al., 2010). This component has key observational implications because it represents inflowing material that is enriched and hence can be traced in metal absorption. Indeed, we will show (as in Oppenheimer et al., 2010) that wind recycling provides a dominant inflow contribution at the present cosmic epoch, which is by default lacking in models that do not include outflows. We will further show that absorption from low ions typically comes from recycling inflows, while absorption from high ions comes mostly from ancient outflows.

We organise our paper as follows: in §2 we introduce our simulations and methods, in §3 we define and explore various categories of inflowing, outflowing, and ambient material, and in §4 we present observational diagnostics to distinguish among these categories. In §5 we examine the physical conditions of these categories, in §6 we discuss numerical considerations in our (and alternate) simulation methods, and in §7 we present our conclusions.

## 3.2 Simulations & Analysis

### 3.2.1 The Code and Input Physics

We use our modified version (Oppenheimer & Davé, 2008) of the N-body+entropy-conserving smooth particle hydrodynamic (EC-SPH) code GADGET-2 (Springel, 2005), which is more fully described in §2.1 of Davé et al. (2010). Our main simulation for this work is identical to that in Davé et al. (2013), and we refer the reader to that work for a more detailed description.

We assume a  $\Lambda$ CDM cosmology (Hinshaw et al., 2009):  $\Omega_M = 0.28$ ,  $\Omega_\Lambda = 0.72$ ,  $h = H_o/(100 \text{ km s}^{-1} \text{ Mpc}^{-1}) = 0.7$ , a primordial power spectra index  $n = 0.96$ , an amplitude of the mass fluctuations scaled to  $\sigma_8 = 0.82$ , and  $\Omega_b = 0.046$ . We use a

cubic volume of  $32h^{-1}$  Mpc on a side with  $512^3$  dark matter and  $512^3$  gas particles, and a softening length of  $\eta = 1.25h^{-1}$  kpc (comoving, Plummer equivalent). The gas particle mass is  $4.5 \times 10^6 M_\odot$ ; dark matter particle mass is  $2.3 \times 10^7 M_\odot$ . The stellar component of a Milky Way mass galaxy is thus represented with  $\approx 2 \times 10^4$  particles.

We incorporate cooling processes using primordial abundances as described by Katz et al. (1996), with metal line cooling based on tables from Wiersma et al. (2009a) that assume ionisation equilibrium in the presence of the Haardt & Madau (2001) background. Star formation follows a Schmidt (1959) Law calibrated to the Kennicutt (1998) relation, following Springel & Hernquist (2003). The ISM is modelled using the sub-grid recipe of Springel & Hernquist (2003), where a gas particle above a density threshold of  $n_H = 0.13 \text{ cm}^{-3}$  is modelled as a fraction of cold clouds embedded in a warm ionised medium following McKee & Ostriker (1977). We use the Chabrier (2003) initial mass function (IMF) throughout. We account for metal enrichment from Type II supernovae, Type Ia SNe, and AGB stars, and we track four elements (C,O,Si,Fe) individually, as described in more detail in Oppenheimer & Davé (2008).

This simulation includes galactic outflows, which are implemented using a Monte Carlo approach. These outflows are tied to the SFR,  $\dot{M}_{wind} = \eta \times SFR$ , where  $\eta$  is the mass loading factor. For this work we focus on the hybrid energy/momentum driven winds, or “ezw” model. In the ezw model, the wind speed and mass loading factor depend on the galaxy velocity dispersion  $\sigma$ :

$$v_w = 3\sigma\sqrt{f_L - 1} \quad (3.1)$$

$$\eta = \sigma_o/\sigma, \text{ if } \sigma > 75 \text{ km s}^{-1} \quad (3.2)$$

$$\eta = (\sigma_o/\sigma)^2, \text{ if } \sigma < 75 \text{ km s}^{-1} \quad (3.3)$$

Here,  $f_L=[1.05,2]$  is the luminosity in units of the Eddington luminosity required to expel gas from a galaxy potential. These values are taken from observations Rupke et al. (2005). As described further in Oppenheimer & Davé (2008), these values for  $f_L$  include a metallicity dependence and an additional kick (to get the particle out of the galaxy) to simulate the continuous pumping of gas argued for by Murray et al. (2005). The mass loading factor  $\eta$  works out to 1.17 for  $10^{13} M_\odot$  halos and 5.83 for  $10^{11} M_\odot$  halos.  $\sigma_o = 150 \text{ km s}^{-1}$ , and  $\sigma$  is the galaxy’s internal velocity dispersion, broadly constrained to match IGM enrichment at high redshift (Oppenheimer & Davé, 2008).

These scalings roughly capture the behaviour in recent models of outflows from the interstellar medium by Murray et al. (2010) and Hopkins et al. (2012). We note that the scalings for this “ezw” model, and those in previous work by our group with the momentum-driven or “vzw” model (e.g. Oppenheimer & Davé, 2008; Davé et al., 2010, 2011a,b; Oppenheimer et al., 2012; Ford et al., 2013a), which follow the scalings of Murray et al. (2005) are identical for higher mass systems. It is only in lower mass systems, i.e. those with  $\sigma < 75 \text{ km s}^{-1}$ , where the ezw model differs from the vzw model. We focus exclusively on the ezw model as our favoured wind model for two reasons: 1) it captures the most up-to-date small-scale outflow models and 2) it is in best agreement among our models with observations of the stellar and H I mass functions (Davé et al., 2013). Nonetheless, results for our previously-favoured vzw model that does not include the steeper  $\eta$  at dwarf mass scales are quite similar.

In this simulation, we also add an artificial quenching mechanism in higher mass halos, as described in more detail by Davé et al. (2013). This is not a physical model, but an empirical prescription to stochastically quench star formation in high-mass galaxies in order to match observations and improve simulation

speed; see (Davé et al., 2013, particularly their eq. 5) for details. This model yields a quenching efficiency of 50% at  $M_{\text{halo}} = 10^{12.1} M_{\odot}$ , increasing rapidly to higher halo masses. We expect that the CGM of higher mass halos would be significantly impacted by our ad hoc quenching, but in this work we focus on halos with mass  $\leq 10^{12} M_{\odot}$ .

### 3.2.2 Generating spectra with SPECEXBIN

We use SPECEXBIN, described in more detail by Oppenheimer & Davé (2006), to calculate the physical properties of the gas. SPECEXBIN averages physical properties of the gas along a given sight line, then uses look-up tables calculated with CLOUDY (Ferland et al., 1998, version 08.00) to find the ionisation fraction for the relevant ionic species. We use the same version of SPECEXBIN as in Ford et al. (2013a), which includes a prescription for self-shielding from the ionisation background. This prescription results in a density threshold of approximately  $0.01 \text{ cm}^{-3}$  above which H I is fully neutral and moves all the magnesium into Mg II. See Figure 1 of Ford et al. (2013a) for an example of a simulated spectrum.

We fit Voigt profiles to the absorption features using AUTOVP (Davé et al., 1997). As in Ford et al. (2013a), we consider all components within  $\pm 300 \text{ km s}^{-1}$  to be associated with a galaxy, and we combine any components into systems with  $\Delta v < 100 \text{ km s}^{-1}$ . We apply the same column density limits as in Ford et al. (2013a),  $10^{16} \text{ cm}^{-2}$  for H I and  $10^{15} \text{ cm}^{-2}$  for metal lines. All lines stronger than this are set to this value to avoid having a single large saturated absorber skew the results, since such high column absorbers generally have highly uncertain column densities from Voigt profile fitting. As we showed in Ford et al. (2013a), very weak lines are also poorly constrained given our assumed S/N=30, so we do not consider lines weaker than  $30 \text{ mÅ}$ .

For this work, we focus on targeted lines of sight (LOS). We randomly select

central galaxies in two different halo mass bins:  $10^{10.75-11.25} M_{\odot}$  (labelled  $10^{11} M_{\odot}$ ) and  $10^{11.75-12.25} M_{\odot}$  (labelled  $10^{12} M_{\odot}$ ). For  $10^{11} M_{\odot}$ , we select 250 galaxies, while for  $10^{13} M_{\odot}$  there are only 221 central galaxies in the simulation so we use all of them in our sample. We choose impact parameters ranging from 10 kpc out to 300 kpc, with the spacing increasing slightly with impact parameter. As in Ford et al. (2013a) we produce four LOS per galaxy at a position  $x, y$ :  $x+b, x-b, y+b, y-b$ , for a total of 1,000 LOS per  $b$  per mass bin (844 for  $10^{13} M_{\odot}$ ). We do not present results within 10 kpc of galaxies since we cannot resolve the detailed internal structure of the interstellar medium (ISM), and in any case we are more interested in probing CGM gas in absorption towards background objects that rarely lie at such small impact parameters. For parts of this work we restrict our study to gas within the virial radius of a central galaxy. We define the virial radius as the radius enclosing the virialization overdensity for our assumed cosmology, as described in (Davé et al., 2010, see their eqs. 1 and 2), which at  $z = 0.25$  corresponds to roughly 90 times the critical density. The median central galaxy stellar mass is  $5.89 \times 10^8$  and  $3.63 \times 10^{10} M_{\odot}$  for our  $10^{11} M_{\odot}$  and  $10^{13} M_{\odot}$  halos, respectively.

We look at H I, Mg II, Si IV, C IV, O VI, and Ne VIII Ford et al. (2013a). We select these ions as they are some of the most commonly observed species in the low-redshift CGM, spanning a wide range of ionisation potentials. All the metal lines have doublets, making their identification in observed spectra more straightforward.

### 3.3 Inflows and Outflows

#### 3.3.1 Identifying Inflowing and Outflowing Gas

To examine the dynamical state of CGM gas, we must first determine whether a given gas particle is inflowing, outflowing, or ambient. This is not trivial, because the constant cycling of baryons within halos can conflate inflowing, outflowing, and ambient gas.

Our approach is to make these divisions based on information available in the simulations: the particles' past history and future fate. For this, we require two additional pieces of information from the simulations: The future location of particles, and the time when each wind particle was ejected.

The first piece of information is the particles' future location. For this, we cross-correlate all the non-ISM particles in our simulation at  $z = 0.25$  with their location at  $z = 0$ , which is 3 Gyr later. If during this time a particle has been accreted into the ISM of a galaxy, or has turned into a star, or has been cycled through the ISM and subsequently ejected in an outflow, we identify it as an “accreting” particle. *Accretion is thus defined as any gas that was not in the ISM at  $z = 0.25$ , but is either in or has passed through the ISM or has turned into a star by  $z = 0$ .* By definition, the ISM consists of all gas with  $n_H \geq 0.13 \text{ cm}^{-3}$ , the density threshold at which star formation is allowed.

Next, we need the time of ejection for each wind particle. We record each wind ejection event during the simulation so that for any given time we can determine the *wind age* of a given particle. If a particle *is not accreting* but has a non-zero wind age, it is considered an “outflow” particle. Note that the wind age can be quite large if a particle was ejected in the early universe, and hence being an outflow particle under this definition does not necessarily imply that it is currently on its way out from a galaxy. For particles ejected multiple times, we only record the



most recent ejection. Finally, we define “ambient” gas as particles that will not accrete by  $z = 0$  and was never ejected in a wind before  $z = 0.25$ . Thus we have the following divisions:

1. **Pristine Accretion.** This is any accreting gas that has never been ejected in a wind. In general, this gas tends to have quite low metallicity since it has never been in the ISM of a galaxy. It can have non-zero metallicity, however, due to enrichment from tidal stripping or in-situ star formation at an earlier epoch.
2. **Recycled Accretion.** This is all accreting gas that was once ejected in a wind at least once before  $z = 0.25$ .
3. **Young Outflows.** These are gas particles that are not in the ISM at  $z = 0.25$ , are not accreting, and have been ejected from the galaxy in a wind between 0 and 1 Gyr before  $z = 0.25$ . We choose 1 Gyr as this is roughly the time a particle would take to leave the halo if it simply got kicked into the a wind, never scattered or slowed down due to forces other than gravity. For our cosmology, 1 Gyr before  $z = 0.25$  is approximately  $z = 0.36$ .
4. **Ancient Outflows.** Same as young outflows, only particles ejected more than 1 Gyr ago (before  $z = 0.36$ ).
5. **Ambient.** Gas particles that are not in the ISM of a galaxy at  $z = 0.25$ , are not going to accrete onto a galaxy by  $z = 0$  and that have never been in a wind by  $z = 0$ .

All gas particles that are not in the ISM at  $z=0.25$  are in one of these five categories. Note, in particular, that the distinction between outflow (AO and YO) material and recycled accretion material, and the distinction between ambient

(AMB) material and pristine accretion (PA), is whether the gas will accrete by  $z = 0$ . We note that in this prescription there is no metal mixing between the categories. A gas particle that is ambient does not, for example, pick up metals from an ancient outflow particle. While this may not be physical, it is the cleanest way to set up this experiment of examining the baryon cycle, otherwise the definitions of the various categories would overlap.

Note that young and ancient outflows are subdivided by time since ejection, but in general ancient outflows end up farther away from galaxies, while outflows ejected more recently tend to stay closer. This reflects the “outside-in” IGM enrichment scenario occurring in our simulations as described in Oppenheimer et al. (2012). Also, recycled accretion can in principle escape the halo before re-accreting.

We visualise these categories in Figure 3.1, which shows a typical galaxy in a  $10^{13} M_{\odot}$  halo (left panels) and in a  $10^{11} M_{\odot}$  halo (right panels). We plot all the gas within the virial radius, 262 physical kpc for the  $10^{13} M_{\odot}$  halo and 112 physical kpc for the  $10^{11} M_{\odot}$  halo. Both galaxies are shown approximately edge-on. In each panel we plot the stars in white. In the top panels we plot the accreting material with recycled accretion in dark blue and pristine accretion in light blue. In the middle panels we plot recent outflows in green and ancient outflows in orange. In the lower panels we plot the ambient gas in red.

These images reveal some qualitative trends regarding these categories. Let us first examine the geometry. One may expect accreting material to flow in along the filaments, parallel to the disk of the galaxy, and outflowing material to come out perpendicular to the plane of the disk. However, the real picture is not so simple. First, only pristine accretion is expected to be along the filaments while recycled accretion, having been ejected from a galaxy, tends to be less confined

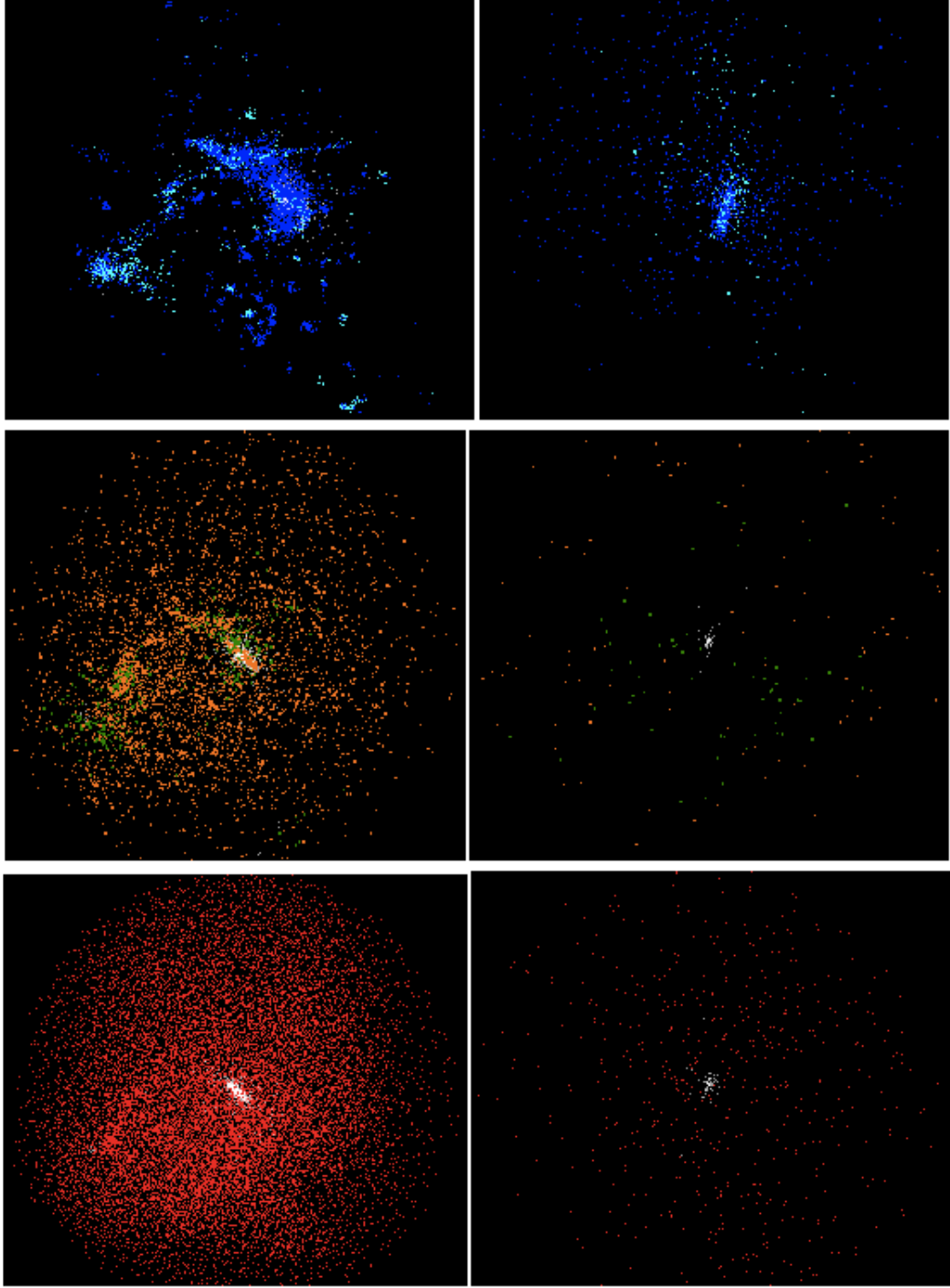


Figure 3.1: Left panels: SPH particles around a galaxy at  $z = 0.25$  with halo mass  $M_{halo} = 10^{13} M_{\odot}$  and a panel width of 525 physical kpc. Right panels: SPH particles around a galaxy with halo mass  $M_{halo} = 10^{11} M_{\odot}$ , panel width is 225 kpc. Top panels show recycled accretion (dark blue), and pristine accretion (light blue). Middle panels show young outflows (green) and ancient outflows (orange). Lower panels show ambient gas (red). All panels also include stars (white).

to filaments. Second, the filaments and disks are not always aligned (Danovich et al., 2012), so even pristine material flowing in along a filament may not be parallel to the galaxy. Third, at low redshift, the cross section of filaments can actually be larger than the galaxies at their intersections Katz et al. (2003). This geometry precludes the possibility of clear filamentary accretion at these redshifts, quite unlike at high redshift, where filamentary accretion is much more dominant Kereš et al. (2009); van de Voort et al. (2012); Shen et al. (2013); Fumagalli et al. (2011, 2013). Additionally, only cold mode accretion (dominant at high redshift) is filamentary, while hot-mode accretion (relatively greater contribution at low- $z$ ) is expected to be quasi-spherical (Katz et al., 2003). For both masses in Figure 3.1, neither recycled nor pristine accretion is clearly coming in along a well-defined axis. For the  $10^{13} M_{\odot}$  halo, the recycled accretion appears to follow some sort of structure while for the  $10^{11} M_{\odot}$  halo it is more diffuse.

Moving to the middle panels we see that in the  $10^{13} M_{\odot}$  case the young outflows generally are close to the main galaxy, its satellite, or the bridge that connects them. In the  $10^{11} M_{\odot}$  case they are more diffuse. Interestingly, in neither the  $10^{13} M_{\odot}$  or  $10^{11} M_{\odot}$  case do the young outflows show an obvious polar axis preference, as one might have expected, despite the fact that the material is ejected in the direction of  $\mathbf{v} \times \mathbf{a}$ . In part this is because our “young” outflows are not that young, and in many cases may already be rejoining the accretion flow as recycled winds. For both masses ancient outflows are diffusely distributed. The ambient gas in the bottom panel fills the halo roughly spherically, without a preferred direction. We will show that much of the ambient material is in a hot hydrostatic gaseous halo, which is much more prominent at  $10^{13} M_{\odot}$  than at  $10^{11} M_{\odot}$  (Kereš et al., 2005; Gabor & Davé, 2012).

Figure 3.1 also shows some clumpy features, particularly in the accreting gas.

These clumps are larger than the softening length, and have two possible origins. Some of these clumps could be physical in nature. As described in Kereš et al. (2009), at low redshift, filaments are lower density and can be more easily destroyed in a halo. These filamentary remnants can break up and become clouds within halos. Some of these clumps, however, are likely numerical effects from our particular SPH implementation. They could affect results for our low ionization lines, like Mg II and H I. We note that we broadly match COS-Halos observations of strong H I and Mg II (Ford et al., in prep), but we are currently working on improvements to our SPH implementations (Huang et al., in prep) that should mitigate the unphysical clumps (as in Hu et al. (2014)). We plan to investigate low ionization lines further in those simulations.

To visualise these categories more quantitatively, in Figure 3.2 we show the wind age versus the  $z = 0$  overdensity of all non-ISM gas particles (at  $z = 0.25$ ) that have ever been ejected in an outflow. The vertical line demarcates the ISM overdensity threshold at  $z = 0$ , i.e.  $n_H = 0.13 \text{ cm}^{-3}$ . Particles with densities greater than the ISM threshold at  $z = 0$  are considered to be recycled accretion. Particles that are not in the ISM at  $z = 0$  are subdivided by their wind age into ancient outflows (wind age  $> 1 \text{ Gyr}$ ) and young outflows (wind age  $\leq 1 \text{ Gyr}$ ). The other two categories, pristine accretion and ambient, do not appear in this plot since they have never been in a wind by definition. This figure shows not just how we have divided our categories but also the distribution of the gas particles. One can see there are more particles in the ancient outflow category than in young outflows, and that the number of particles in the recycled accretion category is large. We will quantify this in greater detail in later sections.

We emphasise that we do not *just* look at the  $z = 0$  ISM densities (as shown in Figure 3.2) to determine whether or not a particle will accrete by  $z = 0$ . As

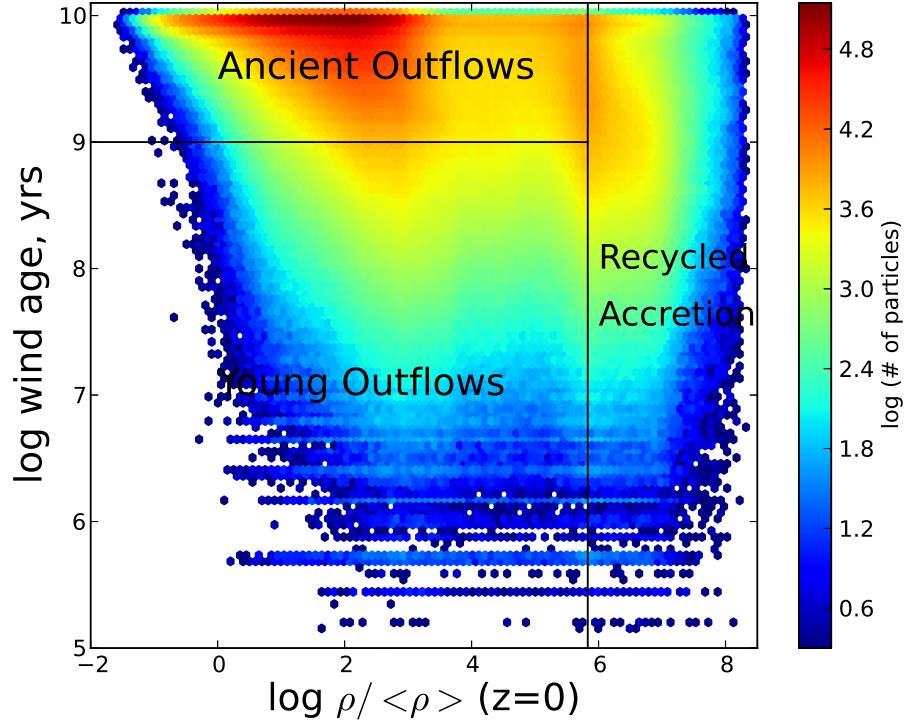


Figure 3.2: The time (relative to  $z = 0.25$ ) since last wind ejection vs. density at  $z = 0$  of all gas not in the ISM at  $z = 0.25$ . The vertical line denotes ISM densities at  $z = 0$ . Gas to the right of the line is defined as accreting, because it will join the ISM of a galaxy by  $z = 0$ . Gas to the left is defined as not accreting, unless it forms a star or gets launched into a wind (not shown on this plot). The horizontal line at 9.0 shows the separation of young from ancient outflows.

Table 3.1: Fate of the accreting material

log(Halo Mass)	Star	Wind Ejection	ISM
11.0	10%	18%	72%
11.5	23%	30%	47%
12.0	31%	35%	34%

we explained earlier, if a particle turns into a star or enters the galaxy and is subsequently ejected we also consider that particle as being accreted. In Table 3.1 we show, in three halo mass bins, what fraction of the accreting mass at  $z=0.25$  will by  $z=0$  end up in stars, in the ISM, or be ejected in a wind. In some cases, between  $z = 0.25$  and  $z = 0$ , a particle is ejected multiple times and so at  $z = 0$  is again at ISM densities; in those cases we give a preference to the ISM.

We note that the values in Table 3.1 are for the gas that recycles onto the galaxy only, and different mass galaxies recycle different fractions of their gas mass. Of the material that does recycle, it is useful to see what happens to it. For  $10^{11}M_{\odot}$  halos, most of the accreting mass ends up in the ISM, not in stars. This is because in low-mass galaxies, gas has a lower density and hence a longer timescale for star formation. For  $10^{11.5}M_{\odot}$  halos just under half ends up in ISM. For  $10^{13}M_{\odot}$  halos, the distribution is almost completely evenly split amongst stars, ISM, and wind ejection, owing to higher gas densities and shorter star formation timescales. The contribution of star formation and wind ejection to the mass budget of accreting material is significant. Separately tracking wind ejection and star formation events also gives us a finer time resolution in the gap between  $z = 0.25$  and  $z = 0$ . Note that Table 3.1 does not imply that galaxies have 50% gas fractions, as most stars formed from gas accreted at  $z > 0.25$ .

### 3.3.2 Mass Budgets

To begin analysing the gas in these various categories, we first examine their mass fractions. We do this both for all the gas in the simulation and for gas within the virial radius of dark matter halos, which we identify as CGM gas. As we discussed in §1, there are various definitions for CGM in the literature, and in Ford et al. (2013a) we argued for 300 kpc as an appropriate radius for the CGM based on the metal absorption extent, at least for  $\sim L^*$  galaxies. However, we also showed that the extent of absorption depends on the particular metal ion and there was not a clean distinction between enriched and unenriched regions. Hence, here we will use a CGM definition that is perhaps more removed from direct observations but is well-motivated and well-defined theoretically, namely the virial radius. Our definition for the virial radius is discussed in section § 2. This is at least something that is directly quantifiable and whose extent scales with the galaxy mass.

Figure 3.3 shows pie charts for the total mass (upper left) and metal mass (upper right) of all non-ISM gas particles in the simulation at  $z = 0.25$ , broken down by category, while the middle and bottom panels show analogous pie charts considering only non-ISM gas within high- and low-mass halos, respectively. We choose  $M_{halo} = 10^{11.5} M_{\odot}$  as the dividing line between high- and low-mass halos because that is where we see a crossover between hot and cold gas fractions, which we discuss later. We define particles as within the halo if  $R \leq R_{vir}$ . (For reference, we note that ISM gas makes up 1.8% of the total gas mass of the simulation at  $z = 0.25$ .)

In the upper left panel, we see that most of the non-ISM gas mass in the simulation consists of ambient material. Even though outflows in our simulations are ubiquitous and have mass loading factors typically of unity or above (Oppen-



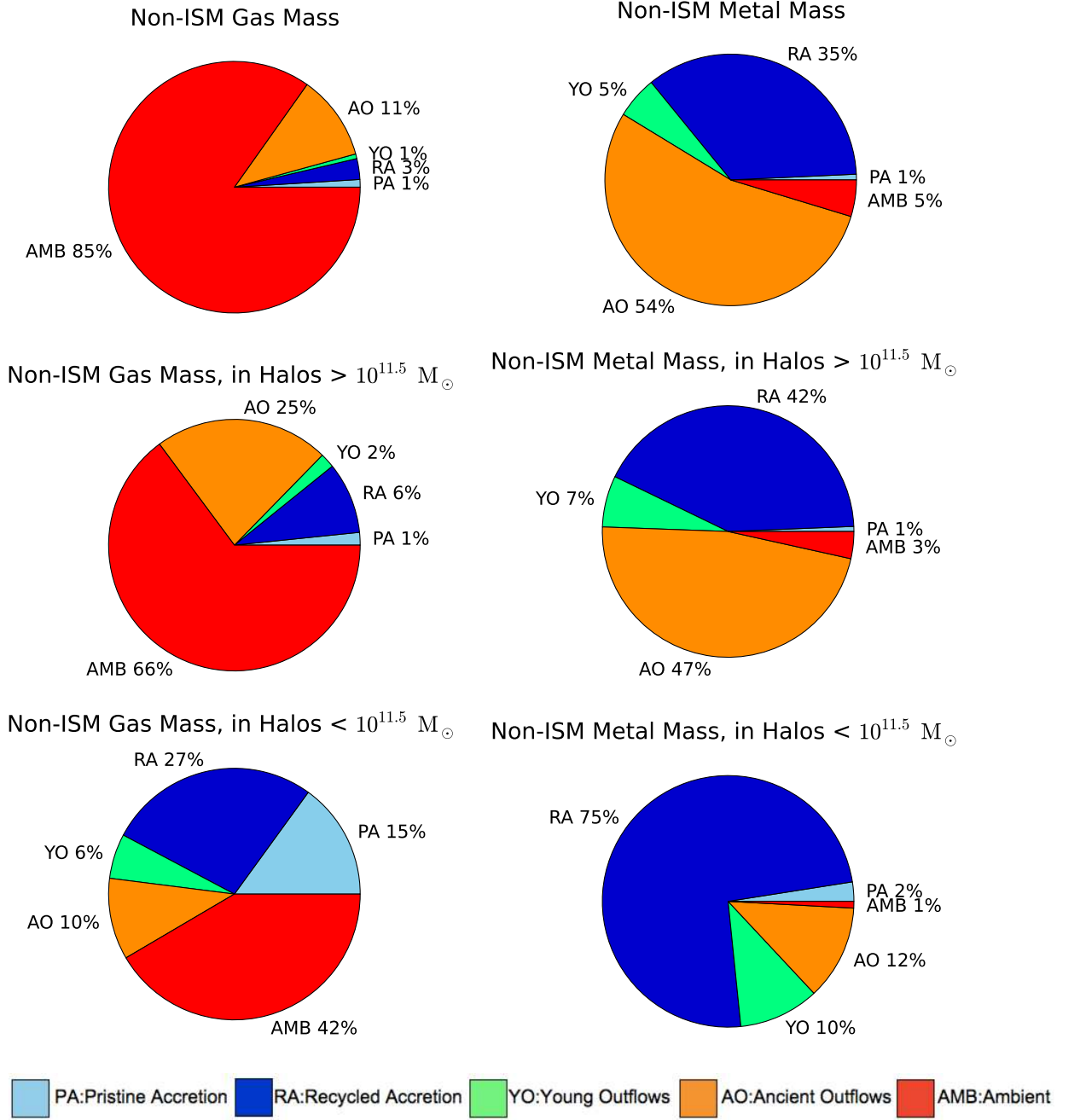


Figure 3.3: The non-ISM gas mass budget (left) and gas-phase metal budget (right) at  $z = 0.25$ . Upper plots show the full simulation, and lower plots show only gas within the virial radius of a halo at  $z = 0.25$ , for high (middle) and low (bottom) mass halos. Ambient is gas that has never been in a wind, before or after  $z = 0.25$ , that is not accreting. Ancient outflow is for non-accreting gas particles ejected in a wind more than 1 Gyr before  $z = 0.25$ . Young outflow is for non-accreting gas particles ejected in a wind  $\leq 1$  Gyr before  $z = 0.25$ . Recycled accretion is gas that has been ejected in a wind by  $z = 0.25$ , and will join or pass through the ISM of a galaxy or become a star by  $z = 0$ .

heimer & Davé, 2008), the majority of baryons in the Universe have never been in a wind since the baryonic fraction in galaxies is small, only 7% in this model. Ambient gas, much of which consists of diffuse gas in the IGM, accounts for 85% of all baryons; this material does not participate in the baryon cycle by  $z = 0$  since it has neither been in an outflow nor has it been accreted. Ancient outflow is the next largest category at around 11%, which is still larger than the fraction of baryons in stars (6%), showing that the mass in outflows exceeds that in stars globally, as noted in our earlier simulations (Oppenheimer & Davé, 2008). Young ( $\leq 1$  Gyr old) outflows comprise only about 1% of the mass, which is not surprising since the outflow rate roughly tracks the star formation rate, and this is much smaller at the present epoch than at high redshifts. The global accreting gas mass fraction from  $z = 0.25 - 0$  is 4%, of which the vast majority was previously in a wind (3%). Pristine accretion over the 3 Gyr from  $z = 0.25$  to  $z = 0$  only accounts for 1% of all baryons. Of the material that accretes between  $z = 0.25$  and  $z = 0$ , 25% of it (by mass) is pristine accretion; the other 75% is recycled accretion.

The story is quite different if one considers the metal mass (upper right pie chart). Now ancient outflows contain 54% of all cosmic metals and recycled accretion contains over one-third. Young outflows, which contain only 1% of the total mass, still contain 5% of the metals. Ambient material, having essentially never resided inside a galaxy, contains a very small amount of metals relative to its mass fraction, and pristine accretion likewise has a negligible metal mass content. The metals that are present in the ambient or pristine accretion gas has three possible sources within our simulations: Type Ia supernova, AGB stars, or tidal stripping. The metals in pristine accreting material mostly owes to tidally stripped ISM material, which then reaccrues. Pristine accretion has an average metallicity of  $0.07Z_{\odot}$ , while recycled accretion has on average approximately so-

lar metallicity. It is worth emphasising that overall accreting material is typically significantly metal enriched, and hence does not usually have low metallicity as is sometimes assumed, at least at these low redshifts.

In the middle and lower panels of Figure 3.3 we restrict ourselves to only non-ISM material within the virial radius of dark matter halos, i.e. the CGM, which includes roughly 20% of the total gas mass and 70% of the total metal mass of non-ISM gas particles. From the mass fractions in the lower left panels, we see that the fraction of CGM material participating in the baryon cycle is significantly larger for both low- and high-mass halos – the inflow and outflow categories are more prominent. Nonetheless, ancient outflows still dominates over young outflows, and recycled accretion dominates over pristine accretion. High-mass halos have a larger percentage of ambient material, since they can keep their gas hot via a stable virial shock (Birnboim & Dekel, 2003) and prevent it from falling back in. The relative contribution of accretion in high-mass halos is smaller than in low-mass ones, also because of temperature: hot halos can prevent infall.

The importance of “halo fountains”, i.e. recycled accretion that never leaves the halo, is shown in the metal fraction plot within halos (lower right). For high-mass halos, almost half the metal mass within the halos at  $z = 0.25$  will, by  $z = 0$ , be accreted onto galaxies. The remaining half of the metals are mostly in ancient outflows that are still trapped or recaptured within halos via “outside-in” enrichment (Oppenheimer et al., 2012), with young outflows having a slightly increased metal proportion relative to their gas mass because outflows today are somewhat more metal-rich than outflows at earlier epochs. This owes to the upwards evolution of galaxies along the galaxy mass-metallicity relation in these models (Davé et al., 2011b). For the low-mass halos, the contribution from recycled accretion is dominant: fully 75%. In these low-mass halos, the metals either escape the halo

completely or fall back in, whereas in high-mass halos there is a hot halo that can keep the metals bound to the halo but not falling back in.

In Figure 4.9, we investigate the CGM mass budgets further by breaking down our inflow/outflow categories by their phase. We consider four phases: hot ( $T > 10^5$  K), cold ( $T < 10^5$  K), ISM ( $n_H \geq 0.13 \text{ cm}^{-3}$ ), and stars. The top panel shows the fractional CGM gas mass, relative to the total mass, by phase as a function of halo mass. The black line shows the total baryonic fraction, which hovers around but is slightly below the universal baryon fraction of 0.164, (dot-dot-dot-dash horizontal line), until it starts to drop at  $M_{\text{halo}} \lesssim 10^{11.5} M_{\odot}$ . The hot and cool gas fractions cross over at roughly this mass, with the CGM becoming hot gas-dominated at higher masses as is typically seen in these types of simulations (e.g. Kereš et al., 2005; Gabor & Davé, 2012; Nelson et al., 2013). (This crossover also serves as justification for the mass breakouts shown in Figure 3.3.) The stellar and ISM gas fractions have a peak at  $M_{\text{halo}} \approx 10^{12} M_{\odot}$ ; star formation is suppressed at lower masses by increasingly strong outflows and at higher masses by our quenching prescription. The overall shape agrees reasonably well with that inferred from halo abundance matching studies at  $z = 0.1$  (e.g. Behroozi et al., 2013). As shown in Behroozi et al. (2013), there is very little evolution in  $M_{\text{bar}}/M_{\text{halo}}$  as a function of  $M_{\text{halo}}$  from  $z = 1$  to  $z = 0.1$ , so comparing this work's  $z = 0.25$  data to Behroozi et al. (2013) at  $z = 0.1$  is acceptable. There are some differences at higher masses, because we include satellites in the stellar content of our halos while Behroozi et al. (2013) does not include them. As shown in Berlind et al. (2003), satellites make a larger contribution to the stellar mass budget at larger halo masses. If we exclude satellites (orange dashed line), we get much better agreement with Behroozi et al. (2013). This is essentially equivalent to saying that the stellar mass function in this model agrees well with the obser-

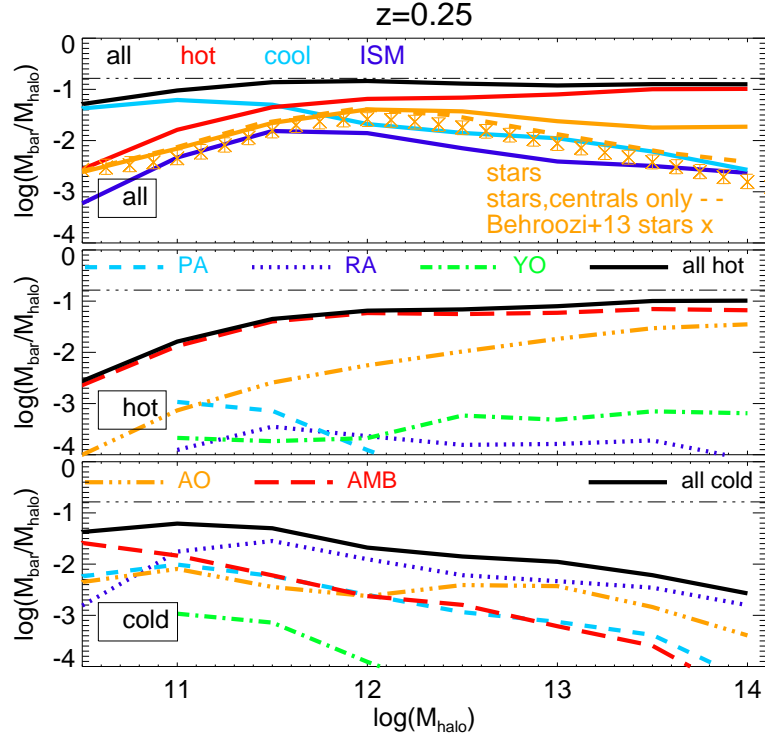


Figure 3.4: Upper panel: the fraction of baryons that are hot ( $> 10^5$  K; red) , cool ( $< 10^5$  K; light blue), the ISM (i.e. star-forming; dark blue), and in stars (orange) vs. halo mass at  $z = 0.25$ . We plot the total baryon fraction in halos (solid black). The black horizontal dot-dot-dot-dash line represents the global ratio  $\Omega_b/\Omega_m$ . We also plot the fraction of baryons in just the hot phase (middle panel) and the cold phase (bottom panel) vs. halo mass divided into categories as labelled.

vations, which was shown directly by Davé et al. (2013).

In the middle and lower panels we consider the hot and cold (non-ISM) CGM components, demarcated at  $10^5 K$ , and split them in our inflow/outflow categories as labelled. We note that our prescription for outflows does not explicitly heat the winds, even in the presence of a hot halo. While winds can shock once the hydro forces are turned on, in practice the high level of enrichment results in rapid cooling that keeps the particle at  $\sim 10^4$  K. The hot component should thus be considered a lower limit on the amount of energy added by winds. Ongoing improvements to our wind model (Gabor et al., in prep) may increase the hot fraction.

The black lines show the total hot (red line in upper panel) and total cool (light blue in upper panel) fractions for reference. The hot phase is completely dominated by ambient gas at all masses. This indicates that hot halo baryons are generally not participating in the baryon cycle, at least in our simulations. Ancient outflows are approximately an order of magnitude smaller in mass fraction, except at the largest masses where the outflows are more efficiently retained or re-accreted within group potentials and rise to become half the ambient gas mass. The other categories provide an essentially negligible contribution to the hot gas. We note that in our models we eject the winds at the ISM temperature, which are then allowed to interact with the CGM gas once it escapes the ISM. However, given that it is metal enriched it tends to cool quickly even if it shock-heats initially. This enhances the recycling of that material, and hence hot halo gas contains little of this component.

By contrast, the cool phase has more mass undergoing baryon cycling. For halos with  $M_{\text{halo}} > 10^{11} M_{\odot}$ , recycled accretion dominates the mass budget, owing to short recycling times in massive halos (Oppenheimer et al., 2010). For

smaller mass halos, ambient gas again dominates, and pristine accretion becomes the most important accretion channel. This transition from enriched to pristine accretion in the cool gas could provide an interesting signature of recycling in absorption lines.

To recap, we divide all non-ISM gas at  $z = 0.25$  into five categories: **pristine accretion**, which holds a small fraction of both the total gas mass and the metal mass but dominates accretion in dwarf galaxy halos; **recycled accretion**, which dominates accretion for sizeable halos and holds a substantial fraction of their metal mass; **young outflows**, which are a sub-dominant component of mass and metals in the CGM, **ancient outflows**, which hold roughly half the total metal mass in the CGM; and **ambient material**, which contains a small fraction of the metals but a majority of the gas mass, particularly the hot gas mass, both globally and within the CGM.

### 3.3.3 Relation to Dynamics

We have defined inflows and outflows based on their future and past history relative to  $z = 0.25$ . It is interesting to see how these definitions relate to the actual dynamics of the gas at  $z = 0.25$ . One expected trend would be that outflows, particularly young outflows, should have an outward radial velocity relative to the galaxy and that inflowing gas should have a negative radial velocity. To examine this, we calculate the radial velocity  $v_r$  of gas particles relative to the nearest central galaxy, and compare it to the halo virial velocity  $v_{\text{vir}}$ .

Figure 3.5 shows  $v_r/v_{\text{vir}}$  vs. wind age for all non-ISM particles in the simulation. For ages in the range of roughly  $10^7$  to  $10^9$  years, our dividing line between young and ancient outflows, there is a clear asymmetry in this distribution towards positive  $v_r$ , i.e. outflowing gas, which is much more pronounced for more recently ejected winds. A more subtle trend is that, excluding the gas that is in the

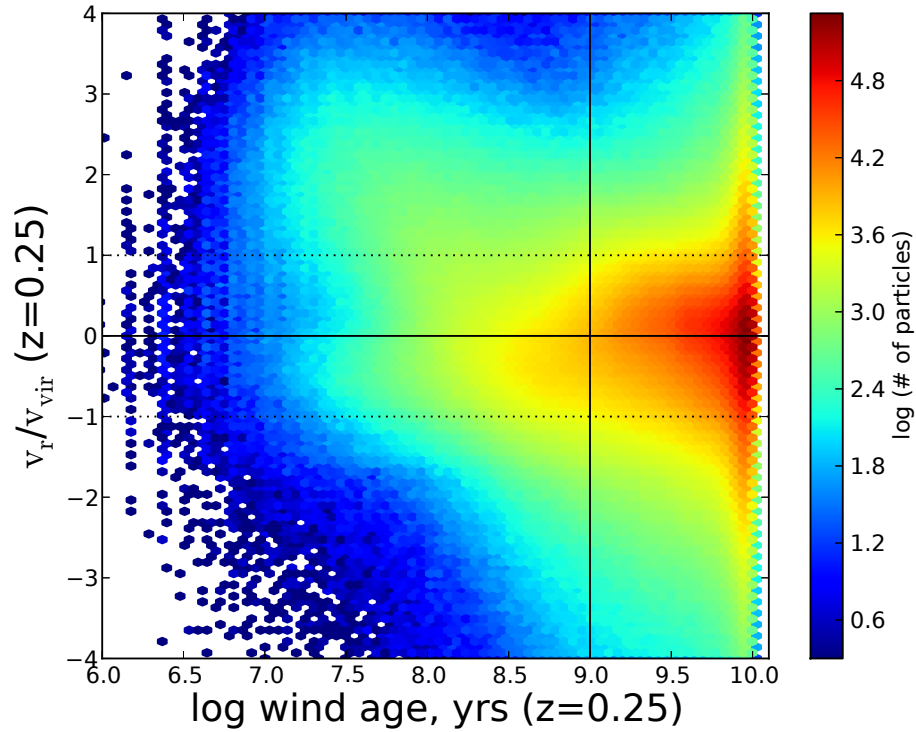


Figure 3.5:  $v_r/v_{\text{vir}}$  vs. wind age for all non-ISM gas particles in the simulation at  $z = 0.25$ .

outflowing “plume” to small age and large  $v_r$ , there is a negative velocity for the remaining wind gas. This corresponds to wind recycling, which we will explore in more detail below. Despite the presence of clearly outflowing gas, even recent outflows can span a range of velocities, including negative. This indicates that instantaneous radial velocity alone is not a robust identifier of relatively recent ejection.

Another approach to examining how our adopted categories relate to the dynamics of the gas is to look at velocity-radius plots. In such plots, the outflows would be expected to have a large positive radial velocity close to galaxies, diminishing as it moved further away, while inflows might be expected to show up as a net negative velocity, perhaps increasing as one approaches a galaxy.



Figure 3.6 shows the radial velocity (scaled to the virial velocity) versus radius (scaled to the virial radius) split into our categories as labelled. We associate each gas particle with the galaxy to which it is most bound. Because satellite galaxies can both eject winds and accrete gas, which could confuse our analysis, in these plots we restrict ourselves to gas particles associated with central galaxies. The scale for each panel is logarithmic in particle number, and spans the same range in each panel for ease of comparison. We note that each category does *not* have the same number of particles. The top two panels show accretion, pristine (left) and recycled (right). The middle two panels show young (left) and ancient (right) outflows. The bottom panels show ambient gas (left) and the sum of all the categories, i.e. all non-ISM gas (right). The solid line indicates zero velocity and the dotted lines delineate the virial velocity.

We begin by looking at all gas particles in the simulation, not in the ISM at  $z = 0.25$  and associated with central galaxies (lower right panel) at  $z = 0.25$ . With the exception of an inflowing plume at large  $r/r_{\text{vir}}$ , which we discuss in more detail below, in general the distribution is fairly symmetric. The distribution is also fairly smooth: there is not a neat “outflow” plume, a tight “inflow” plume, or a distinct “rotating with disk” component. Rather, one sees a more ambiguous picture, and hence robustly deciding which positive velocity gas to call outflows versus rotation or ambient motion can be quite difficult. This is why we choose to make our distinctions not based on the velocity, but in the manner described in §2.1

Looking at the different categories, pristine accretion (upper left) has the peak of its distribution at or slightly less than zero, depending on  $r/r_{\text{vir}}$ , indicating an inflow. There is also a slight inflowing plume at large radius, as seen in the “all non-ISM” panel. It is remarkable that so much pristinely accreting material has

positive velocities, and it shows that accretion is not so easily identified as merely inward-moving gas. There is a lot of random motion in the halo, so even material that will eventually accrete (onto either a central or satellite galaxy) can be moving away from the central galaxy, as shown here. Recycled accretion (upper right) shows similar trends: the peak of its distribution (yellow region) is shifted slightly below zero, but much of the material has a positive velocity, especially at radii  $\approx 0.1r_{\text{vir}}$ . This is recent wind material, which will turn around and accrete by  $z = 0$ .

The middle two panels show the outflows, young (left) and ancient (right). The young outflows show a distinct asymmetry towards outflowing gas. However, at any radius, young outflows are both moving towards and away from the galaxy. In other words, there is not an obvious demarcation in radial velocity that will uniquely isolate outflows occurring within the last  $\approx \text{Gyr}$ . One could demarcate the plume at high  $v_r$  and low  $r$ , but this will contain only a small fraction of the young outflowing material. Meanwhile, the ancient outflows show, unsurprisingly, even less asymmetry, with the exception of the the same inward plume seen earlier.

The ambient gas (lower left) shows essentially perfect symmetry about  $v = 0$ , as one would expect for gas that is neither in a wind nor going to be accreted. However, there is a strong concentration within the large radius plume, which is seen in the other panels as well. This owes to massive halos only ( $> 10^{11.5} M_{\odot}$ ); lower mass halos do not have this feature. This plume simply owes to the gravitational growth of structure, as gas falls into halos at large radii. Such gas gives rise to an infall signature at large radii as observed at  $z \sim 2$  (Rudie et al., 2013). However, once it falls into the halo, ambient gas does not continue its motion towards the galaxy, but instead settles into a virialised halo that has essentially no

net velocity relative to the galaxy.

In summary, the various categories of inflow and outflows show distinct trends in their kinematics. Accretion has a net negative inflow, although some of that material has positive velocities. Young outflows have a distinct asymmetry towards having more outwards moving gas, but there is still a wide range of radial velocities in this category, even at small radii. In terms of wind age, the youngest outflows show a clear outflowing tendency, but this signature mostly disappears for wind ages above a Gyr. Such ancient winds show little net infall or outflow from within the halo, and in many ways are much more like ambient material. Generally, it is difficult to separate these categories cleanly using cuts in velocity space, even when one includes radial distance information.

### 3.4 Observables

With a better understanding of the dynamical state of the CGM in hand, we now turn our focus to the observable signatures of accretion, outflows, and ambient material. In principle, a sufficient suite of observed absorption line tracers could directly constrain both the physical state and dynamics of the gas relative to a nearby galaxy. However, in practice, absorbers around halos are sparse and are not commonly visible in multiple metal tracers. Together with the uncertainty over the multi-phase nature of CGM, it is challenging to extract robust information directly from the data. Hence simulations such as ours can provide some insights into mapping specific ions onto gas with specific physical and dynamical properties.

In Ford et al. (2013a) we focused on how absorbers trace the physical conditions of the gas, namely the density and temperature. Here, we extend this to now consider the dynamical state of the gas, and determine whether there is

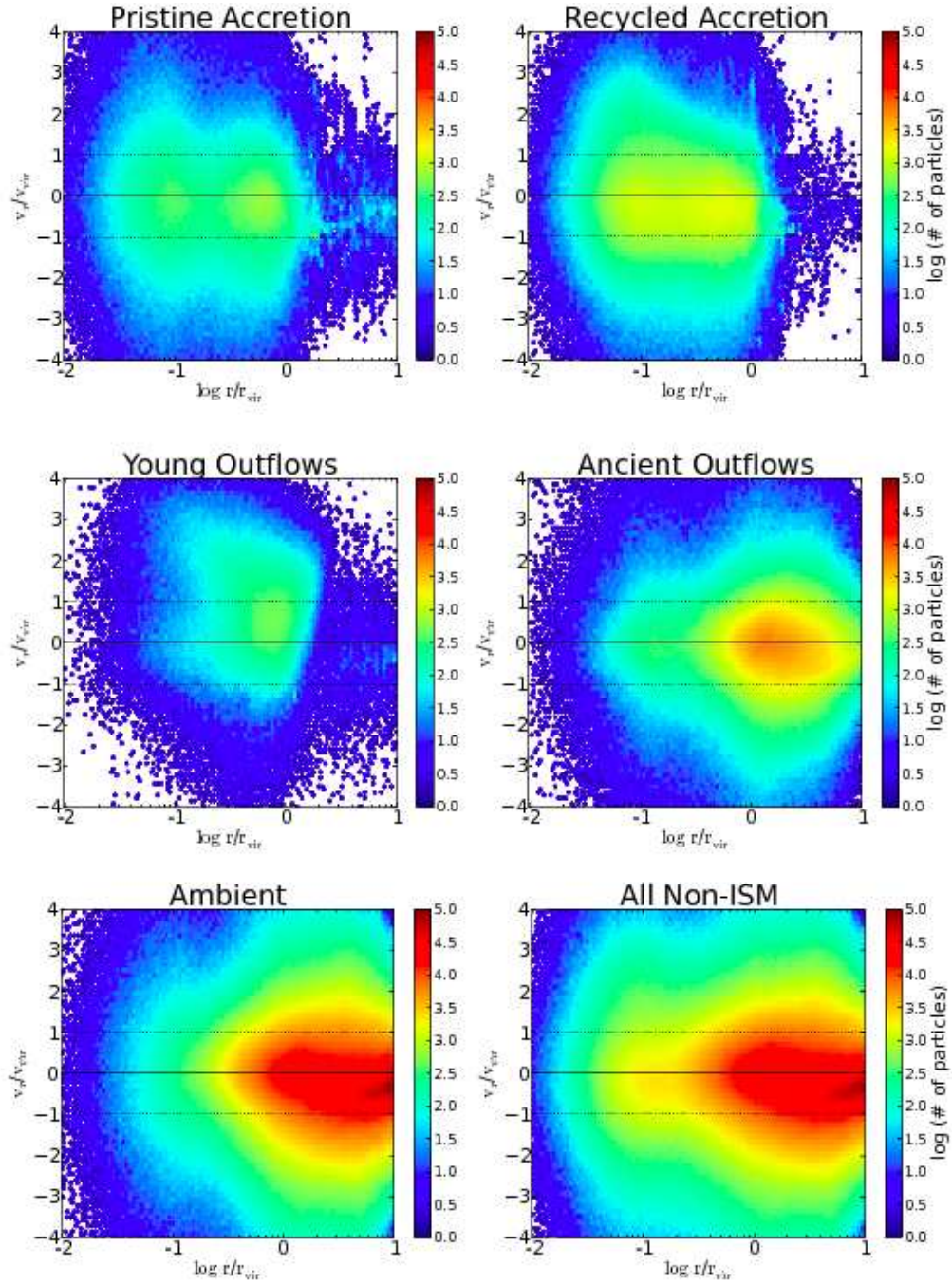


Figure 3.6:  $V \cdot r/\text{abs}(r)$  (divided by the virial velocity) vs. radial distance from the host galaxy (divided by the virial radius), for non-ISM gas at  $z = 0.25$  divided into each of the categories as labelled. To guide the eye, we have added solid horizontal lines at  $v = 0$ , and dotted horizontal lines at  $v = \pm v_{\text{vir}}$ .

some reliable mapping between certain absorption line tracers and whether gas is inflowing, outflowing, or ambient.

#### 3.4.1 Column Density vs. Impact Parameter

In Figure 3.7 we plot the mean column density per line of sight of different species (as labelled) versus impact parameter for galaxies with a halo mass of  $10^{11} M_{\odot}$  (left panels) and  $10^{13} M_{\odot}$  (right panels). We start at 10 kpc, which is the typical extent of the ISM, and go out to 300 kpc, roughly delineating the CGM as argued in Ford et al. (2013a). We compute this by summing the column density within  $\pm 300 \text{ km s}^{-1}$  of the galaxy (for all lines of sight), and then divide by the number of lines of sight. We choose to plot a mean versus a median to promote a fairer comparison with the data, since a median is sensitive to the (often variable) detection threshold. We then subdivide the mean column density by inflow/outflow category. In practice, we create a simulation snapshot containing only gas particles of a given category, obtain absorption spectra using `Specexbin` (Oppenheimer & Davé, 2008), and get column densities by fitting Voigt profiles using `AutoVP` (Davé et al., 1997). The solid black line is for all the gas in the simulation, and the coloured broken lines show the breakdown by category, as indicated in the legend. The solid black line is akin to what an observer would actually see, the coloured lines are what an observer would see if the universe consisted only of gas in the labelled category.

Looking at HI absorption in  $L^*$  halos ( $10^{13} M_{\odot}$ ; top right panel), we see that recycled accretion provides the dominant contribution at impact parameters less than about 75 kpc (all distances are physical). Beyond that, ambient gas and ancient outflows make up the bulk of the absorption. In  $10^{11} M_{\odot}$  halos (top left panel), ambient gas dominates at all impact parameters greater than about 25 kpc, followed by ancient outflows. At very small impact parameters, recycled accre-

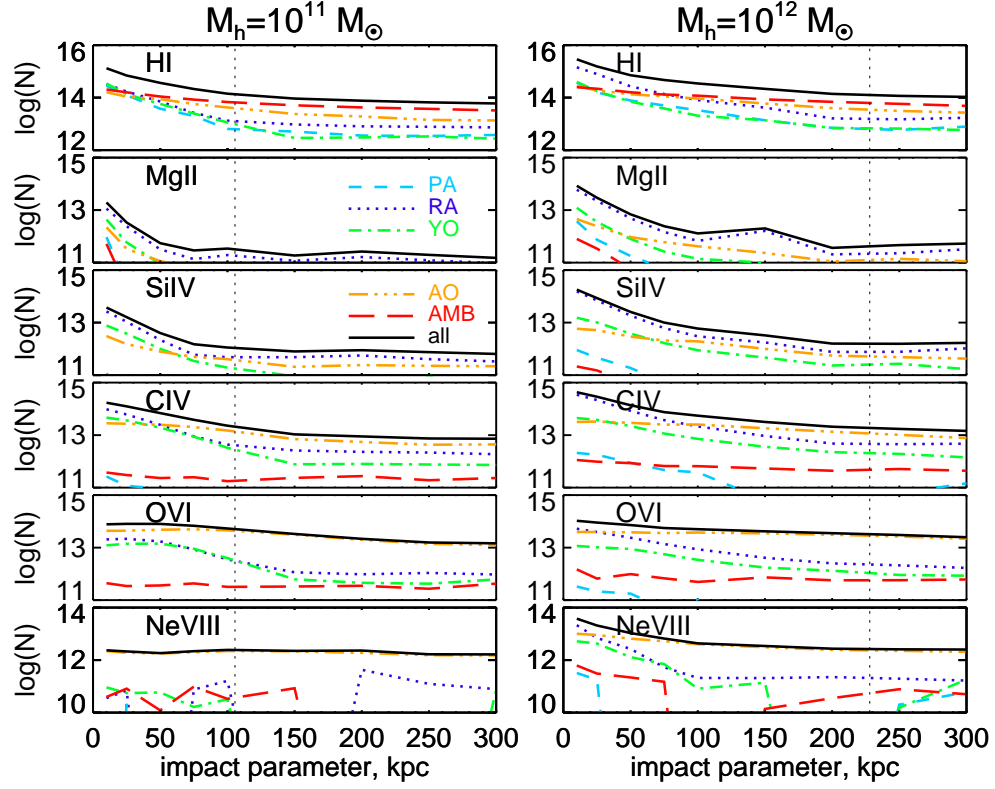


Figure 3.7: The average column density per LOS for targeted lines of sight around  $10^{11} M_{\odot}$  (left panels) and  $10^{13} M_{\odot}$  (right panels) halos for different species (as labelled). The black solid line includes all the gas. Coloured lines indicate results from including only absorption from: pristine accretion (light blue dashed), recycled accretion (dark blue dotted), young outflows (green dot-dashed), ancient outflows (orange dot-dot-dashed), and ambient (red long-dashed). Vertical lines indicate the approximate virial radius at the midpoint of each mass bin. Note the yrange is not the same for each ion, though it always spans 4 dex.

tion also becomes important for low-mass halos. Both theoretical and observational works have claimed that accretion can be probed via high-column density HI lines (Fumagalli et al., 2011; van de Voort et al., 2012; Lehner et al., 2012) and our results support this claim, although in our case we are probing lower column density gas than the Lyman Limit systems (LLS) typically considered in those works. In our case, the typical column density at 25 kpc is  $10^{15} \text{cm}^{-2}$ , which is well below a LLS but strong nonetheless.

For Mg II, the majority of absorption owes to recycled accretion at all impact parameters and at both halo masses. Outflowing material altogether provides a much lower contribution to the absorption; close in, young outflows are more prominent, while beyond 50 kpc ancient outflows contribute more. Low-metallicity gas, i.e. pristine accretion and ambient gas, makes only a negligible contribution. At all impact parameters, Mg II traces gas that will fall into galaxies by  $z = 0$ . Physically, gas in our simulations that is sufficiently cold and dense to give rise to Mg II absorption cannot support itself against gravity, and hence accretes on a dynamical timescale. Thus our simulation indicates a tight connection between Mg II absorption and star formation that occurs within 1-2 dynamical timescales.

The story is similar for Si IV: recycled accretion is the most important source for absorption at all impact parameters and halo masses. However, it is less dominant than in the Mg II case. Once again young outflows dominate the outflow contribution close in, but the crossover point with ancient outflows occurs farther out, at  $\approx 50$  kpc. Hence Si IV, despite its rather high ionisation state, behaves much like Mg II because the typical temperature and density giving rise to Si IV absorption is more similar to Mg II than to that of higher ions (Ford et al., 2013a).

For C IV the behaviour changes somewhat and also becomes more dependent

on halo mass. For  $10^{13}M_{\odot}$  halos at low impact parameters, recycled accretion provides the dominant contribution to the total absorption, but beyond about 100 kpc ancient outflows become the largest contributor. For  $10^{11}M_{\odot}$  halos, within 50 kpc, recycled accretion, young outflows, and ancient outflows all are equally important, while at larger impact parameters ancient outflows dominate, followed by recycled accretion and then young outflows. Hence, depending on the impact parameter and the halo mass, C IV can trace recycled winds, and either young or ancient outflows.

For the high ions O VI and Ne VIII, recycled accretion dominates at small impact parameters in large halos, otherwise ancient outflows dominate. Interestingly, the shape of the black line for the high ions is flatter than for low or mid level ions – the strength of the absorption depends less on the proximity to the galaxy, as noted by Ford et al. (2013a).

Material that has never been in a wind (ambient or pristine accretion) does not provide a significant amount of absorption in metal lines. For H I, however, ambient gas plays a major role, more than any other category at impact parameters  $\geq 100$  kpc (although ancient outflows and recycled accretion are not too far behind). This is not surprising given the huge amount of mass contained within the ambient gas, as seen in Figure 3.3. However, at smaller impact parameters, recycled accretion provides a substantial contribution for H I (for the  $10^{13}M_{\odot}$  halos, it is the dominant contribution). This region typically contains the strongest H I lines (Ford et al., 2013a). Although ambient gas contributes more of the mass budget than recycled accretion (see Fig 3.3), the ambient gas tends to be hot and ionized, as we will show in §5.3. Hence, recycled accretion likely dominates the high-column density H I absorbers at  $z = 0.25$ .

In summary, we see distinct trends in the type of material traced by absorption



as a function of ionisation potential. Low metal ions, particularly close to galaxies, generally arise from recycled accretion, while high ion absorption is from ancient outflows. This latter finding is consistent with the analysis of Tumlinson et al. (2011), who detect large amounts of O VI in the CGM and determine that it must have been generated by protracted earlier epochs of star formation and winds.

### 3.4.2 Fractional Column Density Distributions

Column density distributions (CDDs) provide a more detailed look at the strengths of individual absorbers within our various categories. Figure 3.8 shows the “fractional CDD” for each of our ions, for our two halo mass bins ( $10^{11} M_{\odot}$  left panels,  $10^{13} M_{\odot}$  right panels), at an impact parameter of 25 kpc (upper panels) and 100 kpc (lower panels). The lines are colour-coded by category: pristine accretion (light blue), recycled accretion (dark blue), young outflows (green), ancient outflows (orange), and ambient gas (red). We define fractional CDD as the fraction of the total absorption *in that column density bin* that owes to a given category. Where colored lines do not extend, there are no absorbers in that particular column density bin. In some cases the lines do not add up to one, that is because occasionally there is contribution from ISM gas (not plotted here) to the total. For Ne VIII at 100 kpc, we note that the colored lines overlap in some cases.

In these plots we can identify some general trends as a function of ionisation potential. For H I, there is more strong absorption from recycled accretion than pristine accretion. At impact parameters of 25 kpc in  $10^{13} M_{\odot}$  halos the strongest metal lines are almost always dominated by recycled accretion. The trend is particularly strong for low ions and is even true for O VI, although strong Ne VIII lines have comparable contributions from both young and old outflows. Strong metal absorption at this impact parameter traces material that will fall into the

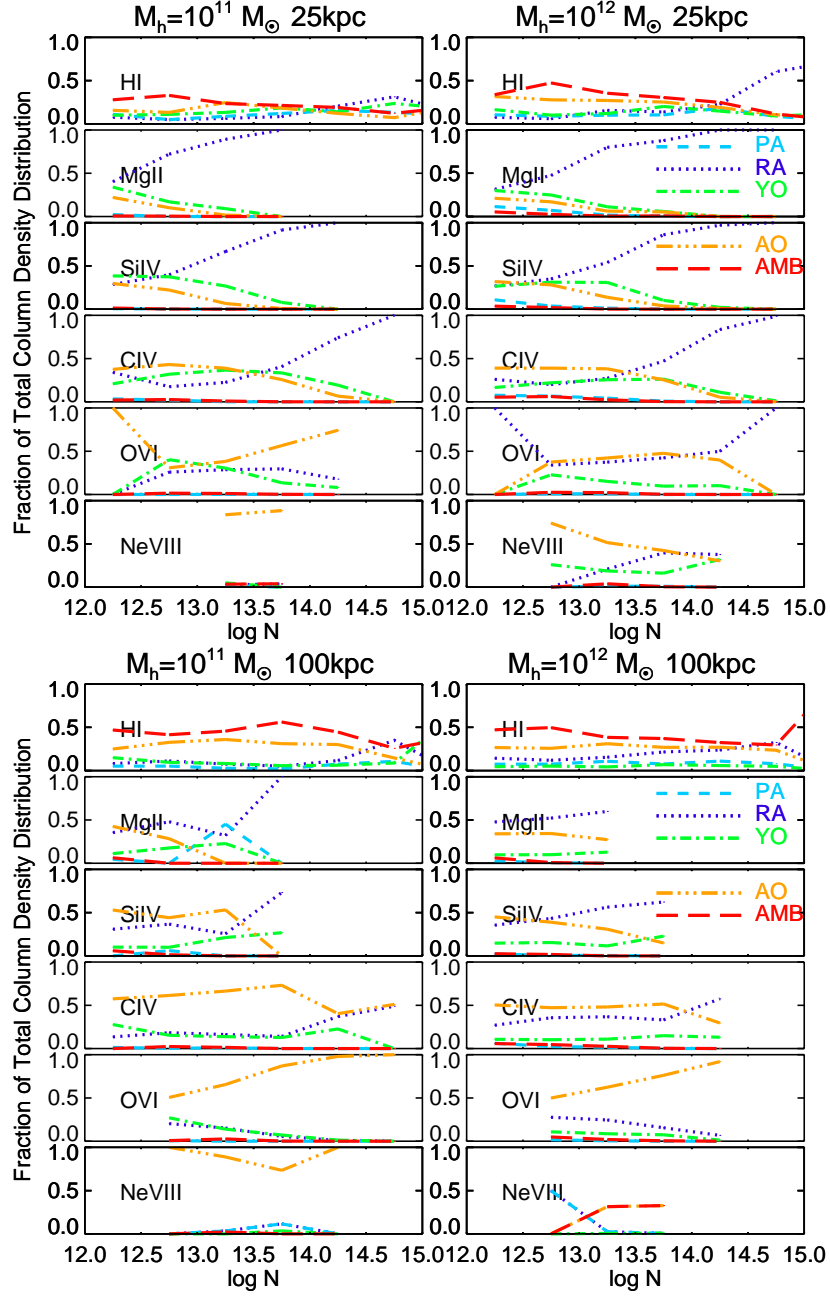


Figure 3.8: Fractional column density distributions, i.e. the fraction of absorption in bins of size  $\log N = 0.5$  owing to the various categories for different species (as labelled) at impact parameters of 25 kpc (top panels) and 100 kpc (bottom panels), for  $10^{11} M_{\odot}$  halos (left panels) and  $10^{13} M_{\odot}$  halos (right panels). Where lines do not extend, there is no column density in that bin from any gas.

galaxy within a few Gyr; just as for the strongest H I absorbers. At lower metal columns outflows become important and can even dominate. Generally young outflows are more important for lower ions and ancient outflows are more important for higher ions. Low column H I absorption owes mostly to ambient gas and less to ancient outflows. These trends also hold for  $10^{11} M_{\odot}$  halos except that ancient outflows now dominate at all columns for the high ions.

At an impact parameter of 100 kpc for  $10^{13} M_{\odot}$  halos, the trends look somewhat different. For low ions the strongest observable metal lines still come from recycled accretion, but the contribution from outflows can be significant at lower columns, and at this larger impact parameter it is almost always ancient outflows that are more important than young outflows. It is likely that the low ions still arise from gas close to galaxies, but perhaps close to substructures such as what is seen in Figure 3.1. In contrast, O VI is completely dominated by ancient outflows, consistent with the findings of Oppenheimer & Davé (2009). Young outflows contribute but do not dominate at any column density. For our mid ion C IV, the main contribution is from ancient outflows except for very strong absorbers around  $10^{13} M_{\odot}$  halos, where recycled accretion is prominent. Meanwhile, the H I is usually dominated by ambient gas with important contributions from ancient outflows for both halo masses with recycled accretion also becoming important at higher columns.

### 3.4.3 Covering Fractions

A key observable is the covering fraction of absorbers down to some particular column density or equivalent width limit. Here we sum all absorbers within  $\pm 300$  km/sec of the targeted galaxy for each of our lines of sight, above an equivalent width limit of  $0.05 \text{ \AA}$ . We use summed equivalent widths rather than individual components to minimize sensitivity to details of the line identification and

deblending algorithm.

Figure 4.4 shows the covering fractions for our various ions, for our two halo mass bins. The total is shown as the black line and can be compared to what is observed. The coloured lines show the theoretical covering fraction including only the gas in the labelled category. Note that the coloured lines do not sum to the black line – we compute the covering fraction of each category individually above our chosen equivalent width limit of  $0.05\text{\AA}$ .

#### HI

has a near-unity covering fraction at all impact parameters and halo masses, owing mostly to ambient gas. Ancient outflows have large covering fractions within  $\sim 100\text{kpc}$  for both halo masses and recycled accretion also becomes substantial for  $10^{13}M_{\odot}$  halos. Pristine accretion and young outflows also have comparable non-trivial covering fractions for both halo masses but it is clearly much smaller than recycled accretion in  $10^{13}M_{\odot}$  halos. Hence even HI does not typically trace pristine inflows in these halos, because as we showed in Fig 3.3, the accreting mass budget is actually dominated by recycled accretion at these epochs. We note, however, that the difference between pristine accretion and ambient gas is whether or not it will accrete onto a galaxy by  $z = 0$ , so some of what is defined as ambient gas may yet become pristine accretion.

As expected, the metal lines almost never show significant covering fractions from either ambient or pristine accretion, as the metal content tends to be quite low. The remaining categories follow trends similar to those seen for the column densities: low ionisation line covering fractions tend to be almost always dominated by recycled accretion, while C IV is dominated by recycled accretion close in but by ancient outflows further out. O VI is dominated by ancient outflows everywhere, except for at very low impact parameters around  $10^{13}M_{\odot}$  halos.

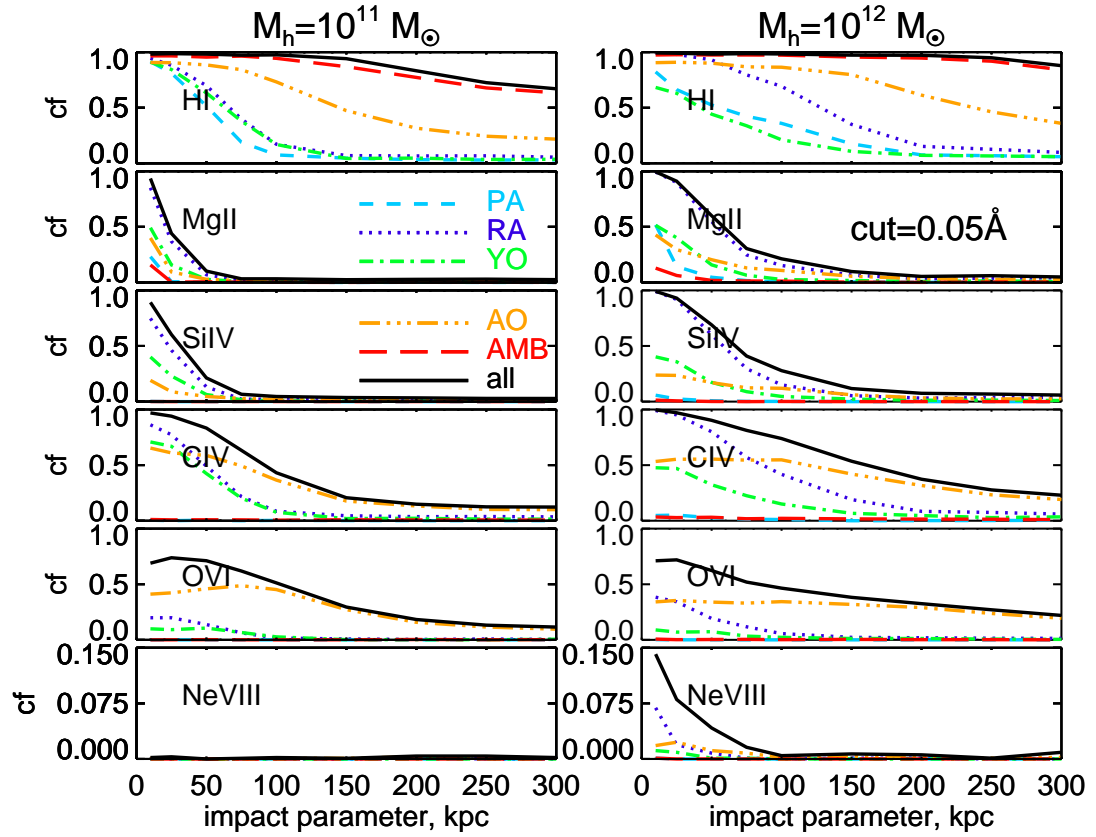


Figure 3.9: Covering fractions for  $10^{11} M_{\odot}$  (left panels) and  $10^{13} M_{\odot}$  (right panels) halos, showing the fraction of sight lines with equivalent widths  $> 0.05 \text{ \AA}$  for the species as labelled. The black line includes all the gas and the broken coloured lines are split into the categories as labelled. Note the different y-axis range for Ne VIII, and note that individual categories are computed separately and do not sum to the black line.

Qualitatively, this trend holds for all halo masses, although the overall metal line covering fraction, particularly at small impact parameters, falls towards smaller halos.

These results are intended to qualitatively illustrate the behaviour of covering fractions, and show that they mimic trends seen in other statistics. We will present a more detailed comparison of covering fractions versus COS-Halos data, including covering fractions as a function of equivalent width, using simulated spectra chosen to match the COS-Halos sample, in an upcoming paper (Ford et al. 2014, in preparation).

### 3.5 Physical Conditions

#### 3.5.1 Mass and metal profiles

To better understand why the absorption patterns detailed in the previous section arise, we now examine the physical conditions in the halo associated with the inflowing and outflowing gas. We begin by considering the mass and metal profiles associated with our various categories. Figure 3.10 shows these profiles as a function of  $R/R_{\text{vir}}$ , out to the virial radius. We emphasize this is a 3-D radial profile, not projected as impact parameter. The left panels show the mass fraction as a function of radius in each category, while the right panels show the metal fractions. The two rows show our two halo mass bins. We include only gas around central galaxies, since our LOS are only around central galaxies. As explained in §3.3, each gas particle is assigned to a galaxy to which it is most bound. If a particle is assigned to a satellite galaxy we do not include it in Figure 3.10.

Let us first consider recycled accretion. Broadly speaking, for both mass bins, the percent of gas mass and metal mass in recycled accretion decreases with increasing  $R/R_{\text{vir}}$ . This soon-to-be recycled material is fairly close to galaxies,

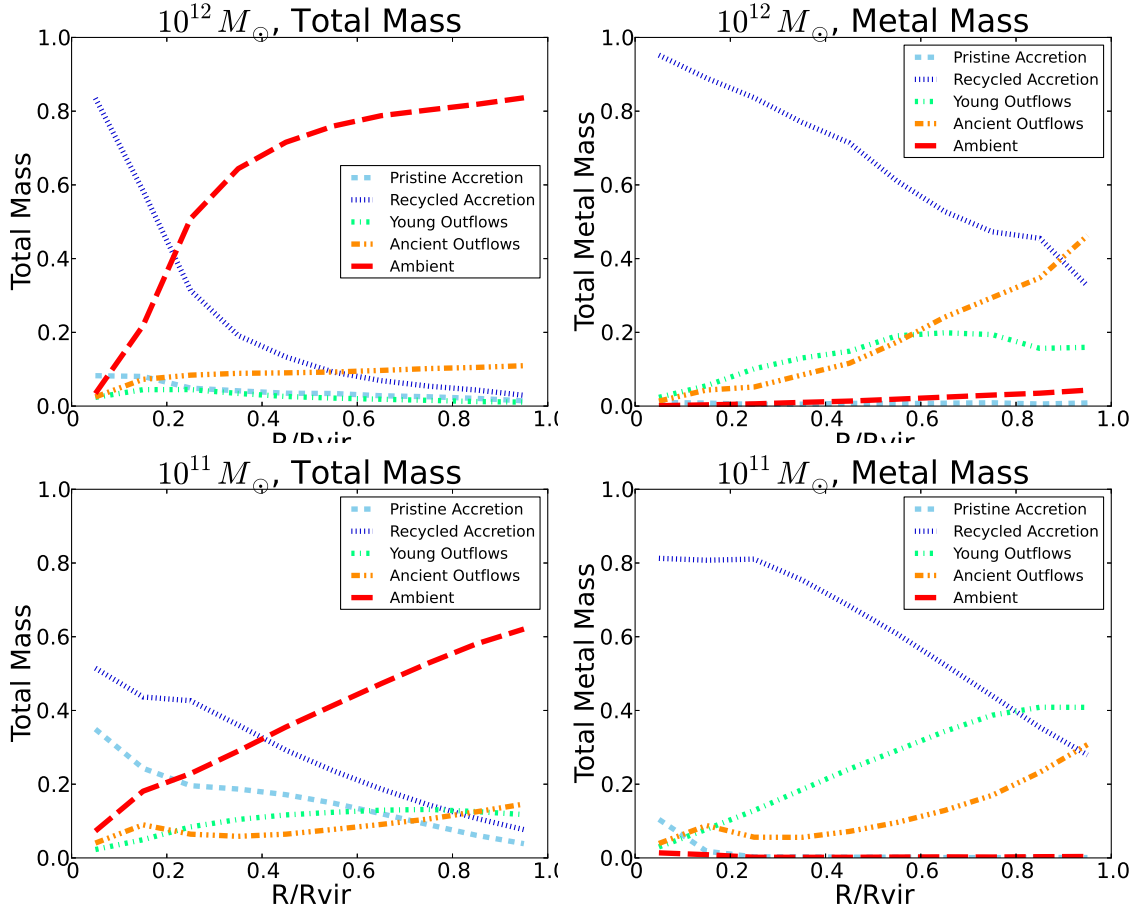


Figure 3.10: Left panels: fraction of the total mass of non-ISM gas particles in various categories as a function of  $R/R_{vir}$  at  $z = 0.25$ , as labelled. Right panels: fraction of the total *metal* mass. Top panels are for  $10^{13} M_{\odot}$  halos and the lower panels are for  $10^{11} M_{\odot}$  halos. Only central galaxies are considered.

which explains why it is predominantly found in cooler, denser gas and explains why HI at low impact parameters comes more from recycled accretion than from ambient gas. In Figure 3.7 we noted that, at least for the more massive halos, metal absorption from recycled accretion is fairly strong close to galaxies, while ancient outflows become more dominant at larger impact parameters. This is why in the case of the  $10^{13} M_{\odot}$  halo at low impact parameters there is substantial absorption in O VI from recycled wind material – because very close to  $10^{13} M_{\odot}$  galaxies, most of the metals are found in recycled accretion material. Hence, even though much of the recycled wind material close to galaxies is cool and dense, the high enrichment level still allows for significant O VI absorption. Meanwhile, the low metal ions have rapidly dropping absorption profiles with radius, while high ions have radial profiles that are more flat. The low metal ions necessarily arise in cool, enriched gas, which typically has a short recycling time. In  $10^{13} M_{\odot}$  halos the recycled accretion is peaked within  $r < 0.3 R_{\text{vir}}$ , while for  $10^{11} M_{\odot}$  it is spread more smoothly out to  $R_{\text{vir}}$ .

For pristine accretion, we see that the percentage of the gas and metal mass also drops with increasing  $R/R_{\text{vir}}$ . The percentage of mass in ambient gas increases with radius, becoming the dominant component at large radii, but the ambient gas contains few metals. The percentage of the gas mass in ancient outflows changes little with radius, but the percentage of the metal mass increases appreciably. The percentage of mass in young outflows is fairly flat with radius but the metal mass rises. These profiles set the baseline for where metals are located within the CGM, which is then convolved with the physical conditions to give rise to the actual amount of absorption.



### 3.5.2 Velocity and kinematics

We can also track the kinematics of our absorbers, as shown in Figure 3.11. In this Figure we focus on Mg II and O VI, as examples of low and high ions. We include only recycled accretion (blue), young outflows (green), and ancient outflows (orange), since the other categories do not contribute significantly to the metal absorption. To measure the kinematics of CGM absorbers relative to their galaxy, we subtract the galaxy’s systemic velocity and plot a histogram of the velocities of the absorbers. Here we show components, not systems, and all absorbers above 30 mÅ are plotted. We show both halo bins,  $10^{11} M_{\odot}$  and  $10^{13} M_{\odot}$ , at impact parameters of 25 kpc and 100 kpc. For comparison we show the approximate escape velocity ( $v_{esc} = \sqrt{2GM/r}$ ) as dashed lines, using the impact parameter (25 kpc or 100 kpc) as the radius and the midpoint of each mass bin as the mass.

For both the  $10^{13} M_{\odot}$  and  $10^{11} M_{\odot}$  halos we see that most of our absorbers lie within the escape velocities of their host halos, at least at these impact parameters, for both Mg II and O VI. We note that for  $10^{13} M_{\odot}$  halos, this is true by definition, as we only consider those absorbers within  $\pm 300 \text{ km s}^{-1}$  as associated with a galaxy, and the escape velocity at these impact parameters is  $\geq 300 \text{ km s}^{-1}$ . However, one can see the distribution trailing off; even if we did not make this cut at  $300 \text{ km s}^{-1}$  it is unlikely we would see significant numbers of absorbers past  $300 \text{ km s}^{-1}$ . In general, the shape of the velocity distributions for the different categories are similar, showing that there is no strong kinematic trend that distinguishes inflow from young or ancient outflow.

### 3.5.3 Phase Space Plots

A key diagnostic of the physical conditions of an absorber is its location in the temperature-overdensity phase space. In Ford et al. (2013a) we extensively exam-

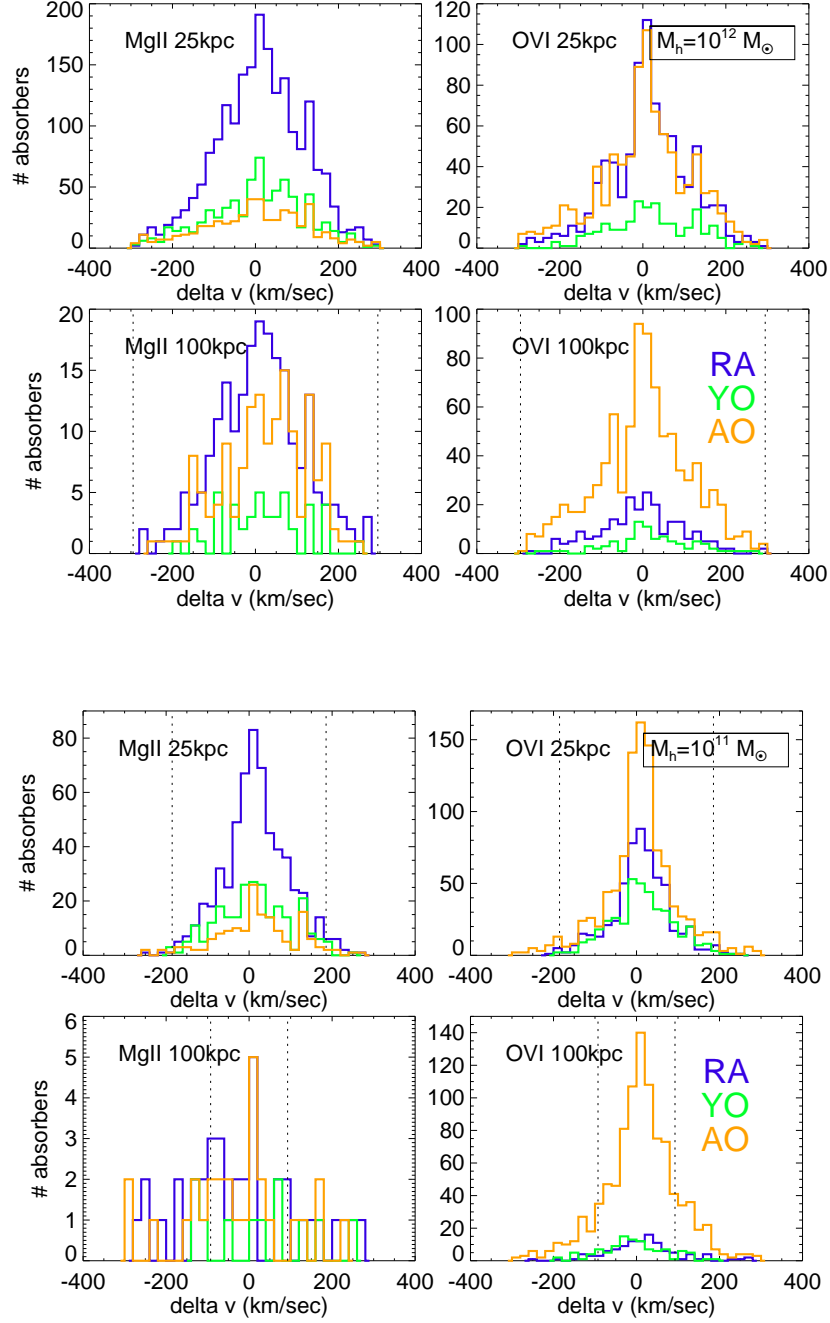


Figure 3.11: Histograms of velocity, relative to the galaxy systemic velocity, of absorbers split into recycled accretion (blue), young outflows (green), and ancient outflows (orange), for Mg II & O VI, at 25 kpc & 100 kpc as labelled for  $10^{13} M_{\odot}$  (top panels) and  $10^{11} M_{\odot}$  (bottom panels) halos. Vertical lines demarcate the escape velocity at the midpoint of each mass bin for  $R=25$  kpc or 100 kpc as labelled. (Escape velocity for  $10^{13} M_{\odot}$  halos at 25 kpc,  $590 \text{ km s}^{-1}$ , is outside the range of the plot). Note the different y-axis range for each panel.

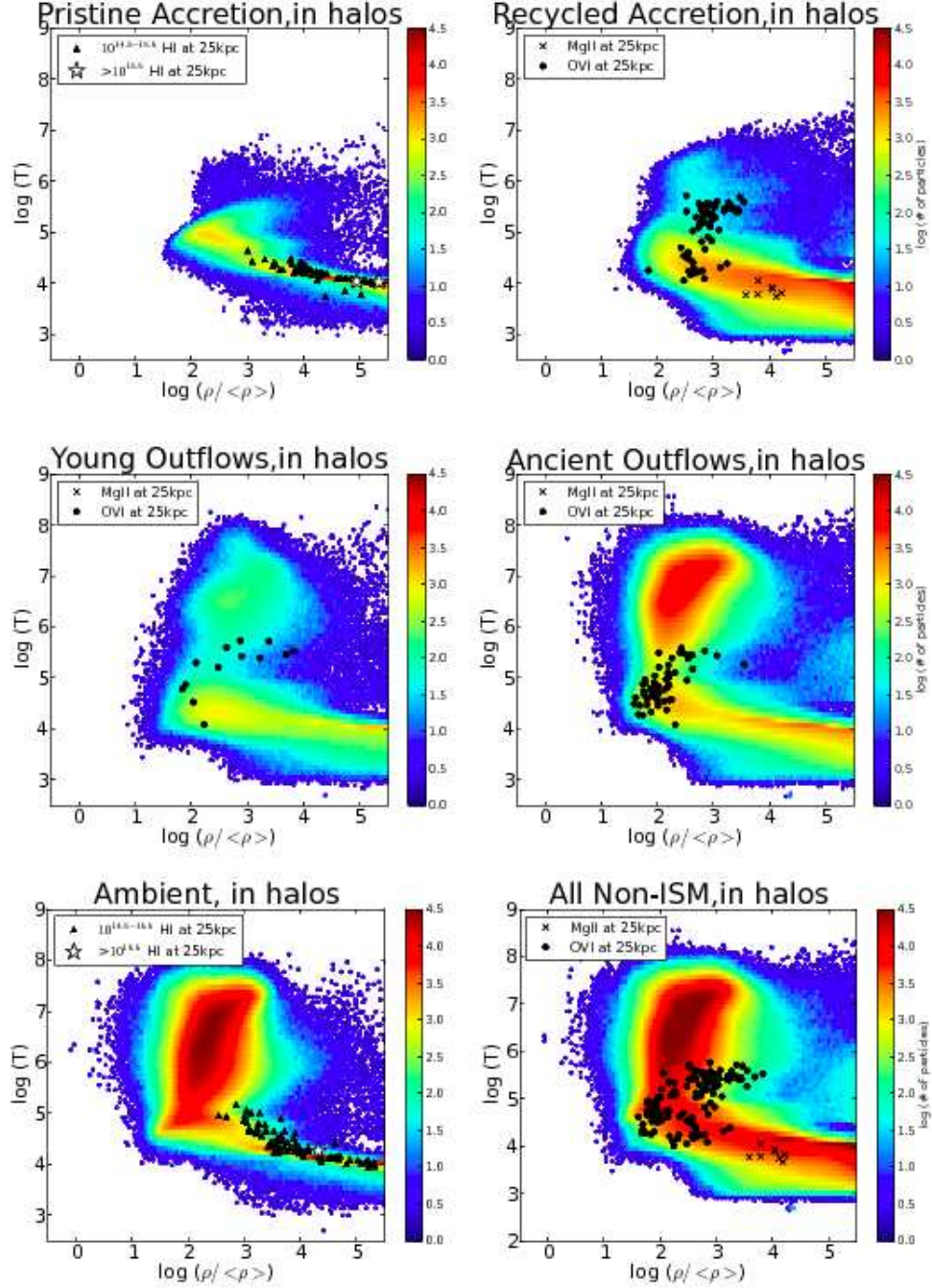


Figure 3.12: Distribution of gas in temperature-density phase space, for our five categories and for all non-ISM gas, as labelled. We overplot the location of strong ( $N > 10^{14}$ ) absorbers of Mg II and O VI in  $10^{13} M_{\odot}$  halos at 25 kpc, for all non-ISM gas, as well as broken out by category for recycled accretion, young outflows, and ancient outflows. In the pristine accretion and ambient panels, where there is no strong Mg II or O VI absorption in  $10^{13} M_{\odot}$  halos at 25 kpc, we overplot the location of H I absorbers of various strengths as labeled. The colourbar is the same in each panel, showing the log number of particles.

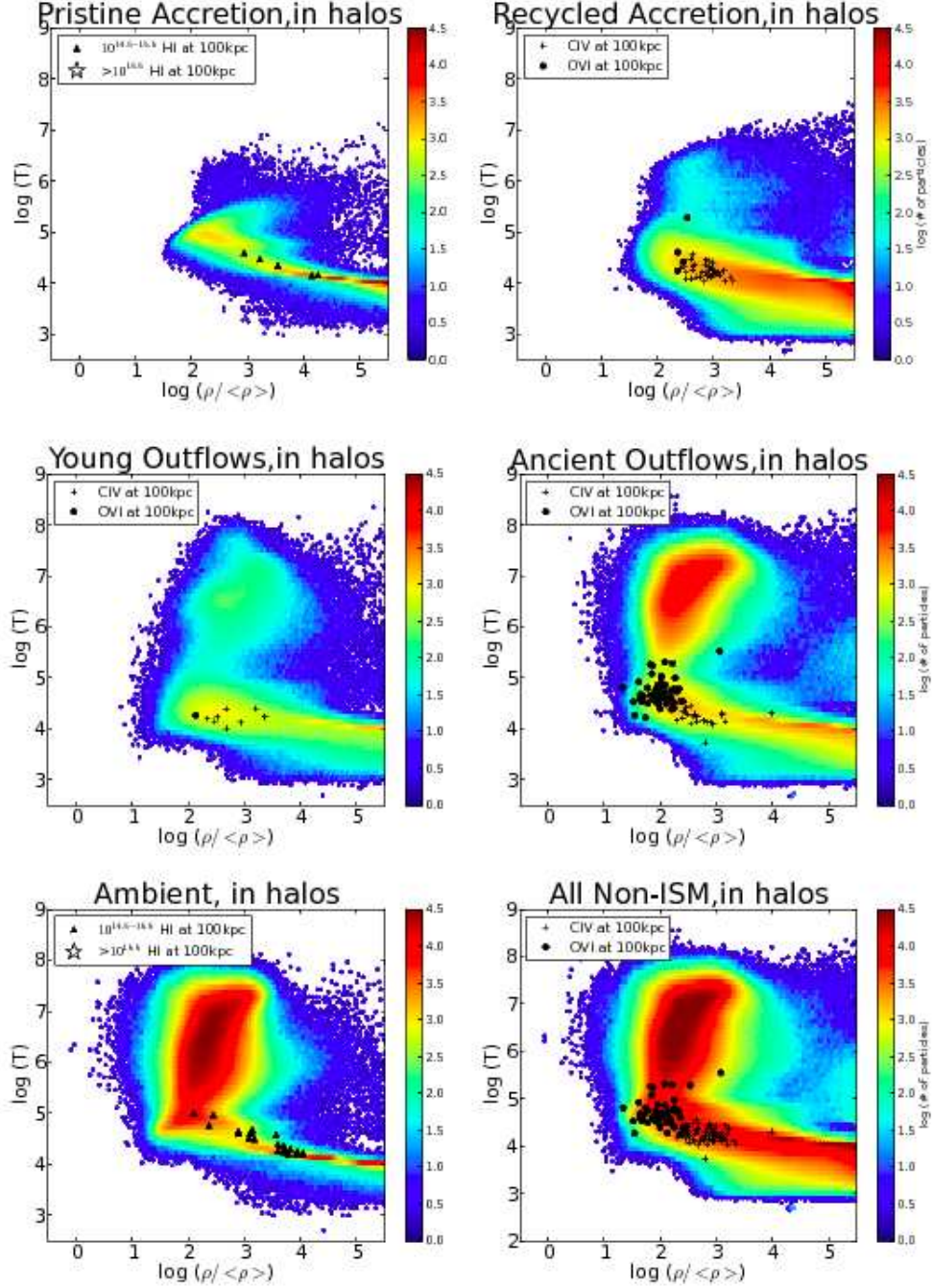


Figure 3.13: Phase space distributions as in Figure 3.12. We overplot the location of strong ( $N > 10^{14}$ ) absorbers of C IV and O VI in  $10^{13} M_{\odot}$  halos at 100 kpc, for all non-ISM gas, as well as broken out by category for recycled accretion, young outflows, and ancient outflows. In the pristine accretion and ambient panels, where there is no strong C IV or O VI absorption in  $10^{13} M_{\odot}$  halos at 100 kpc, we overplot the location of H I absorbers of various strengths as labeled. The colourbar is the same in each panel, showing the log number of particles.

ined the location of absorbers in this phase space using similar simulations. Unsurprisingly, we found that low ionisation potential absorption like Mg II arises in cooler, denser environments, while high ionisation potential absorption such as O VI and Ne VIII exist in warmer, more diffuse environments, with Si IV and C IV being intermediate (see Figure 6 of Ford et al., 2013a). Here we expand on that work by examining where our different inflow/outflow categories lie in phase space, and which absorbers might be tracing such gas. We focus here on Mg II, C IV, and O VI as representative of low, mid, and high ionisation potential lines; other transitions follow trends based on their ionisation potential. We will also examine H I in pristine accretion and ambient gas, since this gas generally gives rise to weak if any metal absorption.

In Figure 3.12, we show phase space contours of halo gas in each category at  $z = 0.25$  (first 5 panels), as well as all non-ISM gas particles (last panel) within halos. The legend for the coloured contours is indicated on the right, showing the logarithmic number density of particles at each position in phase space; for ease of comparison it is the same in all panels, even though not all the categories have the same total number of particles.

In the recycled accretion, young outflow, and ancient outflow panels we overplot, as the black symbols, the location in density and temperature space of Mg II (x's), and O VI (filled circles) absorbers that arise from particles in that category. For clarity, we have only plotted the strong absorbers ( $N > 10^{14} \text{ cm}^{-2}$ ), and only around  $10^{13} M_{\odot}$  halos at impact parameters of 25 kpc. In the pristine accretion and ambient panels, there are no strong Mg II or O VI absorbers around  $10^{13} M_{\odot}$  halos at 25 kpc. Instead, we plot the H I absorbers around  $10^{13} M_{\odot}$  halos at 25 kpc, for the strengths as labelled.

Both pristine (upper left) and recycled (upper right) accretion consist almost

exclusively of cooler ( $T < 10^5$  K) gas. Gas at temperatures  $T > 10^5$  K is unlikely to accrete onto galaxies between  $z = 0.25$  and  $z = 0$ . Nonetheless, there is some recycled accretion gas extending up to hotter temperatures at moderate overdensities ( $\sim 10^3$ ), where the cooling time becomes sufficiently short that gas can radiate away its thermal energy.

Considering metal lines, Mg II absorbers trace the densest recycled accretion gas, typically with  $\delta > 10^4$ , while O VI traces more diffuse and often significantly hotter halo gas. Both O VI and Mg II arise from recycled accretion at 25 kpc, but never from the same phases of this gas! Much of the absorption arises in cooler photo-ionised gas, but the hotter plume of recycled accretion gas mentioned above gives rise to substantial O VI absorption as it transitions through the collisional ionisation fraction maximum for O VI at around 300,000 K. Therefore, we expect a significant amount of collisionally-ionised oxygen arising in halos, though as we argued in Oppenheimer et al. (2012) and Ford et al. (2013a) it is not globally dominant relative to photo-ionised O VI absorption. We emphasize that we have only plotted the strong absorbers here, which for O VI is often collisionally ionised. At 25 kpc there is substantial strong O VI absorption from both recycled accretion and ancient outflows, while at larger impact parameters, it chiefly arises in ancient outflows, (Figure 3.7 and in Figure 3.13 below).

Young and ancient outflows (middle panels) are generally at somewhat lower densities, and they show more significant amounts of gas near the virial temperature. Note that in lower mass halos (not shown as a separate subdivision), there is very little of this hotter gas component (e.g. Kereš et al., 2009). O VI absorption still comes from the same general region in these panels as in the recycled accretion panel: warm, low density gas that is both photo-ionised and collisionally-ionised. Although ancient outflows do have some material roughly

in the right density/temperature range for strong Mg II absorption, we note that close to galaxies there is very little metal mass in ancient outflows, as shown in Figure 3.10.

In the lower panels we see even hotter material in the ambient gas (left panel). This material generally has too low a metal content to provide much strong O VI absorption and, furthermore, it has been shock heated to temperatures that are too high for strong Mg II absorption. It is interesting that most of the O VI absorption in our models comes from infalling or (formerly) outflowing gas, not from ambient halo gas. In part this owes to our definition of ambient gas as never having been in an outflow, so it is very difficult for this gas to become enriched. Nonetheless, this indicates that there may be a substantial amount of warm-hot gas within halos that is not traceable via metal lines, and one must rely on, e.g., broad H I absorbers to characterise this gas (e.g. Richter, 2012).

In Figure 3.13 we show the same coloured regions as in Figure 3.12, but have overplotted absorption at impact parameters of 100 kpc instead of at 25 kpc; at larger impact parameters, ancient outflows dominate the absorption in high ions. Because there is almost no Mg II absorption at 100 kpc, we choose instead to plot C IV with O VI. One can see that O VI comes from warmer, less dense gas, but is rarely collisionally ionized at temperatures  $> 10^5$  K. C IV absorption resides at intermediate overdensities between O VI and Mg II as shown in the previous figure.

These plots help answer the question: why is O VI absorption mostly coming from ancient outflows? It is because ancient outflows have more material at the temperatures and densities favourable for O VI formation (and for the formation of high metal ions in general). Conversely, absorption in the low ions largely comes from cold, dense gas that is likely to accrete, so it arises in the recycled



accretion category rather than the outflow category. Intermediate ions can have significant contributions from recycled accretion, young outflows, or ancient outflows, depending on the impact parameter.

Moving to H I we see that at 25 kpc (Fig 3.12) the strong ( $N > 10^{14.5} \text{cm}^{-2}$ ) H I absorbers for pristine accretion arise at high densities ( $\delta \geq 10^3$ ). In the relation between overdensity and H I column density given by Davé et al. (2010), H I absorbers with  $N = 10^{14.5-15.5} \text{cm}^{-2}$  are predicted to lie at  $\delta = 10^2 - 10^3$ , albeit with substantial scatter. Why does pristine accretion not have absorbers in this overdensity range? The absorbers clearly follow the overall peak of the pristine accretion distribution (red/yellow region), and there is simply not enough pristine accretion material in the that overdensity regime to give rise to H I absorption.

This is different from their distribution in the ambient case, where there is strong H I at not only high overdensities, but also at intermediate overdensities of  $\delta = 10^2 - 10^3$ . This is because there is more mass in ambient material than in pristine accretion material, as shown in Figure 3.10. The strong absorbers in ambient material can lie at  $T > 10^{4.5} \text{K}$ , and there is more spread in the temperatures as well: pristine accretion absorbers are all at temperatures  $T < 10^5 \text{K}$ , while some ambient absorbers arise in hotter gas  $T > 10^5 \text{K}$ , though most are from cooler gas. In both pristine accretion and ambient, the very strong ( $N > 10^{15.5} \text{cm}^{-2}$ ) absorbers (two for pristine accretion, one for ambient) exist at high overdensities,  $> 10^4$ , consistent with the relation given by Davé et al. (2010): stronger H I absorption comes from highest density gas, close to galaxies. Note that if we were to display H I absorbers in the recycled accretion panel, there would be significantly more such strong absorbers at these overdensities.

By 100 kpc (Fig. 3.13), there is much less strong H I and no very strong H I in either category. This is because the overdensity drops with radius, so at larger



impact parameter there is less dense material to give rise to H I absorption. There are more absorbers in ambient than in pristine accretion, because at large radius there is more ambient than pristine material, as seen in Figure 3.10. Like the low/mid metals, H I absorbers generally follow the peak of the gas distribution, excluding areas that are too hot.

Overall, a given metal ion will absorb at similar densities and temperatures across all categories. Whether there is substantial absorption in a given ion from a given category largely depends on how much material in that category lies at the right temperature/density combination for absorption. It is also a function of the total amount of metal mass in a category at a given radius from the galaxy, as discussed in the previous section. Hence in principle, a suite of absorbers spanning a range of ionisation states can probe the full range of physical conditions as a function of radius in the CGM, with the exception of hot unenriched gas.

### 3.6 Numerical Considerations

Our predictions depend on both our physical model of galaxy formation and our numerical implementation of that physical model. Key elements of the physical model include the  $\Lambda$ CDM cosmological framework, the adopted cosmological parameter values, standard hydrodynamic and radiative cooling processes, the star formation prescription, and, critically, the *ezw* wind prescription that sets mass loading factors and ejection speeds. In the absence of winds, different implementations of SPH, adaptive mesh refinement (AMR), and moving mesh hydro simulations show reasonable but not perfect convergence on the mechanisms and rates of galaxy growth. All methods show that halos with  $M \lesssim 10^{11.5} M_{\odot}$  are fed by filaments of cold ( $T \sim 10^4$  K) gas that penetrate far inside the halo virial radius, and that large halos of shock heated gas (typically  $T \gtrsim 10^6$  K) develop only

at higher halo masses (e.g., Kereš et al. 2005, 2009; Ocvirk et al. 2008; Agertz et al. 2009; Brooks et al. 2009; Ceverino et al. 2010; Nelson et al. 2013). This cold-to-hot transition can be understood analytically in terms of the ratio of gas cooling time to the halo dynamical time (Binney, 1977; Rees & Ostriker, 1977; Silk, 1977; White & Rees, 1978; White & Frenk, 1991; Birnboim & Dekel, 2003; Dekel & Birnboim, 2006). In the critical regime near  $10^{12} M_{\odot}$ , there is some disagreement among numerical methods on whether cold filaments persist all the way to the central galaxy (Nelson et al., 2013), though this appears to be a shifting of transition boundaries in mass and redshift rather than a universal difference of behaviour.<sup>1</sup> Another significant difference, probably more important for galaxy growth rates, arises in the density profiles and consequent cooling rates of the shock heated gas component. The entropy-based formulation of SPH (Springel & Hernquist, 2002) implemented in GADGET-2, and thus in our simulation here, appears to be especially effective at maintaining separation of fluids in different phases and reducing cooling of the hot gas component, relative to other formulations of SPH or to the moving mesh code AREPO (Kereš et al., 2009; Nelson et al., 2013).

While numerical differences of this sort would have some quantitative impact on the kinds of predictions presented here, the more important numerical uncertainties have to do with the implementation of galactic winds themselves. As discussed in §2, we follow Springel & Hernquist (2003) in implementing winds via ejection of particles from the star-forming ISM. Because these wind particles tend to be metal-rich, and because they leave the galaxy at ISM temperatures, they typically have short cooling times and remain cold even when they interact with a surrounding hot halo. Wind particles retain their heavy elements by

---

<sup>1</sup>For example, the  $10^{11.5} M_{\odot}$  shown by Nelson et al. (2013) at  $z = 2$  (their figure 7) looks significantly different between GADGET (SPH) and AREPO (moving mesh), but the  $z = 3$  snapshots of the same halo are nearly identical between the two codes (D. Keres 2013, presentation at IAP Colloquium on Origin of the Hubble Sequence).

construction, so there is mixing with the ambient halo gas only to the extent that the particles representing these components become mixed. This behaviour may be a reasonable representation of reality, but it is also possible that instabilities mix wind gas and ambient halo gas on scales below the resolution of our simulation (and perhaps below the resolution of any current cosmological simulations of galaxy formation).

There are strong circumstantial arguments for galactic winds with phenomenology roughly like that of our *ezw* model, including the low observed ratios of stellar mass to halo baryons, the widespread presence of intergalactic and circumgalactic metals, and direct observations and high-resolution simulations of galaxy outflows. We therefore expect that the global mass and metal budgets in our simulation are approximately correct. However, the detailed density and temperature structure of ejected and recycling gas, and therefore the absorption in individual ionic species, is necessarily more uncertain, and our predictions here should be regarded as specific to our physical model and numerical implementation of winds. In future work we will use a wind formulation that incorporates an explicit subgrid model for mixing of metals and exchange of thermal energy between wind particles and their neighbours, which will enable us to investigate a range of possible behaviours. Extensive mixing would blur the distinctions between “outflow” gas and “ambient” gas, and between “recycled” and “pristine” accretion, complicating some of the descriptions we have adopted in this paper. More generally, numerical simulations of stellar feedback and the baryon cycle are in a phase of rapid progress, with an increase in the sophistication of models and the range of numerical approaches. We expect that comparison of results from different simulations, and comparison of these results to rapidly improving observations of circumgalactic gas and galactic outflows, will

lead to numerous insights and much progress over the next several years.

### 3.7 Conclusions

We examine the physical and dynamical state of gas around galaxies in a  $32h^{-1}\text{Mpc}$ , quarter-billion particle cosmological hydrodynamic simulation. We concentrate on  $z = 0.25$ , and use past and future simulation snapshots to delineate which particles have been ejected from galaxies (and how long ago), which particles are falling into galaxies by  $z = 0$ , whether or not they have previously been part of a galaxy’s ISM, and which particles are ambient material not participating in the baryon cycle. We use these categories to examine both observable and physical properties of the gas, to elucidate a connection between observational absorption line probes of the CGM and its dynamical state, i.e. whether it is inflowing, outflowing, or ambient. As in our earlier simulations Oppenheimer et al. (2010), recycled accretion of enriched gas that is ejected in winds and then re-accreted plays a major role in low-redshift galaxy accretion.

Our main findings are as follows:

1. Most of the absorption of low-ionisation potential metal species owes to enriched material that will fall back into galaxies within a few Gyr. This occurs because low-ionisation species preferentially trace cold, dense, enriched environments, and hydrodynamic interactions generally cannot prevent this gas from accreting.
2. Most of the absorption of high-ionisation potential metal species owes to outflows ejected much earlier than the present epoch, “ancient outflows”. This occurs because high-ionisation potential species tend to be prominent in warmer, more diffuse environments. Some of this high-ionization material is also re-accreting onto galaxies.

3. The metal mass fraction in recycled accretion drops off steeply with  $R/R_{vir}$  (see Figure 3.10), which gives rise to a rapid drop in absorption with impact parameter for low ions. The metal mass in ancient outflows increases mildly with  $R/R_{vir}$ , which partly explains why the absorption profile of the high ions stays relatively flat out to the virial radius.
4. Low-mass halos ( $<10^{11.5} M_{\odot}$ ) have a greater proportion of recycled material than high-mass halos ( $>10^{11.5} M_{\odot}$ ). Even though high-mass halos assemble proportionally more of their mass via recycled accretion than pristine accretion (Oppenheimer et al., 2010), recycled accretion represents a proportionally larger fraction of the circumgalactic medium around low-mass halos.
5. Where absorption of a given ion is found, that absorption exists at roughly similar densities and temperatures among the various categories. Hence, absorbers with a range of ionisation potentials can broadly trace out the density and temperature structure of the CGM. The strengths of various absorption lines within various inflow/outflow categories primarily reflects the phase space location and metallicity of the gas in those categories.
6. HI predominantly traces non-accreting material that has never been in a wind, i.e. “ambient”. Ambient material holds the majority of mass in the halo and is quasi-spherical, which is why it dominates the HI absorption and produces a high covering fraction out to the virial radius. There is more strong HI from recycled accretion than pristine accretion, although some ambient material may accrete and become pristine accretion.
7. Accreting material is not unenriched. Recycled accretion dominates the mass and metal budget of accreting material, and this component is sig-

nificantly enriched.

8. Mg II provides a good tracer of accreting material that was once in a wind (“recycled accretion”). Virtually all strong Mg II absorbers arise in this category of gas. Si IV, despite its high ionisation level, behaves more like Mg II than a high ion.
9. C IV represents an intermediate ion. At small impact parameters it mostly arises in recycled accretion, but at larger impact parameters it mostly arises from ancient outflows. The crossover impact parameter is  $\sim 100$  kpc in  $L^*$  halos, and moves to smaller impact parameters for smaller halos; for our lowest mass halos, C IV predominantly arises in ancient outflows at all impact parameters.
10. O VI and Ne VIII almost exclusively trace ancient outflows, at nearly all impact parameters and halo masses (very small impact values around  $10^{13} M_\odot$  halos being the exception). A substantial fraction of strong O VI halo absorbers come from transition gas at  $\sim 300,000$  K and is cooling out of hot gas near the virial temperature. Photoionised gas at  $\sim 10^4$  K also contributes many O VI absorbers, and most of the absorbers at impact parameters  $\geq 100$  kpc, in agreement with Oppenheimer & Davé (2009).
11. In small halos the majority of the accreting mass at  $z = 0.25$  is ejected back into a wind by  $z = 0$ , with only about a quarter of the mass remaining as stars or in the ISM. In larger halos, by  $z = 0$  the accreting mass is split evenly between stars, ISM gas, and gas re-ejected as a wind.
12. With our definition of accretion (at  $z = 0.25$ ) as any gas that will join a galaxy by  $z = 0$ , velocity is not very useful for distinguishing accreting gas

from outflowing gas. The radial velocity distribution of gas in the recycled accretion, young outflow, and ancient outflow categories is very similar, with the exception that material moving at high outward velocities at small radii does tend to be recently ejected material.

13. Accreting material is not necessarily parallel to the disk, and outflowing material is not necessarily perpendicular to the disk.
14. Of gas not in the ISM at  $z = 0.25$ , 86% of the mass and 6% of the metal mass has never been in a wind by  $z = 0$ .

By decomposing our simulated gas distribution into inflows and outflows, we better understand how the material in the CGM by  $z = 0.25$  arose, and what its eventual fate is. These results underscore the dynamic nature of the CGM, including how much material is participating in the “baryon cycle”, particularly in halo fountains. This means that accreting material is often enriched, and inflows can be traced using metal lines. We emphasize that low ions trace fundamentally different gas (cold, dense, accreting) than high ions (warm, diffuse, from ancient outflows not accreting), and that inflows and outflows have different distributions both in physical and temperature-density phase space. While there is often co-location of gas in various phases giving rise to both low and high ions, it is dangerous to assume that it arises in a single-phase gas. H I has more strong absorption from recycled accretion than pristine accretion, which simply reflects the fact that recycled accretion is dominating the inflow mass budget at low redshifts in our models.

There are clear observational diagnostics amongst ambient material, inflows, and outflows, and even between young ( $\leq$  Gyr) and ancient ( $>$  Gyr) outflows. In general H I traces ambient material, Mg II and Si IV trace recycled accretion, C VI

traces both recycled accretion and ancient outflows depending on impact parameter, with O VI and Ne VIII tracing ancient outflows. We also find differences between low ( $<10^{11.5} M_{\odot}$ ) and high ( $>10^{11.5} M_{\odot}$ ) mass halos, because high-mass halos suppress infall owing to their higher halo gas temperatures. Assembling these diagnostics into a full census of CGM gas remains a work in progress, but these results can aid in interpreting and understanding absorption-line observations of the CGM.

This paper is the second in a series (Ford et al., 2013a, being the first) to confront successful models for galaxy-IGM coevolution with absorption line observations of CGM gas. With direct comparisons to observations from COS soon forthcoming, and ongoing improvements to our simulation methodologies, we hope to answer such questions as “what is the most realistic description for outflows in simulations?”, “what is the phase space structure of the CGM, and how patchy is it?”, “how well mixed are the metals?”, “what fraction of outflows end up bound to the halo?” and “how tightly are the CGM and its host galaxy linked?”. Through these types of investigations, we aim to further constrain our simulations while gaining additional insights into the CGM and the dominant physical processes that impact it.

### 3.8 Acknowledgements

We thank Jason Tumlinson, Molly Peeples, Cameron Hummels, and Annalisa Pillepich for useful discussion. Partial support for this work came from NASA ATP grants NNX10AJ95G and NNX12AH86G, HST grants HST-GO-11598 and HST-GO-12248, NASA ADP grant NNX08AJ44G, NSF grants AST-0847667, AST-0907998, AST-0908334, and AST-133514, and the South African National Research Chairs program. The simulations used here were run on computing facilities



owned by the Carnegie Observatories. Computing resources used for this work were made possible by a grant from the the Ahmanson foundation, and through grant DMS-0619881 from the National Science Foundation.

## CHAPTER 4

BARYON CYCLING IN THE LOW-REDSHIFT CIRCUMGALACTIC MEDIUM: A  
COMPARISON OF OBSERVATIONS TO SIMULATIONS

This chapter has not yet been submitted but we will soon be sending it to coauthors for approval. Coauthors on this chapter include **Jessica K. Werk** (Astronomy Department, University of California Santa Cruz), **Romeel Davé** (University of the Western Cape, Bellville, Cape Town 7535, South Africa; South African Astronomical Observatories, Observatory, Cape Town 7925, South Africa; African Institute for Mathematical Sciences, Muizenberg, Cape Town 7945, South Africa; Astronomy Department, University of Arizona, Tucson, AZ 85721, USA), **Jason Tumlinson** (Space Telescope Science Institute), **Jason X. Prochaska** (Astronomy Department, University of California Santa Cruz), **Benjamin D. Oppenheimer** (Leiden Observatory, Leiden University, PO Box 9513, 2300 RA Leiden, Netherlands; CASA, Department of Astrophysical and Planetary Sciences, University of Colorado, Boulder, CO 80309, USA), **Molly Peeples** (Space Telescope Science Institute), **Neal Katz** (Astronomy Department, University of Massachusetts, Amherst, MA 01003, USA), **Juna A. Kollmeier** (Observatories of the Carnegie Institution of Washington, Pasadena, CA 91101, USA), **Robert Thompson** (Astronomy Department, University of Arizona, Tucson, AZ 85721, USA) and **David H. Weinberg** (Astronomy Department and CCAPP, Ohio State University, Columbus, OH 43210, USA), and other members of the COS-Halos team.

## Abstract

We analyze the low-redshift ( $z \approx 0.2$ ) circumgalactic medium by comparing observations from the COS-Halos absorption line data set to absorption around a matched galaxy sample from two cosmological hydrodynamic simulations with different prescriptions for galactic outflows, namely hybrid energy/momentum driven wind (ezw), and constant winds (cw). We compare direct observables including equivalent widths per unit redshift, median equivalent widths, covering factors, ion ratios, and kinematics. Our simulations are generally in good agreement with all these observations, with occasional interesting exceptions. The two outflow models are not discriminated by the observations, even though they result in substantially different phase distribution and kinematics of halos gas. We show that this similarity owes mainly to our comparison here at fixed stellar mass rather than at fixed halo mass, which suggests that CGM properties are more closely tied to the stellar mass of galaxies rather than halo mass. The modest discrepancies that are seen between models and data suggest that they predict too much cool gas containing metals and not enough hot gas, and/or that the metals are not sufficiently well-mixed, which probably reflects our model assumption of ejecting outflows as cool and unmixing gas. We further examine the baryon cycle in each simulation, and show that the ezw model has twice the fraction of halo gas participating in the baryon cycle as cw. At impact parameters of  $\lesssim 50$  kpc, recycling winds dominates the absorption of low ions and even H I, while O VI almost always arises from metals ejected long ago. These results highlight the

ability of absorption line data around galaxies such as COS-Halos to inform models for how outflows operate, and provides useful intuition about interpreting the physical and dynamical state of observed CGM gas.

## 4.1 Introduction

The circumgalactic medium (CGM) represents a key unexplored area for galaxy formation studies. In this tenuous multi-phase gas that surrounds galaxies lies clues to the primary processes that drive galaxy evolution such as gaseous inflows and outflows (e.g. Kereš et al., 2005; Dekel et al., 2009; Davé et al., 2012; Lilly et al., 2013). Studying the CGM is therefore an emerging frontier of galaxy evolution that connects galaxies to the intergalactic medium via such baryon cycling processes.

Recent pioneering observations with *Hubble's* Cosmic Origin Spectrograph (COS) have characterized the CGM in unprecedented detail. We now know there can be more oxygen in the halos around star-forming galaxies than inside them Tumlinson et al. (2011), that the CGM likely holds the missing baryons and missing metals Werk et al. (2014), and that star-forming and passive galaxies have different O VI signatures Tumlinson et al. (2011). Recent work by Stocke et al. (2013) and Tripp & Song (2012) has also used COS to probe the CGM out to several hundred kiloparsecs, and observations by Prochaska et al. (2011); Rudie et al. (2013) have established a characteristic extent of the metal-enriched CGM to be very roughly  $\sim 300$  kpc. In addition to these observations that characterize the CGM, there is a wealth of observational data detecting outflows at a variety of redshifts (Martin, 2005; Rupke et al., 2005; Tremonti et al., 2007; Weiner, 2009; Rubin et al., 2012; Pettini et al., 2001; Steidel, 2001; Veilleux et al., 2005), indicating that most if not all galaxies drive winds at some point in their evolution, enriching the CGM and IGM with mass and metals in the process.

The physical mechanisms that drive these outflows are not well characterized. While observations can probe individual sight lines around individual galaxies, we do not yet have an overall picture of the metallicity, covering factor, and phase

of the outflowing material. We have poor knowledge of how these quantities vary with the galaxy’s mass, star formation rate, environment, or redshift. What exactly happens to the winds after they leave the galaxy is also still not well constrained. Simulations suggest the presence of “halo fountains” , where baryons are ejected from the galactic disk only to rain back down again, but the details of this “outside-in” enrichment (Oppenheimer et al., 2012) can vary in simulation according to the prescription input for wind model. The relative contribution of this “recycled accretion”, versus inflows that come in pristine from the IGM, at the very least depends on galaxy mass and impact parameter (Ford et al., 2013b), if not star formation rate, environment, and the mechanism by which winds are launched.

To make progress, we would like to better constrain outflow mechanisms by comparing carefully to rapidly-accumulating observations of CGM gas, and to connect these observations to how the baryon cycle operates in different outflow models. This is the primary aim of this work. We build upon earlier work by (Tumlinson et al., 2011, 2013; Werk et al., 2012; Ford et al., 2013a,b) by carefully comparing observations and simulations to better constrain the CGM at low redshift. The primary data set we employ is COS-Halos (Tumlinson et al., 2013), which is a galaxy-selected study of hydrogen and metal absorption at impact parameters of  $\lesssim 150$  kpc towards 44 galaxies at  $z \sim 0.2$ . The primary simulations we employ include several prescriptions for galactic outflows, so that we can test our sensitivity to this key input parameter against the latest data. While this is not an all-encompassing comparison of all available models to all available data, this work serves as a template for such comparisons to highlight how observations such as COS-Halos can constrain the physical processes driving the baryon cycle.

Our paper is organized as follows: in §2 we discuss our observational methods, in §3 we describe our simulations, in §4 we compare direct observables, in §5 we describe variations with wind model including variations in baryon cycling, in §6 we compare inflows and outflows in simulations to observed quantities, and in §7 we summarize our conclusions.

## 4.2 COS-Halos Data Set

We draw our observational sample from the COS-Halos data set, described in detail in Tumlinson et al. (2011, 2013); Werk et al. (2012, 2013). The main motivation behind COS-Halos is to characterize the CGM and understand its role in galaxy formation. Because COS is more sensitive than its predecessors, COS allows for better selection of sight lines based on galaxy population. Indeed, a main difference between COS-Halos and previous QSO absorption-lines studies is that galaxies are chosen in advance of absorbers but without spectroscopic redshifts. The galaxies in the COS-Halos data set were also chosen to be somewhat isolated, as described in further detail in Tumlinson et al. (2013).

COS-Halos observed 39 quasars within the projected CGM around 44 galaxies with  $0.1 L^* < L < 3 L^*$  at  $z \approx 0.2$ . These galaxies have stellar masses ranging from  $10^{9.5-11.5}$ , with photometric redshifts  $z_{phot} \approx 0.15 - 0.4$  and a range of  $(u-r)$  color. They are between 15 and 160 kpc (projected) from a background, UV-bright quasar. The signal-to-noise is between 7-15 per resolution element (FWHM  $\approx 15$  km s $^{-1}$ ). The ions covered by COS include H I 1216, Si II 1260, C II 1335, Si III 1206, Si IV 1394, and C III 977. These ions span a range of ionization energies, as given in Table 4.1. Each ion has a unique detection threshold, also given in Table 4.1. The COS-Halos sight lines were supplemented by Keck/HIRES echelle spectra for 35 quasars, to include coverage for Mg II (2796, 2803Å) for galaxies at  $z > 0.1$ . The

Keck/HIRES data has higher spectral resolution and generally higher S/N than the COS data.

### 4.3 Simulation Methods

#### 4.3.1 The Code and Input Physics

For this paper we use our modified version (Oppenheimer & Davé, 2008) of the N-body+entropy-conserving smooth particle hydrodynamic (EC-SPH) code GADGET-2 (Springel, 2005), more fully described in Oppenheimer & Davé (2008). Our main simulation is identical to that used in Davé et al. (2013); Ford et al. (2013b), and further details can be found there. Briefly, we assume a WMAP-9 concordant  $\Lambda$ CDM cosmology (Hinshaw et al., 2009):  $\Omega_M = 0.28$ ,  $\Omega_\Lambda = 0.72$ ,  $h = H_o/(100 \text{ km s}^{-1} \text{ Mpc}^{-1}) = 0.7$ , a primordial power spectra index  $n = 0.96$ , an amplitude of the mass fluctuations scaled to  $\sigma_8 = 0.82$ , and  $\Omega_b = 0.046$ . The volume is  $32h^{-1} \text{ Mpc}$  on a side with  $512^3$  gas particles and  $512^3$  dark matter particles. The gas particle mass is  $4.5 \times 10^6 M_\odot$ ; dark matter particle mass is  $2.3 \times 10^7 M_\odot$ . The main simulation snapshot we use for this work is at  $z = 0.25$ , the closest snapshot we have to the redshifts in the observational data set.

This simulation includes galactic outflows, which are tied to the star formation rate (SFR),  $\dot{M}_{wind} = \eta \times \text{SFR}$ , where  $\eta$  is the mass loading factor. For this work we select two wind models to study in detail. The first is our hybrid energy/momentum driven winds or “ezw” model. This model is our favoured wind model because it most accurately captures the relevant small-scale physics associated with the transition from momentum-driven winds to energy-driven winds at low masses (Hopkins, 2013), as well as reproducing observations of the stellar and HI mass functions (Davé et al., 2013). In the ezw model, the wind speed and mass loading factor depend on the galaxy velocity dispersion  $\sigma$ :



$$v_w = 3\sigma\sqrt{f_L - 1} \quad (4.1)$$

$$\eta = \sigma_o/\sigma, \text{ if } \sigma > 75 \text{ km s}^{-1} \quad (4.2)$$

$$\eta = (\sigma_o/\sigma)^2, \text{ if } \sigma < 75 \text{ km s}^{-1} \quad (4.3)$$

Here,  $f_L=[1.05,2]$  is the luminosity in units of the Eddington luminosity required to expel gas from a galaxy potential.  $\sigma_o = 150 \text{ km s}^{-1}$ , and  $\sigma$  is the galaxy's internal velocity dispersion, broadly constrained to match IGM enrichment at high redshift (Oppenheimer & Davé, 2008). This simulation also includes a prescription for quenching, described in further detail in Davé et al. (2013); Ford et al. (2013b).

Our second wind model is a constant wind (“cw”) model, where the mass loading factors and wind speeds are the same for each galaxy, regardless of mass. In the cw model,  $\eta = 2$  and  $v_w = 680 \text{ km s}^{-1}$ . The latter is similar to that used in the Overwhelmingly Large Simulations (OWLS) reference model of Schaye et al. (2010). The cw simulation used here has the same physics described in Ford et al. (2013a), including Wiersma et al. (2009a) metal-line cooling, but with a different box size (here,  $32h^{-1} \text{ Mpc}$ ) and resolution (here,  $512^3$  dark matter and  $512^3$  gas particles). This allows for consistency with the “ezw” model above, and allows us to resolve galaxies similar in size to those in the COS-Halos dataset.

The constant wind model is not our favored model. It is in worse agreement with measurements of C IV at high redshift (Oppenheimer & Davé, 2006) and the mass-metallicity relation (Finlator et al., 2008; Davé et al., 2011b). However, it has not yet been tested against the COS-Halos data set at low- $z$ . We include this wind model because it serves as a useful contrast to the variable ezw wind model. Through this comparison we can comment on not just *whether* winds

are necessary to match observations, but *what type* of winds are necessary. We can also gain insight into how baryons cycle in the different wind models, how they affect the gas around galaxies, and how such processes are manifested in observations.

#### 4.3.2 Generating Spectra With Specexbin

Once we run our simulations, we use SPECEXBIN to calculate physical properties of the gas along lines of sight. SPECEXBIN is described in more detail in Oppenheimer & Davé (2006), but briefly, it averages physical properties of the gas along a given sight line and then uses look-up tables calculated with CLOUDY (Ferland et al., 1998, version 08.00) to find the ionisation fraction for the relevant ionic species. We use the same version of SPECEXBIN as in Ford et al. (2013a,b). See Figure 1 of Ford et al. (2013a) for an example of a simulated spectrum.

We choose our lines of sight (LOS) in our simulations to best mimic the LOS in the COS-Halos data set. Each COS-Halos LOS has a stellar mass and impact parameter  $b$ . For each LOS, we select all the central galaxies in our simulations that are within  $\pm 0.125$  dex in stellar mass of the observed points. Once those galaxies are selected, we produce four LOS at the specified impact parameter,  $x+b$ ,  $x-b$ ,  $y+b$ ,  $y-b$ , that matches the COS-Halos LOS. Due to variance in the halo mass function, not every impact parameter has the same number of LOS. Once the model LOS are selected and run, we use the Voigt profile fitter AUTOVP (Davé et al., 1997) to generate artificial spectra (see Ford et al. (2013a) for an example) and fit column densities and equivalent widths. For consistency with observations we consider all components within  $\pm 600 \text{ km s}^{-1}$  to be associated with a galaxy, and sum them for a total equivalent width, unless otherwise stated. We note that this differs from our approach in earlier work Ford et al. (2013a), where we only considered components within  $\pm 300 \text{ km s}^{-1}$  to be associated with a

Table 4.1: Ion Properties

Ion	Energy (eV)	Detection Threshold ( $\text{\AA}$ )
H I	13.6	0.2
Mg II	15.04	0.1
Si II	16.35	0.15
C II	24.38	0.08
Si III	33.49	0.1
Si IV	45.14	0.1
C III	47.89	0.25
O VI	138.1	0.1

galaxy. However, as shown in Figures 8 and 15 of that work, the absorption drops off substantially after  $\pm 300 \text{ km s}^{-1}$ , so there is little difference between these two limits, and we prefer here to mimic the procedure applied to the COS-Halos data set.

We choose a suite of ions to examine for this work, to get the fullest possible information on the physical conditions of the CGM. As found in earlier work, Werk et al. (2012); Ford et al. (2013a,b), a range of ionisation potentials are necessary to probe different phases of the CGM. Generally, low ionization potential metal lines probe high density, low temperature regions close to galaxies, while high ionization potential metal lines probe warmer, more diffuse gas that can be detected further from galaxies. In addition to H I 1216 we investigate Mg II 2796, Si II 1260, C II 1335, Si III 1206, Si IV 1394, C III 977, and O VI 1032 to compare to observations of those ions. These metal lines have good observational constraints at low redshift, and probe a range of ionization energies, as shown in Table 4.1.

#### 4.4 Comparison of Direct Observables

We now show a direct comparison between our simulations and COS-Halos data. This work represents the first direct comparison of the *ezw* and *cw* models against observations of absorption lines in targeted LOS at low redshift.

##### 4.4.1 Overall CGM Absorption

The most direct absorption line observable is the equivalent width. We first present results of the the summed equivalent width divided by the total pathlength ( $dEW/dz$ ) versus impact parameter. We calculate  $dEW/dz$  by summing the equivalent width in all LOS probed at that impact parameter and dividing by the total pathlength (within  $\pm 600$  km/s) represented by all LOS at that impact parameter. This sum is a useful diagnostic because, to first order, whether our simulations are producing the right amount of hydrogen and many metals are in the CGM around these galaxies.

Figure 4.1 shows  $dEW/dz$  in H I and metal ions, where we show our probed metal ions in order of increasing ionization energy. We bin both observed and model points in 25 kpc bins. The observed COS-Halos points are shown in black, the observed model values in solid blue for *ezw* and dotted red for *cw*. The error bars on the model points are range bars, showing 16%-84% of the model values. The errors on the observed points represent the average errors on all constrained detections in the 25 kpc bins. These errors do not include errors on LOS that are upper limits, lower limits, or non-detections; hence the errors shown here are a lower limit on the actual error. The errors on the model points have been slightly offset horizontally for ease of viewing.

Overall, for most metals, there is a the general trend of increasing absorption at lower impact parameters. There is a notable trend with ionization potential:

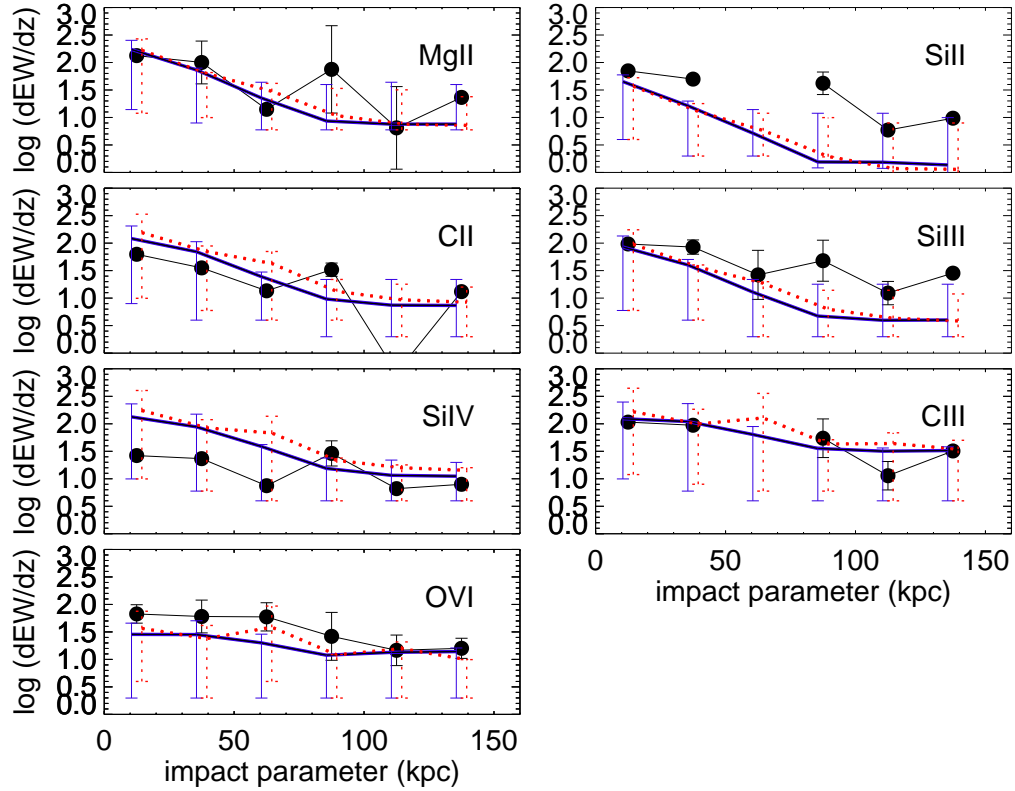


Figure 4.1: Summed equivalent width divided by total pathlength ( $dEW/dz$ ) over all LOS at a given impact parameter, as a function of impact parameter. Black points are from the COS-Halos dataset, with error bars averaged from well-constrained detections only, no limits or non-detections. Blue solid lines are for the ezw model, red dotted lines from the cw models. Both models have range bars showing 16%-84% of the model values. The errors on the model points have been horizontally offset slightly for easier viewing.

low ions like Mg II have sharper dropoffs with impact parameter in the model values than higher ionization species C III and O VI. This highlights the trend that low ions tend to arise closer to galaxies (Ford et al., 2013a). All these trends are true in both the observations and the simulations.

Examining the trends more closely, Mg II and both C II and C III are well-reproduced in the model, while the low Si ions are underproduced and Si IV is overproduced. Note that owing to very low statistics, the Si II errorbars are likely an underestimate. O VI is underproduced in the models, which is a recurring trend as we will see in upcoming comparisons. Nonetheless, overall the agreement is generally quite good, and suggests that the amount of CGM enrichment in both these simulations is roughly in accord with observations. The similarity in the predictions of the two wind models is striking, particularly since the amount of CGM metals and the phase space distribution of the gas in these two models is somewhat different (Ford et al., 2013b).

#### 4.4.2 Equivalent Widths vs. Impact Parameter

While the cumulative equivalent width provides a global measure of the overall absorption strength, the median equivalent width versus impact parameter is the key indicator of how the absorption is distributed within the CGM as a function of distance from galaxy.

Figure 4.2 shows the equivalent width versus impact parameter for COS-Halos data compared to our simulations, for our set of probed ions. Here we have placed the ions in order of increasing ionization potential from low to high. The black points are from the COS-Halos dataset. The circles represent detected values while the up and down facing triangles are lower and upper limits, respectively. Error bars are included in black, in many cases they are smaller than the size of the symbols. Note that the detection thresholds for each ion are given

in Table 4.1.

The blue crosses and red diamonds show the results for the ezw and cw models, respectively. These points represent the median equivalent width of all LOS with detections above the threshold at a given impact parameter. The error bars on the model points span the 16-84% range of EW values at that impact parameter, to illustrate the scatter in EW at a given impact parameter. To avoid clutter, we only show the model error bars for points  $\approx$  every 25 kpc.

It is important to note that Figure 4.2 conflates the trends between stellar mass and impact parameter, owing to the fact that we have produced a matched sample impact parameters for the COS-Halos galaxies (as shown in Figure 4.3). As such, the model points do not decrease smoothly with impact parameter, as was seen in our previous work where we selected narrow bins in halo mass (Ford et al., 2013a). Instead, some points at larger impact parameters have higher equivalent widths than at smaller impact parameters, reflecting the dependency on both impact parameter and mass, as seen in Ford et al. (2013a). Additionally, this degeneracy washes away some trends with ionization potential: the equivalent widths of the low ionization species do not drop off as steeply as found in Ford et al. (2013a,b). This similarly impacts Figure 4.1. These issues are more prominent for the observed points than the simulation points, since the simulations points are averages from a larger sample.

For H I, both models are in broad agreement with the data across the 0-150 kpc range, showing strong absorption in every line of sight. The typical EW is much higher than seen in random lines of sight through the IGM (Davé et al., 2010; Ford et al., 2013a), showing that there is substantial cool gas within these halos. There is little sensitivity to winds, at least as can be discriminated from the COS-Halos data, which is reminiscent of the lack of sensitivity to winds in the

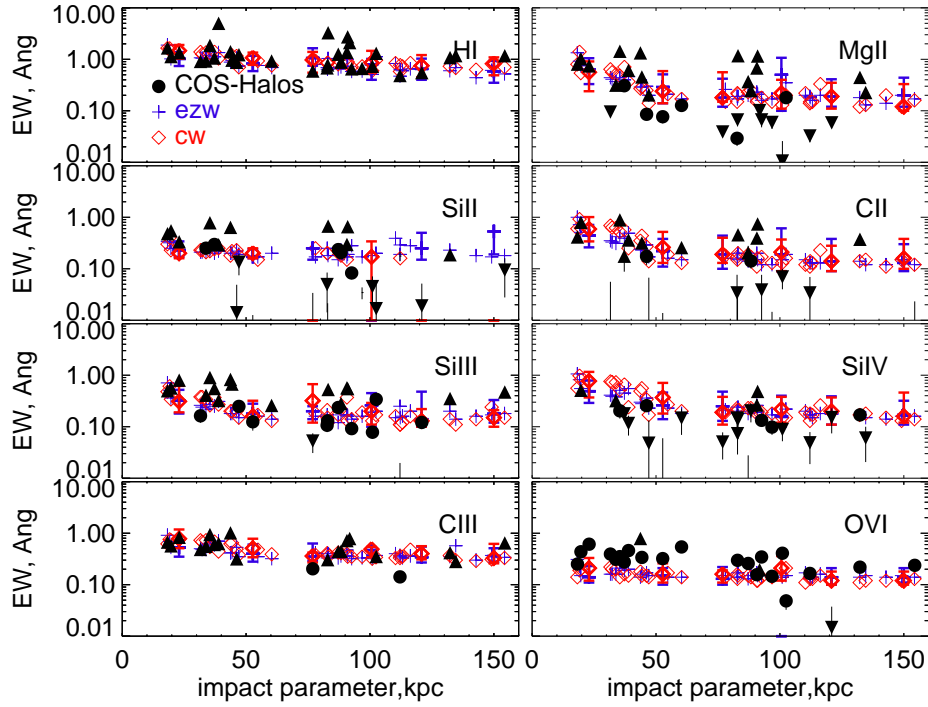


Figure 4.2: Equivalent width vs. impact parameter for observed points (black — circles for exact values, up and down facing triangles for lower and upper limits respectively); as well as ezw (blue crosses) and cw (red diamonds) models. Ions are ordered according to increasing ionization energy (right to left, top to bottom). See Table 4.1 for detection thresholds. Model points do not smoothly decrease, owing to degeneracy between stellar mass and impact parameter.



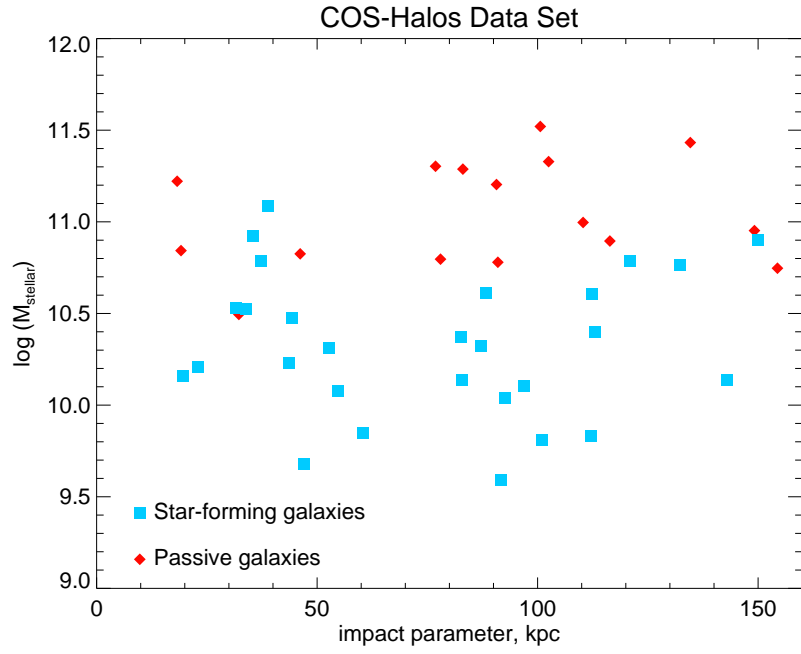


Figure 4.3: Stellar mass vs. impact parameter for the observed COS-Halos data set. Star forming galaxies are separated from passive galaxies at  $\text{sSFR} = 10^{11} M_{\odot}/\text{yr}$ , as given by Tumlinson et al. (2011).

$\text{Ly}\alpha$  forest (Davé et al., 2010). There are however a small number very strong absorbers, with lower limits above most of the simulation points; constraining the actual equivalent width in these systems may provide an interesting challenge to models, if they suggest a larger covering fraction of very strong H I than predicted. But current uncertainties prevent any strong constraints emerging from these few systems.

The metal lines provide a more direct test of pollution from galactic outflows. In general, both models provide an excellent match to the mean trend seen in the observations, with the possible exception of Si IV and O VI (discussed below). This is a non-trivial success of these galactic outflow models in sufficiently enriching the CGM to observed levels. Though we do not show it, a model without winds would dramatically fail this basic test, as discussed in Ford et al. (2013a).

While the general trend is good, for the low ions (Mg II, Si II, C II, and Si III), the scatter is substantially larger in the data than in the simulations. This could reflect variations in the ionization conditions or metallicities that are not properly captured within our simulations. Recall that we assume a spatially-uniform metagalactic ionizing background with no local contribution from the nearby galaxy or shielding from dense regions; these assumptions may need to be relaxed if we want to capture detailed variations properly, though doing so would require full radiative transfer simulations that are prohibitively expensive.

The mid and high ions tend to show smaller observed scatter than the low ions, more comparable to that seen in the simulations. Since low ions tend to arise closer to galaxies and in denser gas (Ford et al., 2013a), this suggests that locally-varying ionization conditions, and not locally-varying metallicity, is responsible for the larger scatter in the low ions.

The two minor but clear discrepancies in the overall level absorption between

models and data are for Si IV and O VI, and they are in the opposite sense – the simulations produce slightly too much Si IV, and somewhat too little O VI, with both trends exacerbated at low impact parameters such that the discrepancy is  $\times 2 - 3$  there. This may suggest that the overall phase of the CGM gas is not well modeled in these simulations, in the sense that there should be more hot diffuse gas that gives rise to high ions and less warm diffuse gas that gives rise to mid-ions. Details of wind implementation can strongly impact the phase of CGM gas. For instance, the models of Hummels et al. (2013) run with the AMR hydro code Enzo show substantially hotter CGM gas; it remains to be seen if those models are in better detailed agreement with COS-Halos data. This highlights the importance of a proper treatment of wind propagation, heating, and mixing, which is a challenging problem in current simulations, and shows that detailed comparisons to data can provide interesting constraints on these processes.

Somewhat disappointingly, the two wind models are in good agreement with each other and the COS-Halos observations do not obviously discriminate between them. This is surprising since previous work by Ford et al. (2013a) showed large differences in absorption line profiles in every ion between a cw and a momentum-driven wind model similar to ezw. While differences between ezw and cw can be found in other diagnostics (Davé et al., 2013) and will be more prominent in other CGM statistics that we explore later, for the equivalent widths at least there are not large differences between models. We will explore the reasons for this in later sections.

#### 4.4.3 Covering Fractions

Another easily-accessible observational statistic is the covering fraction of a given ion, to get a sense for how patchy the CGM absorption is. This is because both observations and simulations suggest the CGM is multi-phase (Tripp et al., 2008;

Ford et al., 2013b) We define covering fraction as the fraction of LOS with a detection above a given ion-specific threshold (see Table 4.1).

Figure 4.4 shows the covering fraction as a function of impact parameter for our set of ions. As in Figure 4.2, we plot ions from low to high ionization potential. The observed data points are binned from 0-75 kpc and 75-150 kpc. The solid black line represents the median covering fraction, and the dotted black lines represent the uncertainties. The models are plotted as individual points, because in the simulations we have multiple LOS at each impact parameter and are able to define a unique covering fraction at each impact parameter. In this manner one can get a sense of the variability in covering fraction as a function of impact parameter, albeit with the same degeneracy in stellar mass noted earlier.

To get a sense of the dependence on mass versus impact parameter, we have separated the model points into low mass and high mass bins. The separation between low and high mass is  $M_{\text{stellar}} = 10^{11} M_{\odot}$ , slightly above the median stellar mass of the COS-Halos dataset  $M_{\text{stellar}} = 10^{10.6} M_{\odot}$  but the mass at which quenching becomes dominant in the ezw model (the cw simulation does not include a quenching model). Points representing low stellar masses are open, those representing high stellar masses are filled. There are no clear trends with stellar mass in the model points, however, showing that for the covering fractions the trends with impact parameter are much stronger than those with stellar mass.

For H I, the simulations almost always have unity covering fraction above its detection threshold of  $0.2 \text{ \AA}$ . The covering fraction in COS-Halos is also very close to unity, but formally slightly below. The high covering fraction of H I is noted in the COS-Halos sample for both star-forming and passive galaxies (Thom et al., 2012).

We note that we are able to reproduce these high H I covering fractions in pas-

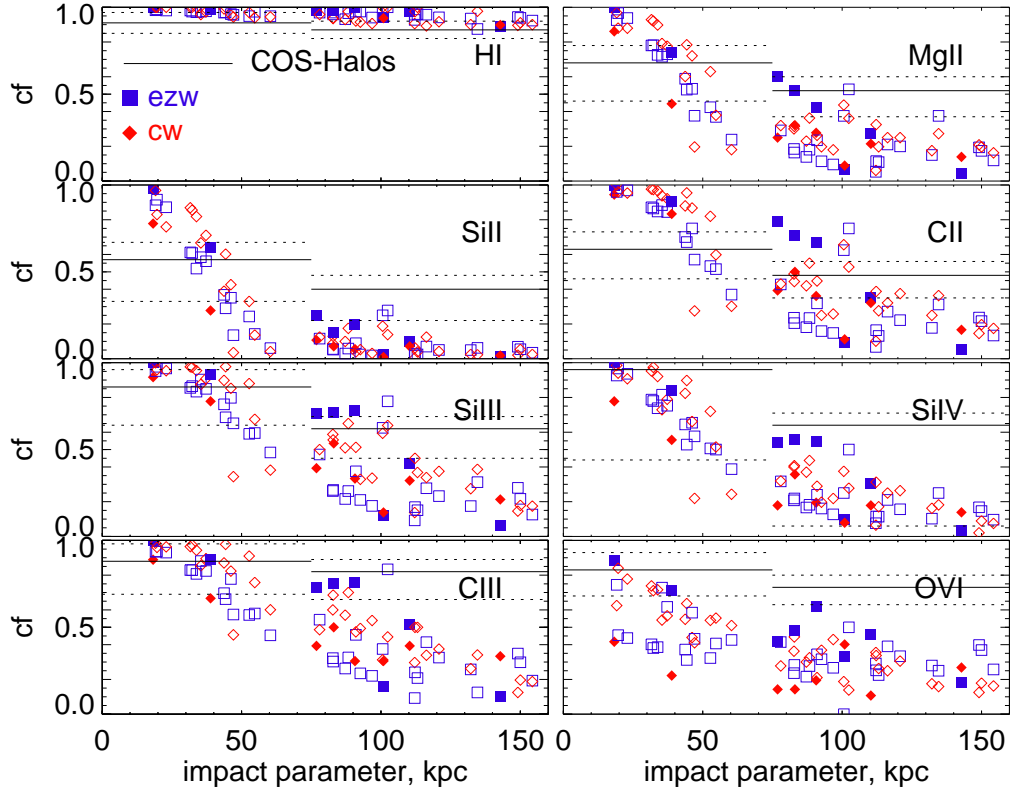


Figure 4.4: Covering fraction of COS-Halos data (black solid lines are values, black dotted lines are errors), compared to model points from the ezw (blue squares) and cw (red diamonds) simulations. Open symbols are plotted at impact parameters with corresponding low stellar masses ( $< 10^{11} M_{\odot}$ ), filled symbols are for high stellar masses.

sive systems with our heuristic quenching prescription (present in the ezw model but not the cw model). Figure 4.5 shows the specific star formation rate (sSFR) vs. stellar mass for ezw (blue) and cw (red) models. We include only those galaxies selected to match the COS-Halos LOS. Many of the massive galaxies in ezw have zero SFR, and those quenched galaxies are plotted at the bottom as downward facing triangles. Of the 48  $M_* > 10^{11} M_\odot$  galaxies in the ezw sample, all but 9 are quenched, with sSFR=0. Yet, the high-mass points in Figure 4.4 still reproduce the observed H I data fairly well. Hence this particular heuristic quenching model does not remove H I from halos, although it adds substantial energy to the halo by heating ISM gas to well in excess of the virial temperature. While we are not claiming that this lends physical validity to our heuristic quenching model, we note that such data could provide interesting constraints on more physically-motivated models of quenching (e.g. Gabor, 2013).

Further exploring Figure 4.4, we see that for low ions (Mg II, Si II, C II, Si III, and C III) the models generally agree with data at impact parameters 0-75 kpc but drop below the data at larger impact parameters. For mid and high ions Si IV and O VI however, the model covering fractions are already too low at all impact parameters, with the match worsening at higher impact parameters. While there is scatter in the model points, there is not a single impact parameter bin in a single ion where one model is consistently different from another. Rather, both models match (or mismatch) the data in similar ways.

The mismatch at higher impact parameters has three possible origins: there could be not enough metals in the simulation, the metals could be in other ionization states not shown here, or the metals could be in the wrong spatial distribution which could happen if the metals were not mixed properly. The reasonable match to equivalent widths in the previous section suggests that the total amount

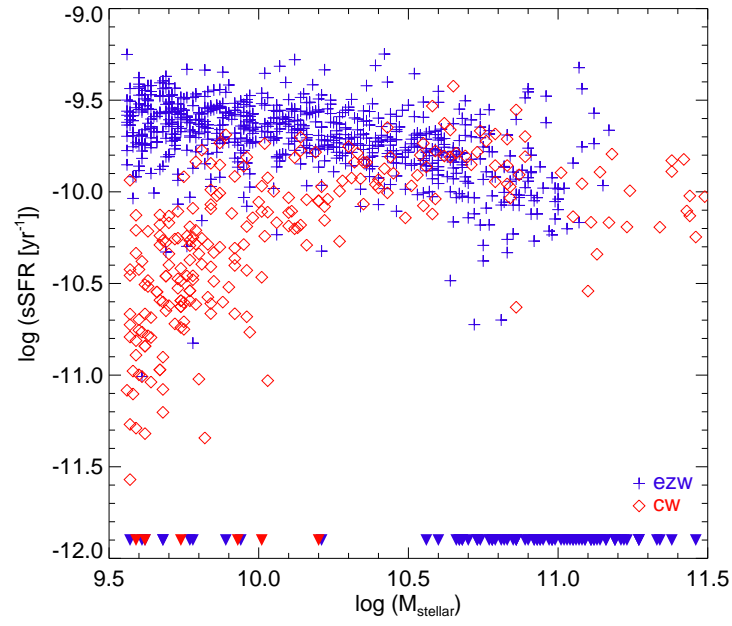


Figure 4.5: sSFR rate vs. stellar mass for the galaxies in the ezw (blue) and cw (red) models that match the COS-Halos LOS. Some galaxies have  $\text{sSFR}=0$ , those are plotted as downward facing triangles at the bottom of the plot.

of metals is roughly correct. The fact that the covering fraction is low in *all* ions probed (e.g. in Si II, Si III, and Si IV) would suggest that they are not hidden in other ionization states. Hence by elimination we are generally left favoring the final interpretation, that the metals are there but are poorly or incorrectly mixed. We will also favor this interpretation for examining ion ratios in the next section.

In our simulations, we do not mix metals into CGM gas from the particles that are ejected from the ISM, and hence it is perhaps not surprising that there is too little metal mixing in our models. It is not obvious how much mixing should occur; again, it is challenging to model mixing of outflowing gas properly. Nonetheless, it is interesting that the covering fraction can potentially provide a good constraint on this crucial physical process of how outflows and the CGM interact.

#### 4.4.4 Ion Ratios

Ion ratios provide a complementary test for the physical conditions of the absorbing gas. Ratios between metal ions and hydrogen provide an estimate of the metallicity in the gas traced by that ion, while ratios between ions of the same element provide a constraint on the physical conditions of the gas. Unfortunately, owing to the paucity of data in COS-Halos, we are limited to studying ratios of ion equivalent widths summed over 600 km/s intervals, which likely erases some of the detailed information about physical conditions through the CGM. Nonetheless, this still provides an interesting constrain on CGM properties in our simulations.

Selected ion ratios are shown in Figure 4.6. As before, COS-Halos data is plotted in black, and model points (ezw: blue crosses, cw: red diamonds) represent the median value of the ratio at each impact parameter. For the observed points, downward facing triangles indicate that the ratio is an upper limit, upward fac-



ing triangles indicate the ratio is a lower limit, circles indicate an actual value, and diamonds indicate a less constrained value (for example, and upper limit of one ion divided by the upper limit of another). In the left panels, we plot the log of ratio of equivalent widths of a low, mid, and high ion relative to H I, as a probe of the metallicity of gas traced by that range of ionisation potentials. In the right panels, we show the ratio of two Si and C lines, as well as a ratio of a low (Mg II) to high (O VI) line.

The low ion ratio (Mg II/H I) shows broadly good agreement with observations, albeit the scatter in the data is much larger than in the models. As we argued earlier, this may arise owing to local variations in ionisation conditions. Nonetheless, there is a hint that the models produce slightly too high a ratio, indicating that the metallicity in the low ionisation gas is a bit too high. There is also a non-trivial offset between wind models, that  $ezw$  is slightly higher than  $cw$ , though the scatter in the data is far too large to discriminate between the models.

The mid ion Si IV shows clearly higher ion ratios in the simulations compared with data. This indicates that the metallicity of warm diffuse gas is too high in these simulations. This is likely the main reason why Si IV equivalent widths are generally too high in the models compared to data (as seen in Figure 4.2). Similarly, the O VI ion ratio is predicted to be too low, suggesting that the hot diffuse phase is not sufficiently enriched in these models, and likewise explains why the O VI equivalent widths are too low. These trends hold true for both wind models, indicating that it is not specific to which wind model we use, but rather may be indicative of an overall failure in the way we implement winds, namely by ejecting cool, unmixed ISM particles. Again, we emphasize that the results are generally in the right ballpark, which is already a non-trivial success, but these ion ratio comparisons further refine and highlight issues with our models,

and demonstrate the ability of COS-Halos data to provide important insights into galactic outflow and ionisation processes in the CGM.

The right panels of Figure 4.6 plot different metal ions against each other, removing the dependence on metallicity and allowing us to test physical conditions of the gas more directly. The ratio of Si II/Si III at low impact parameters shows an overall trend of increasing ratio with impact parameter, and both models and are in good agreement with the data from  $\approx 0$ -100 kpc. Beyond 100 kpc, the ezw model has a higher ratio than data, indicating more cooler gas than observed. Meanwhile, the cw model also shows very low Si II/Si III ratio, typically showing essentially no Si II and hence dropping off this plot at these large impact parameters. The scatter is less than in the ratios versus H I, suggesting that the ionisation conditions giving rise to particular ions are more uniform in the CGM.

The C II/C III (middle right panel) shows a different trend, decreasing outwards as might be expected for less cold and dense gas towards the outskirts of halos. The scatter is tighter, suggesting that this ratio probes slightly more diffuse gas on larger scales. Both models and the data are in excellent agreement, although C II mostly disappears at large impact parameter while the models continue to show absorption in this ion. These plots strongly suggest that the physical conditions in the CGM are properly represented in both wind models.

The Mg II/O VI ratio shows an enormous scatter in the observations, indicating that these two ions arise in different phases that do not trace each other well. There is, perhaps surprisingly, no clear trend with impact parameter, as one might expect for a simple model in which the low ion arises only near the central galaxy and the high ion arises throughout the halo (Ford et al., 2013a). This suggests that the Mg II is occurring throughout the halo, perhaps in satellite galaxies or cold dense clouds interspersed with warmer diffuse gas. Meanwhile, the mod-

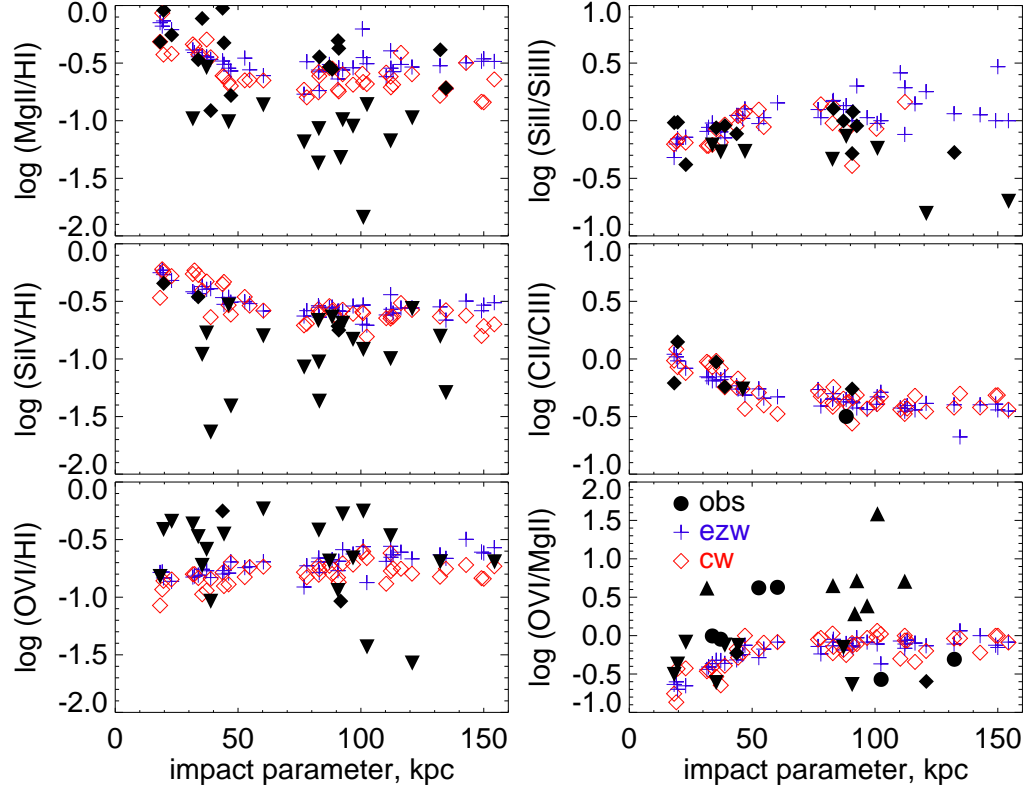


Figure 4.6: Comparison between the log of the ratio of equivalent width (in milliÅ) in the COS-Halos data set (black symbols: circles for constrained values, downward triangles for upper limits, upward triangles for lower limits, and diamonds for less constrained values, such as a lower limit divided by a lower limit), as well as ezw model (blue crosses) and cw model (red diamonds). Left panels show various metals vs. HI, probing metallicity. Right panels show metal ratios, probing physical conditions.

els show a rising trend at small impact parameter which flattens at larger impact parameter. The median ratio does not show a large scatter, suggesting perhaps that Mg II and O VI are more tightly correlated in these models than they should be.

In summary, by examining ion ratios we can isolate trends with metallicity and ionisation state in the CGM as traced by various ions. While there is broad agreement between models and data, clear trends emerge that suggest that the metallicity within certain phases is too high (for warm diffuse gas traced by mid ions) or too low (for hotter diffuse gas traced by high ions). Ion ratios generally show good agreement with data, albeit with smaller scatter and perhaps some discrepancies at large impact parameter ( $\gtrsim 100$  kpc) where the low ions disappear in the data. The differences between our two wind models are small compared to the differences between the models and the data, which may owe to the similar purely kinetic implementation of winds in our two runs. Such ion ratios provide new and interesting challenges to models of CGM gas.

#### 4.4.5 Kinematics

With spectroscopic redshifts for all its galaxies, COS-Halos provides complementary information on the kinematics of absorbing gas relative to the systemic velocity of the host galaxy. In principle, kinematics can distinguish outflowing gas from inflowing, but in practice this is not so definitive (Ford et al., 2013b). Nonetheless, the kinematics provide an additional constraint on CGM models. In this analysis we will no longer sum absorption within  $\pm 600$  km/s of the galaxy, but instead consider individual components in order to elucidate the kinematics.

In Figure 4.7 we quantify where (in a kinematic sense) most of the absorption is coming from in the observed data, and how this compares to the model predictions. To do so, we lay out a colored “checkerboard” for our ezw model, our

favoured model. The cw model gives very similar results, so we do not show it here. On the x-axis, we bin our model data into 25 kpc bins. For each of those bins, we calculate the total column density for all LOS with impact parameters in that bin, for all absorption within  $\pm 600 \text{ km s}^{-1}$ . While column density is not a direct observable in COS-Halos, we use it in this section because we will compare it against velocity offset observations, and in any case we are interested in the kinematic position of the absorption rather than the strength. Then, within each impact parameter bin, we bin our model data into  $100 \text{ km s}^{-1}$  velocity bins.

We color code each block by the fraction of the absorption (i.e. column density) coming from a given velocity interval. Blue blocks indicate that more than 30% of the total column from  $\pm 600 \text{ km s}^{-1}$  is coming from a given velocity interval at that impact parameter, green blocks indicate 20-30%, yellow shows 10-20%, and orange shows less than 10% is coming from that velocity interval. We note that these percentages are for the specific impact parameter bin only, and not for the entire 0-150 kpc range, so each vertical column of coloured blocks is independent. We only consider metals, as the H I kinematics are not expected to be a good tracer of outflows.

For Mg II, Si II, C II, Si III, and C III, there are multiple observed points in the 0-25 kpc bin that are not usually found in the simulations (orange region,  $< 10\%$  of the total column density). Past 25 kpc, however, most of the observed points are in higher probability regions. Interestingly, all of the Si IV absorption is in regions of at least 20% (yellow, green, or blue), regardless of impact parameter. O VI has some observed absorption in the orange regions further out, past 50 kpc, but is otherwise well matched. Note that for this figure we do not sum observed points within  $\pm 600 \text{ km s}^{-1}$  but instead plot individual components.

Overall, both the simulations and the observations suggest that most of the

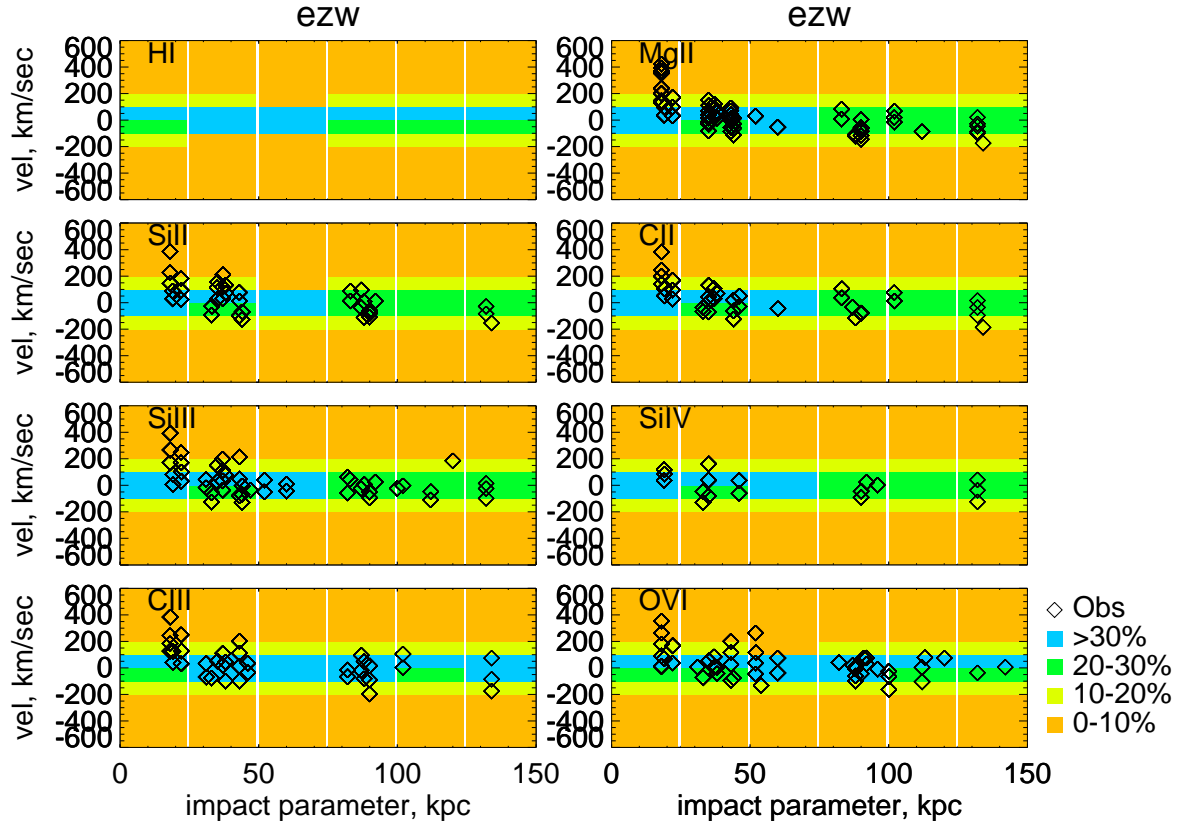


Figure 4.7: Distribution of column density along the line of sight. Ezw model data has been binned both in impact parameter and in velocity space (cw, not shown here, is similar). Blue blocks show that 30% or more of the column density between -600 and +600 is concentrated in that velocity bin. Green shows 20-30%, yellow between 10-20%, and orange less than 10%. Overplotted as black diamonds are the COS-Halos observed points.

absorption occurs roughly within the virial velocity of the galaxy’s halo. Only the absorbers at the smallest impact parameter show a sign for an outflow, and it is difficult to assess the significance of this because it is only one system (with several absorbers within it), and there may be systematic uncertainties in identifying the kinematic centre of any given system. Otherwise, the simulations broadly match the observed kinematics reasonably well, and do not indicate an abundance of strongly outflowing gas at the present epoch, in general agreement with the outside-in enrichment scenario of Oppenheimer et al. (2012).

#### 4.5 Amount and Physical Conditions of CGM Gas

In general, we have found rather modest differences in observational tracers of absorption between our two wind models. While *ezw* is our favoured wind model, in the observations presented above it often does no better or worse than the constant wind model in matching the data. This is somewhat curious, since earlier work (e.g. Oppenheimer & Davé, 2008; Ford et al., 2013a,b) showed significant observable differences between these wind models. The question then arises, what range of CGM physical conditions are represented by these two wind models?

##### 4.5.1 Halo Mass-Stellar Mass Relationship

We start by comparing a basic quantity of our simulated galaxies in order to set the stage for quantifying CGM absorption, namely the relationship between stellar mass and halo mass. Our earlier CGM work compared models at fixed *halo* mass since our expectation was that similar mass halos would contain similar amounts of physical conditions of CGM gas, but in this work we compare models to data at fixed *stellar* mass since that is how the COS-Halos galaxies were selected. However, our two wind models have different halo mass-stellar mass

relationships. This is shown in Figure 4.8. Blue points show the relationship for cw, black for ezw. We add solid lines to show the median values, and cut this plot off at the stellar mass resolution limit of our simulation of  $1.4 \times 10^8 M_\odot$ .

The stellar mass range relevant to this work is  $10^{9.5-11.5} M_\odot$  (see Figure 4.8). In this range the constant wind model has generally a higher halo mass than ezw at a given stellar mass. This is because constant winds are “stronger”, in the sense that they blow more material out of the galaxy, so the less gas is available to form stars. Interestingly, this difference washes out what would otherwise be noticeable differences in equivalent width versus impact parameter for the two wind models. For example, Figure 9 of Ford et al. (2013a) shows that for a momentum-driven wind model (similar to the ezw model used here), higher mass halos have *higher* column density at fixed impact parameter (and similar trends hold for equivalent widths). Figure 14 of that same work shows that for fixed halo mass, the constant wind model has a *lower* column density at fixed impact parameter. So, at fixed stellar mass, the constant wind model has higher halo masses than ezw, which raises its column density at fixed impact parameter. The differences in column due to wind model are thus offset by differences in column due to halo mass. As a result, for the observables presented above, the two wind models match much better at fixed stellar mass than at fixed halo mass.

This brings us to an interesting conclusion, that in our models the CGM metal absorption properties are more tied to the stellar mass than to halo mass. On the one hand, this is surprising since the CGM represents halo gas, which one might think would be more closely tied to halo mass. That said, the metals in the CGM are formed by the stars in the galaxies and then ejected, so perhaps it is not so surprising that the amount of CGM metals is more closely tied to the stellar mass. In Finlator et al. (2008) and Davé et al. (2011b) we argued that the



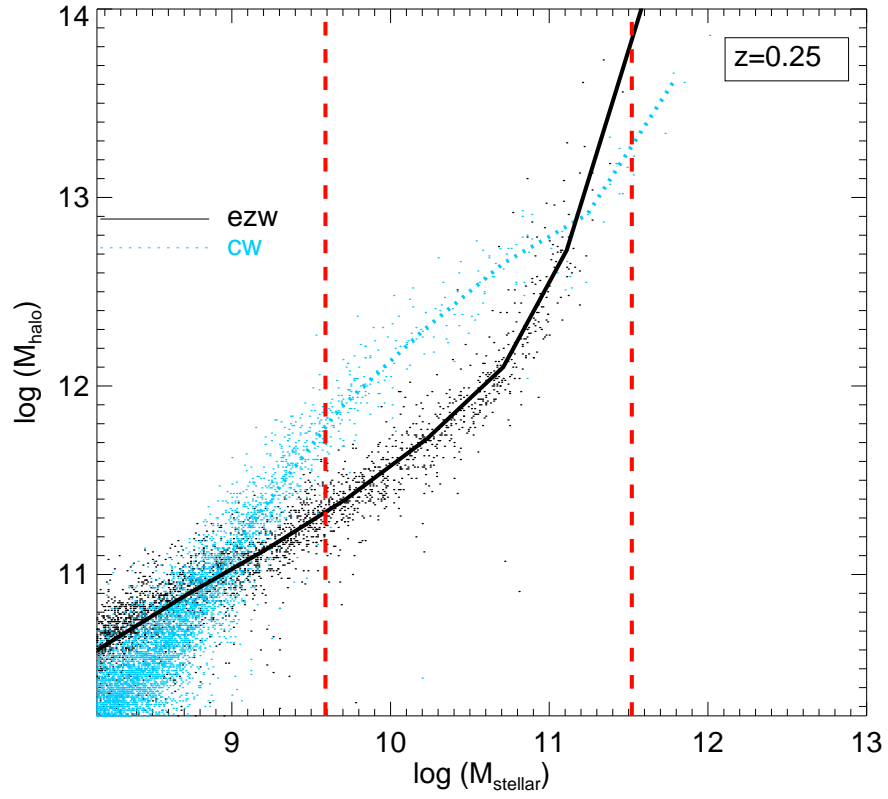


Figure 4.8: Stellar mass-halo mass relationship for central galaxies in the ezw (black) and cw (blue) at  $z=0.25$ . The points show values for individual galaxies, the lines show medians. The stellar mass range of the COS-Halos data set is bounded by dashed red lines.

metals retained inside the galaxy, as traced by the mass-metallicity relation, is strongly governed by outflows tied to stellar mass (required to give rise to a tight stellar mass-metallicity relation), and evidently in these simulations the metals deposited into the CGM are likewise strongly governed by outflows tied to the stellar mass.

#### 4.5.2 Baryonic Fractions within Halos

Different prescriptions for outflows also lead to different fractions of hot, cool, and star-forming ISM gas, which in our simulation we take to be all gas with  $n_H \geq 0.13 \text{ cm}^{-3}$ . Here we examine the breakdown of CGM gas in our two wind models.

Figure 4.9 shows the enclosed baryonic fraction within halos as a function of radius. For this section we restrict ourselves to gas and stars in halos ( $r < R_{\text{vir}}$ ), and to only those galaxies that were chosen for our LOS above. In this manner, we only examine those halos in the stellar mass range of interest. We note that the ezw model is better sampled, as there are 763 halos in that model that are within 0.125 dex in stellar mass of a COS-Halos sight line, vs. 244 for constant winds, but these should still be enough to sample the relevant trends.

Let us examine Figure 4.9 in detail. The baryonic mass fraction in halos is divided by the cosmic baryon fraction ( $\Omega_b/\Omega_M$ ). A value of zero on the y-axis indicates the closed baryon fraction, and shows more or less where the baryons would reside in the absence of outflows (Davé, 2009). The solid black line shows the total fraction of baryons (stars+gas) in halos for the ezw model, as a function of mass enclosed from the selected galaxy. Owing to outflows, this is slightly lower than the universal baryon fraction, the difference shows what is lost from the halo due to outflows. The dotted black line shows the baryon fraction for the cw model, which is substantially lower than for the ezw model. Owing to its

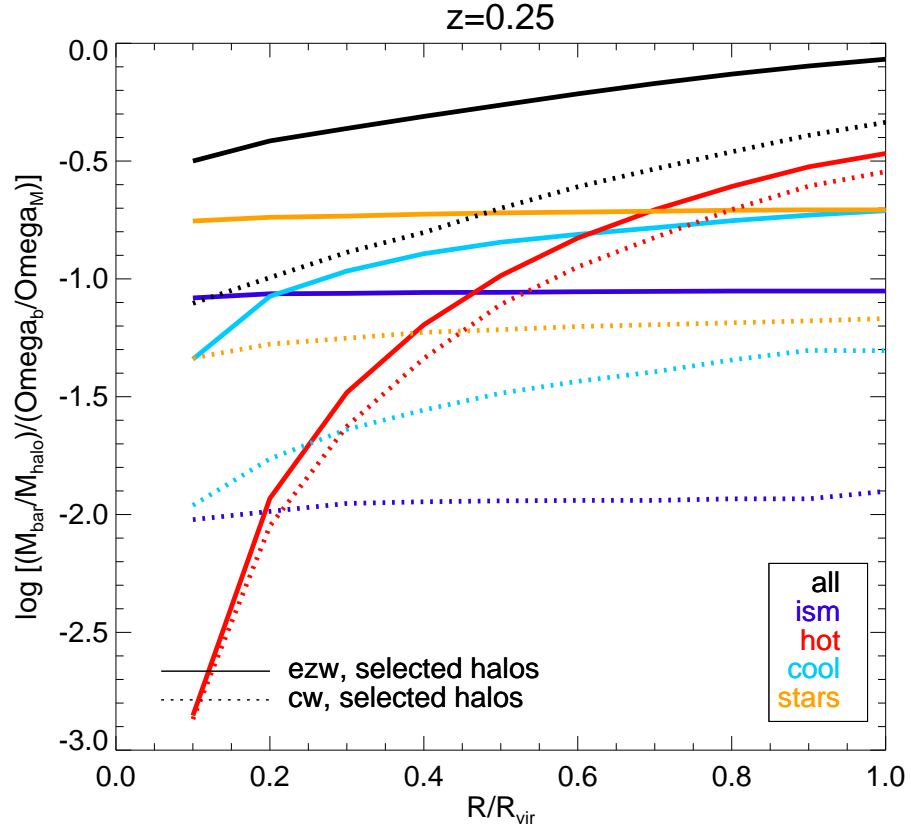


Figure 4.9: Baryonic content of selected galaxies for ezw (solid) and cw (dotted) wind models as a function of enclosed radius. The black lines show total baryon fraction in selected halos for ezw and cw models. Dark blue, red, light blue, and orange lines show fractions of ISM (star-forming) gas, hot gas ( $> 10^5$  K), cool gas ( $< 10^5$  K), and stars, respectively.

larger wind speeds in this halo mass range, the constant wind model carries more of its baryons out of halos into the IGM than the *ezw* model does. Both models push baryons out preferentially from the central regions, where most of the star formation (and hence outflow generation) is occurring.

Of the baryons that remain in the halo, far fewer are in the ISM in the *cw* than *ezw* model, by nearly an order of magnitude. There are fewer stars in the *cw* model as well, though only by a factor of three. The reasons for this are two-fold: more gas is blown out of the ISM, making less available for star formation; and, strong outflows can actually heat the surrounding area, preventing accretion of fresh gas that would otherwise replenish the loss (Oppenheimer et al., 2010; van de Voort, 2011). The radial profile of the ISM fraction is quite flat, owing to satellite galaxies tracing dark matter within the halo.

Interestingly, the hot ( $T > 10^5 \text{K}$ ) baryon fraction is not very different in the two models, and increases strongly with radius. In contrast, the cool baryon fractions are substantially higher in *vzw* as compared to *cw*, and show a slight increase with radius.

In summary, we see that our two wind models distribute baryons differently, even though observationally they generally give similar absorption line properties. This suggests that the amount of CGM gas is not sufficiently constrained by current data to distinguish between viable outflow models.

#### 4.5.3 Mass Budgets of Inflowing and Outflowing Gas

Here we investigate how the baryon cycle operates in different wind models, by further breaking down the mass budgets from the previous section into the amount of inflowing and outflowing gas. To do so, we must first define inflowing and outflowing gas (and the remainder which we shall call ambient gas).

Earlier work (Ford et al., 2013b) examined inflowing and outflowing gas in

detail for the ezw model; here, we wish to contrast ezw with cw. The first step is to characterize inflowing and outflowing gas, described in more detail by (Ford et al., 2013b). Briefly, we identify five different kinematic categories of gas, utilizing the past and future information we have within simulations. Since we are interested in CGM and not ISM, each of these categories excludes gas that is in the ISM at  $z = 0.25$ . The categories are:

1. **Pristine Accretion.** This is gas that is accreting, meaning it is not in the ISM of a galaxy at  $z = 0.25$  but will end up in the galaxy (as either an ISM particle, star particle) or pass through the galaxy before being ejected as a wind by  $z = 0$ . Pristine accretion is accreting gas that has not previously been in a wind.
2. **Recycled Accretion.** This is gas that is accreting, but has been in a wind prior to  $z = 0.25$ .
3. **Young Outflows.** This is gas that was ejected in a wind “recently”, relative to  $z = 0.25$ . We define recently as 1 Gyr prior to  $z = 0.25$  ( $z = 0.36$  for our cosmology), as this is roughly the time a particle would take to leave the halo if it simply got kicked into the a wind, never scattered or slowed down due to forces other than gravity.
4. **Ancient Outflows.** This is gas that was ejected in a wind longer than 1 Gyr ago (before  $z = 0.36$ ).
5. **Ambient.** This is gas that will not accrete onto a galaxy by  $z = 0$ , and has never been in a wind by  $z = 0$ . One can think of ambient material as gas that is neither inflowing nor outflowing, and hence not participating in the baryon cycle.

Since this work is focused particularly on the CGM, we examine the gas breakdown of just particles residing within (defined as  $r < R_{\text{vir}}$ ) any of our selected halos (763 for ezw, 244 for cw). This is shown in Figure 4.10. The top panels are for all non-ISM gas in halos, the lower panels are for metals. The left panels are for ezw, the right panels are for cw. We note these are percentages of total amounts, and that the constant wind model has fewer baryons in halos, as shown in Figure 4.9.

In the upper panels we see a difference in the amount of ambient material in the two wind models. While both models have large percentages in ambient material, the constant wind fraction is slightly higher (93% vs. 85%). Hence the constant wind model has about half the material participating in the baryon cycle compared to ezw, likely due to heating of gas that would prevent inflows, which – if it condensed and formed stars – could later generate outflows. The constant wind model also has less ancient outflow material than ezw in halos. This is because the outflows are more likely to travel outside the CGM, into the IGM, in the cw model. The amount in young outflows is very similar in both models, which makes sense because the wind speeds and mass loading factors in these models are similar around  $L^*$  where the majority of star formation is occurring now. Less material is in recycled accretion in the constant wind model than in the ezw model. This is because winds in the cw model are blown farther out and heated, and are hence less likely to condense back onto a galaxy.

In the lower panels we examine differences in the metal content of halos. We note there are fewer metals in the cw model than ezw: the baryon count is lower (see above), and the metallicity is lower (see Figure 12 of Ford et al. (2013a) for a comparison of cw with a similar momentum-driven wind model). The metals that are generated are more likely to leave the CGM in the cw model than in

momentum-driven wind models (see Figure 13 of Ford et al. (2013a)). As shown here, for ezw the majority of metals come from recycled accretion, however in cw the metals either leave the halo or remain too hot (see Figure 12 of Ford et al. (2013a)) to recycle. As in the total mass, the amount of metals in young outflows is similar between the models. In the ezw model, ancient outflows make up 37% of the metal budget, but in the cw model they are slightly less, about 33%. For the ezw model, the contribution of material that has never been in an outflow (pristine accretion and ambient), is small, which makes sense because most metals are created in outflows. For the cw model, however, there are fewer metals to start with, so the contribution of pristine accretion and ambient material is proportionally higher. In our simulations, metals can be found in gas that has never been in an outflow due to Type Ia supernova, AGB stars, or tidal stripping.

In summary, we have shown that the constant wind model has less baryon cycling compared to ezw. Strong winds lead to a lower stellar fraction, which leads to fewer stellar-driven outflows over time. Of the outflows that remain, strong and fast winds blow more gas into the IGM than in the ezw model, and strong winds also prevent accretion of material. While there are differences in the kinematic state of CGM gas, they do not translate into substantially different observable CGM properties.

#### 4.6 Comparison of Data to Inflows and Outflows in Simulations

A holy grail of CGM absorption line work is to be able to tell if a given absorber is from inflowing, outflowing, or ambient material (e.g. Burchett et al., 2013). Finding observational diagnostics for targeted LOS in simulations was the subject of our earlier work (Ford et al., 2013b), in which we found that low metal ions tend to trace recycled winds while high metal ions traced ancient outflows. Here, we

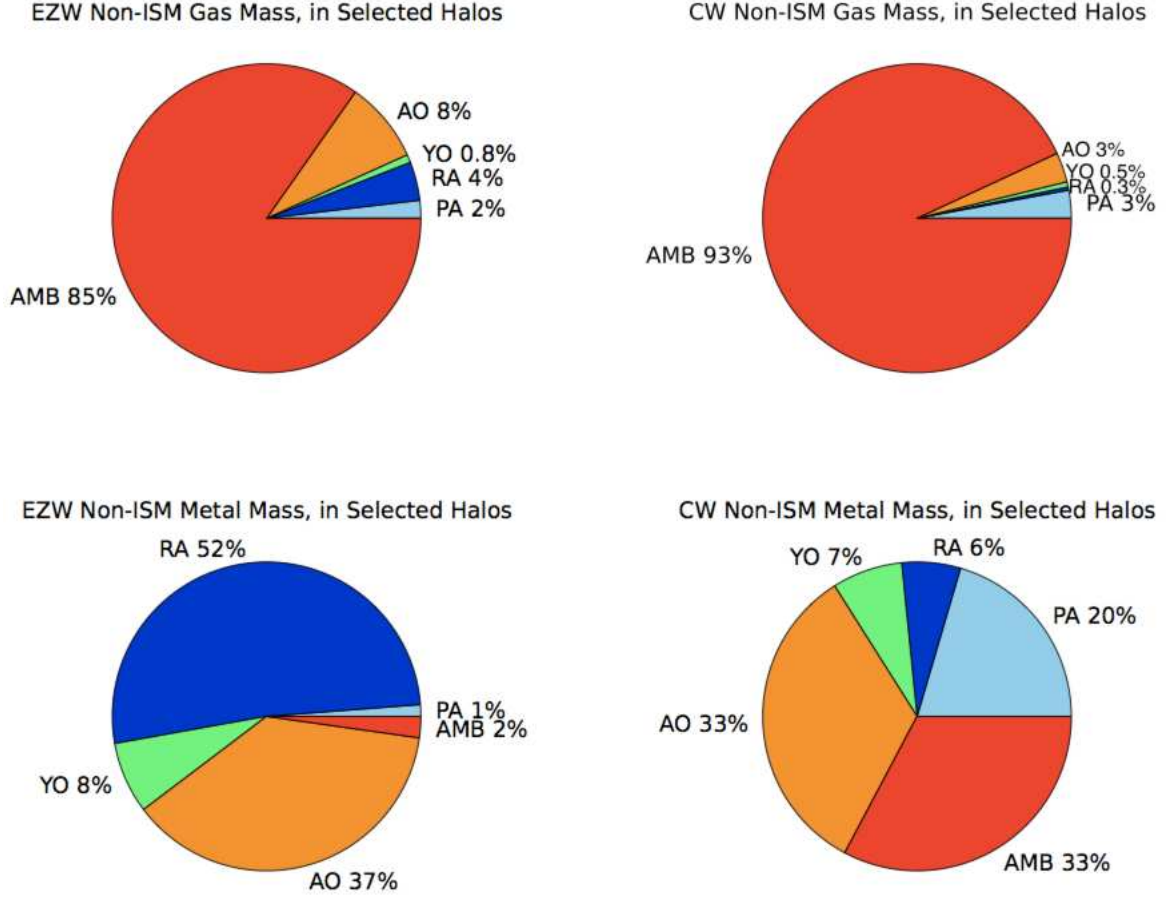


Figure 4.10: Mass budgets of all non-ISM gas within (defined as  $r < R_{vir}$ ) our selected ezw halos (left) and cw halos (right). Top level shows all non-ISM gas particles, lower row is metals only.



aim to check if these trends are evident in our simulated LOS that mimic the COS-Halos dataset, and thereby provide some intuition about how COS-Halos traces the baryon cycle.

In Figure 4.11 we show (black symbols, both panels) the equivalent widths (or upper and lower limits, shown in down- and up- facing triangles, respectively) from the COS-Halos data set, as well as equivalent widths for the model points (ezw, upper; cw, lower) broken out by inflow/outflow category. We calculate these colored points in the manner described in Ford et al. (2013b), by making new simulation snapshots containing *only* those gas particles that fit the definition of the various categories, rerunning LOS through them, generating spectra, and fitting column densities. The ions are ordered from low to high ionization energies, as in earlier figures. Unlike in earlier plots, for the individual categories here we plot the median of all LOS, not just detections. By slicing our simulation particles into sparser boxes, we increase the number of non-detections, which we need to take into account. We then plot the category with the *greatest* contribution to the overall equivalent width at each impact parameter (note that this is less than the total equivalent width that was shown in Figure 4.2).

Let us begin with the upper set of plots for ezw. For H I at impact parameters greater than 50 kpc, the main contributor to the equivalent width is ambient gas, although occasionally ancient outflows are more dominant. At impact parameters  $< 50$  kpc the dominant contribution is from recycled accretion. This is quite consistent with and reinforces the findings of Ford et al. (2013b), even though this sample introduces some degeneracy between stellar mass and impact parameter.

For Mg II, recycled accretion dominates at low impact parameters, but beyond 50 kpc there are sporadic contributions from ambient, pristine accretion, and ancient outflows. This is likely because Mg II absorption (and low ions gen-

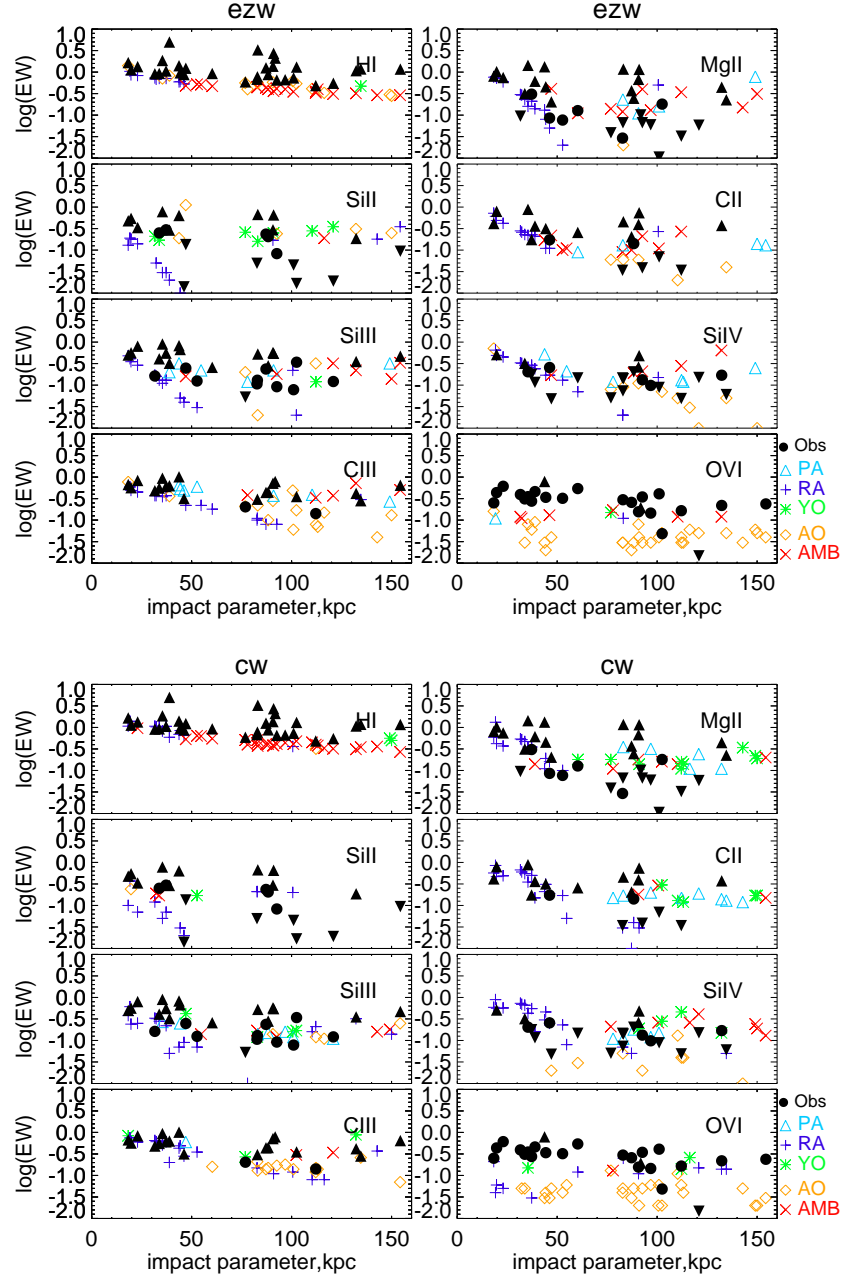


Figure 4.11: Equivalent width versus impact parameter for the COS-Halos data set (black circles, both panels), as well as for ezw (upper) and cw (lower) models (colored triangles), for various ions ordered from low to high ionization energy. The model points represent the median value of all LOS at that impact parameter. Light blue triangles show pristine accretion, dark blue crosses recycled accretion, green asterisks young outflow, orange diamonds ancient outflow, and red crosses ambient. To avoid clutter, we only plot the category with the greatest contribution to the overall equivalent width at each impact parameter.

erally) drops off very quickly with impact parameter (Ford et al., 2013a); beyond  $\approx 75$  kpc the absorption is likely coming from satellites, not the central galaxy, and the contribution from the categories becomes less easy to disentangle. Similarly for the other low ions (Si II, C II, Si III, and C III) absorption at low impact parameter is generally from recycled accretion. However, farther out, there is a mix of contributions from various dynamical states. Indeed, there is even some substantial contribution from pristine accretion and ambient gas, two categories that do not have a great deal of metals in ezw (Figure 4.10). For mid ion Si IV, there is not an obvious trend with impact parameter, although it is more likely that recycled accretion dominates at low impact parameter. In contrast, for O VI, ancient outflows is dominant at nearly all impact parameters, consistent with the idea that O VI is coming from a diffuse halo around the galaxy, built up over long periods of star formation Tumlinson et al. (2011); Oppenheimer et al. (2012).

In the lower panels we show the contributions of inflowing and outflowing material in the cw model. The trends are virtually identical to that seen in the ezw model, with the possible exception that Si IV and even O VI show more recycled accretion dominance at low impact parameter.

This is interesting because young outflows have a similar portion of the metal budget in both models, as seen in Figure 4.10. For O VI, the dominant component at most impact parameters is from ancient outflows, as in ezw.

In summary, the most clear trend is that at small impact parameters ( $< 50$  kpc), recycled accretion dominates the absorption of low ions (including H I), and that ancient outflows dominates O VI absorption. Most H I, meanwhile, arises from ambient gas at larger impact parameters. These trends mimic the expectations from Ford et al. (2013b), hence the broad intuition developed in our previous work can be used to roughly interpret absorption line data from COS-Halos and

similar studies, even though they may be less clear owing to a conflation of impact parameter and halo mass trends.

#### 4.7 Conclusions

In this work, we have focused our simulations on the COS-Halos survey data set in order to compare two wind models as closely as possible with the latest available CGM absorption line observations, as well as to further refine the intuition about the baryon cycle that one can obtain by examining such data. In particular, we have compared the COS-Halos data to absorption of H I, Mg II, Si II, C II Si III Si IV, C III, and O VI in 44 sightlines out to an impact parameter of 160 kpc around galaxies with stellar masses between  $10^{9.5} \lesssim M_* \lesssim 10^{11.5} M_\odot$  at  $z = 0.25$ , roughly mimicking the COS-Halos survey, drawn from cosmological simulations including prescriptive outflows with a constant wind model and our favoured hybrid energy/momentum-driven wind model. Our main conclusions are as follows:

1. Our favoured wind model, ezw, is in broad agreement with key absorption line observables from COS-Halos, namely equivalent width versus impact parameter, covering fractions, ion ratios, and kinematics. The constant wind model also is in good agreement with all these observables, and is not obviously distinguished by the available data.
2. Nonetheless, there are small but non-trivial discrepancies that hint at missing or poorly represented physics in the simulations. These include:
  - The amount of absorption in Si IV, a mid ion, is generally too high compared to data, while the amount in high ion O VI is too low. The ion ratios Si IV/H I and O VI/H I echo these trends. This is likely to be an issue related to how much metals are deposited into the warm and hot

diffuse phases of the CGM, in the sense that our model puts too much metals in warm ( $\sim 10^4\text{K}$ ) gas and not enough in hotter ( $\sim 10^5\text{K}$ ) gas. This occurs in both wind models, hinting that the underlying cause may be the way in which we eject winds as cold, unmixing gas from the ISM.

- The large scatter in the equivalent widths at a given impact parameter for low ionisation lines are not well reproduced in the simulations. This suggests that local effects perhaps owing to local ionisation sources and self-shielding may be necessary to fully explain the distribution of these low ions.
  - The covering fractions for essentially all metal ions are too low at larger impact parameters, and for higher ions they are too low at all impact parameters. Again, this is true for both wind models, which show only small differences. We argue that this may owe to the lack of metal mixing in our simulations, which prevents diffusion of metals into larger surface areas.
3. The constant wind model pushes relatively more baryons out of halos than ezw, and prevents infall by adding more energy to surrounding gas. The net effect is to substantially suppress the baryon cycle in cw relative to our ezw model.
  4. Despite the differences in the baryon cycle, the COS-Halos observation are not able to distinguish between these models. This lack of discrimination is surprising given our previous results in Ford et al. (2013a,b), but is mostly understood by noting that previously we compared models at a fixed halo mass, while here we compare at a fixed *stellar* mass. This suggests that CGM

metal absorption properties are more closely tied to stellar mass than halo mass.

5. Both *ezw* and *cw* models show large contribution from recycled accretion at low impact parameters ( $\lesssim 50$  kpc) in low ions including H I, and from ancient outflows O VI at most impact parameters, in agreement with our previous results (Ford et al., 2013b).

The overall agreement between hydrodynamic simulations including galactic outflows and the most recent observations of CGM gas offers encouraging support for the baryon cycling paradigm. The observations are broadly consistent with the simulation picture of large-scale outflows of gas in  $\sim L^*$  star-forming galaxies (and/or their progenitors), and our models suggest that much of the metals seen in today’s CGM were deposited during the active period of cosmic star formation at  $z \sim 1 - 3$  when outflows are commonly observed (Steidel et al., 2010).

Nonetheless, we have also shown that the COS-Halos observations can provide interesting, if indirect, constraints on the nature of outflows and how they mix with surrounding gas. Our implementation of galactic outflows makes some intrinsic assumptions about mixing that may not be accurate in detail, while other simulation make different assumptions for driving outflows that could in principle result in quite different observable characteristics of the CGM (e.g. Hummels et al., 2013). The generic discrepancies between our models and current observations suggest that we must improve our models of outflow ejection, propagation, and mixing, which is not very surprising given their currently heuristic approach, but our analysis here provides crucial observational constraints on any such refinements. This work is intended to be a starting point to foster more such CGM comparisons within the community, in order to make progress towards a fuller

understanding of the baryon cycle and its implications for the evolution of galaxies and their surrounding gas.

#### 4.8 Acknowledgements

Support for program GO 11598 was provided by NASA through a grant from the Space Telescope Science Institute, operated by the Association of Universities for Research in Astronomy, Inc., under NASA contract NAS 5-26555. Much of the data presented herein were obtained at the W.M. Keck Observatory, which is operates as a scientific partnership among the California Institute of Technology, the University of California and the National Aeronautics and Space Administration. The Observatory was made possible by the generous financial support of the W.M. Keck Foundation. The authors wish to recognize and acknowledge the very significant cultural role and reverence that the summit of Mauna Kea has always had within the indigenous Hawaiian community. We are most fortunate to have the opportunity to conduct observations from this mountain.

Additionally, partial support for this work came from NASA ATP grants NNX10AJ95G and NNX12AH86G, HST grants HST-GO-11598 and HST-GO-12248, NASA ADP grant NNX08AJ44G, NSF grants AST-0847667, AST-0907998, AST-0908334, and AST-133514, and the South African National Research Foundation's Research Chairs program. The simulations used here were run on computing facilities owned by the Carnegie Observatories. Computing resources used for this work were made possible by a grant from the the Ahmanson foundation, and through grant DMS-0619881 from the National Science Foundation.

*Facilities:* Keck: I (HIRES), *Hubble* (COS)

## CHAPTER 5

## CONCLUSIONS

## 5.1 Summary

In this thesis, I have characterized the low redshift CGM using simulations and comparisons to data. In chapter 2, I characterized the physical conditions, extent, and absorption profiles of H I and various metal lines as a function of halo mass and wind model. I found that low ions trace cold, dense regions close to galaxies, and high ions trace warmer, more diffuse regions. I found that the characteristic distance for the CGM is  $\approx \pm 300 \text{ km s}^{-1}$  along the LOS and 300 kpc, although even at 1 Mpc there is still an excess of absorption over random LOS. I also found that, in general, higher mass halos have slightly more absorption of H I and metal lines than lower mass halos. I investigated three different wind models and found differences in metal distribution, density, temperature, and absorption profiles.

In chapter 3 I investigated inflows, outflows, and the baryon cycle. I used a unique particle tracking scheme to characterize all non-ISM gas as pristine accretion (accreting for the first time), recycled accretion (accreting, but has been in a wind before), young outflows (not accreting, outflows less than a Gyr old), ancient outflows (not accreting, outflows more than a Gyr old), and ambient material (neither inflowing nor outflowing, not participating in the baryon cycle). I found that most of the mass comes from ambient material, and nearly half of the metal mass comes from recycled accretion. This contrasts with earlier thinking that all inflows are low metallicity. I presented observational diagnostics of the five different categories: H I absorption mostly comes from ambient material, absorption in low ions like Mg II mostly comes from recycled accretion, absorption from high ions like O VI mostly comes from ancient outflows, and pristine



accretion and young outflows make only minor contributions.

In chapter 4, I compared results from “ezw” (a variable wind model) and constant wind (cw) models to observations from the COS-Halos dataset. I found that, due to selection on stellar mass and not halo mass, many of the differences between cw and ezw cancel out, leaving both models in comparable agreement with the data. I also found that baryons cycle very differently in ezw and cw, with cw allowing for less baryon cycling, since its winds are stronger, blowing more of the gas further out where it is less likely to cool and condense back onto the galaxy.

These efforts represent a significant step forward in our understanding of the low-redshift CGM. The field is just getting started, so there are many opportunities to learn more. In the following section I outline some ideas for next steps.

## 5.2 Next Steps

There are many chances for theory and observation to continue to be used together to further our knowledge of the CGM. Some of the current data have not yet been fully compared to simulations but could easily be (the COS-Dwarves data set on lower mass halos, for example). Moreover, numerous observational efforts currently in prep by Martin et al., Shapley et al., Tumlinson et al., and many others are set to dramatically increase our knowledge of the CGM at a variety of scales and around different galaxy types. Additionally, there are also efforts underway (Gabor et al., Hopkins et al., Keres et al., Faucher-Giguère et al., in prep) to improve simulation methodology and develop more self-consistent wind models. All of those efforts will be extremely important moving forward.

Below are some ideas that I personally find extremely interesting. Because my thesis work shows that the present-day CGM is largely a relic, I would love

to know what happens to the CGM, and the CGM-galaxy connection, at higher redshift. When does the bulk of material build up in the CGM, and how does that relate to the growth rate of the galaxy? There are also some interesting mysteries about the CGM at higher redshift, that, if solved, could tell us something fundamental about galaxy evolution.

### 5.2.1 Evolution of CGM with Redshift

Since different wind models produce distinct CGM properties at low redshift, it is expected that the CGM will evolve differently in contrasting wind models. The question is, how sensitive is CGM evolution to wind model, and what does that tell us about the CGM-galaxy connection? To answer these questions, I would like to track galaxies and their halos over cosmic time, from  $z=0$  to  $z=3$ , for different wind models. In detail, I will ask the following questions:

1. To what extent do the CGM and galaxy grow together? Do they gain mass at the same rate — i.e., does a 20% increase in galaxy mass imply a 20% increase in CGM mass? By tracking total mass in the CGM vs. total mass in the galaxy, I can calculate their relative growth rates.
2. How do different phases of the CGM and galaxy mass evolve? How do the baryonic fractions (hot, cool, ISM, stars) evolve with redshift? This will specify not just how the baryonic content of the halo is growing, but how the composition is evolving as well.
3. What are the relative CGM mass fractions of inflowing, outflowing, and ambient material, and how does this balance evolve with time? I will relate these fractions to the star formation rate (SFR) and galaxy mass. What happens to the CGM during the peak of star formation at  $z = 2$ ? Is this

also the peak of metal-enriched CGM formation? Are winds from non-stellar sources, such as massive black holes, required to explain the observed quenching of star formation?

4. How are physical conditions correlated with star formation rate? Tumlinson et al. (2011) showed different profiles of O VI vs. impact parameter for star-forming and passive galaxies, but the reason for this dichotomy is still unclear. One could gain insight into this by tracking the evolution of metallicity, density, and temperature.

### 5.2.2 Effects of Mergers and Starbursts on the CGM-Galaxy Relationship

In addition to bulk properties described above, it would be very useful to study how the CGM evolves around specific galaxies during mergers and starbursts, formative events with disruptive potential. Results from both simulations and observations suggest that metals in the present-day CGM not only were deposited long ago, but also have somehow remained there (or were re-accreted). How do mergers and starbursts influence the CGM, particularly its metals? To investigate this, one could use higher resolution, zoom-in simulations to address the following issues:

1. What happens to the CGM during a galaxy merger? What fraction of the CGM mass remains in the CGM, is accreted onto the galaxy, or is expelled into the intergalactic medium (IGM)? Does the CGM heat up because of energy injection from the merger, or cool down due to increased density?
2. What happens to the CGM during a starburst? Does its mass increase at a dramatic rate, or is there a time lag? Does it change temperature or metallicity? Where does outflowing gas go during a starburst? Do starbursts

cause such chaotic motion that outflowing gas is trapped, never traveling very far? Or do strong bursts drive greater gas fractions into the IGM? If outflowing gas makes it into the CGM, what happens next? Do starbursts allow for greater cooling, increasing the chances that CGM material accretes back onto the galaxy?

### 5.2.3 Further Comparisons of Wind Models to Observations

Because different wind models predict a variety of different observables, comparisons with data are vital to further constrain the models and indicate which processes and assumptions are most influential. In this thesis I have already begun comparisons at low redshift, but it would be very interesting to extend this to higher redshift. This would include:

1. Tracking the evolution of direct CGM observables — column densities, equivalent widths, covering fractions — in simulations for targeted LOS around galaxies of different masses. I will compare my results to CGM observations at higher redshift (Steidel et al., 2010; Prochaska et al., 2013). This will tell us if our models are working at multiple redshifts, or if they break down at a certain time. Additionally, I will track when these observables are set in simulations, and if they change or stay constant with time. Recent results by Matejek & Simcoe (2012) suggest that the Mg II structure of halos was established very early on and has evolved little since. This is a key CGM puzzle: how can absorption properties vary little when the properties of the galaxy change so much?
2. Investigating the match (or lack thereof) between models and data for dwarf galaxies ( $M_{\text{halo}} < 10^{11} M_{\odot}$ ). This comparison is important because the effects of winds on low-mass galaxies are expected to be fundamentally different

from mid- or high-mass galaxies. When many supernovae explode in a mid/high-mass galaxy starburst, the galaxy's gas can be *disrupted*. However, for a low-mass galaxy, the baryonic content can be nearly *destroyed*, as potential wells are too shallow to contain exploding gas. Also, the halos of low-mass galaxies are generally cooler, changing the way they accrete gas.

3. Comparing the effects of contrasting wind models on baryon distribution, since models spread out baryons in distinct ways. Published observations of high-redshift H I (Rudie et al., 2012) serve as a proxy for the underlying baryon distribution, which I can compare to results from simulations with different wind models to understand what sets the baryon distribution.

In working on the above issues, I will be able to track the CGM through cosmic time, comment on the relevant physical processes, explain the agreement or disagreement of models and simulations, understand how the CGM and galaxy are linked, and say if and how outflows have significant effects on baryon distribution. All of these individually will be significant, but together they have the potential to revolutionize the way we think about galaxy evolution.

## REFERENCES

- Agertz, O., Teyssier, R., & Moore, B. 2009, *MNRAS*, 397, L64
- Aguirre, A., Hernquist, L., Schaye, J., et al. 2001a, *ApJ*, 561, 521
- . 2001b, *ApJ*, 560, 599
- Baldry, I. K., Glazebrook, K., Driver, S. P. 2008, *MNRAS*, 388, 945
- Balogh, M. L., Pearce, F. R., Bower, R. G., & Kay, S. T. 2001, *MNRAS*, 326, 1228
- Becker, G. D., Sargent, W. L. W., Rauch, M., & Calverley, A. P. 2011, *ApJ*, 735, 93
- Behroozi, P. S., Wechsler, R. H., & Conroy, C. 2013, *ApJ*, 770, 57
- Bell, E. F., McIntosh, D. H., Katz, N., Weinberg, M. D. 2003, *ApJ*, 585, L117
- Berlind, A. A., Weinberg, D. H., Benson, A. J., et al. 2003, *ApJ*, 593, 1
- Binney, J. 1977, *ApJ*, 215, 483
- Birnboim, Y., & Dekel, A. 2003, *MNRAS*, 345, 349
- Blitz, L., & Rosolowsky, E. 2006, *ApJ*, 650, 933
- Bordoloi, R., Lilly, S. J., Knobel, C., et al. 2011, *ApJ*, 743, 10
- Bouché, N., Dekel, A., Genzel, R., et al. 2010, *ApJ*, 718, 1001
- Bouche, N., Hohensee, W., Vargas, R., et al. 2012, *MNRAS*, 426, 801
- Bregman, J. N. 2007, *ARA&A*, 45, 221
- Brook, C. B., Stinson, G., Gibson, B. K., et al. 2012, *MNRAS*, 419, 771

- Brooks, A. M., Governato, F., Quinn, T., Brook, C. B., & Wadsley, J. 2009, *ApJ*, 694, 396
- Burchett, J. N., Tripp, T. M., Werk, J. K., et al. 2013, *ApJL*, 779, L17
- Ceverino, D., Dekel, A., & Bournaud, F. 2010, *MNRAS*, 404, 2151
- Chabrier, G. 2003, *PASP*, 115, 763
- Chen, H.-W. 2012, *MNRAS*, 427, 1238
- Chen, H.-W., Lanzetta, K. M., & Webb, J. K. 2001, *ApJ*, 556, 158
- Chen, H.-W., & Mulchaey, J. S. 2009, *ApJ*, 701, 1219
- Chen, H.-W., Helsby, J. E., Gauthier, J.-R., et al. 2010, *ApJ*, 714, 1521
- Chen, H.-W. 2012, *MNRAS*, 427, 1238
- Churchill, C. W., Mellon, R. R., Charlton, J. C., et al. 2000, *ApJS*, 130, 91
- Cooksey, K. L., Thom, C., Prochaska, J. X., & Chen, H.-W. 2010, *ApJ*, 708, 868
- Cooksey, K. L., Kao, M. M., Simcoe, R. A., O'Meara, J. M., & Prochaska, J. X. 2013, *ApJ*, 763, 37
- Danforth, C. W., Shull, J. M., Rosenberg, J. L., & Stocke, J. T. 2006, *ApJ*, 640, 716
- Danforth, C. W., & Shull, J. M. 2008, *ApJ*, 679, 194
- Danforth, C. W., Keeney, B. A., Stocke, J. T., Shull, J. M., & Yao, Y. 2010, *ApJ*, 720, 976
- Danforth, C. W., Stocke, J. T., Keeney, B. A., et al. 2011, *ApJ*, 743, 18
- Danforth, C. W., Tilton, E. M., Shull, J. M., et al. 2014, *ArXiv e-prints*

- Danovich, M., Dekel, A., Hahn, O., & Teyssier, R. 2012, *MNRAS*, 422, 1732
- D’Odorico, V., Calura, F., Cristiani, S., & Viel, M. 2010, *MNRAS*, 401, 2715
- Davé, R., Hernquist, L., Weinberg, D. H., & Katz, N. 1997, *ApJ*, 477, 21
- Davé, R., Hernquist, L., Katz, N., Weinberg, D. H. 1999, *ApJ*, 511, 521
- Davé, R., Cen, R., Ostriker, J. P., et al. 2001, *ApJ*, 552, 473
- Davé, R., & Oppenheimer, B. D. 2007, *MNRAS*, 374, 427
- Davé, R., Oppenheimer, B. D., Sivanandam, S. 2008, *MNRAS*, 391, 110
- Davé, R. 2009, in *Astronomical Society of the Pacific Conference Series*, Vol. 419, *Galaxy Evolution: Emerging Insights and Future Challenges*, ed. S. Jogee, I. Marinova, L. Hao, & G. A. Blanc, 347
- Davé, R., Oppenheimer, B. D., Katz, N., Kollmeier, J. A., & Weinberg, D. H. 2010, *MNRAS*, 408, 2051
- Davé, R., Oppenheimer, B. D., & Finlator, K. 2011a, *MNRAS*, 415, 11
- . 2011b, *MNRAS*, 416, 1354
- Davé, R., Finlator, K., & Oppenheimer, B. D. 2012, *MNRAS*, 421, 98
- Davé, R., Katz, N., Oppenheimer, B. D., Kollmeier, J. A., & Weinberg, D. H. 2013, *astro-ph* 1302.3631
- Davé, R., Katz, N., Oppenheimer, B. D., Kollmeier, J. A., & Weinberg, D. H. 2013, *astro-ph* 1302.3631
- Dekel, A., & Birnboim, Y. 2006, *MNRAS*, 368, 2



- Dekel, A., Birnboim, Y., Engel, G., et al. 2009, *Nature*, 457, 451
- Erb, D. K., Shapley, A. E., Pettini, M., et al. 2006, *ApJ*, 644, 813
- Faucher-Giguère, C.-A., Lidz, A., Zaldarriaga, M., & Hernquist, L. 2009, *ApJ*, 703, 1416
- Faucher-Giguère, C.-A., & Kereš, D. 2011, *MNRAS*, 412, L118
- Ferland, G., Korista, K. T., Verner, D. A., Ferguson, J. W., Kingdon, J. B., Verner, E. M. 1998, *PASP*, 110, 761
- Ferrara, A., Scannapieco, E., Bergeron, J. 2005, *ApJL*, 634, 37
- Finlator, K., Dave, R., Papovich, C., Hernquist, L. *ApJ*, 639, 672
- Finlator, K., & Davé, R. 2008, *MNRAS*, 385, 2181
- Finlator, K., Oppenheimer, B. D., & Davé, R. 2011, *MNRAS*, 410, 1703
- Ford, A. B., Oppenheimer, B. D., Davé, R., Katz, N., Kollmeier, J. A., & Weinberg, D. H. 2013 a, *MNRAS*, 432, 89
- Ford, A. B., Davé, R., Oppenheimer, B. D., et al. 2013, b, *ArXiv e-prints*
- Fukugita, M., Hogan, C. J., & Peebles, P. J. E. 1998, *ApJ*, 503, 518
- Fukugita, M., & Peebles, P. J. E. 2004, *ApJ*, 616, 643
- Fumagalli, M., Prochaska, J. X., Kasen, D., et al. 2011, *MNRAS*, 418, 1796
- Fumagalli, M., O’Meara, J. M., Prochaska, J. X., & Worseck, G. 2013, *ApJ*, 775, 78
- Gabor, J. M., Davé, R., Oppenheimer, B. D., & Finlator, K. 2011, *MNRAS*, 417, 2676

- Gabor, J. M., & Davé, R. 2012, *MNRAS*, 427, 1816
- Gabor, J. 2013, in *IAU Symposium*, Vol. 295, *IAU Symposium*, ed. D. Thomas, A. Pasquali, & I. Ferreras, 350–353
- Genzel, R., Tacconi, L. J., Gracia-Carpio, J., et al. 2010, *MNRAS*, 407, 2091
- Goerdt, T., Dekel, A., Sternberg, A., et al. 2010, *MNRAS*, 407, 613
- Governato, F., Willman, B., Mayer, L., et al. 2007, *MNRAS*, 374, 1479
- Haardt, F., & Madau, P. 2001, in *Clusters of Galaxies and the High Redshift Universe Observed in X-rays*, ed. D. M. Neumann & J. T. V. Tran
- Hellsten, U., Hernquist, L., Katz, N., & Weinberg, D. H. 1998, *ApJ*, 499, 172
- Hinshaw, G., Weiland, J. L., Hill, R. S., et al. 2009, *ApJS*, 180, 225
- Hopkins, P. F., Quataert, E., & Murray, N. 2012, *MNRAS*, 421, 3522
- Hopkins, P. F. 2013, *MNRAS*, 428, 2840
- Hu, C.-Y., Naab, T., Walch, S., Moster, B. P., & Oser, L. 2014, *ArXiv e-prints*
- Hui, L., Gnedin, N. Y., & Zhang, Y. 1997, *ApJ*, 486, 599
- Hummels, C. B., Bryan, G. L., Smith, B. D., & Turk, M. J. 2013, *MNRAS*, 430, 1548
- Jarosik, N., Bennett, C. L., Dunkley, J., et al. 2011, *ApJS*, 192, 14
- Kacprzak, G. G., Churchill, C. W., Steidel, C. C., Murphy, M. T., & Evans, J. L. 2007, *ApJ*, 662, 909
- Kacprzak, G. G., Churchill, C. W., Ceverino, D., et al. 2010, *ApJ*, 711, 533
- Kacprzak, G. G., Churchill, C. W., & Nielsen, N. M. 2012, *ApJL*, 760, L7

- Katz, N., Weinberg, D. H., & Hernquist, L. 1996, *ApJS*, 105, 19
- Katz, N., Keres, D., Dave, R., & Weinberg, D. H. 2003, in *Astrophysics and Space Science Library*, Vol. 281, *The IGM/Galaxy Connection. The Distribution of Baryons at  $z=0$* , ed. J. L. Rosenberg & M. E. Putman, 185
- Kennicutt, Jr., R. C. 1998, *ApJ*, 498, 541
- Kereš, D., Katz, N., Weinberg, D. H., & Davé, R. 2005, *MNRAS*, 363, 2
- Kereš, D., Katz, N., Fardal, M., Davé, R., & Weinberg, D. H. 2009, *MNRAS*, 395, 160
- Kereš, D., & Hernquist, L. 2009, *ApJL*, 700, L1
- Kollmeier, J. A., Weinberg, D. H., Davé, R. & Katz, N. 2003, *ApJ*, 594, 75
- Kollmeier, J. A., Miralda-Escudé, J., Cen, R., & Ostriker, J. P. 2006, *ApJ*, 638, 52
- Lehner, N., Howk, J. C., Thom, C., et al. 2012, *MNRAS*, 424, 2896
- Lehner, N., Howk, J. C., Tripp, T. M., et al. 2013, *ApJ*, 770, 138
- Lilly, S. J., Carollo, C. M., Pipino, A., Renzini, A., & Peng, Y. 2013, *ApJ*, 772, 119
- Martin, C. L. 2005, *ApJ*, 621, 227
- Martin, C. L., Shapley, A. E., Coil, A. L., et al. 2013, *ApJ*, 770, 41
- Matejek, M. S., & Simcoe, R. A. 2012, *ApJ*, 761, 112
- Ménard, B., Scranton, R., Fukugita, M., & Richards, G. 2010, *MNRAS*, 405, 1025
- McKee, C. F., & Ostriker, J. P. 1977, *ApJ*, 218, 148
- Murray, N., Quataert, E., & Thompson, T. A. 2005, *ApJ*, 618, 569

- Murray, N., Quataert, E., & Thompson, T. A. 2010, *ApJ*, 709, 191
- Mulchaey, J. S., & Chen, H.-W. 2009, *ApJL*, 698, L46
- Murray, N., Quataert, E., & Thompson, T. A. 2005, *ApJ*, 618, 569
- Nelson, D., Vogelsberger, M., Genel, S., et al. 2013, *MNRAS*, 429, 3353
- Nielsen, N. M., Churchill, C. W., Kacprzak, G. G., & Murphy, M. T. 2013, *ApJ*, 776, 114
- Ocvirk, P., Pichon, C., & Teyssier, R. 2008, *MNRAS*, 390, 1326
- Oppenheimer, B. D., & Davé, R. 2006, *MNRAS*, 373, 1265
- . 2008, *MNRAS*, 387, 577
- . 2009, *MNRAS*, 395, 1875
- Oppenheimer, B. D., Davé, R., & Finlator, K. 2009, *MNRAS*, 396, 729
- Oppenheimer, B. D., Davé, R., Kereš, D., et al. 2010, *MNRAS*, 406, 2325
- Oppenheimer, B. D., Davé, R., Katz, N., Kollmeier, J. A., & Weinberg, D. H. 2012, *MNRAS*, 420, 829
- Peeples, M. S., Werk, J. K., Tumlinson, J., et al. 2013, *ArXiv e-prints*
- Pettini, M., Shapley, A. E., Steidel, C. C., et al. 2001, *ApJ*, 554, 981
- Pontzen, A., Governato, F., Pettini, M., et al. 2008, *MNRAS*, 390, 1349
- Prochaska, J. X., Weiner, B., Chen, H.-W., Mulchaey, J., & Cooksey, K. 2011, *ApJ*, 740, 91
- Prochaska, J. X., Hennawi, J. F., & Simcoe, R. A. 2013, *ApJL*, 762, L19

- Rees, M. J., & Ostriker, J. P. 1977, *MNRAS*, 179, 541
- Richter, P. 2012, *ApJ*, 750, 165
- Rubin, K. H. R., Prochaska, J. X., Koo, D. C., & Phillips, A. C. 2012, *ApJL*, 747, L26
- Rudie, G. C., Steidel, C. C., Trainor, R. F., et al. 2012, *ApJ*, 750, 67
- Rudie, G. C., Steidel, C. C., Shapley, A. E., & Pettini, M. 2013, *ApJ*, 769, 146
- Rupke, D. S., Veilleux, S., & Sanders, D. B. 2005, *ApJ*, 632, 751
- Savage, B. D., Lehner, N., Wakker, B. P., Sembach, K. R., & Tripp, T. M. 2005, *ApJ*, 626, 776
- Schaye, J. 2001, *ApJ*, 559, 507
- Schaye, J., Dalla Vecchia, C., Booth, C. M., et al. 2010, *MNRAS*, 402, 1536
- Schmidt, M. 1959, *ApJ*, 129, 243
- Shen, S., Madau, P., Conroy, C., Governato, F., & Mayer, L. 2013, *ArXiv e-prints*
- Silk, J. 1977, *ApJ*, 211, 638
- Simcoe, R. A., Cooksey, K. L., Matejek, M., et al. 2011, *ApJ*, 743, 21
- Sembach, K. R., Wakker, B. P., Savage, B. D., et al. 2003, *ApJS*, 146, 165
- Smith, I. W. M. 2011, in *IAU Symposium*, Vol. 280, *IAU Symposium*, 361–371
- Songaila, A. 2001, *ApJL*, 561, L153
- Springel, V., & Hernquist, L. 2002, *MNRAS*, 333, 649
- . 2003, *MNRAS*, 339, 289

- Springel, V. 2005, MNRAS, 364, 1105
- Springel, V., & Hernquist, L. 2002, MNRAS, 333, 649
- . 2003, MNRAS, 339, 289
- Steidel, C. C., & Sargent, W. L. W. 1992, ApJS, 80, 1
- Steidel, C. C. 2001, in Bulletin of the American Astronomical Society, Vol. 33, American Astronomical Society Meeting Abstracts #198, 863
- Steidel, C. C., Erb, D. K., Shapley, A. E., et al. 2010, ApJ, 717, 289
- Stinson, G. S., Brook, C., Prochaska, J. X., et al. 2012, MNRAS, 425, 1270
- Stocke, J. T., Penton, S. V., Danforth, C. W., et al. 2006, ApJ, 641, 217
- Stocke, J. T., Keeney, B. A., Danforth, C. W., et al. 2013, ApJ, 763, 148
- Sutherland, R. S., & Dopita, M. A. 1993, ApJS, 88, 253
- Tacconi, L. J., Genzel, R., Neri, R., et al. 2010, Nature, 463, 781
- Tepper-García, T., Richter, P. Schaye, J., Booth, C. M., Dalla Vecchia, C., Theuns, T., Wiersma, R. P. C. 2011, MNRAS, 413, 190
- Thom, C., & Chen, H.-W. 2008, ApJL, 683, 22
- Thom, C., Tumlinson, J., Werk, J. K., et al. 2012, ApJL, 758, L41
- Tilton, E. M., Danforth, C. W., Shull, J. M., & Ross, T. L. 2012, ApJ, 759, 112
- Torrey, P., Vogelsberger, M., Genel, S., et al. 2013, ArXiv e-prints
- Tremonti, C. A., Heckman, T. M., Kauffmann, G., et al. 2004, ApJ, 613, 898

- Tremonti, C. A., Moustakas, J., & Diamond-Stanic, A. M. 2007, *ApJL*, 663, L77
- Tripp, T. M., Savage, B. D., & Jenkins, E. B. 2000, *ApJL*, 534, L1
- Tripp, T. M., Sembach, K. R., Bowen, D. V., et al. 2008, *ApJS*, 177, 39
- Tripp, T. M., Meiring, J. D., Prochaska, J. X., et al. 2011, *Science*, 334, 952
- Tripp, T. M., & Song, L. 2012, *ApJ*, 746, 173
- Tumlinson, J., Thom, C., Werk, J. K., et al. 2011, *Science*, 334, 948
- Tumlinson, J., Thom, C., Werk, J. K., et al. 2013, *ApJ*, accepted
- van de Voort, P. O. 2011, *MNRAS*, 411, 37
- van de Voort, F., Schaye, J., Altay, G., & Theuns, T. 2012, *MNRAS*, 421, 2809
- Veilleux, S., Cecil, G., & Bland-Hawthorn, J. 2005, *ARAA*, 43, 769
- Wakker, B. P., & Savage, B. D. 2009, *ApJS*, 182, 378
- Walker, Connie 1991, University of Arizona Ph.D. Thesis
- Weiner, B. J. 2009, in *American Institute of Physics Conference Series*, Vol. 1201, American Institute of Physics Conference Series, ed. S. Heinz & E. Wilcots, 142–145
- Werk, J. K., Prochaska, J. X., Thom, C., et al. 2012, *ApJS*, 198, 3
- Werk, J. K., Prochaska, J. X., Thom, C., et al. 2013, *ApJS*, 204, 17
- Werk, J. K., Prochaska, J. X., Tumlinson, J., et al. 2014, *ArXiv e-prints*
- White, S. D. M., & Rees, M. J. 1978, *MNRAS*, 183, 341

- White, S. D. M., & Frenk, C. S. 1991, *ApJ*, 379, 52
- Wiersma, R. P. C., Schaye, J., & Smith, B. D. 2009a, *MNRAS*, 393, 99
- Wiersma, R. P. C., Schaye, J., Theuns, T., Dalla Vecchia, C., & Tornatore, L. 2009b, *MNRAS*, 399, 574
- Wiersma, R. P. C., Schaye, J., Dalla Vecchia, C., et al. 2010, *MNRAS*, 409, 132
- Wolfe, A. M., Gawiser, E., & Prochaska, J. X. 2005, *ARA&A*, 43, 861
- Zu, Y., Weinberg, D. H., Davé, R., Fardal, M., Katz, N., Kereš, D., & Oppenheimer, B. D. 2011, *MNRAS*, 412, 1059